LYMAN-α LASER AND EMISSION STUDIES OF A NON-DEBYE, Z-PINCH PLASMA

A Thesis Submitted for the Degree of

DOCTOR OF PHILOSOPHY

in the

UNIVERSITY OF LONDON

by

KENNETH GEORGE HERBERT BALDWIN

The Blackett Laboratory
Imperial College of Science and Technology
London SW7 2BZ

July, 1983

ABSTRACT

A z-pinch discharge device was designed and constructed specifically to produce a dense, non-Debye argon/hydrogen plasma with only a few particles per Debye sphere. Interferometric measurements indicated that a range of electron densities were obtained between 10^{24}-$10^{25}m^{-3}$, i.e. a factor of ∿3 higher than in previous work in this laboratory. Plasma temperatures of 2-3.5±0.5eV
w :d from the relative abundance of argon ion species lines.
1 ›ye z-pinch source enabled extension of Lyman-α lineshape
s igher densities than had hitherto been obtained, particularly
t density dependence of the previously observed line wing
s eatures which arise from the strong interparticle inter-
a such plasmas.

·der that the Lyman-α opacity as well as the detailed
s lineshapes could be measured, a coherent tunable Lyman-α
s constructed to observe the line wings in absorption. The VUV radiation was generated by phase-matched frequency upconversion, using dye laser radiation focussed into a krypton-filled, frequency tripling cell. The UV dye laser oscillator was pumped by a nitrogen laser, and the tunable output (3620-3700Å) was amplified by a ruby-laser pumped, dye amplifier cell. The 100kW peak dye laser output, when focussed into the tripling cell, produced 10^5-10^6 photons/pulse of Lyman-α radiation.

Due to the lack of an optimal dye laser pumping system, this VUV output was insufficient to carry out an absorption experiment. However emission lineshape studies were undertaken over a range of density conditions, including those achieved previously in this laboratory. No satellites were seen under any conditions, although a small feature ∿+8Å in the red wing of Lyman-α was observed at the highest density ($7.8\times10^{24}m^{-3}$), while some red wing asymmetry was observed at densities of 1.9 and $4.6\times10^{24}m^{-3}$.

ACKNOWLEDGEMENTS

I would like to thank my supervisor, Professor D.D. Burgess, for initiating this project and for encouraging and advising me during my research. His efforts and enthusiasm were also instrumental in enabling me to undertake my studies at Imperial College originally.

I am also indebted to Mr. G. Kolbe from whose experimental expertise I learnt much during the course of my work here. To Mr. P. Ruthven I owe a special thanks for turning my ideas and drawings into reality in the construction of the equipment for this project.

All members of the Spectroscopy Group have my gratitude for their fruitful discussions and advice during the years I have enjoyed working with them.

Finally, I would like to thank the Royal Society, who through the 1979 Rutherford Scholarship supported me during the course of my studies.

TABLE OF CONTENTS

Page No.

CHAPTER 1: SPECTROSCOPY OF NON-DEBYE PLASMAS

1.1 Introduction 14

1.2 The Weak Coupling Approximation in Debye Plasma Shielding 17

- 1.2.1 Dynamic Shielding 20

1.3 Spectroscopic Effects in Dense, non-Debye Plasmas 22

- 1.3.1 Reduction of the Ionization Potential 22
  - 1.3.1.1 Reduction of the Number of Bound States 24
  - 1.3.1.2 Difficulties in the Determination of Continuum Lowering 27
- 1.3.2 Perturbation of the Emitter Energy Levels 29
  - 1.3.2.1 Calculation of the Energy Level Shift for the (n=2) Upper State of Lyman-α due to a Charged Perturber 29
  - 1.3.2.2 Lyman-α Asymmetry 33
  - 1.3.2.3 The Emitter-Perturber Interaction Potential 34
- 1.3.3 Statistical Effects on Line Broadening 35
- 1.3.4 Plasma Oscillations in Non-Debye Plasmas 38
- 1.3.5 Plasma Satellites in Non-Debye Plasmas 41
- 1.3.6 Thomson Scattering in Non-Debye Plasmas 43

1.4 Background to the Present Work 45

CHAPTER 2: SATELLITES TO LYMAN-α ARISING FROM CLOSE EMITTER-PERTURBER INTERACTIONS

2.1 The Formation of Satellite Features 48

2.2 Theoretical Studies of Satellites to Lyman-α 50

2.3 Experimental Observations of Lyman-α Satellites 54

2.4 Effects of Multiple Perturbers on Satellite Features 57

Page No.

CHAPTER 2/continued

2.5 Temperature Dependence of Satellites 59
2.6 Z-Scaling of Satellite Features 60
2.7 Lyman-α at High Densities 63
2.8 Estimate of the Lyman-α Satellite Opacity 65

CHAPTER 3: Z-PINCH DESIGN AND DIAGNOSTICS

3.1 Design Criteria 69
3.2 Diagnostic Limitations in Dense Z-Pinch Plasmas 70
  3.2.1 Continuum Opacity Calculations 72
3.3 Z-Pinch Construction 75
3.4 Z-Pinch Circuitry 77
3.5 Current Waveform Analysis 81
3.6 Spatially Resolved Broadband Emission Studies 84
3.7 Time Resolved Broadband Emission Studies 87
3.8 Spectrographic Survey 92
3.9 Measurement of the Continuum Opacity 95
  3.9.1 Relation of the Opacity Variation to the Z-Pinch Dynamic Behaviour 97
  3.9.2 Wavelength Variation of Continuum Opacity 100
  3.9.3 Effect of the Continuum Opacity on Lineshape Studies 102
3.10 Choice of Interferometry as a Density Diagnostic 103
  3.10.1 Contributions to the Plasma Refractive Index 103
  3.10.2 The Interferometry Experiment 106
  3.10.3 Interpretation of Interferometry Traces 108
  3.10.4 Analysis of Interferometry Data by Abel inversion 111
  3.10.5 Interferometric Electron Densities 117
3.11 Validity of Local Thermodynamic Equilibrium 120
3.12 Calculation of the Ionization Balance in a Dense, Non-Debye, Argon Plasma 124

CHAPTER 3/continued

Page No.

3.13 Choice of a Temperature Diagnostic 128

3.13.1 A Temperature Estimate from the Presence of Higher Ion Stages 130

3.14 Summary 131

CHAPTER 4: THE COHERENT LYMAN-α SOURCE

4.1 Introduction 134

4.2 Theory of Third Harmonic Generation 135

4.3 Previous Schemes for Coherent Lyman-α Generation 138

4.4 Estimate of the Lyman-α Power Required for the Present Absorption Experiment 143

4.5 The Ruby Pump Laser and the Choice of Dye Laser System 145

4.6 The Dye Laser Oscillator 149

4.6.1 The Doubled-Ruby Pumped Oscillator 150

4.6.2 The Nitrogen Laser Pumped Oscillator 152

4.6.3 A.S.E. Reduction in the Dye Oscillator 153

4.7 The Doubled-Ruby Pumped Amplifier System 155

4.7.1 Synchronization of Oscillator and Amplifier Pulses 156

4.7.1.1 Identification of the Population Inversion Peak 156

4.7.1.2 Elimination of Jitter between Oscillator and Amplifier Pulses 158

4.7.2 Amplifier Saturation and Single Amplifier Operation 159

4.8 Generation of Lyman-α Radiation 161

4.8.1 The Krypton Tripling Cell 161

4.8.2 Windows for VUV Transmission 163

4.8.2.1 Crystal Windows 163

4.8.2.2 Capillary Arrays 163

4.8.2.3 Single Capillary, Differential Pumping System 165

4.8.3 The Lyman-α Detection System 165

4.8.4 Tests for VUV Generation near Lyman-α 166

Page No.

CHAPTER 4/continued

4.8.5 Estimate of the Lyman-α Flux 167

4.8.6 Explanation for the Low Tripling Efficiency 167

4.9 Evaluation of the Coherent Lyman-α Source for an Absorption Experiment 169

CHAPTER 5: LYMAN-α EMISSION LINESHAPE STUDIES

5.1 Introduction 170

5.2 Monochromator and Detection System 170

5.3 Monochromator Calibration 173

5.4 Lyman-α Emission Profile Measurements 177

5.4.1 Lyman-α Profiles at the Highest Diagnosed Density (n_e=7.8x$10^{24}$$m^{-3}$; T_e = 3.0eV) 179

5.4.1.1 An Estimate of the Possible Impurity Species 181

5.4.1.2 Examination of Impurity Lines in the Continuum Spectrum 186

5.4.1.3 Detailed Examination of the Lyman-α near Line Wing 188

5.4.2 Lyman-α Profiles at Intermediate Densities (n_e=4.6x$10^{24}$$m^{-3}$; T_e∿ 2.5eV) 190

5.4.3 Lyman-α Profiles at Densities (n_e=1.9x$10^{24}$$m^{-3}$; T_e=2eV) Similar to Baker (1977) 190

5.5 Explanation of the +8Å Feature 196

5.6 Explanations for the Appearance of Baker's Satellites 198

5.6.1 Differences in Plasma Conditions 198

5.6.2 Plasma Satellites to Lyman-α 201

5.6.3 Molecular Hydrogen Lines 202

5.6.4 Impurity Lines 203

5.6.4.1 Scaling of the Satellites Observed by Baker with H/Ar^+ Concentration 207

5.6.4.2 Absence of Impurity Lines in the Present Experiment 208

5.7 Lineshape Asymmetry Results 209

Page No.

CHAPTER 5/continued

5.8 Interpretation of Asymmetry Results 212

5.8.1 Trivial Causes of Asymmetry 213

5.8.2 Quasistatic Ion Quadrupole Asymmetries 215

5.8.3 Calculation of the Total Lyman-α Asymmetry at $n_e=7.2 \times 10^{22}m^{-3}$ 216

5.8.4 Comparison of Experimental and Theoretical Asymmetries 217

5.8.5 Line Shifts as a Cause of Apparent Asymmetry 218

5.8.5.1 The Quadratic Stark Effect 218

5.8.5.2 The Plasma Polarisation Shift 219

5.9 Summary of Lyman-α Emission Profile Results 220

CHAPTER 6: CONCLUSION

6.1 Aims of the Present Project 221

6.2 Creation of the Dense, Non-Debye Z-Pinch Plasma 222

6.3 Development of the Coherent Lyman-α Source 222

6.4 Emission Measurement of the High Density Lyman-α Profiles 223

6.5 Further Calibrated Emission Profile Studies 224

6.6 Subsequent Enhancement of Lyman-α Generation at the Rutherford UV Radiation Facility 225

6.7 Extension of the Plasma Diagnostics 226

REFERENCES 228

LIST OF FIGURES AND TABLES

		Page No.
Figure 1.1:	Laboratory and astrophysical plasmas in relation to the limits of Debye plasma behaviour	16
Figure 1.2:	Comparison of I.P. depression and pressure ionization with the Inglis-Teller limit	25
Figure 1.3:	Contributions to the static energy shift of the Lyman-α π components	32
Figure 2.1:	Occurrence of satellites at extrema in the interparticle difference potential	49
Table 2.1:	Predicted and experimental Lyman-α satellite wavelengths	55
Figure 2.2:	Z-scaling of the electrostatic emitter-perturber potential	62
Figure 3.1:	Continuum opacity vs. wavelength as a function of T_e	74
Figure 3.2 :	Cross-section of the high density linear z-pinch	76
Figure 3.3:	Z-pinch discharge circuitry	79
Figure 3.4:	High voltage trigger circuitry	82
Figure 3.5	Comparison of current waveforms for Baker's z-pinch and the present z-pinch	83
Figure 3.6:	The effect of electrode configuration on the deflection of the discharge current	85
Figure 3.7:	Broadband emission studies of end zones	88
Figure 3.8:	Reproducibility of peak emission traces	89

Page No.

Figure 3.9: Z-pinch operating conditions and 6328Å opacities 91

Table 3.1: Indentification of UV emission lines 94

Figure 3.10: Distribution of Ar ion lines with z-pinch conditions 94

Figure 3.11: Continuum absorption experiment at 6328Å 96

Figure 3.12: Variation of continuum absorption with z-pinch conditions 99

Figure 3.13: Nitrogen laser (3371Å) absorption experiment 101

Figure 3.14: Mach-Zehnder, laser interferometry experiment 107

Figure 3.15: Interferometric traces at 5kV, 6 torr 109

Figure 3.16: Coordinate geometry of Abel inversion 109

Figure 3.17 Abel inverted fringe shift measurements and uncertainty estimates 114

Figure 3.18: Electron density as a function of filling pressure and bank voltage 119

Table 3.2: Electron density and plasma duration required for L.T.E. in an argon plasma 122

Table 3.3: Ionization balance in an argon plasma for n_e=1-10x10^{24}m^{-3} and T_e=2-5eV 126

Figure 3.19 Relative abundance of argon ion stages in L.T.E. as a function of n_e and T_e 127

Figure 3.20: Number of particles per Debye sphere as a function of z-pinch operating conditions 132

Figure 4.1: The effect of krypton pressure on coherent Lyman-α generation (Cotter, 1979) 139

		Page No.
Table 4.1:	Comparison of Lyman-α generation schemes	140
Figure 4.2:	Black body power radiated at Lyman-α as a function of wavelength and temperature	142
Table 4.2:	Absorption coefficients for PPF and PBD dyes	147
Figure 4.3:	Burn pattern of the frequency doubled ruby laser	148
Figure 4.4	The Littman configuration dye oscillator	148
Figure 4.5:	Oscillator tuning range using PPF dye	151
Figure 4.6:	Oscillator tuning range using PBD dye, and techniques for A.S.E. reduction	151
Figure 4.7:	Amplifier fluorescence output showing gain depletion by A.S.E.	157
Figure 4.8:	Relation of the ruby laser pulse intensity to the pulse delay	157
Figure 4.9:	The final dye laser configuration	160
Figure 4.10:	The krypton filled, frequency tripling cell	162
Figure 4.11:	Diffraction pattern from a capillary array	164
Figure 4.12:	The single capillary, differential pumping port	164
Figure 5.1:	The monochromator slit differential pumping system	171
Figure 5.2:	Photomultiplier quantum efficiency vs. wavelength	171
Figure 5.3:	Digitized emission traces at 1250Å	174
Figure 5.4:	Monochromator instrument profile from the NI standard lines near 1200Å	176

Page No.

Figure 5.5: Lyman-α emission profiles from a hollow cathode discharge 176

Figure 5.6: Lyman-α emission profiles at 5kV, 1 torr 179

Figure 5.7: Argon continuum emission at 5kV, 1 torr 182

Figure 5.8: Relative abundances of the ion stages for possible pinch impurity species 184

Table 5.1: Possible impurity lines in the spectra at 5kV, 1 torr 186

Figure 5.9: Detailed Lyman-α line centre profiles at 5kV, 1 torr 189

Figure 5.10: Lyman-α emission profile at 5kV, 2 torr 191

Figure 5.11: Detailed line centre Lyman-α at 5kV, 2 torr 192

Figure 5.12: Lyman-α emission profiles at 5kV, 5 torr 194

Table 5.2: Impurity lines at $\sim$+5Å and $\sim$+8Å from Lyman-α 196

Figure 5.13: Ar ion populations at $n_e = 2\text{x}10^{24}\text{m}^{-3}$ as a function of temperature 200

Table 5.3: Hydrogen Werner band lines near the Lyman-α satellites observed by Baker 203

Figure 5.14: Lyman-α emission spectra obtained by Baker (1977) 204

Table 5:4: Impurity species lines near the Lyman-α satellites observed by Baker 205

Figure 5.15: Asymmetries measured in the Lyman-α profiles at the three conditions in the present z-pinch 211

Figure 5.16: Comparison of the present asymmetries with other predicted and observed asymmetries 214

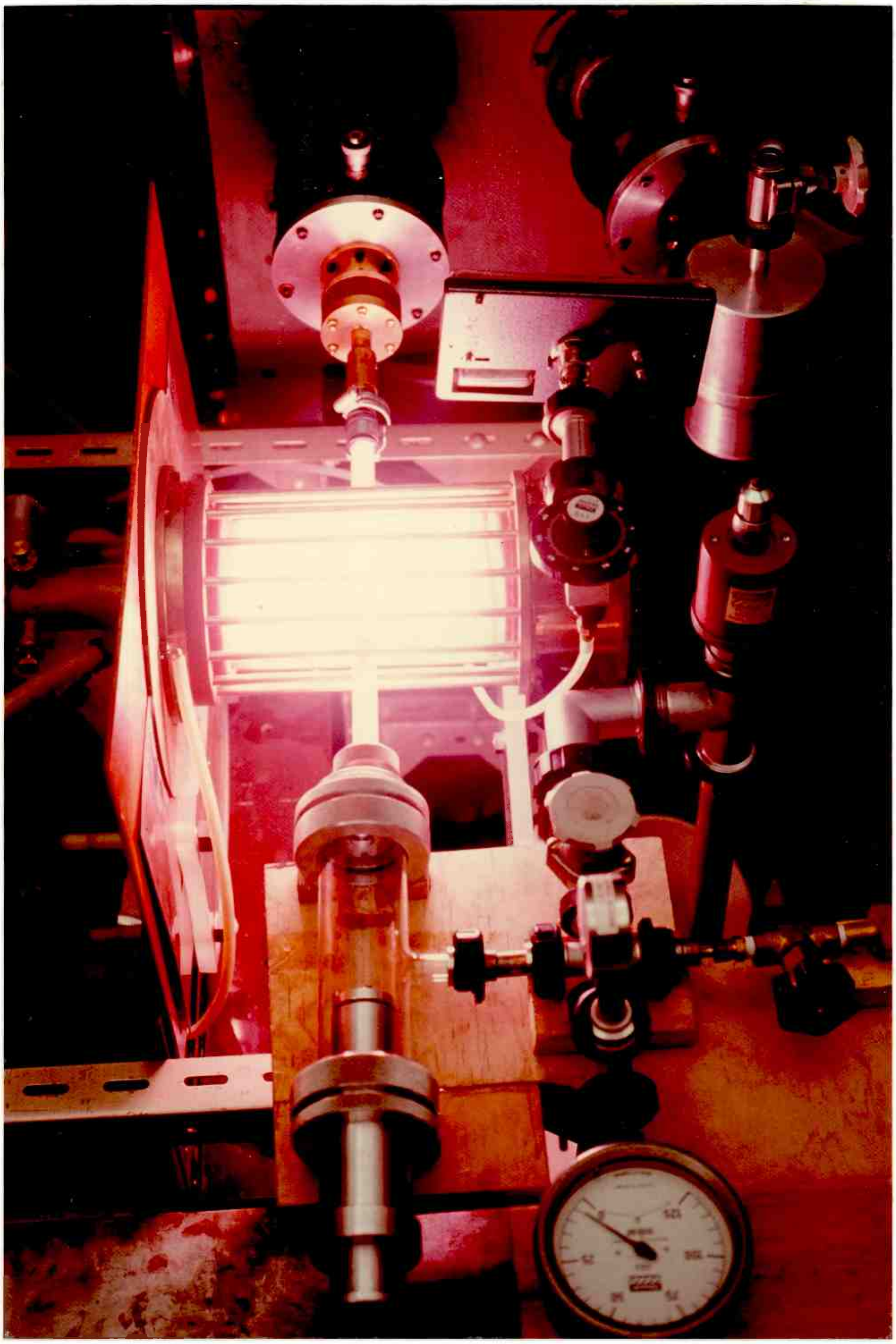

The high density, non-Debye z-pinch plasma device, with the krypton tripling cell (for the generation of coherent Lyman-α radiation) connected to the near side-arm port.

CHAPTER 1

SPECTROSCOPY OF NON-DEBYE PLASMAS

1.1 Introduction

One field curently of interest in modern physics is the study of dense matter. The behaviour of matter at high densities has applications ranging from the theory of metals (e.g. Mattuck, 1967) to the development of inertial confinement fusion (More, 1982). The common element linking these areas of research is the presence of strong interactions between charged particles at high densities.

The strength of the interparticle interaction is defined by the coupling parameter

$$\Gamma = \frac{Ze\phi}{kT} = \frac{Z^2e^2}{4\pi\varepsilon_0 R_0} \cdot \frac{1}{kT} \qquad (1.1)$$

where Ze is the particle charge, ε_0 is the vacuum permittivity and k is Boltzmann's constant. ϕ is the potential due to one of the particles (number density n) evaluated at the mean interparticle separation

$$R_0 = \left(\frac{3}{4\pi n}\right)^{1/3} \qquad (1.2)$$

Γ is thus the ratio of the interparticle electrostatic energy to the particle kinetic energy. Particles are then described as strongly coupled if $\Gamma >> 1$. As will be shown in Section 1.2, this criterion also corresponds to the breakdown of the Debye-Huckel model for plasma behaviour (hence the equivalent use of the terms "strongly coupled" and "non-Debye" when applied to plasmas).

The criterion $\Gamma = 1$ gives the following relationship between the number density and temperature (T) of particles j:

$$n_j(m^{-3}) = 5.15\times10^{13} Z_j^{-6} T_j^3(K) \qquad (1.3)$$

When evaluated for electrons, this criterion can be used to define the boundary between weakly coupled (Debye) and strongly coupled (non-Debye) plasma behaviour. This boundary is shown in Figure 1.1 along with the conditions found in a number of laboratory and astrophysical plasmas (adapted from Burgess, 1978). At very high plasma densities electron degeneracy can also occur, as the inter-electron separation becomes smaller than the electron de Broglie wavelength ($\lambdabar_B$) i.e.

$$\lambdabar_B = \frac{\hbar}{m_e v_e} = \left(\frac{h^2}{8\pi^2 m_e kT}\right)^{\frac{1}{2}} > R_0 \qquad (1.4)$$

Here m_e and v_e are the electron mass and velocity, and h is Planck's constant. Electron degeneracy also occurs in metals, for which the strong coupling regime is in fact regarded as a low density limit. This is because very strong coupling causes the electrons to form degenerate regions of high density at the points of a lattice (Mattuck, 1967), leaving only a few electrons above the Fermi surface that are free to interact (Kittel, 1971).

It is apparent from Figure 1.1 that almost all the plasmas shown lie in the regime described by Debye behaviour. However, there are some laboratory plasma sources which approach the non-Debye limit, such as the laser compressed plasmas produced in research into inertial confinement fusion. Similar values of Γ have also been achieved using simpler devices such as the linear z-pinch e.g. Baker and Burgess (1979) in this laboratory, and Finken et al. (1978) elsewhere. These devices, operating at lower temperatures and densities than laser compressed plasmas, have the advantage of being

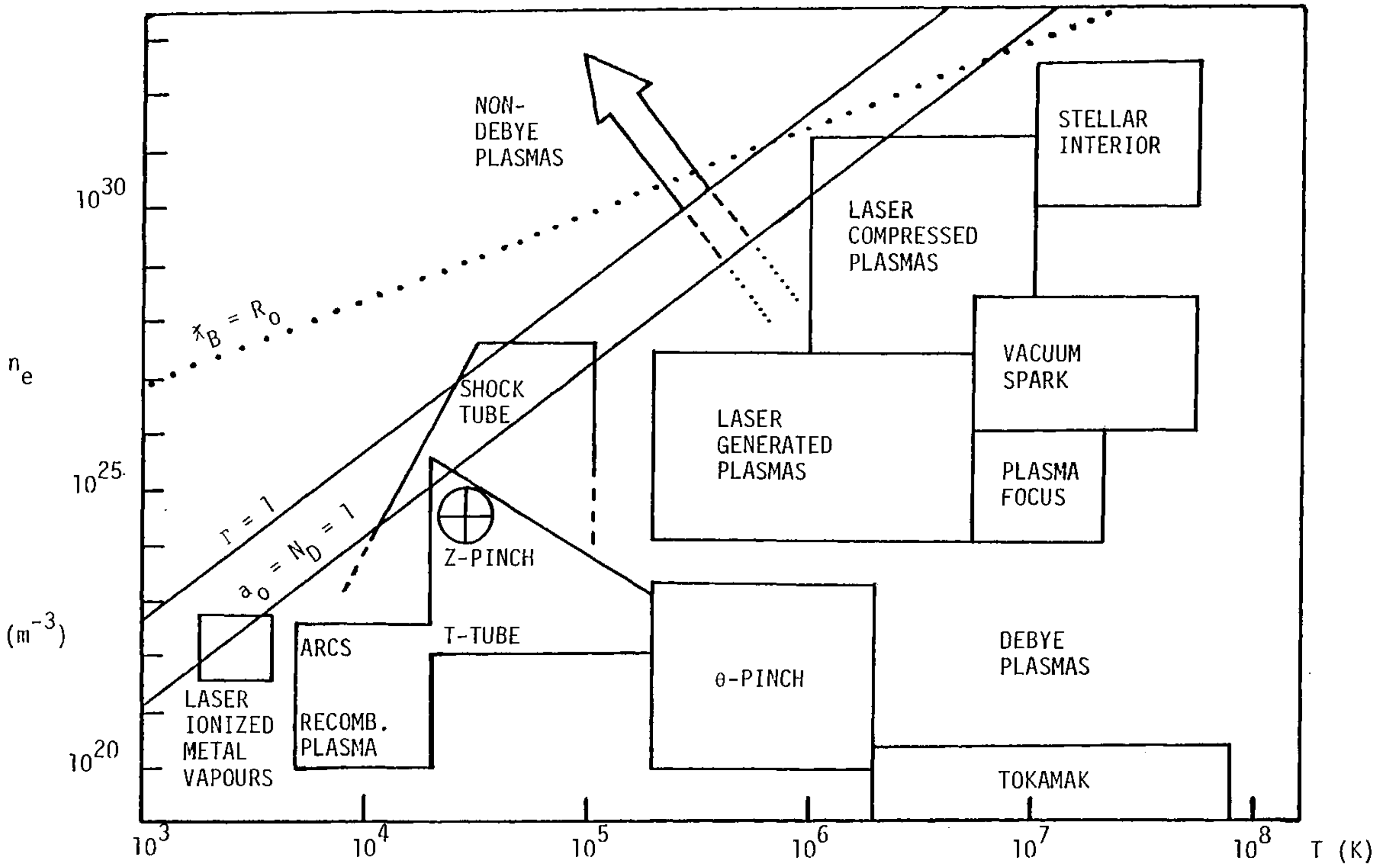

Figure 1.1: Common laboratory and astrophysical plasmas in relation to the limits of Debye plasma behaviour (adapted from Burgess, 1978).

⊕ - the conditions achieved in the present experiment.

more readily diagnosed by conventional spectroscopic methods in the visible and UV. Laser compressed plasmas, on the other hand, are characterized by much higher temperatures and therefore radiate mainly in the x-ray region, for which little accurate spectroscopic data such as cross-sections and rate coefficients, exists (De Michelis and Mattioli, 1981).

Studies of spectroscopic effects that may result from non-Debye plasma behaviour can therefore be more readily undertaken in sources such as the z-pinch device described in this thesis. Some of the expected spectroscopic effects are discussed later in this chapter. However, the absence to date of readily diagnosable sources of non-Debye plasmas has meant that even the limited theoretical work that exists at present (e.g. Vinogradov et al., 1974; Peacock, 1978; Burgess, 1978 and 1982; More, 1982) is still incomplete and subject to verification. Projects such as the one presented in this thesis have as their aim the study of spectroscopic effects brought about by non-Debye behaviour: effects which may then be scaled to the densities and temperatures obtained in laser compression experiments while maintaining the same value of Γ. In this way diagnostic techniques applicable to inertial confinement fusion may also be developed.

1.2 The Weak Coupling Approximation in Debye Plasma Shielding

A fundamental characteristic of plasma behaviour is the shielding of the electric potential of a charged particle due to the presence of surrounding changes in the plasma. The exact form that this shielding takes (i.e. the way in which the potential is reduced as a function of distance from the test particle) is, however, dependent on the particular model chosen for the plasma.

The usual Debye-Huckel model is applied to plasmas for which the weak coupling approximation is valid (i.e. where $\Gamma << 1$). The approximation arises in the derivation of the shielded potential (e.g. Griem, 1964, p.137). Starting with the Boltzmann relation for the time-averaged (smooth) charge distribution $\rho_z(r)$ in the potential $\phi_z(r)$ of a charge z gives

$$\rho_z(r) = e\left[-n_e \exp\left(\frac{e\,\phi_z(r)}{kT}\right) + \sum_{z',a} z'n_{z',a} \exp\left(\frac{-z'e\phi_z(r)}{kT}\right)\right] \quad (1.5)$$

The assumption $e\phi << kT$ is applied in expanding the exponentials to give

$$\rho_z(r) = \frac{-e^2\phi_z(r)}{kT}\left(n_e + \sum_{z',a} z'^2 n_{z',a}\right) \quad (1.6)$$

Employing the above expression for $\rho_z(r)$ in Poisson's equation

$$\frac{\partial^2\phi(r)}{\partial r^2} + \frac{2}{r}\frac{\partial\phi(r)}{\partial r} = -\frac{1}{\varepsilon_0}\rho_z(r) \quad (1.7)$$

yields the usual Debye shielded potential

$$\phi_z(r) = \frac{ze}{4\pi\varepsilon_0 r} e^{-r/\lambda_D} \quad (1.8)$$

where λ_D is the Debye radius

$$\lambda_D = \left[\frac{\varepsilon_0 kT}{e^2(n_e + \sum_{z',a} z'^2 n_{z',a})}\right]^{\frac{1}{2}}$$

$$= \left[\frac{\varepsilon_0 kT}{e^2 n_e(1+\langle z\rangle)}\right]^{\frac{1}{2}} \quad (1.9)$$

and <z> is the mean ion charge (which can be omitted if only electron shielding is considered). The Debye radius then represents the distance beyond which the potential of the charge z is effectively shielded.

The weak coupling approximation is also implicit in the use of the Boltzmann relation. The Boltzmann relation is derived from the Vlasov equation, in which the effects of particle correlations on the particle distribution functions are neglected (Sanderson, 1981). In strongly coupled plasmas particle correlations will become important, and hence the neglect of the correlation term in the Vlasov equation will become invalid (simultaneously with the breakdown of the exponential expansion above).

Another assumption implicit in the derivation of the shielded potential is that the charge distribution in the region of the potential be continuous. This assumption requires that the number of particles N_D in a sphere of one Debye radius be large. Considering for simplicity electrons only, this requirement can be written as

$$N_D = n_e \frac{4\pi\lambda_{De}^3}{3} = a_o^{-3} \qquad (1.10)$$

$$\gg 1$$

where

$$a_o = \frac{R_o}{\lambda_D} = \sqrt{3\Gamma} \qquad (1.11)$$

The criterion $a_o = 1$ then yields the condition

$$n_e(\mathrm{m}^{-3}) = 1.91\times10^{12} T_e^3 \ (\mathrm{K}) \qquad (1.12)$$

which is also plotted in Figure 1.1.

The physical significance of the breakdown in the Debye model can be seen more clearly from the definition of a_0, since the concept of shielding by particles within one Debye length is meaningless if $\lambda_D < R_0$. The exact form of the shielded potential between two charges in a non-Debye plasma is not, however, readily apparent, although it is clear that the Debye radius is no longer the appropriate shielding scale length.

1.2.1 Dynamic Shielding

The derivation of the Debye shielding radius in the previous section is an essentially static treatment, applicable only to particles with velocities less than the mean thermal velocity. Shielding of the potential from a suprathermal particle is less effective, since the majority of particles cannot move quickly enough to counteract the rapidly varying local field produced by the suprathermal particle (Pines and Bohm, 1952).

Inclusion of dynamic effects on shielding in the time domain involves a complicated analysis of time-ordered interactions between particles in the plasma. Treatment of dynamic shielding is therefore best carried out in the Fourier domain, where the frequency ω of the changing field due to the moving particle is considered. In a weakly coupled plasma the effective potential can be evaluated using diagrammatic techniques in the so-called random phase approximation or R.P.A. (in which only the lowest order terms in the particle-plasma interaction are included i.e. the ring diagrams - see e.g. Mattuck, 1967). Using this technique, the Fourier transformed effective potential energy is (Mattuck, 1967)

$$V_{\mathrm{eff}}^{\mathrm{RPA}}(q,\omega) = \frac{V_q}{\varepsilon_{\mathrm{RPA}}(q,\omega)} \tag{1.13}$$

where q is the momentum transfer in the shielding interaction, and V_q the Fourier transform of the Coulomb interaction i.e.

$$V_q = \frac{e^2}{\varepsilon_0 q^2} \tag{1.14}$$

The quantity $\varepsilon_{RPA}(q,\omega)$ is the generalized frequency dependent dielectric function. The usual longitudinal dielectric function for an equilibrium plasma (neglecting damping) is given by the Bohm and Gross dispersion law (e.g. Bekefi, 1966)

$$\varepsilon_{RPA}(q,\omega) = 1 - \frac{\omega^2_p}{\omega^2}\ [1 + 3q^2\lambda_D^2\ (\frac{\omega_p^2}{\omega^2})] \tag{1.15a}$$

where $\omega_p = \sqrt{n_e e^2/\varepsilon_0 m_e}$ is the electron plasma frequency. In the static (ω=0) limit the dielectric function becomes

$$\varepsilon_{RPA}(q,\ 0) = [1+(q\lambda_D)^{-2}] \tag{1.15b}$$

When substituted into Equation (1.13) this yields

$$V_{eff}^{RPA}\ (q,\ 0) = \frac{e^2/\varepsilon_0}{(q^2+\lambda_D{}^{-2})} \tag{1.16}$$

which, following a Fourier transformation, gives the usual expression for the static Debye shielded interaction:

$$V_{eff}^{RPA}(r) = \frac{e^2}{4\pi\varepsilon_0 r}\cdot e^{-\ r/\lambda_D} \tag{1.17}$$

Calculation of the frequency dependent dielectric function can also be carried out without the RPA (for $\Gamma \sim 1$), and numerical methods have been proposed to evaluate the dielectric function in moderately coupled plasmas (e.g. Boercker et al. mentioned later in Section 1.3.6). However no published theory exists at present that can described dynamic shielding of the electric potential in the regime $\Gamma \gg 1$.

1.3 Spectroscopic Effects in Dense, Non-Debye Plasmas

The strong interparticle coupling that characterizes non-Debye plasmas will have two main effects on the spectroscopic behaviour of the plasma:

1) The radiating system will be strongly perturbed by the plasma environment. (This is because a particular ion stage will be dominant at temperatures kT equal to a certain fraction of the electron binding energy for that ion stage. Since kT is less than the mean interparticle interaction energy, then the optical electron will experience perturbations that are significant compared to the electron binding energy.)

2) The statistical behaviour of the plasma particles will be affected by the strong interparticle correlations.

The expected consequences of these effects have been described elsewhere in detail before (Vinogradov et al., 1974; Peacock, 1978; Burgess 1978 and 1982; and More, 1982). A brief discussion of some of the important effects will be given in the following sections.

1.3.1 Reduction of the Ionization Potential

Polarization of the surrounding plasma by the electron and ion produced in an ionizing event causes a reduction in the effective ionization potential (I.P.) of the parent species. As will be shown in this section, I.P. depression becomes important for dense, non-Debye plasmas where the coupling between particles is very strong.

An expression for the I.P. depression can be derived thermodynamically by requiring that the free energy of the plasma be minimized when in equilibrium (Ecker and Kroll, 1963). The electrostatic interaction between particles produces a free energy term that must be added to the free energy of the non-interacting plasma (which includes only the ideal gas contributions of electrons and ions plus the ion internal energies). When the free energy of the interacting plasma is minimized, a modified Saha equation is obtained for the equilibrium ionization balance (Ecker and Kroll, 1963).

$$\frac{n_{i+1} \; n_e}{n_i} = \frac{2u_{i+1}}{u_i} \left(\frac{2\pi m_e kT}{h^2} \right)^{3/2} e^{-(E_i - \Delta E_i)/kT} \tag{1.18}$$

Here n_i, u_i and E_i are the number density, partition function and ionization energy of the lower ionization stage. The difference between Equation (1.18) and the Saha equation for a non-interacting plasma is the appearance of the ΔE_i term which represents a lowering of the ionization potential. The magnitude of the lowering is given by

$$\Delta E_i = -\frac{\partial \Delta F_c}{\partial N_{i+1}} + \frac{\partial \Delta F_c}{\partial N_i} - \frac{\partial \Delta F_c}{\partial N_e} \tag{1.19}$$

where N_i is the total number of particles i and ΔF_C is the additional contribution to the free energy due to the particle interactions. For a Debye plasma (Griem, 1962):

$$\Delta F_c = -\tfrac{1}{2}\left(N_e + \sum_i N_i Z_i^2\right) \frac{e^2}{4\pi\varepsilon_o \lambda_D} \qquad (1.20)$$

from which the established value for the I.P. depression in a Debye plasma is (Griem, 1962)

$$\Delta E_i(\lambda_D) = \frac{Z_{i+1}\, e^2}{4\pi\varepsilon_o \lambda_D}$$

$$\sim \frac{e^2}{4\pi\varepsilon_o R_o} \sqrt{3\Gamma} \qquad (1.21)$$

Hence for a given density, the magnitude of the I.P. depression increases as the plasma becomes more strongly coupled.

However, for $\Gamma > 1$ the Debye model is no longer valid, and the expression for the I.P. depression usually adopted is the "ion sphere" result of Stewart and Pyatt (1966) for a plasma of ion charge Z_i:

$$\Delta E_i(R_o^i) \sim \frac{3}{2} \frac{Z_i e^2}{4\pi\varepsilon_o R_o^i} \qquad (1.22)$$

Since for $\Gamma > 1$ the kinetic energy is much less than the interparticle electrostatic energy, the I.P. depression is therefore determined purely by the particle density surrounding the ion. For the region $\Gamma \sim 1$ (where $R_o^i \sim \lambda_D$), there is a more or less smooth transition of the magnitude of the I.P. depression between the two regimes.

Values for the I.P. depression over a range of plasma conditions are plotted in Figure 1.2, both for the Debye and ion-sphere results.

1.3.1.1 Reduction of the Number of Bound States

The I.P. depression affects the ionization balance not only directly (via the exponential term in the Saha equation) but also indirectly by reducing the number of bound states contributing

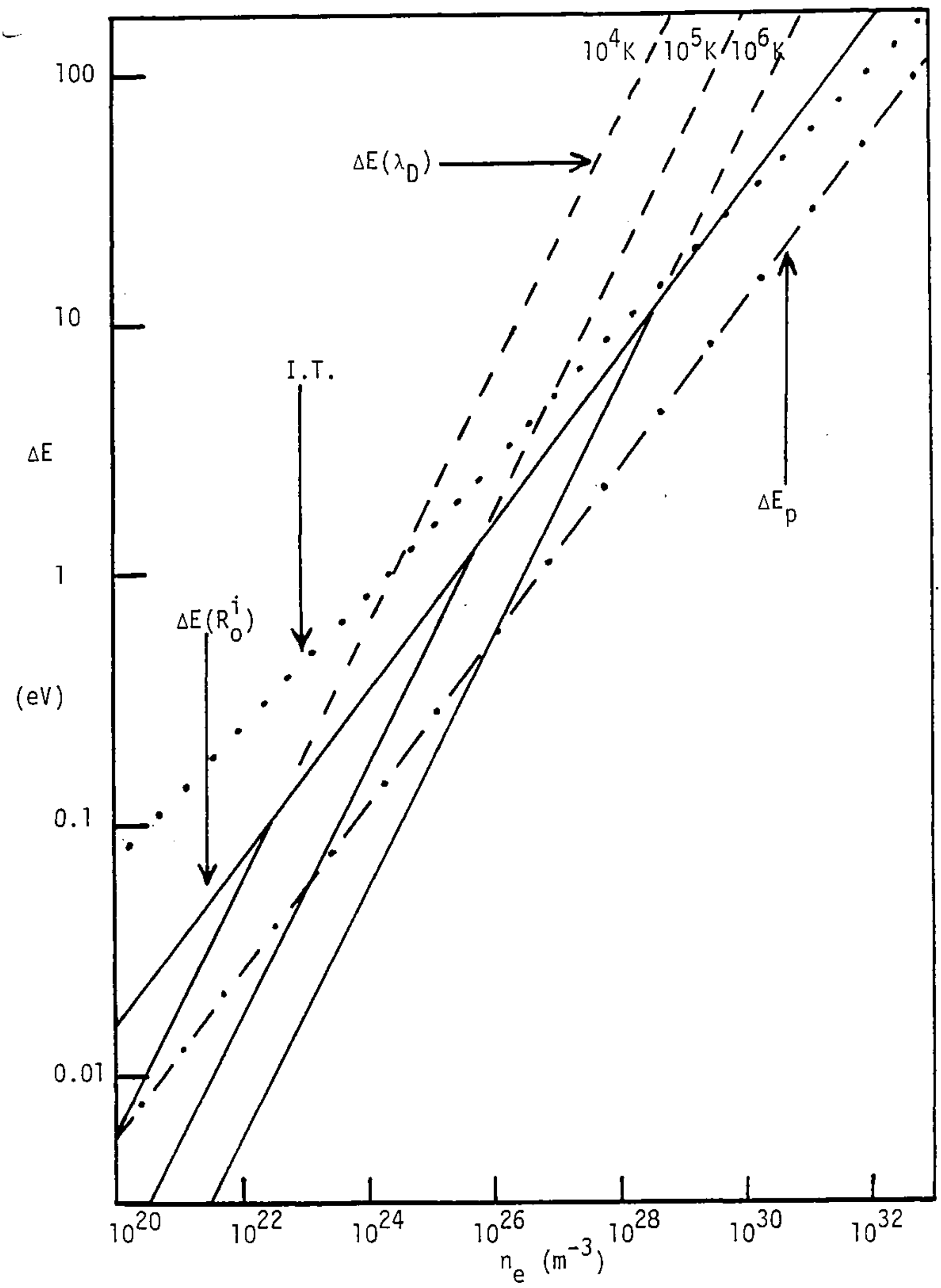

Figure 1.2: Comparison of ionization potential depression, pressure ionization and Inglis-Teller line merging for hydrogen:

(a) $\Delta E(\lambda_D)$-the Debye value for the I.P. depression (Ecker and Kroll, 1963).

(b) $\Delta E(R_o^i)$-the ion sphere value for the I.P. depression (Stewart and Pyatt, 1966).

(c) ΔE_p-the energy below the continuum of the highest bound state defined by pressure ionization.

(d) I.T.-Inglis-Teller advance of the series limit $\sim 4z^{4/5}(r_o^3 n_e)^{4/15}$.(13.6e) (Griem, 1964 p125), where r_o is the Bohr radius.

to the partition functions. The elimination of bound states must first be distinguished from Inglis-Teller line merging, which occurs for the higher members of a line series in which the upper levels are broadened by strong perturbations from particles in the nearby continuum (e.g. Griem, 1964, p.125). Although such lines are no longer distinguishable, this does not alter the fact that their high lying upper levels are still bound, and therefore should contribute to the partition function.

However it is not clear whether the highest bound level energy is limited only by the I.P. depression, or whether the limit is determined by pressure ionization. Pressure ionization is defined as the disappearance of bound states caused by the close proximity of perturbing particles at high densities. More (1982) lists three mechanisms that occur simultaneously:

1) overlapping of adjacent wavefunctions
2) overcoming of the electron binding energy by neighbouring ions
3) compression of free electrons inside bound electron orbitals.

All three mechanisms define the highest bound state principal quantum number (n) as

$$r_n = \frac{r_o n^2}{Z_e} = R_o \qquad (1.23)$$

where r_o is the Bohr radius and Z_e the emitter charge. More shows this to be true for Debye plasmas as well, since if $R_o << r_n << \lambda_D$ the orbital electron will undergo scattering many times before the completion of an orbit, and hence cannot be considered as a true bound level. What More does not state is that for hydrogenic ions, since the energy of level n below the continuum is

$$\Delta E_n = \tfrac{1}{2}\,\frac{Z_e\,e^2}{4\pi\varepsilon_0 r_n} \qquad (1.24)$$

then the pressure ionization condition $r_n = R_0$ defines the highest bound state at an energy below the continuum equal to one third the value of the ion-sphere I.P. depression. Hence for non-Debye plasmas, the highest bound state energy should be defined by the ion-sphere I.P. depression. The energy below the continuum (ΔE_p) of the highest bound state defined by pressure ionization is compared with values of the I.P. depression in Figure 1.2, as a function of density. In the Debye case, $\Delta E(\lambda_D)$ is temperature dependent as shown, and at high densities (such that $N_D < 1$) ceases to be valid (dashed lines). $\Delta E(\lambda_D)$ is then replaced by the ion-sphere result, $\Delta E(R_0^i)$.

Consideration of Figure 1.2 shows that only for low density Debye plasmas is pressure ionization important in determining the upper limit on bound levels. As the density increases (for a constant temperature) first the Debye depression and then the ion-sphere depression have the largest values. For the near non-Debye plasmas considered in this project ($n_e \sim 10^{24}$ -10^{25}, $T \sim 3$eV), as expected $\Delta E(\lambda_D)$ and $\Delta E(R_0^i)$ yield similar values for the I.P. depression ($\sim$ 0.5eV). The effect of I.P. depression on the number of bound levels is therefore significant since in hydrogen, for example, the highest bound principal quantum number then expected is n=5. Figure 1.2 indicates that at very high densities <u>no</u> bound states may exist (the so-called one-component plasma* - More, 1982). A more drastic effect on the spectroscopic properties of a non-Debye plasma cannot be imagined.

1.3.1.2 Difficulties in the Determination of Continuum Lowering

Determination of the highest bound level (even on a theoretical basis) is complicated by a number of factors:

* Electron degeneracy is also assumed in a one-component plasma.

1) Lower angular momentum states, which (classically) extend further from the nucleus than higher momentum states of the same energy, will be preferentially pressure ionized (Zimmerman and More, 1980).

2) Tunnelling of electrons can occur close to the top of the potential barrier caused by the spatial field gradient of a nearby charged perturber, while the electron is still strictly bound. The orientation of the distorted three-dimensional potential surface with respect to the electron orbital is also important since it is possible for the electron to be bound in two dimensions but not the third.

3) It is not clear whether pressure ionization and ionization potential dpression are in fact different physical processes at all, particularly if pressure ionization is viewed as due to the compression of free electrons inside bound orbitals.

Even assuming that a theoretical upper limit on the bound energy levels can be defined, it is difficult in practice to actually measure the amount of continuum lowering (by, for example, observing the shortest wavelength resonance line). This is again the result of merging of the lines above the Inglis-Teller limit (which is calculated for hydrogen (Griem, 1964, p.125) as shown in Figure 1.2). Invariably ΔE for the series limit is greater than for I.P. depression. For example, calculations by Lee (private communication) show that for the Lyman β, γ and δ lines (with $h\nu$ = 12.09, 12.75 and 13.04eV respectively), the predicted half-widths are some 0.2, 0.3 and 0.7eV for the conditions expected in this experiment ($n_e=10^{25}m^{-3}$, T_e=3eV). The Lyman δ and ϵ lines will therefore be completely merged, although the highest bound state is still $n=5$. Hence the validity of the I.P. depression models discussed above cannot be tested by measuring the apparent continuum lowering in this plasma.

1.3.2 Perturbation of the Emitter Energy Levels

As mentioned in Section 1.3, the radiating system will be strongly perturbed in a non-Debye plasma. The strong interactions not only cause the disappearance of the higher lying states, but also cause the remaining bound energy levels to be strongly perturbed. The consequent effects on calculation of the magnitude of such perturbations are outlined in this section.

In a Debye plasma, the effect of the plasma environment on the emitter energy levels is usually calculated by first assuming a form for the perturbing interaction (often a multipolar expansion e.g. Sholin, 1969). This is normally followed by a perturbation theory treatment of the effect (to first and second order) on the unperturbed eigenvalues and wavefunctions. Although there are sometimes limits to this procedure in Debye plasmas, there are nearly always serious difficulties in calculating such effects in dense, non-Debye plasmas. This is because at very close separations a multipolar expansion may not be valid, and because for very strong interactions, a perturbation theory treatment cannot be applied.

1.3.2.1 Calculation of the Energy Level Shift for the (n=2) Upper State of Lyman-α due to a Charged Perturber

The limitations on the validity of the methods normally used in the calculation of energy level shifts can be illustrated by considering a perturber of point charge Ze located at a distance R_o from a hydrogen atom. The interaction potential is

$$V(r) = \frac{Ze^2}{4\pi\varepsilon_o}\left(\frac{1}{R_o} - \frac{1}{\sqrt{R_o^2 + r^2 - 2R_o r\cos\theta}}\right) \tag{1.25}$$

where r is the distance to the optical electron. This expression can be expanded (following Sholin, 1969) in powers of $\lambda = n^2\frac{r_0}{R_0}$ (r_0=Bohr radius) as

$$V = \lambda^2 V_2 + \lambda^3 V_3 + \lambda^4 V_4 + \ldots \qquad (1.26)$$

where V_2, V_3 and V_4 correspond to dipole, quadrupole and octupole terms in the multipolar expansion. To first order, and considering only the dipole term, the correction to the unperturbed energy i.e. the linear Stark effect, is

$$\Delta E^{(1)}_{\text{DIPOLE}} = \frac{3}{2}\frac{Zn(n_1-n_2)e^2 r_0}{4\pi\varepsilon_0 R_0^2} \qquad (1.27)$$

where n is the principal quantum number, while the atomic wavefunctions are expressed in terms of the parabolic quantum numbers (n_1, n_2, m). Since Lyman-α is the simplest of the hydrogen lines to calculate (hence its importance in theoretical line broadening studies), the n=2 states (1,0,0), (0,1,0) and (0,0,1) will be used in this evaluation. (The n=1 ground state will be comparatively unperturbed since the ionization energy from n=1 is 13.6eV c.f. only 3.4eV from n=2.) Hence

$$\Delta E^{(1)}_{\text{DIPOLE}} = \frac{\pm 3 Ze^2 r_0}{4\pi\varepsilon_0 R_0^2} \qquad (1.28)$$

for the two shifted π(m=0) components, with the σ(m=1) component experiencing no linear Stark shift.

The first order quadrupole contribution is of next highest order in λ, and is given by

$$\Delta E^{(1)}_{\text{QUADRUPOLE}} = \frac{-Ze^2 r_0^2\, n^2}{4\pi\varepsilon_0 2R_0^3}\,[6(n_1-n_2)^2 - n^2+1] \qquad (1.29)$$

which for the shifted/unshifted components yields

$$\Delta E^{(1)}_{\mathrm{QUADRUPOLE}} = \frac{\mp 6Ze^2r_0^2}{4\pi\varepsilon_0 R_0^3} \tag{1.30}$$

Hence the ratio of quadrupole to dipole shifts for the π components is given by

$$\frac{\Delta E^{(1)}_{\mathrm{QUADRUPOLE}}}{\Delta E^{(1)}_{\mathrm{DIPOLE}}} = \frac{2r_0}{R_0}$$

$$= 1.71\mathrm{x}10^{-10} \quad n_i^{1/3}(m^{-3}) \tag{1.31}$$

where n_i is the number density of perturbers. This ratio is plotted for a range of number densities in Figure 1.3. As can be seen, the quadrupole term can represent a significant contribution to the first order energy correction at high densities.

This analysis can be extended to the next highest terms (λ^4), which include contributions from second order in perturbation theory. The first two terms below (the quadratic Stark or second order dipole; and the second order quadrupole) fall into this category, while the third term arises from the next first order multipolar contribution (the octupole term):

$$\lambda^4E^{(4)} = \frac{-Z^2e^2r_0^3\ n^4}{4\pi\varepsilon_0.16R_0^4}\ [17n^2-3(n_1-n_2)^2-9m^2+19]$$

$$-\frac{3Ze^2r_0^3\ n^3(n_1-n_2)}{4\pi\varepsilon_0.16R_0^4}\ [n^2+m^2-(n_1-n_2)^2-1]$$

$$-\frac{5Z\ e^2r_0^3\ n^3(n_1-n_2)}{4\pi\varepsilon_0.16R_0^4}\ [23(n_1-n_2)^2-9n^2-3m^2+13] \tag{1.32}$$

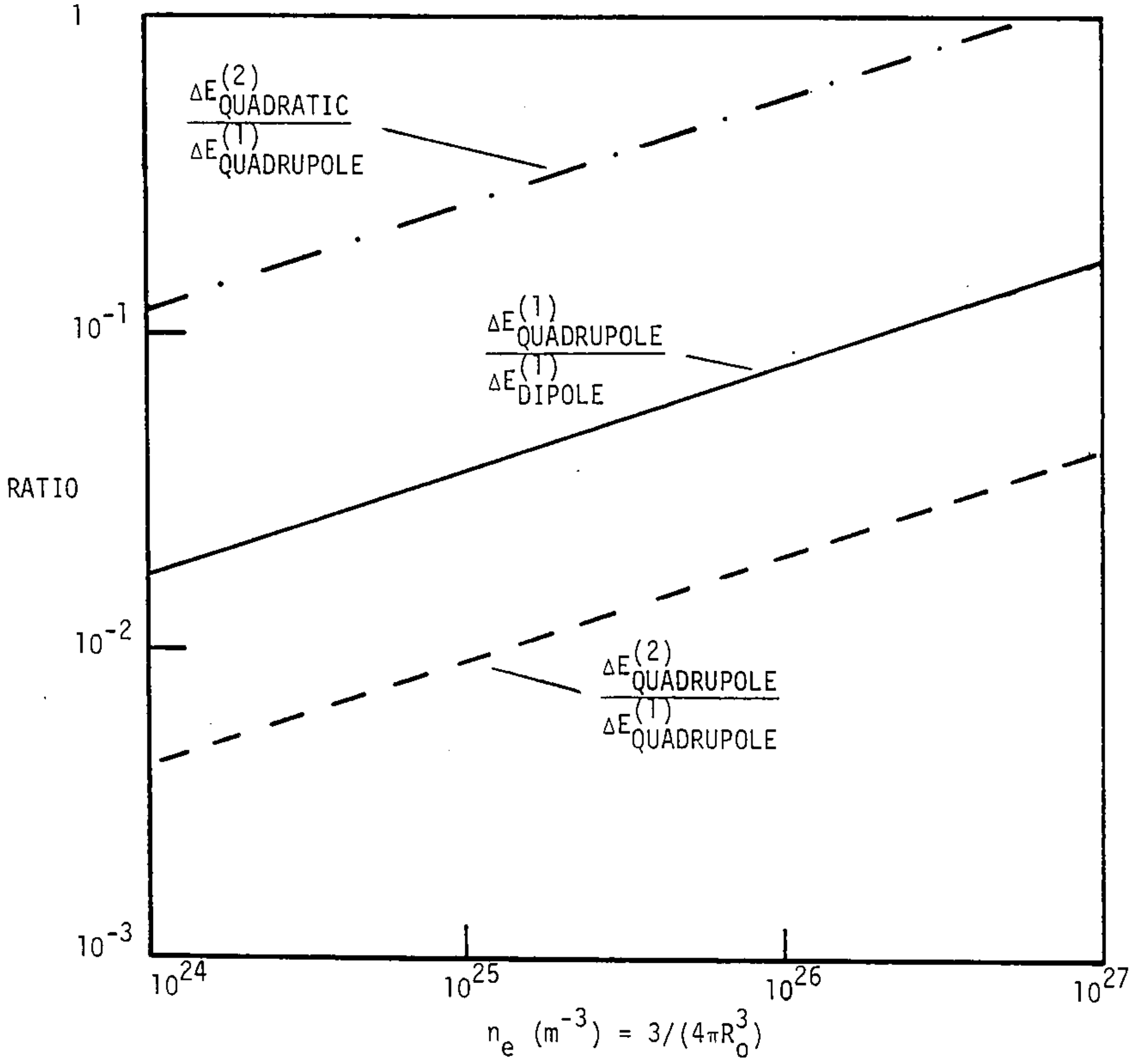

Figure 1.3: Ratio of contributions to the static energy shift of the Lyman-α π components for terms in $\lambda(= n^2 \frac{r_o}{R_o})$ of order ≤4 (as a function of perturber density).

Evaluating each term individually for Lyman-α (n=2) yields the following ratios (again for π components)

$$\frac{\Delta E^{(2)}_{\text{QUADRATIC}}}{\Delta E^{(1)}_{\text{QUADRUPOLE}}} = \frac{14r_o}{R_o} = 1.19\times10^{-9}\ n_i^{1/3}(m^{-3}) \tag{1.33}$$

$$\frac{\Delta E^{(2)}_{\text{QUADRUPOLE}}}{\Delta E^{(1)}_{\text{QUADRUPOLE}}} = \frac{1}{2}\frac{r_o}{R_o} = 4.26\times10^{-11}\ n_i^{1/3}(m^{-3}) \tag{1.34}$$

which are also plotted in Figure 1.3 (there is no octupole contribution from these states). The figure shows that these higher order terms in the perturbation theory also become important at high density. Hence, once quadrupole terms become important as $n^2r_o/R_o \to 1$, it becomes necessary to include all higher order terms in the interaction and perturbation expansion until at $\frac{n^2r_o}{R_o} \sim 1$ such an expansion is no longer valid.

1.3.2.2 Lyman-α Asymmetry

It is not necessary for the limit $\frac{n^2r_o}{R_o} \sim 1$ to be reached for the higher order terms to produce an observable effect on lineshapes. Calculations using the above (static) analysis were applied to the Lyman-α line for ion perturbers by Sholin (1969) and Bacon (1977), at densities of $n_e = 10^{22}$-10^{23} m^{-3} (for which $\frac{n^2r_o}{R_o} << 1$). The calculated change in the relative positions and intensities of the three Stark components due to the quadrupole interaction produced an asymmetry in the Lyman-α line profile. (The contribution due to the electrons was treated dynamically and hence produced a symmetric profile using the impact theory - Griem, 1964, p.69.). Such asymmetries have been observed experimentally in argon/hydrogen plasmas both in this laboratory at moderately high densities ($1\text{-}3\times10^{24}m^{-3}$) by Baker (1977) , and elsewhere at lower densities (e.g. Fussmann, 1975 at $7\times10^{23}m^{-3}$ and 12,200K). Greater asymmetry was observed by Baker, which may have been due to the increasing importance of higher order terms in the expansion at the higher densities. Both observations showed a change to less asymmetry at the same position (5Å) in the line wing. This may be due to the transition from the impact to the static regime for the electrons (whose contributions to the quasistatic asymmetry would then cancel those due to the ions through the charge sign). However this transition occurs at a wavelength separation for electrons (Griem, 1964, p.77)

$$\Delta\lambda \sim \frac{\lambda_0^2\ kT}{ch\ n^2} \tag{1.35}$$

and yet in the two experiments the temperatures differed by a factor of at least two.

1.3.2.3 The Emitter-Perturber Interaction Potential

It is possible that the above change in the asymmetry is due to neglect of the finite extent of the wavefunction for the argon-ion perturber, and also brings into question the use of a multipolar expansion given the small interaction distances involved ($R_0 \sim 40$Å in Baker's experiment). It may be necessary in such cases to use the full emitter-perturber interaction potential, a calculation of which is usually very difficult. An exact set of wavefunctions for both the emitter and perturber is required together with a method for describing the way in which the configurations interact (e.g. Chambaud et al., 1979).

Such calculations can give rise to the prediction of other effects, such as formation of the satellite features treated in more detail in the next chapter. These satellites essentially occur at extrema in the difference potential between the perturbed emitter energy levels, and have been observed in other dense radiating systems (e.g. neutral gases at $\sim 10^{25}\mathrm{m}^{-3}$ - Kielkopf and Allard, 1979).

Satellites have also been observed in high density plasmas e.g. Preston (1977) at $n_e \sim 2\mathrm{x}10^{23}\mathrm{m}^{-3}$, as well as in this laboratory by Baker and Burgess (1979) at $n_e \sim 1\text{-}3\mathrm{x}10^{24}\mathrm{m}^{-3}$. A more complete discussion of the origins of these satellite features will be given in Chapter 2, since the investigation of their occurrence was one of the main objectives of this project. For the moment it is sufficient to note that such satellite features may have a significant role to play in the spectroscopy of non-Debye plasmas, for which strong perturbations of the emitter energy levels is an inherent characteristic.

1.3.3 Statistical Effects on Line Broadening

Strong interparticle correlations will affect the statistical behaviour of non-Debye plasmas, and hence will influence the line broadening processes which probe this behaviour (Griem, 1974). Reviews elsewhere (e.g. Burgess, 1978, 1982) have considered the richness of effects that become prominent at higher densities (such as Doppler narrowing, caused by multiple collisions during a radiating cycle). Here a brief summary will be made only of non-Debye effects on the general line broadening problem arising from changes in the underlying statistical nature of the plasma.

Current line broadening theories may be divided into two types: those that separate the lineshape contribution of electrons and ions by their different dynamic behaviour (the so-called Unified and Fourier Decomposition theories - see Burgess, 1982), and those that treat all perturber contributions identically and simultaneously (the

Model Microfield theories, e.g. Seidel, 1981; Dufty, 1981). The physical assumptions underlying the former theories are more self-evident and will be treated first.

The greater mass of ionic perturbers in comparison with the electrons usually leads to a purely static treatment of ion/emitter interactions under the dynamic theories. The static shifts in the emitter energy levels are calculated for a given ion perturber field and are then averaged over all probable field distributions. It is possible in this simplified situation to include completely the effects of ion-ion correlations and thence to estimate the effect of non-Debye behaviour on the quasistatic line wings. Hooper (1968) has performed such a microfield calculation which shows that the value of the most probable field decreases as Γ increases. This is to be expected since ion-ion correlations reduce the likelihood of very close ($<R_0$) separations in strongly coupled plasmas. Further calculations by Weisheit and Pollock (1981) also showed that for $\Gamma \sim 1$ the microfield reverts to a nearest neighbour distribution as might be expected when only around one particle exists per Debye sphere. However, extension of their calculations to $\Gamma >> 1$ did not yield the anticipated asymptotic behaviour (Lee, private communication) since the distributions remained similar to nearest neighbour values instead of reverting to a closely coupled, multiple neighbour result.

Line broadening due to electrons is treated dynamically by the first group of theories, the electron velocities being considerably greater than the ion velocities. Shielding and correlations are included to some extent in such theories e.g. by the use of cut-offs for electron perturbers at distances greater than $\sim\lambda_D$ (Griem, 1974, p.140), or by assuming an appropriately shielded potential for the electron-emitter interaction (Burgess, 1970a). However either approach encounters difficulties in non-Debye plasmas where the form of the shielding is no longer given by the Debye model. Furthermore the dynamic theories treat some emitter-perturber interactions in a purely binary manner e.g. strong collisions corresponding to close perturber separations (Griem, 1974, p.36). In strongly coupled plasmas non-binary interactions between charged particles are more probable than in Debye plasmas, and hence particle correlations must be included in any complete dynamic model.

Another limitation occurs for those dynamic theories employing the classical path approximation (Griem, 1964, p.68). One requirement of the classical path approximation - that there is no back reaction of the emitter on the perturber - is likely to be violated for non-Debye plasmas. Energy transfer between radiator and perturber will be important when there are strong perturbations to the radiating system. For example, the energy transfer indicated by the large Lyman β, γ and δ widths of 0.2, 0.3 and 0.7eV calculated by Lee (see Section 1.3.1.2) is significant in comparison with the mean thermal energy expected here of only 3eV.

This raises the most fundamental difficulty in the application of current line broadening theories to non-Debye plasmas: the validity of factorising the density matrix for the system

$$\rho_{\text{SYSTEM}} = \rho_{\text{RADIATOR}} \cdot \rho_{\text{PLASMA}} \tag{1.36}$$

into two independent matrices representing the probability distribution of radiator states, and the states of the perturbing plasma (Baranger, 1958). This factorization is also implicit in the Model Microfield theories (Dufty, 1981), which consider the total (electron and ion) plasma interaction on the emitter. The interaction is calculated using an assumed microfield distribution and associated first order auto-correlation function to model the microfield fluctuations. The state of the plasma is, however, assumed to be independent of the radiator, in the same way that averages are carried out separately over emitter and plasma states when calculating the line profile using the dynamic theories. Because the energy transfer between emitter and perturbing systems can be significant compared to kT in strongly interacting plasmas, the states of the plasma and the emitter will no longer be independent. The breakdown of this fundamental assumption means that direct application of current line broadening theories (for weakly coupled plasmas) to non-Debye plasmas is open to question.

1.3.4 Plasma Oscillations in Non-Debye Plasmas

The existence of collective electron behaviour in the form of plasma oscillations depends (in a Debye plasma) on the Debye length being less than the wavelength λ of the plasma oscillation (Pines and Bohm, 1952). For $\lambda < \lambda_D$ the plasma wave is inhibited by Landau damping, in which the individual electrons convert plasma wave energy into thermal motion. However, for non-Debye plasmas (in which $\lambda_D < R_o$) the above criterion for collective plasma oscillations is no longer meaningful.

It is possible that collective plasma oscillations may still exist in a non-Debye plasma provided that the wavelength of the oscillations is much greater than the interparticle separation. The number of particles occurring in one wavelength ($N = \frac{\lambda}{R_o}$) may be estimated by determining the wave vector $\vec{k}$ ($= \frac{2\pi}{\lambda}$) of the most probable oscillation. Using the Bohm and Gross dispersion law, the relation between $\vec{k}$ and the frequency (ω) for the plasma modes is (Drummond, 1961)

$$\omega^2 = \omega_p^2 \; (1+3 \; \vec{k}^2 \; \lambda_D^2) \qquad (1.37)$$

where ω_p is the characteristic frequency of electron oscillations in a zero temperature plasma:

$$\omega_p = \left(\frac{n_e e^2}{\varepsilon_o m_e}\right)^{\frac{1}{2}} \qquad (1.38)$$

The energy density spectrum of plasma modes can be approximated by assuming an energy of $\frac{1}{2}kT$ for each of the modes for which $\kappa^{-1} > \lambda_D$ (Drummond, 1961) viz:

$$W(\omega)\ d\omega = \frac{m_e^{3/2}}{2\pi^4} \cdot \omega \left(\frac{\omega^2 - \omega^2_p}{3kT}\right)^{\frac{1}{2}} d\omega \qquad (1.39)$$

Since for $\kappa^{-1} \sim \lambda_D$ some of the modes will be Landau damped, the energy density is multiplied by the Landau damping factor $e^{i\gamma t}$, where γ is the Landau damping term (Drummond, 1961)

$$\gamma = \frac{i\omega_p}{(\kappa\lambda_D)^3} \sqrt{\frac{\pi}{8}}\ e^{-[\frac{1}{2}(\kappa\lambda_D)^{-2}]} \qquad (1.40)$$

The damping time chosen was the lifetime of the plasma considered, and was found to affect the final calculations only slightly (even for an order of magnitide variation in t). The energy density spectrum (allowing for Landau damping) was then calculated using a programme by Spirit (private communication), and the wavelength λ_{max} of the highest mode density determined.

The results indicated that λ_{max}/λ_D $(= 2\pi/\kappa_{max}\lambda_D)$ was a constant $(C > 1)$ for a given damping time. The constant ratio arises because λ and λ_D appear only via the parameter $\kappa\lambda_D$ in Equations 1.37 and 1.40 above, and hence $\kappa_{max}\lambda_D$ is also a quantity at which the energy density is maximised. Thus in a Debye plasma,

$$\lambda_{max} = C\ \lambda_D >> R_o \qquad (1.41)$$

To estimate λ_{max} for near non-Debye plasmas, the limit $\lambda_D \rightarrow R_o$ was taken by assuming a decrease in the plasma temperature at a fixed density. In this limit λ_{max}/R_o also decreases, and hence fewer electrons exist in one oscillation wavelength. At $\lambda_D = R_o$, a range of characteristic times (from 10^{-6} sec. for z-pinch plasmas to 10^{-12} sec. for laser compressed plasmas) gave values for N of between 50 and 20 respectively. Hence N will exceed unity for $\Gamma(= \frac{R_o^2}{3\lambda_D^2}) < 100$. This result indicates that collective plasma oscillations may exist in non-Debye plasmas, although the dispersion relation and Landau damping terms may not resemble those given above since the Debye radius is no longer a meaningful shielding scale length.

The mean energy density existing in the form of plasma oscillations can be calculated for Debye plasmas by integrating the energy density spectrum in Equation (1.39) over ω. Using $\omega_{max} = 2\omega_p$ (which corresponds to integrating over $0 \leq \bar{k}\lambda_D \leq \delta = 1$) gives

$$W_{osc} = \int_{\omega_p}^{\omega_{max}} W(\omega)d\omega = \delta^3 \frac{n^{3/2} e^3}{2\pi^4 \varepsilon_o^{3/2} (kT)^{\frac{1}{2}}}$$

$$\sim 5\times10^{-3} \frac{kT(K)}{\lambda_D^3 (m)} \quad \text{J m}^{-3} \qquad (1.42)$$

Although Equation (1.42) includes contributions from waves that are partially damped, the use of lower cutoff values (δ) to approximate the effects of partial damping (e.g. Dummond, 1961) only alters the result by the multiplicative factor δ^3.

The ratio of the mean energy density existing in plasma oscillations to the mean thermal energy density $\frac{3}{2}nkT$ is then

$$\frac{W_{osc}}{K.E.} = \frac{\delta^3}{3\pi^4} \frac{n^{\frac{1}{2}} e^3}{\varepsilon_o^{3/2} (kT)^{3/2}}$$

$$\sim 0.014 \; N_D^{-1} \qquad (1.43)$$

Hence, as N_D becomes small, a greater proportion of the plasma energy will exist in the form of plasma oscillations.

1.3.5 Plasma Satellites in Non-Debye Plasmas

The large proportion of energy in plasma oscillations for non-Debye plasma suggests that thermal plasma satellites may be observed (Baranger and Mozer, 1961). Plasma satellites are formed by amplitude modulation of the emitter wavetrain through the emission or absorption of a plasmon (frequency $\sim\omega_p$). Sidebands are thereby produced at frequency separations ω_p from the frequency of forbidden lines only (due to the selection rules for this two quantum process). The line strength of the satellites S± relative to the forbidden line S_F (to second order in perturbation theory) is then given by (Baranger and Mozer, 1961)

$$\frac{S\pm}{S_F} = \frac{1}{2}\,\frac{<E_p^2>}{E_R^2}\;\frac{\Delta^2}{(\Delta\pm\omega_p)^2} \qquad (1.44)$$

Here Δ is the frequency separation between the upper level of the forbidden line and the nearest level to which a dipole transition is allowed. E_R is the mean random electric field,

$$E_R = \frac{e}{4\pi\varepsilon_o R_o^2} \sim \frac{2.6}{4\pi\varepsilon_o}\;.\;e\;[n_e(m^{-3})]^{2/3} \qquad (1.45)$$

and E_p is the mean field due to plasma oscillations defined by

$$W_{osc} = \tfrac{1}{2}\,\varepsilon_o <E_p^2> \qquad (1.45)$$

Equation (1.44) can then be rewritten, using Equations (1.42), (1.45) and (1.46), as (Ya'akobi and Bekefi, 1969)

$$\frac{S\pm}{S_F} \sim 0.19\delta^3 N_D^{-1/3} \frac{\Delta^2}{(\Delta \pm\omega_p)^2} \tag{1.47}$$

This result indicates that plasma satellites will be enhanced relative to the forbidden line as N_D decreases.

However significant mixing of the upper level of the forbidden line may occur with the nearest dipole-allowed transition level due to strong random fields. The degree of mixing can be estimated by considering the quadratic Stark shift $\Delta\omega_q$ relative to Δ. This ratio is given by Griem (1974, p.157)

$$\begin{aligned} \frac{\Delta\omega_q}{\Delta} &\sim -2\left(\frac{S_+}{S_A}\cdot\frac{S_-}{S_A}\right)^{\frac{1}{2}} \\ &\propto N_D^{-1/3}\frac{S_F}{S_A} \end{aligned} \tag{1.48}$$

where S_A is the strength of the allowed line and the assumption $\omega_p^2 << \Delta^2$ is used in Equation (1.47). Hence the mixing will become stronger as N_D becomes small (although the degree of mixing is still dependent on $\frac{S_F}{S_A} \propto \Delta^{-2}$). Furthermore, as the Baranger-Mozer satellite strength relative to the allowed line $(\frac{S\pm}{S_A})$ becomes large, higher order terms in the perturbation series must be included, which may then reduce the satellite intensity relative to the allowed line (Griem, 1974, p.157).

Once the states are completely mixed, no further amplitude modulation can occur. Frequency modulation then takes place which also produces ω_p sidebands. However, when the frequency shifts due to the randomly fluctuating electric field (that produces the mixing) are superimposed, the satellites are smeared out and may no longer be visible (Burgess, 1982). The strong interactions characteristic of non-Debye plasmas will produce considerable mixing (as indicated by Equation (1.48)), and hence may prevent observation of plasma satellites despite the greater energy available in the form of plasma oscillations.

1.3.6 Thomson Scattering in Non-Debye Plasmas

The theory of Thomson scattering (e.g. Salpeter, 1960) has been developed almost entirely on the assumption of a Debye plasma as the scattering medium. The derivation of the Thomson scattering form factor $S(\vec{k},\omega)$ (which gives the wavevector and frequency dependence of the scattered radiation) relies on a perturbation expansion in terms of $N_D^{-1} << 1$, an expansion which no longer converges for $N_D \lesssim 1$. For this reason there have been no published theoretical evaluations of the form factor for non-Debye plasmas. Recently, however, Boercker, Lee and Rogers (private communication) have attempted a calculation of $S(\vec{k},\omega)$ for $\Gamma \lesssim 1$ by evaluating the frequency dependent dielectric function $\varepsilon(\vec{k},\omega)$ (as $S(\vec{k},\omega) \propto \mathrm{Im.}[\varepsilon^{-1}(\vec{k},\omega)]$, e.g. Griem, 1974, p.160). The calculations indicated some variation in the scattering form factor with Γ (in the range $\Gamma = 0-1$). However, Thomson scattering experiments have so far only been performed on plasmas with N_D values as low as 4 (Rohr, 1967) and 9 (Kato, 1972), and have shown no measurable discrepancy with the expected scattering form factor.

The scattering form factor in Debye plasmas exhibits either a collective or a single particle behaviour, depending on the value of the scattering parameter

$$\alpha = \frac{\lambda_L}{4\pi\lambda_D \sin(\theta/2)} = \frac{1}{\Delta\vec{k}\lambda_D} \qquad (1.49)$$

Here λ_L is the laser wavelength and θ the scattering angle relative to the direction of the laser radiation. The parameter Δk represents the momentum transfer (divided by $\hbar$) due to the change in the photon direction. For collective behaviour, the smallest possible oscillation wavelength is the Debye length, and thus the largest value of k_{osc} ($= 2\pi/\lambda_{osc}$) for the plasma wave is of the order of λ_D^{-1} (Pines and Bohm, 1952). If $\Delta k >> \lambda_D^{-1}$ (i.e. $\alpha << 1$) then the momentum transfer $\hbar\Delta k$ is large compared to the largest value of the plasma wave momentum ($\hbar k_{osc} = \hbar/\lambda_D$). Hence scattering takes place from the random thermal density fluctuations of effectively free electrons. This produces a Gaussian scattering profile with a width equal to the Doppler width for the electron temperature.

For $\alpha >> 1$ the interaction of the electron with the Debye shielding cloud surrounding an ion is relatively unaffected by the small momentum change. Scattering then occurs from density fluctuations due to the interaction of the electrons in the ion field. This produces (a) a central unshifted component due to the random thermal motion of the ions (again with a Gaussian profile), and (b) two satellite sidebands occurring at $\Delta\omega \sim \omega_p$ from the ion feature due to the collective oscillations of the electrons.

Evaluation of α for visible or U.V. wavelengths indicates that for plasmas with $\lambda_D = R_o$, the scattering is "collective" for densities greater than $10^{22}m^{-3}$, even at large (90°) scattering angles. The meaning of collective scattering is, however, somewhat unclear for $N_D \lesssim 1$. Theimer (1966) investigated collective scattering in this regime and calculated the total cross sections for the ion and the electron features. Theimer's results showed that as N_D decreased below 0.5 the ion feature cross-section decreased to zero with N_D. However the electron feature cross-section returned to the

Debye value for the total Thomson cross-section for free ($\alpha >> 1$) electrons. In contrast, the recent numerical calculations of $S(\vec{k},\omega)$ by Boercker et al. for $\alpha = 1$ indicate that only the ion feature intensity increases as Γ approaches unity. The latter result could perhaps be due to the stronger electron-ion coupling, with scattering occurring from density fluctuations due to collective motion of the ions (in modes that are not as enhanced in weakly coupled plasmas - Lee, private communication).

1.4 Background to the Present Work

As shown by the discussions in the previous sections, current theories of the spectrocopy of non-Debye plasmas are far from complete. The present project is part of a programme in this laboratory to extend experimentally the understanding of non-Debye plasma behaviour, using low density ($n_e < 10^{26}$ m^{-3}) plasma sources such as the linear z-pinch. The experimental foundation for this programme was the work of Baker (1977, and Baker and Burgess, 1979) who developed a z-pinch that produced electron densities of 1-3x10^{24} m^{-3} at temperatures of 2-2.5eV. This plasma was near the non-Debye limit, with N_D values of between 3 and 5. Part of the purpose of the present project was to investigate more completely the ability of a similar z-pinch to produce plasmas with fewer particles per Debye sphere. The aim was to enable non-Debye spectroscopic studies to be performed over an extended range of density and temperature conditions.

Among the spectroscopic investigations undertaken by Baker were emission line profiles of Lyman-α, using small hydrogen concentrations ($\sim$ 1%) in the predominantly argon plasma. The plasma column of 0.2m length and several millimetres radius (at peak compression) was optically deep at Lyman-α for the conditions above, even for side on observations. The line profile was thus broadened by the opacity, and self-reversed due to the presence of cooler hydrogen in the outer regions of the discharge. Hence observations were carried out well into the line wings (up to 40Å from line centre) and shot-to-shot line profiles were built up using the 5% reproducibility of the pinch emission. The principal results were the wing asymmetries mentioned previously and the presence of the close interaction satellites. These satellites are discussed in more detail in Chapter 2 together with a general review of other satellite spectral features which might be observed.

Since the formation of these satellites was a result of the closely coupled interaction between hydrogen atom and argon-ion perturber, alteration of the plasma density might be expected to influence both the satellite intensities and positions (Section 2.4). The effects of higher order multipole contributions to the line asymmetry would also be more pronounced at higher densities. Therefore, in addition to the extension of the plasma conditions to smaller N_D values for general non-Debye studies, this project was aimed in particular at studying the effects of variation of the plasma conditions on the Lyman-α line wing features. The design of the z-pinch source used to achieve these aims and the diagnostics used to determine the plasma conditions are described in Chapter 3, together with an appraisal of the limitations associated with the analysis of such dense plasma sources.

A further objective of this study was the measurement of high density Lyman-α line shapes in absorption as well as in emission. Recent developments (e.g. Cotter, 1979) in non-linear frequency upconversion of tuneable dye laser radiation have resulted in the production of 10 watt pulses of VUV radiation tunable in the region 1203-1236Å. A summary of the upconversion techniques involved is presented in Chapter 4, together with a description of the development of the coherent Lyman-α source constructed in this study.

Although successful generation of Lyman-α was achieved, the limitations of the ruby-laser pumped dye laser system restricted the VUV power attainable. As a result the coherent Lyman-α output was not visible above the background pinch emission and an absorption lineshape experiment was therefore not possible. Hence Lyman-α lineshape studies were carried out in emission, the results of which are presented in Chapter 5. In the concluding chapter, suggestions for further work on this non-Debye plasma source are presented. These include proposals for exploiting the recent significant enhancement in coherent Lyman-α generation achieved at the Rutherford Laboratory using an improved dye laser system.

CHAPTER 2

SATELLITES TO LYMAN-α ARISING FROM CLOSE EMITTER-PERTURBER INTERACTIONS

2.1 The Formation of Satellite Features

Spectral structures in the wings of lines have been observed a number of times in dense radiating systems (e.g. Hindmarsh and Farr, 1969). These satellite features are a consequence of the close interaction between emitting and perturbing particles which causes the energy levels of the emitter to be altered. The example in Figure 2.1a shows the potential energy curves between an emitter and a static perturber as a function of perturber proximity. The potentials at infinite separation correspond to the unperturbed atomic energy levels of the isolated emitter. Figure 2.1b gives the difference between the potentials of the two curves. The difference potential has extrema at two radial separations, in addition to the extremum at infinity (which corresponds to the atomic transition energy). Since there is a range of r near the extrema over which the difference potential is only slowly varying, the probability of emission at that difference energy is enhanced. The result is the production of satellite features in the wings of the original line as shown in Figure 2.1c.

However, for historical reasons these features became known in the literature as "quasi-molecular" satellites, even though their origins have nothing necessarily to do with molecular formation. Although the example used in Figure 2.1a suggests a molecular interaction due to the presence of the potential wells, it must be emphasized that the satellites do not arise from transitions between vibrational levels that may exist in the potential wells. In fact the position of the

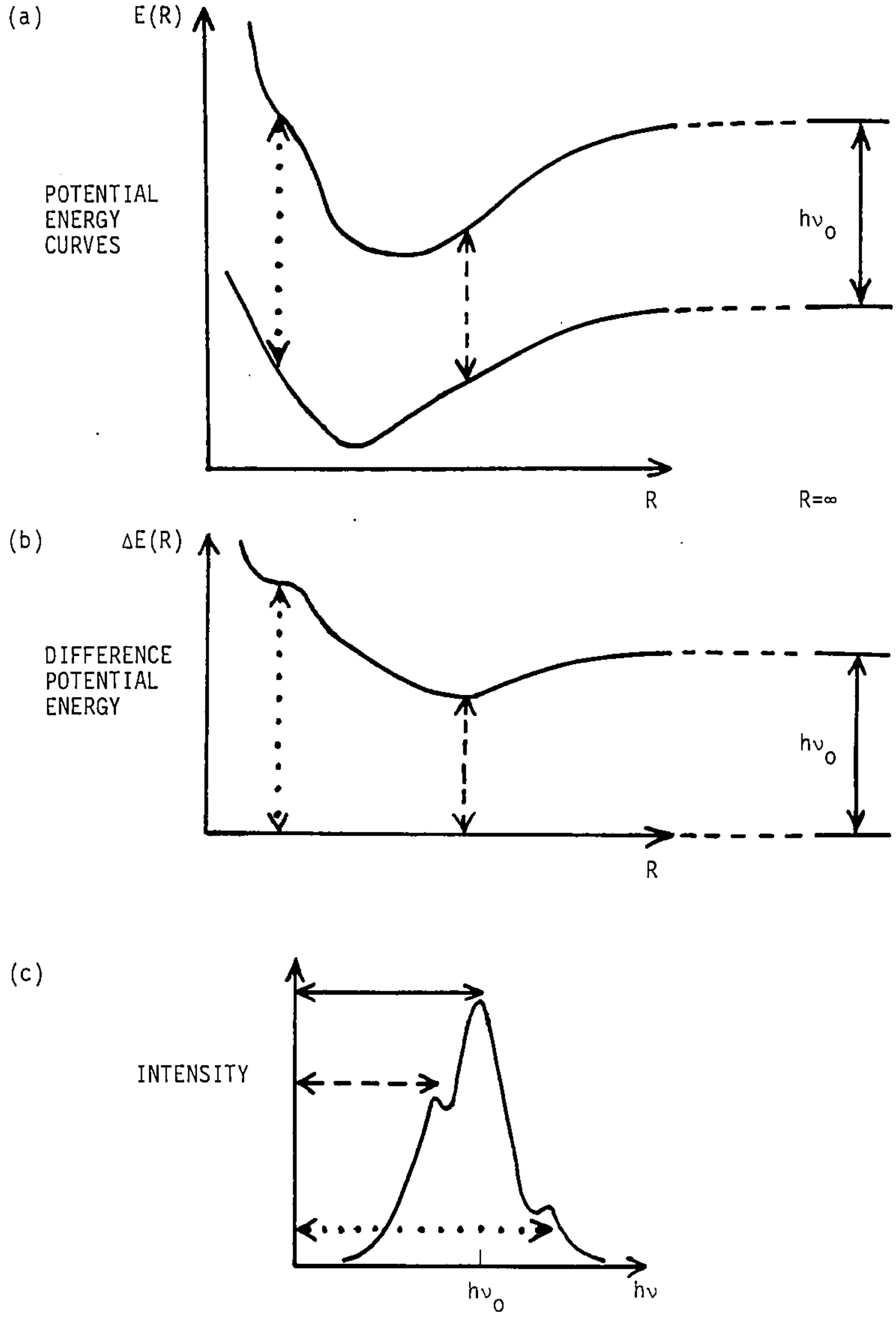

Figure 2.1:Occurrence of satellite features in the wings of the unperturbed line (frequency ν_0) due to extrema in the interparticle difference potential energy. The potential energy curves are shown as a function of the interparticle separation R.

extremum for the blue wing satellite in Figure 2.1c shows that features can also be produced by potential curves with slopes that are purely repulsive.

The following sections will describe further the theory of satellites formed by perturbation of the emitter energy levels. In particular the prediction of satellites in the wings of Lyman-α will be discussed and related to the experimental observations of such features, including the work of Baker mentioned previously.

2.2 Theoretical Studies of Satellites to Lyman-α

The simple quasistatic model outlined above indicates that the line wing intensity at frequency ν will be inversely related to $\frac{d\nu}{dR}$, since the satellite features occur due to the slowly varying difference potential near the extrema. The radial distribution of the perturbers will also affect the lineshape. A simple nearest neighbour distribution yields the following semiclassical expression for the line wing absorption coefficient (Bates, 1952; Stewart et al., 1973)

$$K(\nu) = \frac{32\pi^4 g}{3hc} \; n_l n_p \nu \; \sum_i \; \frac{R_i^{\,2} D(R_i)}{|d\nu/dR|_i} \; \exp\left(\frac{-\delta E_l(R_i)}{kT}\right) \tag{2.1}$$

Here g is a ratio of statistical weights, n_l and n_p the absorber and perturber number densities, D(R) the dipole moment and $\delta E_l(R)$ the change in energy of the lower state compared with that at infinite separation. The sum is over the radial separations which correspond to the absorption frequency ν i.e.

$$h\nu = E_u(R_i) - E_l(R_i) = \Delta E(R_i) \tag{2.2}$$

the so-called "Condon points" R_i.

At the classical satellite frequency it can be seen that Equation 2.1 has a singularity, which originates from the breakdown of the quasistatic approximation. The ions can be regarded as static so long as the collision duration (given by the ratio of the ion velocity to the distance of closest approach) is long compared to the time between collisions (Griem, 1974). The time between collisions is related (via the Fourier theorem) to the frequency separation $\Delta\omega$ from the appropriate line centre. Burgess (1970b) pointed out that the presence of satellite structures in the line wings requires the frequency separation to be evaluated from the satellite centre as well as from the parent line centre (since the parent line and the satellite can be modelled as two separate line profiles). Hence there exists a frequency separation from the satellite centre small enough such that the finite duration of the collision cannot be neglected. Thus the quasistatic approximation must fail in the immediate vicinity of the satellite feature.

In order to obtain realistic satellite profiles using the classical approach, a complete dynamic treatment of the lineshape is therefore necessary. Stewart et al. (1973) circumvented this difficulty simply by introducing a finite Doppler profile for the satellite to remove the divergence caused by the quasistatic model. Using computed H-H^+ potential functions, they performed the first satellite lineshape calculations for an atom perturbed by ions. They predicted satellites at 1233.5, 1240.5 and 1404.9Å in the red wing, and at 1106.5, 1018.0 and 965.0Å in the blue wing of Lyman-α (a similar later calculation by Vallee et al. (1979) using simpler analytic methods confirmed the 1233.5Å satellite). As a consequence of the classical approach used, no intensity of the Lyman-α transition could occur outside the wavelength limits set by the difference potential.

The difficulty of the singular behaviour in the quasistatic approach can be overcome by treating the system quantum mechanically. This was done by Sando and Wormhoudt (1973) for resonance broadening of the Lyman-α line wing. The quantum mechanical technique was later extended to the whole lineshape (including the transition region between quasistatic and impact regimes) by Szudy and Baylis (1975). They used a unified Franck-Condon treatment in which the relative position and kinetic energy of the interacting particles does not change during the radiative transition. The expression for the absorption coefficient then becomes

$$K(\nu) = \frac{64\pi^{9/2} n_1 n_p \nu}{c} \sum_i \frac{R_i^2 D^2(R_i)}{|\Delta E'(R_i)|} Z_i^{\frac{1}{2}} L(Z_i) \exp\left(\frac{-\delta E_1(R_i)}{kT}\right) \qquad (2.3)$$

where $$Z = \tfrac{1}{2} \left(\frac{\mu}{kT}\right)^{1/3} \left(\frac{\Delta E'(R)}{\hbar}\right)^2 \left|\frac{\Delta E''(R)}{\hbar}\right|^{-4/3} \qquad (2.4)$$

$$L(Z) = \int_0^\infty dx\ x^{-2} |A_i(-Zx)|^2 \exp\ (-x^{-3}) \qquad (2.5)$$

where μ is the emitter/perturber reduced mass and $A_i(x)$ is the Airy function. Equation 2.3 reduces to the classical quasistatic expression for large Z, as would be expected as $\Delta E'(R)$ increases from zero away from the extremum.

The effect of this exact calculation is to alter the satellite position only slightly, as was shown by Sando and Wormhoudt for the resonance broadening of Lyman-α. However the quantum mechanical treatment does give a discrete, finite structure to the satellite features without the need to invoke broadening mechanisms. In addition a number of new effects are predicted, such as the oscillations towards line centre caused by quantum mechanical interference of several Condon points contributing at the same frequency. Broadening outside the frequency limits imposed by the difference potential is now possible due to the contribution of complex Condon points, and the profile is predicted to fall off exponentially outside the outermost satellite.

The result of Sando and Wormhoudt (in the high temperature limit) can also be recovered semiclassically. Le Quang Rang and Voslamber (1975) calculated the line profile near the satellite by including the relative emitter-perturber velocity, while treating the rest of the line wing quasistatically. The self consistency of their method was shown by the smooth joining of the quasistatic and dynamic parts of the profile. Using the same H_2^+ molecular potentials as Stewart et al., Le Quang Rang and Voslamber predicted three satellites in slightly different positions at 1234.3, 1241.3 and 1107.0Å, as well as three satellites at 965, 1018 and 1404.9Å in the same positions as obtained by Stewart et al.. However the dynamic method of Le Quang Rang and Voslamber was able to predict satellites of finite intensity without the need to invoke broadening mechanisms to remove the quasistatic singularities.

Much of the theoretical investigation of satellite features had concentrated on simple hydrogenic systems perturbed by protons. However many of the experimental observations of satellites occurred in hydrogen/argon plasmas (as described in the following section). In most of these plasmas, the hydrogen concentration was too low to observe H-H^+ satellites in the wings of Lyman-α lines perturbed predominantly by argon ions. For this reason a prediction of the hydrogen-argon ion interaction was necessary.

A calculation of the H-Ar^+ potentials was undertaken by Chambaud et al. (1979) who performed an ab initio calculation which included the configuration interaction. They considered the levels dissociating at infinity into $Ar^+(3p^5)+H(n=1)$, $Ar^+(3p^5)+H(n=2)$ and $Ar(3p^54s)+H^+$, as the energy of the latter state lies between the former two at infinite separation. The intermediate energy state was found to be important as it produced an avoided level crossing with the $H(n=2)$

state, resulting in an extremum in the n=2→1 difference potential at a separation of ∿8-10Å. The resultant satellite was predicted to occur at 40±8Å in the red wing of Lyman-α. A further satellite at 136±13Å was predicted as the result of another extremum at ∿5Å separation. However the treatment was limited in accuracy due to the use of a pseudopotential to approximate the repulsive effect of the argon inner shell, and also by the use of a quasistatic rather than a full quantum mechanical formalism. In addition, it might be expected that non-adiabatic effects would become important for the 40Å satellite which originated from the avoided level crossing. The satellite may tend to broaden as a result of such effects, although this problem was not addressed by the authors.

A summary of the various predicted Lyman-α satellite wavelengths is given in Table 2.1, together with the wavelengths of the experimentally observed satellite features that are discussed in the following section.

2.3 Experimental Observations of Lyman-α Satellites

Satellite features in the line wings of Lyman-α were first observed by Quefflec and Girault (1974) who detected a feature at 16.5Å in the red wing. The source used was a hydrogen/argon arc, although no details of the plasma conditions obtained in this experiment were given. However, it was noted that as the H_2 concentration was increased at constant arc current (thereby lowering the temperature through H_2 dissociation), the satellite intensity decreased in keeping with a decrease in the ion and atomic hydrogen concentrations. The experiment was repeated in a H/He mixture and a similar effect occurred at the same wavelength, thus indicating that proton perturbers were responsible (in rough agreement with the predictions of Stewart et al. and Le Quang Rang and Voslamber - Table 2.1).

THEORETICAL SATELLITE WAVELENGTH SEPARATION FROM LYMAN-α (Å)	EXPERIMENTAL SATELLITE WAVELENGTH SEPARATION (Å)	REFERENCE	PERTURBERS
-250.7		(1) + (4)	Protons
-197.7		(1) + (4)	Protons
-109.2 or 108.7		(1) or (4)	Protons
	- 31.5	(6)	Ar^{2+}
	- 15.9	(6)	Ar^+
	8.3	(6)	Ar^+
	16.5	(3)	Protons
	16.9	(6)	Ar^+
17.8 or 18.6		(1)+(8) or (4)	Protons
	23.9	(6)	Ar^+
24.8 or 25.6		(1) or (4)	Protons
	37	(5)	Ar^+
	38	(2)	Not recognised at the time
	40.1	(6)	Ar^+
40 ± 8		(7)	Ar^+
136 ±13		(7)	Ar^+
189.2		(1) + (4)	Protons
	190	(5)	Ar^+

(1) Stewart et al. (1973): HH^+ Quasistatic nearest neighbour theory

(2) Fussmann (1972): H/Ar arc; 12,200 K, $7 \times 10^{22} m^{-3}$

(3) Quefflec and Girault (1974): H/Ar and H/He arc

(4) Le Quang Rang and Voslamber (1975 and 1981): Ion dynamic theory

(5) Preston (1977): H/Ar arc; 12-14,000 K; $0.9\text{-}2.4 \times 10^{23} m^{-3}$

(6) Baker and Burgess (1979): H/Ar z-pinch; $2\text{-}3 \times 10^4$ K; $1\text{-}3 \times 10^{24} m^{-3}$

(7) Chambaud et al. (1979): Quasistatic theory; HAr^+ potentials

(8) Vallee et al. (1979): Quasistatic HH^+ analytic theory

Table 2.1: Predicted and Experimental Lyman-α satellites grouped by wavelength

Another argon/hydrogen arc study by Preston (1977) at $n_e = 0.9\text{-}2.4\times10^{23}m^{-3}$ and $T_e = 1.2\text{-}1.4\times10^4K$ produced two new satellite features at 37 and 190Å in the red wing of Lyman-α . At constant n_e and T_e the features scaled linearly with hydrogen concentration, and calculations revealed that at different plasma conditions the satellite intensity scaled as $n_2^H n_e$ (where n_2^H is the n=2 state hydrogen number density). Hence Preston concluded that the satellites were due to Ar^+ perturbers. Preston was also able to show that the satellite wavelengths were independent of density over the range of densities obtained ($0.9\text{-}2.4\times10^{23}m^{-3}$). He further pointed out that in some work carried out by Fussmann (1972) at $n_e = 7\times10^{22}m^{-3}$ and T_e =12,000K in a H/Ar arc, there was evidence of a small feature at 38Å in the red wing of Lyman-α (although this was not noticed by Fussmann at the time).

Studies carried out in this laboratory (Baker, 1977; Baker and Burgess, 1979) discovered further satellites to Lyman-α, using a high density ($1\text{-}3\times10^{24}m^{-3}$) relatively cool ($T_e \sim 2\text{-}3\times10^4K$) z-pinch device. Emission profiles yielded features at + 8.3, 16.9, 23.9, 40.1 and -15.9Å all of which appeared to scale linearly with $n_2^H\,Ar^+$. However one feature at -31.5Å seemed to scale with $n_2^H Ar^{2+}$ and was thus attributed to Ar^{2+} rather than Ar^+ perturbers. No satisfactory scaling with proton concentration was found. The absence of any wavelength shifts over the small range of electron densities used ($1\text{-}3\times10^{24}m^{-3}$) ruled out the possibility of plasma frequency satellites being present. Indeed three satellites (at -13.5, -15.9 and +8.3Å) did not correspond to any features observed or predicted previously, as can be seen from Table 2.1.

2.4 Effects of Multiple Perturbers on Satellite Features

The results in Table 2.1 show a significant disparity between experimental and theoretical satellite positions. This may in part be due to inadequate knowledge of the exact emitter-perturber potentials, since only a small change in the potential curves is needed to eliminate (or create) an extremum. Experimentally, small discrepancies may result from the asymmetry in the satellite feature caused by the quasistatic wing of the unperturbed line. Then, as pointed out by Szudy and Baylis (1975), the wavelength of maximum intensity may not correspond to the wavelength of the classical satellite. However this effect would not account for some of the large wavelength differences between various experimental observations, or for the discrepancies with the nearest predicted satellite positions.

One possible explanation is the effect of multiple perturbers on the potential energy curves. The sensitivity of the extrema to small changes in the shape of the potential curves suggests that interactions due to further perturbers may significantly affect the satellite wavelengths and intensities.

Such multiple perturber interactions have been treated theoretically for neutral-neutral systems (Hindmarsh and Farr, 1969). A Lennard-Jones potential was assumed for the two-particle interaction, and the effects of multiple interactions were assumed to be additive (although small non-additive effects do occur even for rare gas systems- Kim, 1975). The calculations predicted that n perturbers would produce a satellite at a wavelength separation from line centre equal to n times the wavelengh separation of the single perturber satellite. This is a direct result of assuming additivity of the emitter-perturber interactions. If E_i^∞ is the unperturbed energy of state i and $\Delta E_i(r)$ the static energy level shift due to a single perturber at radius r, then the derivative with respect to r of the difference energy for n additive perturbers is:

$$\frac{\partial(\Delta E)}{\partial r} = \frac{\partial}{\partial r}\left[\left(E_1^\infty + n\Delta E_1(r)\right) - \left(E_2^\infty + n\Delta E_2(r)\right)\right]$$

$$= n\frac{\partial}{\partial r}\left[\Delta E_1(r) - \Delta E_2(r)\right] \qquad (2.6)$$

Hence the n perturber difference potential will retain extrema at the same radial positions as for a single peturber. Furthermore the n perturber satellite will be shifted by an amount $n\left[\Delta E_1(r)-\Delta E_2(r)\right]$ from the original line centre $(E_1^\infty - E_2^\infty)$.

A number of satellites may therefore be observed at various multiples of the single perturber satellite position from line centre, depending on the probability of the emitter interacting with a given number of perturbers simultaneously. Hence the nth satellite intensity would not be expected to scale exactly with the nth power of the perturber density since the wing intensity is the sum of all n contributions (Niemax, 1980).

Such multiple satellites have been observed in a number of neutral-neutral gas systems, thereby supporting the assumption of additivity of the emitter-perturber interactions. Kielkopf and Allard (1979) were the first to show that multiple satellites in Cs-Xe grew in intensity according to the probability of finding the appropriate number of perturbers within a given distance of the alkali atom (a distance determined by fitting a Poisson distribution to the experimental data). Multiple satellite spectra were also observed by Niemax (1980) who altered the perturber density over an order of magnitude in Cs-Kr and Cs-Xe. This was sufficient to decrease the first satellite intensity at high densities while the secondary satellite intensity increased. It was also noticed that the sharp Cs-Kr satellite resulted in a sharp secondary satellite, while the weak and broad satellite of Cs-Xe produced a barely discernible secondary satellite. Most importantly, a shift in the parent line centre with increasing perturber density was exactly matched by a shift in the satellite positions. The absence of any change in the satellite separations further supported the assumption of scalarly additive multiple perturbers.

For emitters perturbed by ions, however, such an assumption is doubtful since the perturbers themselves will interact due to the strength and range of their electric fields. Hence the effect on the emitter becomes a many body problem involving interparticle correlations. Although microfield calculations have been carried out that include many body correlations (e.g. Hooper, 1968), the effect on the radiator cannot be calculated here using perturbation theory, or by assuming a multiple expansion, in view of the strong interactions involved in satellite formation. Hence the full, three dimensional, emitter-multiple perturber potential surface must be calculated, which is an extremely difficult problem. However, it might be expected that any alteration to the potential curves due to multiple perturbers would produce considerable effects on the satellite intensities and positions. One of the aims of this project was to investigate such effects by measuring the density dependence of the satellites observed by Baker.

2.5 Temperature Dependence of Satellites

In a complete dynamic treatment of the line profile, the satellite lineshape will be affected by the magnitude of the perturber velocity at radial separations near to the extremum. Hindmarsh and Farr (1969) showed that the satellite will broaden and its intensity decrease with increasing temperature. The decreased intensity is due to the reduced probability of emission at the satellite frequency as the perturber spends less time near the extremum.

Observations by McCartan et al. (1974) on neutral systems supported the prediction of greater satellite visibility at lower temperatures. Preston (1977) showed that the satellite widths in a H/Ar arc scaled as $T_e^{\frac{1}{2}}$ over a temperature range of $1.2\text{-}1.4\times10^4$ K. (Note that this scaling is the same as the Doppler width employed by Stewart et al. (1973) to remove the singularities in the quasistatic method.)

Further theoretical work on temperature effects was carried out by Le Quang Rang and Voslamber (1981) who extended their earlier dynamic treatment of ions to include the whole line profile. An increase in the satellite width with temperature was again predicted, although the calculations indicated a linear scaling with temperature. No experimental observations have been made to support this scaling. One of the aims of the present project was to develop a narrowband, coherent Lyman-α source to resolve the width scaling of the satellites observed by Baker, whose resolution was limited to the ½Å instrument width of the monochromator employed in the emission studies.

2.6 Z-Scaling of Satellite Features

Since extrema can exist in the difference potential energy for interactions that are purely repulsive, it may also be possible for satellites to occur in highly ionized plasmas. However both the existence and position of the extrema are highly sensitive to the details of the emitter-perturber interaction and it is therefore difficult to accurately predict the scaling of satellite features with increasing emitter and perturber charge.

The H-Ar^+ satellites observed by Baker do however have the property that both the emitter and the perturber charge on the optical electron are the same (unity). Hence, when attempting to scale the satellite behaviour to highly ionized plasmas, there is the advantage that the emitter-perturber charge ratio will be roughly the same for any of the dominant species (since $(z\pm1)/z \sim 1$ for large z).

To estimate qualitatively the effect of increased emitter and perturber charge on the emitter energy levels, the following simple classical model was used. An emitter (point charge Z_e) and perturber (point charge Z_p), separated by a distance d, produce the following terms for the potential at a position r

$$V(r) = -\frac{e}{4\pi\varepsilon_o}\cdot\frac{Z_e}{r} - \frac{e}{4\pi\varepsilon_o}\cdot\frac{Z_p}{d-r}$$

$$= -\frac{e}{4\pi\varepsilon_o}\cdot\frac{Z_e}{r}\left(1+\frac{Z_p}{Z_e}\;\frac{1}{(\frac{d}{r}-1)}\right) \qquad (2.7)$$

where r(<d) is measured from the emitter. The term due to the repulsion of the two nuclei has been omitted as it affects all electron states equally and hence does not contribute to the difference potential energy. Note that Equation (2.7) does not represent the potential <u>energy</u> curves shown in Figure 2.1a, since the effect on the energy levels due to the electronic state wave functions has not been included.

However the following trends can be deduced from Equation (2.7):

1) For a constant charge ratio $\frac{Z_p}{Z_e}$, the potential will exhibit the same dependence on the perturber separation.

2) Given (1), the fractional charge in the potential (second term in brackets) at a Bohr radius $r_z=\frac{r_o}{z_e}$ will be independent of z, provided that the perturber separation distance also scales as $d_z=\frac{d}{z_e}$ (i.e. by increasing the density by a factor of z^3).

The potential for a number of perturber separations and charge ratios is therefore shown in Figure 2.2a as a function of r_z (in units of $\frac{r_o}{z_e}$). The Coulomb potential is given by $d_z = \infty$, and the family of curves $^zp/z_e=1$ shows the effect of altering the perturber separation. The potential is asymmetric for $^zp/z_e\neq 1$.

The effect of the perturber on the emitter energy levels is then approximated by assuming that the electron position remains fixed at the classical Bohr radius $r_{nz}=\frac{n^2r_o}{Z_e}$. This is a gross

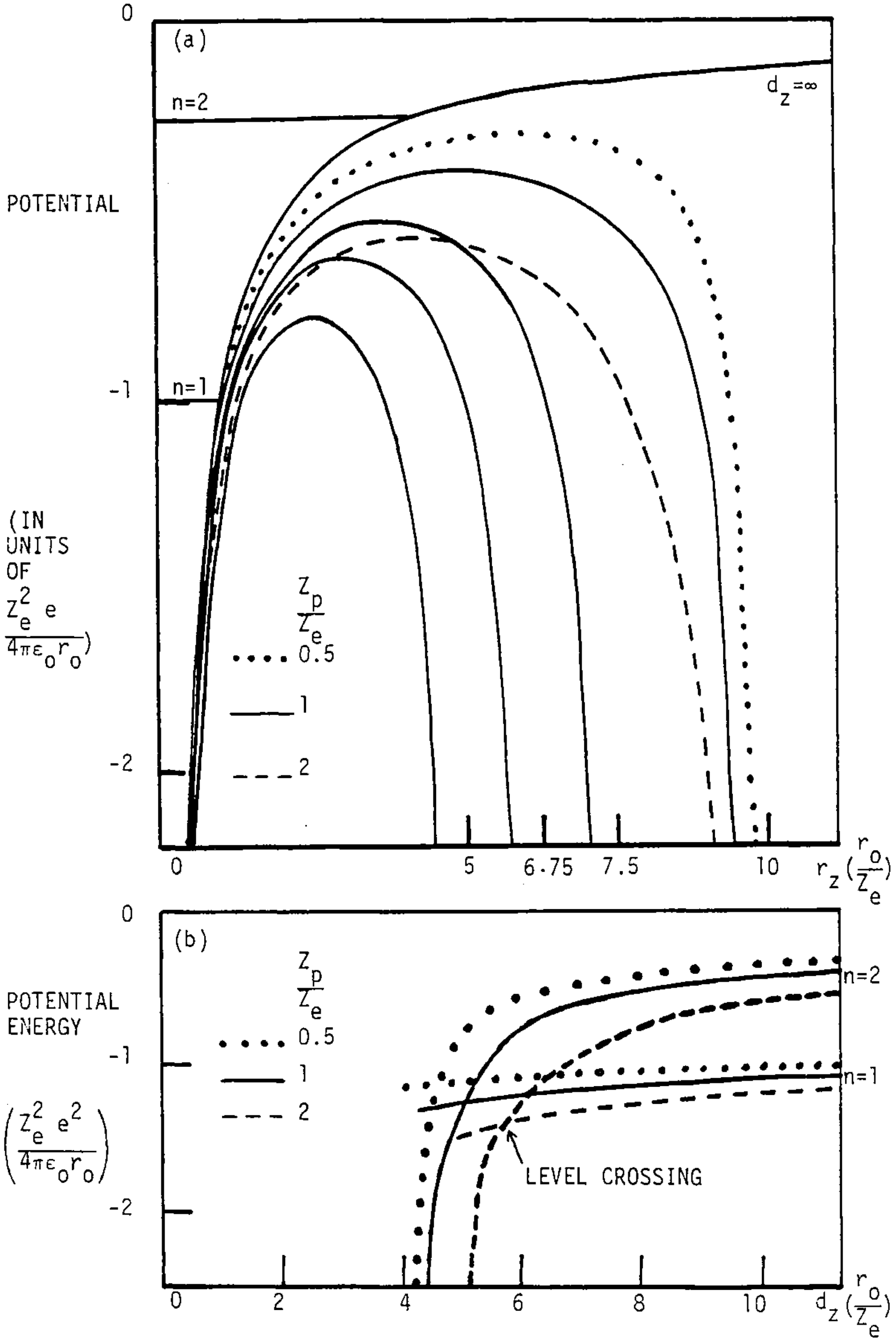

Figure 2.2(a): Potential due to emitter Z_e and perturber Z_p as a function of position r_z(units r_0/Z_e) from the emitter. Different perturber positions d_z(horizontal axis tics) give the solid curves: different charge ratios give the broken curves(for $d_z=10r_0/Z_e$). (b) The electron potential energy at positions corresponding to the radii of the n=1 and 2 states, as a function of perturber separation d_z(units r_0/Z_e), and charge ratio Z_p/Z_e.

simplification since, for example, changes in the electronic state wave functions have been neglected. Although as a result no extrema occur in the difference energy using this approximation ($\frac{\partial}{\partial d}(E(r_2)-E(r_1)) = 0$ only for $r_1=r_2$), the energy levels shown in Figure 2.2b do indicate an interesting feature: namely that as d_z approaches $r_2=4r_z$, the upper energy level (n=2) crosses the lower energy level (n=1). The crossing is due to the stronger interaction between the perturber and the electron in the higher energy state (with larger radius). This result is important since Chambaud et al. (1979) indicated that one of their predicted extrema occurred as the result of an avoided level crossing. Further, the relative perturber/electron separation $\frac{d}{r}$ producing the level crossing is dependent only on $\frac{Z_p}{Z_e}$, enabling scaling of the level crossing separation for plasmas with the same charge ratio.

The likelihood of satellite formation at separations d approaching r occurs simultaneously with the breakdown of the multipole and perturbation expansions discussed in Section 1.3.4.1. Thus lineshape calculations involving such expansions will be unable to accurately predict the occurrence of satellite features. Hence a rigorous examination of the Z-scaling of satellite features requires a complete calculation of the potential energy curves for the highly charged emitter-perturber system. Such a calculation could perhaps be performed by, for example, Z-scaling the wavefunctions used in the H-H^+ calculations of Stewart et al. (1973). While such a calculation may prove difficult, the discussions above indicate no a priori reason why satellite features should not occur in the spectra of highly ionized plasmas.

2.7 Lyman-α at High Densities

This section will present calculations of some of the important parameters relevant to the study of Lyman-α at the densities ($\sim 10^{25} m^{-3}$) and temperatures ($\sim$ 3eV) expected in this z-pinch plasma source.

Firstly, the electron plasma frequency is given by

$$\omega_{pe} = (\frac{n_e e^2}{\varepsilon_o m_e})^{\frac{1}{2}} \sim \frac{2\pi v_e}{\lambda_D}$$

$$\sim 1.8\times 10^{14} \text{rad.s}^{-1} \qquad (2.8)$$

This places a lower bound of $\sim$14Å on the range $\Delta\lambda$ from line centre for which a dynamic treatment of the electrons under the impact theory is valid (Griem, 1974). The argon ion plasma frequency (assuming $n_i = n_e, z=1$) is

$$\omega_{pi} = (\frac{n_i e^2 Z^2}{\varepsilon_o m_i})^{\frac{1}{2}}$$

$$\sim 6.6\times 10^{11} \text{rad.s}^{-1} \qquad (2.9)$$

which corresponds to the impact approximation for ions being valid within 5×10^{-2} Å of the appropriate line centre.

The ion plasma frequency may not, however, provide an appropriate limit to the impact approximation for the ions that actually contribute to the satellite feature. This limit may be better estimated by determining the collision duration v/ρ (where v is the mean ion velocity and ρ the impact parameter at closest approach). The impact approximation applies (Griem, 1974) when the collision duration is much shorter than the time between collisions, (which can be identified via the Fourier theorem with the frequency separation $\Delta\omega$ from the appropriate line centre). Using the mean ion velocity $v \sim 4.6\times 10^3 ms^{-1}$, and the perturber separation corresponding to the minima in the difference potential calculated by Chambaud et al. for

H-Ar$^+$($\sim$5 and 8-10 Å), the relevant impact limits are $\sim$ 0.8Å and $\sim$ 0.4Å respectively. Note that this is considerably greater than the half Doppler width ($\sim$0.08Å) and hence a dynamic treatment of the satellite profile is necessary.

The Lyman-α line itself is also sensitive to ion dynamic effects since the central, dominant σ component is not shifted by static electric fields. This sensitivity is shown in the discrepancy found by Grutzmacher and Wende (1977), whose experimental Lyman-α widths were twice those predicted when ion dynamics were neglected. Lee (private communication) predicts a Lyman-α HWHM of $\sim$1.5Å at the conditions expected here, when both ion and electron dynamic and static effects are included.

Finally, in this plasma the mean interparticle separation ($R_0 \sim$ 29Å for electrons) is of the same order as the Debye length ($\lambda_D \sim$41Å for electrons), thus indicating the strength of interparticle interactions. Further, the mean inter-ion distance (assuming $z \sim 1$) approaches the radial separation of the extrema calculated by Chambaud et al. (1979) above. Once this occurs, effects due to second perturbers become important as was shown by Kielkopf and Allard (1979) for neutral-neutral systems. For the ionized perturbers considered here the interactions are of much longer range, and thus multiperturber effects may be significant in the present experiment.

2.8 Estimate of the Lyman-α Satellite Opacity

It is possible (from the data of Preston) to estimate the optical depth of the satellite features under the conditions expected in the present experiment (n_e=10^{25}m^{-3}, T_e=3eV), assuming that third-particle effects do not significantly alter the shape of the satellite profile. Preston found that the satellite located at $\Delta\lambda$ = 37Å had an intensity relative to the quasistatic line wing of

$$R(\Delta\lambda) = \frac{S(\Delta\lambda)}{S_H^{\alpha}(\Delta\lambda)} = 3.9 \qquad (2.10)$$

Here S_H^{α} $(\Delta\lambda)$ is the Holtsmark asymptotic lineshape function for Lyman-α, given by (Preston, 1977)

$$S_H^{\alpha}(\Delta\lambda) = 1.49\text{x}10^{-15} n_e(\text{m}^{-3})[\Delta\lambda(\text{Å})]^{-\frac{5}{2}}\ \text{m}^{-1} \qquad (2.11)$$

which has a value of 3.8×10^4 m^{-1} at the densities measured by Preston ($n_e = 2.1\text{x}10^{23}\text{m}^{-3}$). Writing the line wing absorption coefficient for Lyman-α gives

$$k_H = \frac{\lambda_{21}^5}{8\pi c} \frac{g_2}{g_1} n_1^H \frac{A_{21}}{\lambda} S_H^{\alpha}(\Delta\lambda)\ [1-e^{-hc/\lambda kT}] \qquad (2.12)$$

Here λ_{21} and A_{21} are the Lyman-α wavelength and Einstein A coefficient respectively, λ is the satellite wavalength and n_1^H the ground state hydrogen population density. Using the previous two equations the optical depth of the satellite under Preston's conditions (n_1^H L = $7.1\text{x}10^{20}\text{m}^{-3}$) was $\tau \sim 6\text{x}10^{-3}$.

Since Preston observed a scaling of the intensity with $n_H^{n=2}$ n_{Ar+} , it is possible to estimate the optical depth at the conditions expected in the present experiment given that for Preston $n_{Ar+}=n_e=2.1\text{x}10^{23}\text{m}^{-3}$. At $n_e=10^{25}\text{m}^{-3}$ and T_e=3eV L.T.E. will hold since (Griem, 1963)

$$n_e > 9\text{x}10^{23}z^7\left(\frac{E_2-E_1(\text{eV})}{13.6z^2}\right)^3\left(\frac{T(\text{eV})}{z^2 13.6}\right)^{\frac{1}{2}}\ \text{m}^{-3} \qquad (2.13)$$

$$\sim\ 10^{23}\ \text{m}^{-3}$$

Thus the neutral hydrogen number density is given by Saha's equation:

$$\frac{n_+ n_e}{n_H} = \frac{4}{u_H}\left(\frac{2\pi m_e kT}{h^2}\right)^{3/2} e^{-\frac{(13.6e-\Delta E_D)}{kT}} \qquad (2.14)$$

Here u_H is the hydrogen partition function, and ΔE_D is the Debye plasma value for the ionization potential depression. The I.P. depression will limit the number of hydrogen bound states according to

$$\Delta E_D = \frac{e^2}{4\pi\varepsilon_o\lambda_D} \sim 0.5\text{eV} < \frac{13.6}{n^2} \qquad (2.15)$$

where the R.H.S. represents the energy of the highest bound state n from the continuum. This gives a maximum of $n = 5$ and hence

$$u_H = \sum_{n=1}^{5} 2n^2 e^{-13.6e(1-\frac{1}{n^2})/kT} = 3.7 \qquad (2.16)$$

Thus $n+/n_H \sim 21$ and since around 50% of the electrons are in the ground state, then $\sim$2.4% of the original hydrogen concentration will contribute to absorption.

Assuming an H:Ar ratio of 1:100 it remains to calculate n_{Ar+}. Since almost the entire electron density comes from the argon atoms and since at 3eV nearly 60% of argon atoms will be singly ionized at $n_e=10^{25}m^{-3}$ (see Section 3.12), then $n_{Ar+} \sim 4\times10^{24}m^{-3}$. Finally, assuming a typical axial path length L of 0.2 m, the optical depth of the satellite under these conditions will be

$$\tau_{sat} = \frac{n_H L n_{Ar+}}{(n_H L n_{Ar+})_{Preston}} \times 6\times10^{-3} \qquad (2.17)$$

$$\sim 0.05$$

or $\sim$5% absorption.

The satellites observed by Baker were considerably more intense and closer to the Lyman-α line centre than were the satellites observed by Preston, with some of the satellites seen by Baker having intensities approaching the intensity of the Lyman-α line.

Thus, assuming that third body effects do not alter the satellite lineshape, the satellite features should be observable in absorption at the conditions expected in the present experiment.

CHAPTER 3

Z-PINCH DESIGN AND DIAGNOSTICS

3.1 Design Criteria

The chief requirement in the design of the z-pinch plasma source was to produce a wide range of operating conditions for the investigation of spectroscopic effects in dense, non-Debye plasmas. In particular this meant an extension of the range of peak compression densities in order to test the density dependence of the Lyman-α satellites observed by Baker (1977), since Baker did not survey completely the limits to the conditions achievable in such pinches (e.g. by variation of the pinch circuitry, discharge current and filling pressure). As well as increasing the compression density, it was desirable that additional heating of the plasma did not occur, so that observations could be made at the same (or fewer) particles per Debye sphere as achieved in Baker's experiments ($N_D \sim 4$). This was a particular limitation in view of the strong temperature dependence of N_D (α $T^{3/2}$) compared to the weaker ($n_e^{-\frac{1}{2}}$) dependence on density. A further requirement was that the plasma be sufficiently stable and reproducible to enable shot-to-shot scanning of line profiles.

In order to achieve higher densities ($n_e > 3 \times 10^{24} m^{-3}$) it was considered necessary to increase the peak current (and hence the compression force available). The greater current flow could however give rise to enhanced plasma heating. To offset this the filling pressure of the 100:1 argon/hydrogen mixture was increased in order that energy losses through ionization and radiation would reduce the energy available for plasma heating. This approach was later supported by observations by the Bochum group (K.H. Finken, private communication) who managed to obtain densities of $5\times10^{23}m^{-3}$ at 10eV using 0.25 torr filling pressure in pure hydrogen, while obtaining $5\times10^{25}m^{-3}$ at 4eV and 5 torr.

However, optimisation of the plasma density and N_D value is somewhat more complicated than this, since the dynamics of the discharge collapse must also be considered (Roberts, 1972). Simple theories of the pinched discharge (Allen, 1957) describe the dynamic behaviour using the shock-piston model in which a current piston drives ahead of it a shock wave. On reaching the pinch axis the shock is reflected and expands to meet the incoming current piston. The piston is then reflected from the shock-heated region, thereby limiting the collapse of the pinch radius. However, Roberts showed that when current penetrates the region between shock and piston, significant Joule heating can occur to further limit the current sheet collapse. This was found to occur (for a given bank voltage) above a certain critical value of the filling pressure P_M at which the electron density was observed to peak.

Identification of this critical filling pressure was therefore important in the present experiment in order to achieve the highest plasma densities possible. Furthermore, at pressures other than P_M undesirable heating of the plasma could occur. At lower pressures the energy deposited in the filling gas would experience fewer losses from radiation and ionization, while for pressures greater than P_M additional heating due to incomplete shock-piston separation may occur.

3.2 Diagnostic Limitations in Dense, Z-pinch Plasmas

As has been shown elsewhere (Baker, 1977 and Finken et al., 1978), the high densities obtainable in z-pinch plasmas impose severe limitations on the techniques available for plasma diagnostics. The greatest difficulties arise from the high opacities of lines and the continuum.

In particular the quadratic dependence on n_e of the continuum and ion line wing opacities can severely limit the observation of emission lines at high densities. Emission lines may not in fact be visible above the black body emission level of such optically deep plasmas. The lines themselves may be optically thick, a difficulty that is further compounded by the fact that this usually necessitates side-on observation of the plasma. Problems then arise due to the need to observe regions of spatially varying density and temperature. Measurement of continuum intensities may in turn be affected by the presence of many overlying lines (particularly in argon plasmas), some of which may be significantly wide with wings of considerable opacity.

Application of laser-based diagnostic techniques may also be restricted by continuum absorption. In the case of interferometric measurements, fringe amplitude is considerably reduced. Measurement of fringes at high density is also limited by the difficulty of counting many fringes of short duration near the peak compression.

Thomson scattering has been performed previously on low density ($\lesssim 10^{23}m^{-3}$) pinches (Smith and Burgess, 1978), and should in principle be applicable at higher densities (since both the scattered signal and the statistical noise of the continuum emission are proportional to n_e). However, the effects of plasma heating through inverse bremmstrahlung absorption of the laser radiation become significant at higher densities. The fractional temperature increase for a pulse intensity I_0 and duration $\Delta\tau$ is given by Evans and Katzenstein (1969) as being

$$\frac{\Delta T}{T} = 5.32\mathrm{x}10^{-41}\left(\frac{n_e(m^{-3})Z}{T(eV)^{3/2}}\right) \lambda^3(\mathring{A})\left(1-e^{-\left(\frac{hc}{\lambda kT}\right)}\right) I_0(W/m^2)\ \Delta\tau(s) \qquad (3.1)$$

To maintain the same percentage plasma temperature increase (2%) as Smith and Burgess but at densities up to $10^{25}m^{-3}$ requires a 100 fold reduction in the power of the ruby laser (at a given temperature).

Furthermore, continuum absorption reduces both the light incident, on the plasma as well as the scattered radiation reaching the detector. These two factors combine to prevent the application of ruby laser Thomson scattering techniques to dense plasmas due to adverse signal-to-noise conditions.

3.2.1 Continuum opacity calculations

Due to the restrictions imposed on diagnostic techniques by the continuum opacity, calculations were carried out to determine the variation of the continuum opacity as a function of wavelength and plasma conditions. Shulz-Gulde (1970) gives the following expression for the continuum absorption coefficient (including induced emission):

$$K_\lambda(T) = \frac{4e^6}{3hc^4(4\pi\varepsilon_0)^3}\left[\frac{2\pi}{3km_e^3}\right]^{\frac{1}{2}}\frac{Z^2 n_e n_i}{T^{\frac{1}{2}}}\lambda^3\left[\exp\left[\frac{hc}{\lambda kT}\right] -1\right]\xi(\lambda,T) \qquad (3.2)$$

This includes the effects both of inverse bremstrahlung (in the low temperature, quasiclassical limit), and of single photon ionization. The factor $\xi(\lambda,T)$ takes into account the quantum mechanical corrections to the free-free absorption via the Gaunt factor g_{ff}, and also includes the difference in atomic structure between argon and hydrogen (incorporated in the weighted sum of photoionization cross sections g_{fb}). The relation of g_{ff} and g_{fb} to the ξ factor is given by

$$\xi(\lambda, T) = \frac{\gamma}{u(T)} g_{fb}\left[1-\exp\left(-\frac{hc}{\lambda kT}\right)\right] + g_{ff}\exp\left(-\frac{hc}{\lambda kT}\right) \qquad (3.3)$$

where γ is the statistical weight of the parent ion and $u(T)$ is the ionic partition function. Values for $\xi(\lambda, T)$ have been calculated (e.g. Hofsaess, 1978) and measured (e.g. Preston, 1977 ; Schnehage et al., 1982) for low temperature (< 20,000K) argon plasmas. No work has been done at higher temperatures where the contribution of higher ionization stages must also be included.

It is possible however to extrapolate the above results to the higher temperatures expected in this plasma (2-4eV) by making use of the relationship between emission and absorption coefficients via Kirchoff's law i.e.

$$\frac{\varepsilon_\lambda(T)}{K_\lambda(T)} = B_\lambda(T)$$

$$= \frac{2hc^2}{\lambda^5} \frac{1}{e^{hc/\lambda kT}-1} \quad d\lambda \quad Wm^{-2}\ ster^{-1} \qquad (3.4)$$

where $B_\lambda(T)$ is the Planck black body function. Results are given by Hofsaess (1978) for the emission coefficient $\varepsilon_\lambda(T)$ up to temperatures of 21,500K, from which the absorption coefficient can be obtained using Equation (3.4). Extrapolation to even higher temperatures can then be achieved by using the experimental observation that $\varepsilon_\lambda(T)$ varies only weakly with temperature, particularly for longer wavelengths (Schnehage et al., 1982).

The continuum absorption coefficients are shown in Figure 3.1 for the known data at ~15,000K, the data calculated using the emission coefficients at 21,500K, and the extrapolations from these calculations that were carried out for higher temperatures. The strong dependence on wavelength is readily apparent with the highest continuum opacity occurring in the visible region. At UV wavelengths the opacity is significantly lower, and suggests that UV Thomson scattering using excimer KrF lasers at 2480Å may be possible,although none were available for this experiment. For the purposes of the Lyman-α lineshape studies considered in this experiment, the effect of the continuum opacity should be relatively unimportant.

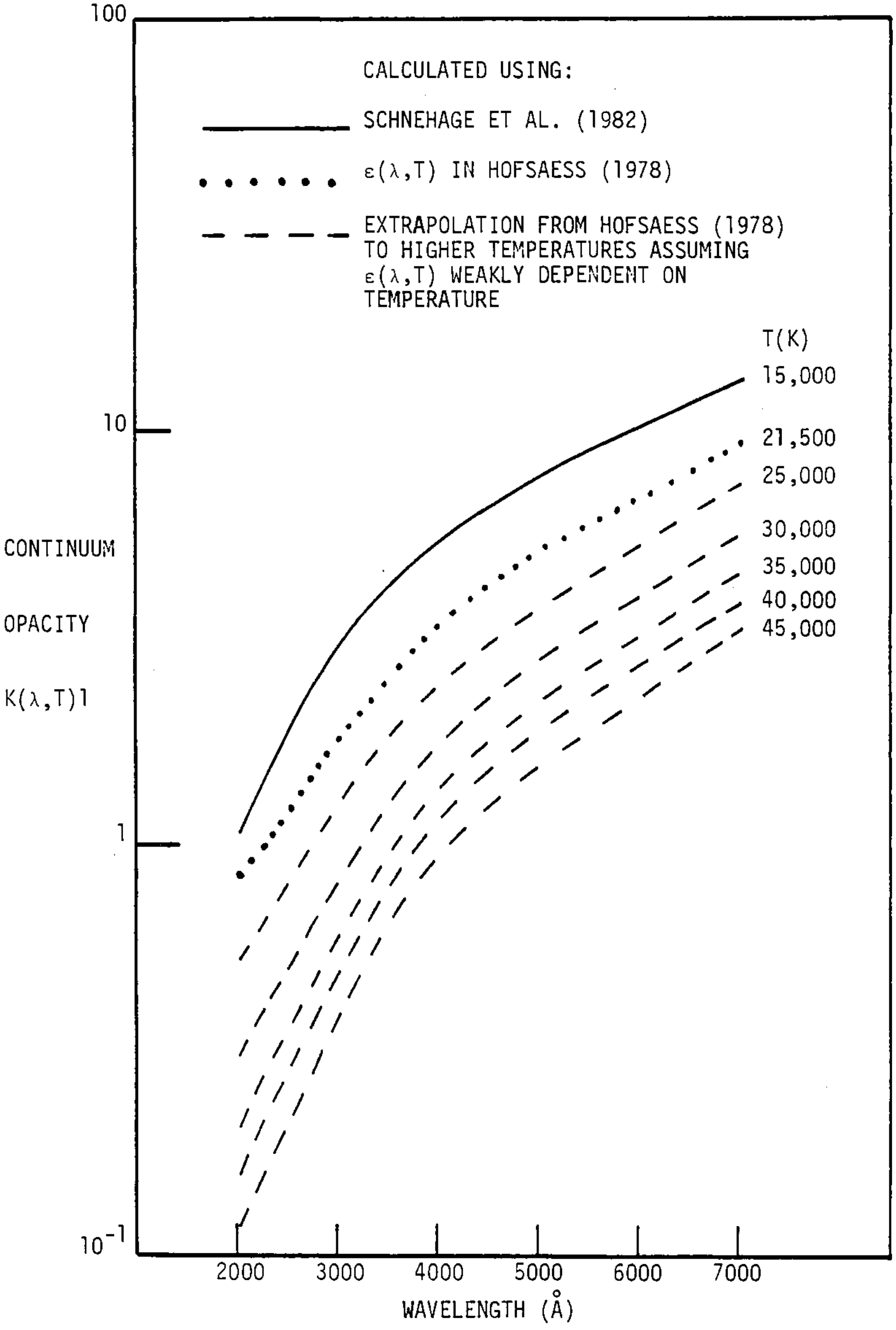

Figure 3.1: Wavelength variation of the continuum opacity K(λ,T)l as a function of temperature (assuming $n_e = 10^{25} m^{-3}$ and l = 5mm).

These calculations indicate the limitations placed on diagnostic techniques due to high continuum opacity, particularly for spectroscopic methods in the visible. Diagnostics were required for this experiment that could be employed over a wide range of conditions, in order to measure the effect of pinch parameter variation on the conditions accessible for dense, non-Debye plasma studies. For this reason a large amount of general survey work was initially carried out on the z-pinch source, prior to selecting suitable diagnostics for the plasma conditions.

3.3 Z-Pinch Construction

So that as few variables as possible were altered in order to reproduce the effects found in Baker's z-pinch, the same physical size of pinch vessel (a pyrex tube 90 mm diameter x 200 mm length) was used. The mechanical stability of the z-pinch was improved,notably through the use of positive clamping by the return rods to ensure better vacuum and electrical contact. The final design is shown in Figure 3.2.

The current feeds from the capacitor bank to the pinch electrodes comprised two parallel brass strips separated only by a thin (3mm) tufnol insulator to reduce inductance. Connection to the brass pinch electrodes was via concentric rings, while the current return path was provided by 16 equally spaced brass rods. It was decided not to use wire gauze for the current return (as used in Baker's pinch) in order to remove any inhomogeneity of the electric field around the side-arm ports. This was particularly important in view of the use of the side-arms for diagnostic purposes, since the conditions near the port had to be representative of those along the rest of the pinch axis. The return rods were spaced as close together as possible to maintain the homogeneity of the electric field, and at the same time allowed a sufficiently wide (12mm) side-arm port for diagnostic measurements across the whole plasma diameter at peak compression.

Flow of the argon/hydrogen mixture was regulated by a needle

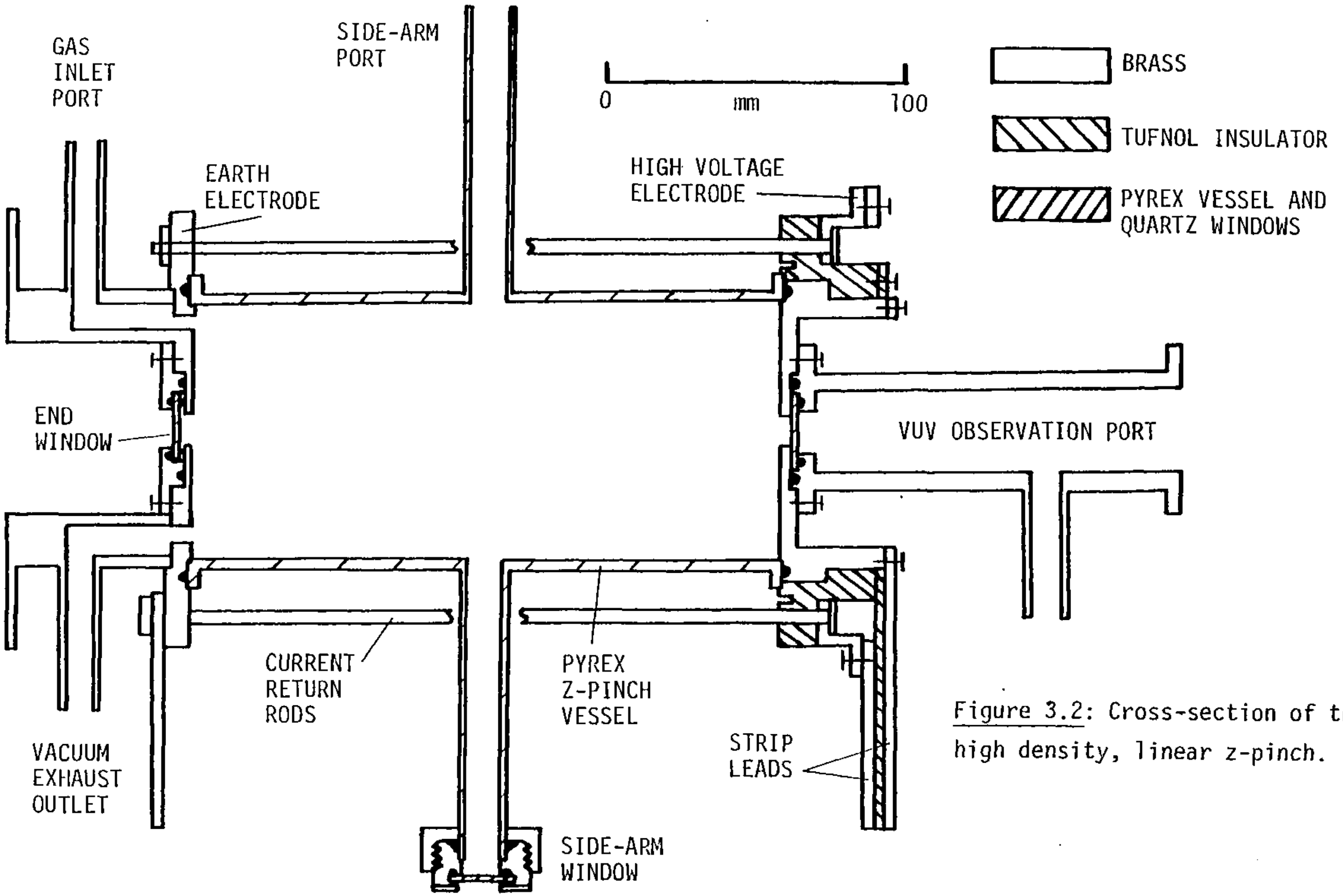

Figure 3.2: Cross-section of the high density, linear z-pinch.

valve, and the gas was introduced into the pinch through three small (5mm) holes arranged in a semicircle in the top half of one end electrode. Extraction of the gas took place similarly through the lower half, and the pinch gas was flowed using a rotary pump to reduce contamination by gaseous impurities. Before firing each day the pinch was evacuated to 10^{-3} torr, and the filling pressure (0.1 to 10 torr ±5%) was monitored during experimental runs using a mercury McLeod gauge.

Observation of the pinch was possible not only through the side arms, but also through two 10mm quartz windows located at the centre of the end electrodes. These windows were kept as small as possible and flush with the electrode surface to reduce any possible effect on the end of the plasma column. Inevitably however the windows became eroded and contaminated by the pinch, making shot-to-shot end-on observations through the windows impossible.

3.4 Z-Pinch Circuitry

Devices such as the linear z-pinch fed by a capacitor bank produce current decay patterns following the usual RLC analysis. Such circuits have a ringing frequency ω governed by

$$\omega^2 = \frac{1}{LC} - \frac{R^2}{4L^2} \tag{3.5}$$

where R, L and C are the total resistence, inductance and capitance of the circuit. The envelope of the ringing amplitude decays with a time constant given by

$$t = \frac{2L}{R} \tag{3.6}$$

When t is sufficiently small (i.e. $\frac{2L}{R} < \sqrt{LC}$) ω is imaginary and the circuit is termed overdamped. However overdamping requires a large value of R for a given L and C and this leads to energy losses in the resistance. Hence underdamping ($R \ll 2\sqrt{\frac{L}{C}}$) is usual (see Figure 3.5 for example) and produces a ringing frequency

$$\omega = \sqrt{{}^{1}/LC} \tag{3.7}$$

In order to maximise the compression force in the pinch it was necessary to increase the current, and this meant decreasing the time over which the capacitors were discharged. As indicated by Equation (3.7), this can be achieved by reducing the circuit inductance and hence the period of the ringing frequency. Further positive and negative current oscillations in the underdamped circuit roughly cancel, and the capacitors are discharged well within the first half cycle. Hence low inductance circuitry is important, and critically damping the circuit will not affect the discharge time.

The circuit used (Figure 3.3) was almost the same as Baker's, employing the same 100 μFd capacitor bank and the same spark gap (the 1 MΩ resistor was used to stop the pinch electrode from floating while the bank was charged). However, special care was taken in this experiment to reduce the circuit inductance. The strip leads from the capacitor bank to the pinch (via the spark gap) were kept as short and as close together as possible, with the pinch mounted directly on top of the capacitors. The leads were just over 1 metre long, 150mm wide (W) and had a mean separation $s \sim 4$mm, giving a total inductance from

$$L/\text{unit length} = 4\pi\times10^{-7}\,\frac{s}{W}\ \text{Henrys/m} \tag{3.8}$$

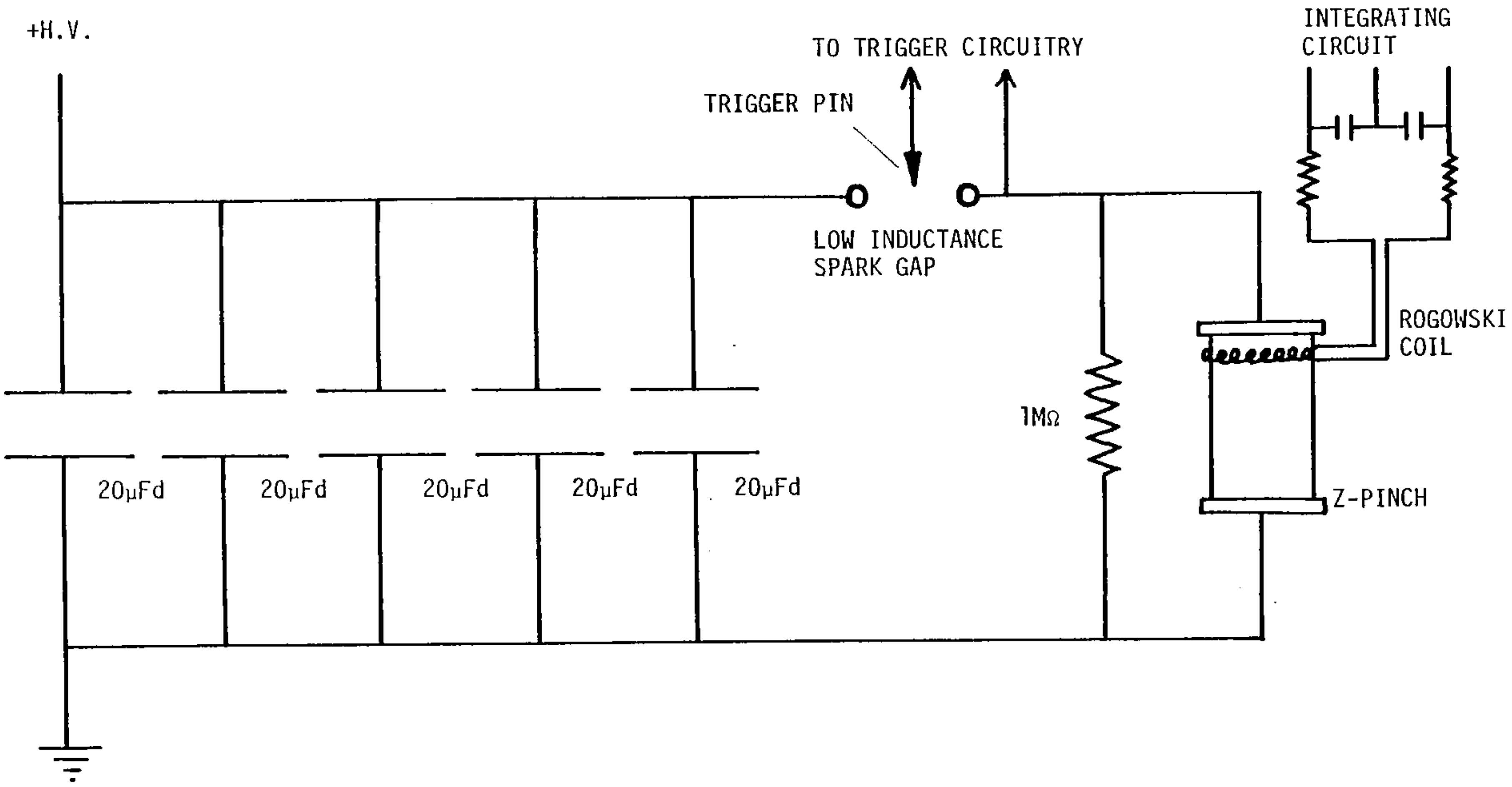

Figure 3.3: Z-pinch discharge circuitry.

of $\sim$40 nH. This can be compared with Baker's estimate of 75 nH for the multistrand coaxial leads used previously. Baker's estimate for the bank inductance was $\sim$15 nH, and the same low inductance spark gap was also used. A measure of the pinch inductance was more difficult in that the radius of the inner conductor (the gas discharge itself) was hard to estimate. Taking the pyrex tube(along which the discharge first breaks down)as a maximum radius, and as a minimum the peak compression radius of $\sim$5mm, the inductance of the compressed plasma

$$\text{L/unit length} = 4\pi \times 10^{-7}\left(\frac{1}{8\pi} + \frac{1}{2\pi}\ln\frac{r_o}{r_i}\right)\ \text{H/m} \qquad (3.9)$$

is 25-130 nH. Taking an average inductance of 75 nH gives a mean total circuit inductance of $\sim$ 130 nH. When the total inductance is combined with the bank capacitance of 100 μFd, the predicted ringing period is $\sim$ 23 μs (c.f. Baker's result of $\sim$32 μS shown in Figure 3.5b).

The current density can be raised further by increasing the amount of charge in the bank (= CV). This is best done by raising the charging voltage rather than by increasing the number of capacitors since the latter would also increase the ringing period. The capacitor bank itself was rated at 10 kV (although one capacitor broke down at 9 kV), but the primary limitation was found to be the spark gap hold-off voltage. When operated under vacuum (using a diffusion pump) Baker managed to achieve 7 kV, and when tested here at a pressure of 4 x 10^{-6} torr, breakdown accurred at around 5 kV. However, at the high pressure end of the Paschen curve, breakdown could be held off indefinitely at pressures of 80 torr (2 kV) to 400 torr (9 kV). Hence the gap was run in a high pressure, continuous flow mode in air. It was found that jitter and reproducibility were best just near the breakdown threshold, and improved when both the trigger pin and its insulator were newly cleaned. Several cleaning shots were also required before each run to ensure reproducibility. With the improvement in peak charging voltage the charge available increased from 0.7 to 0.9 Coulombs, which together with the decrease in circuit ringing time raised the maximum available current by almost a factor of two.

To ensure low jitter and high reproducibility of the discharge, the fast, high voltage trigger circuit shown in Figure 3.4 was constructed. It consisted of two spark gap systems: a secondary spark gap connected across a low inductance 0.05 μFd capacitor charged to $\sim$16 kV, and linked to the main spark gap trigger pin via a 1:4 air core transformer. In this manner a trigger pulse from the thyratron trigger unit to the secondary spark gap would result in a pulse of $\sim$64 kV being delivered to the main spark gap trigger.

3.5 Current Waveform Analysis

In order to determine the circuit characteristics of the z-pinch discharge, the current in the plasma was measured using a Rogowski coil surrounding the pinch vessel. The coil output voltage (α $^{dI}/dt$) was integrated using the differential circuit in Figure 3.3 to eliminate noise pick-up. A typical current waveform is shown in Figure 3.5a, taken at the same conditions as the current waveform shown in Baker's thesis (Figure 3.5b). The ringing time of 21.5 μS from Figure 3.5a implied a circuit inductance of 120 nH (c.f. 130 nH predicted previously). The ringing time of Baker's circuitry was 32 μs (corresponding to 260 nH) and indicates the importance of the measures taken here to reduce the inductance. The 12μs decay time of the waveform for the present pinch yields a circuit (plus plasma) resistance of $\sim$ 0.02Ω. Substitution of this value for R in Equation (3.5) corroborates the underdamped nature of the circuit ($R << \sqrt{2\ ^{L}/C}$ $\sim 0.07\Omega$).

Current traces were taken over a range of filling pressures (0.05 to 10 torr) and at 4, 5 and 6 kV bank voltages (examples are shown in Figure 3.5c). All showed good reproducibility as several

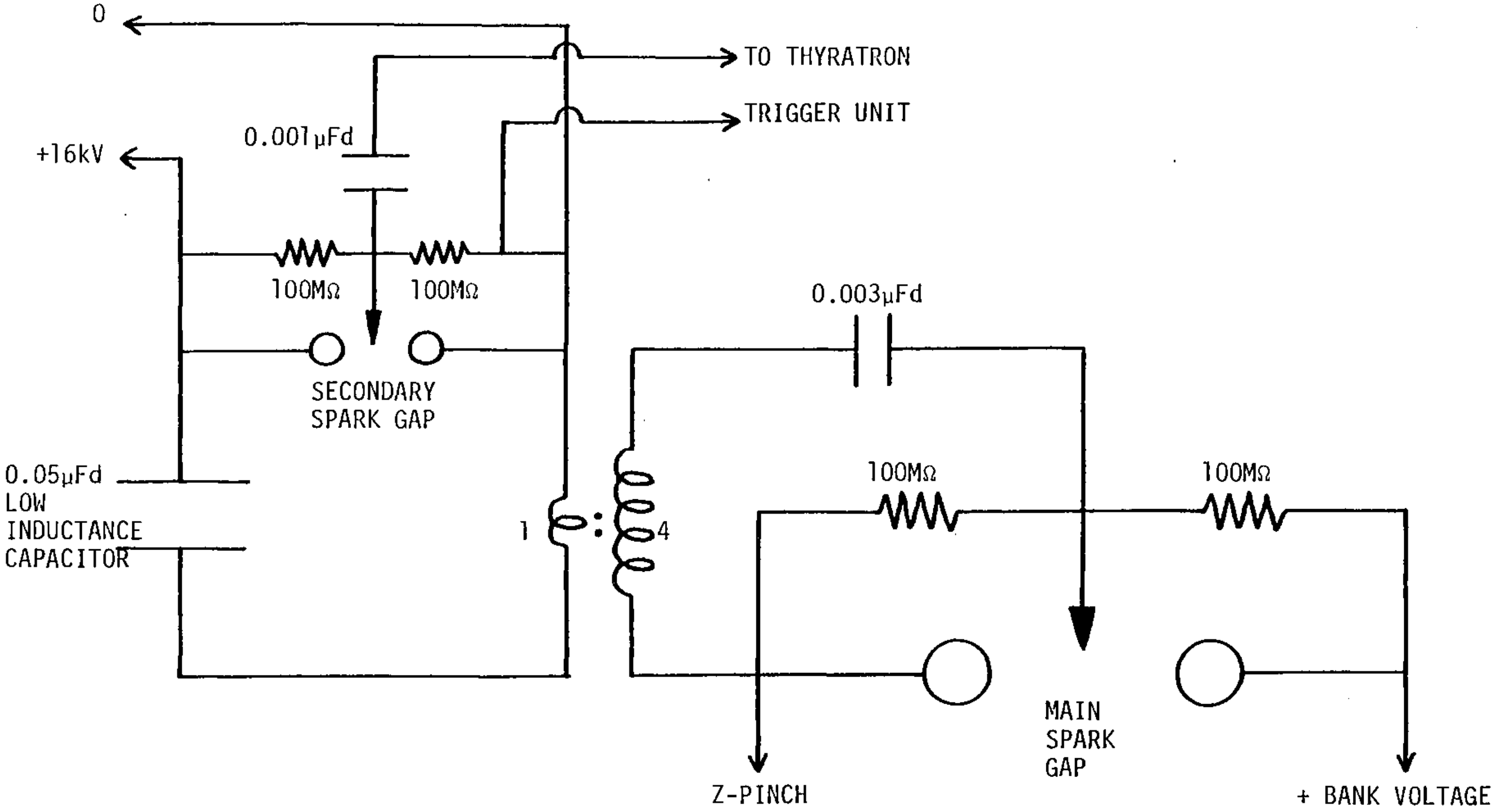

Figure 3.4: High voltage trigger circuitry.

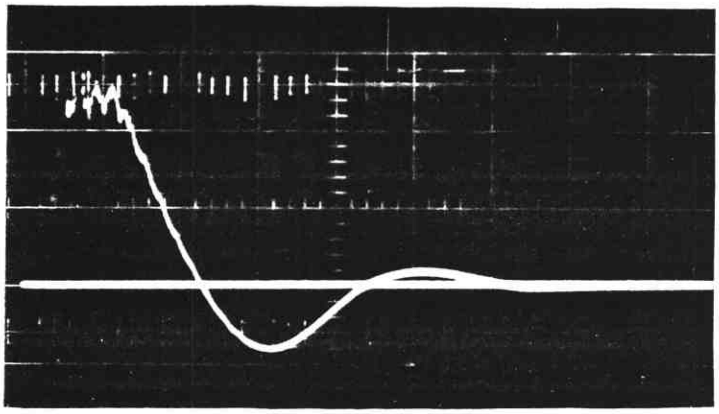

Fig 3.5a: Rogowski current waveform taken from the present pinch at 5kV, 0.2 torr with 5μS/DIV timescale. Ringing time = 21.5μs.

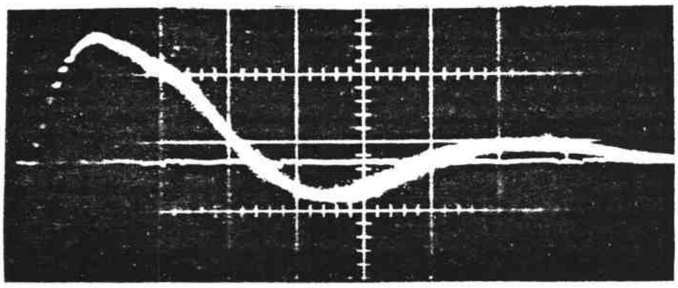

Fig 3.5b: Current waveform taken on Baker's pinch at 5kV, 0.2 torr (timescale 10μS/DIV). Ringing time = 32μs.

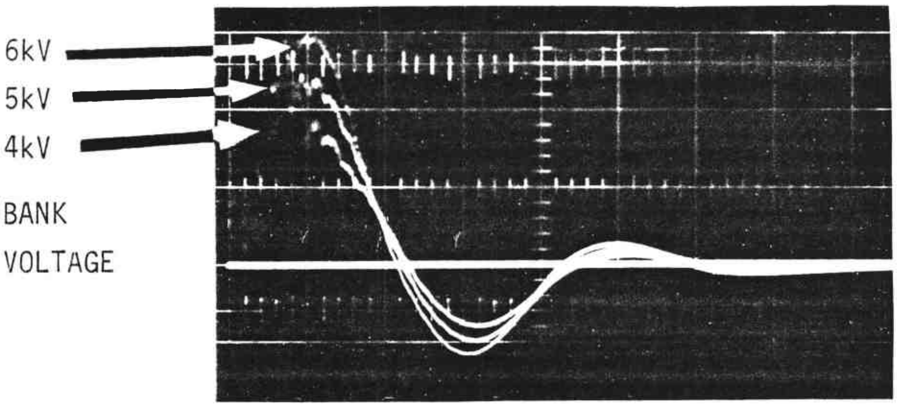

Fig 3.5c: Current waveform variation with bank voltage at constant filling pressure (0.2 torr) from the present pinch (5μS/DIV).

shots taken at a given condition were indistinguishable within the trace width. The current peak was observed to increase as expected with higher bank voltages, but increased only very slightly with an increase in filling pressure. The ringing period was the same for all bank voltages at pressures above 0.1 torr, and decreased only slightly from 22 to 19 μs as the pressure varied from 0.1 to 10 torr. This decrease may be caused by faster collapse of the plasma at lower pressures, due to smaller gas inertia as the current sheet "snowploughs" the ionized gas into the pinch axis (Roberts, 1972) . The faster collapse decreases the radius of the inner "conductor", thereby raising the inductance and hence the ringing time.

3.6 Spatially Resolved Broadband Emission Studies

Examination of the end electrodes revealed uneven pitting around the central window at the strip feed end of the z-pinch. A similar feature was found in the same position (opposite the strip feed) on the end electrode of Baker's pinch. A study of the pinch emission at the electrode surface was then carried out to investigate if the uneven pitting was caused by plasma inhomogeneity in this region.

Polaroid photographs were taken of the gross pinch emission and are shown in Figure 3.6a for both electrodes. The vertical deflection of the plasma at the strip lead electrode is clearly visible, and was thought to be caused by asymmetry of the current flow into that electrode (Figure 3.6b). The strip feeds were then enlarged as shown in Figure 3.6c to allow an even and symmetric distribution of current through the return rods, with resultant uniformity of the field experienced by the plasma at the end electrode. This eliminated the plasma deflection as is shown by Figure 3.6d. No changes in the electrical characteristics of the pinch were observed form the current waveforms using the new strip feed configuration.

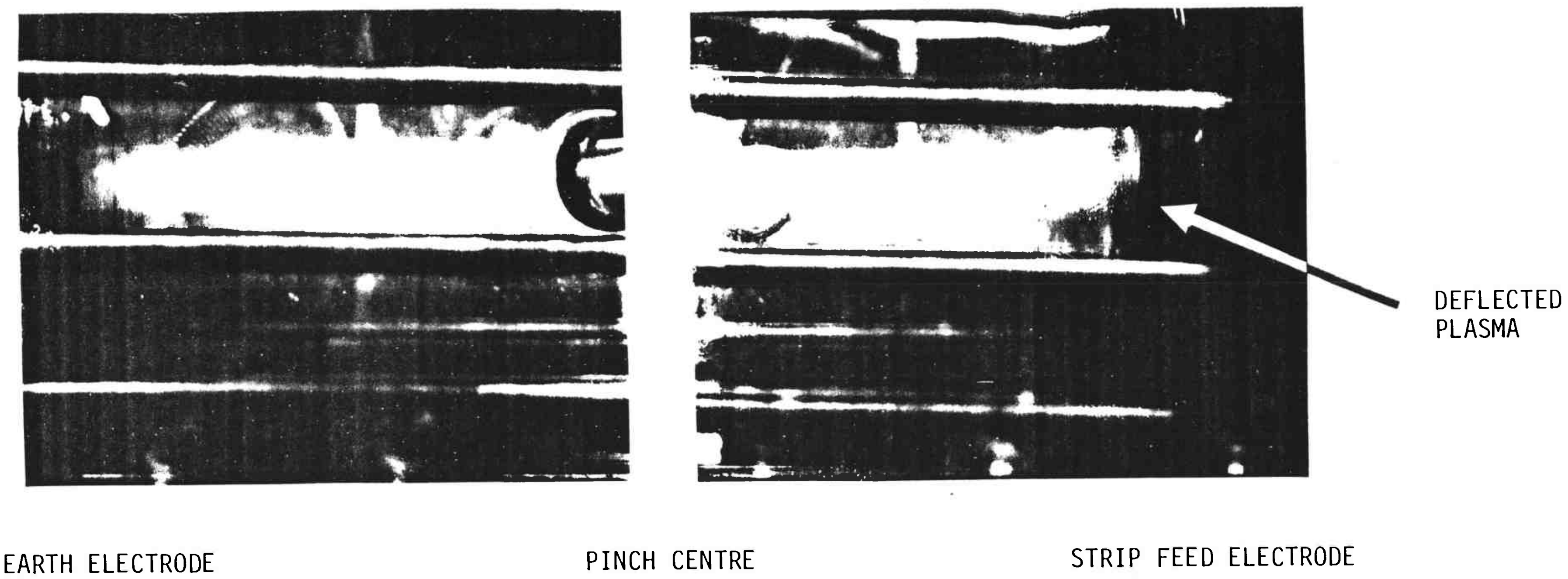

Fig 3.6a: Polaroid photograph taken side on to pinch axis showing deflected (time integrated) pinch emission at the strip feed electrode.

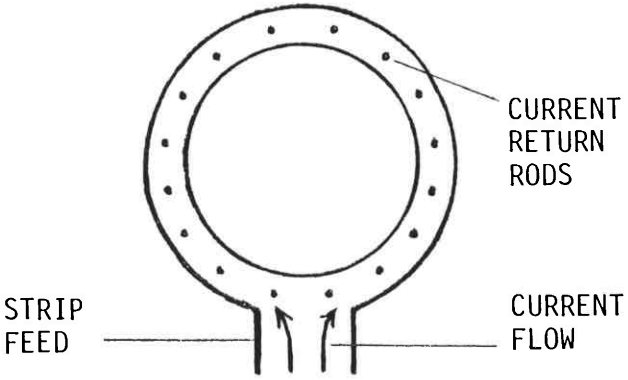

Fig 3.6b: Initial configuration for attaching strip feed to pinch electrode showing asymmetry of current flow.

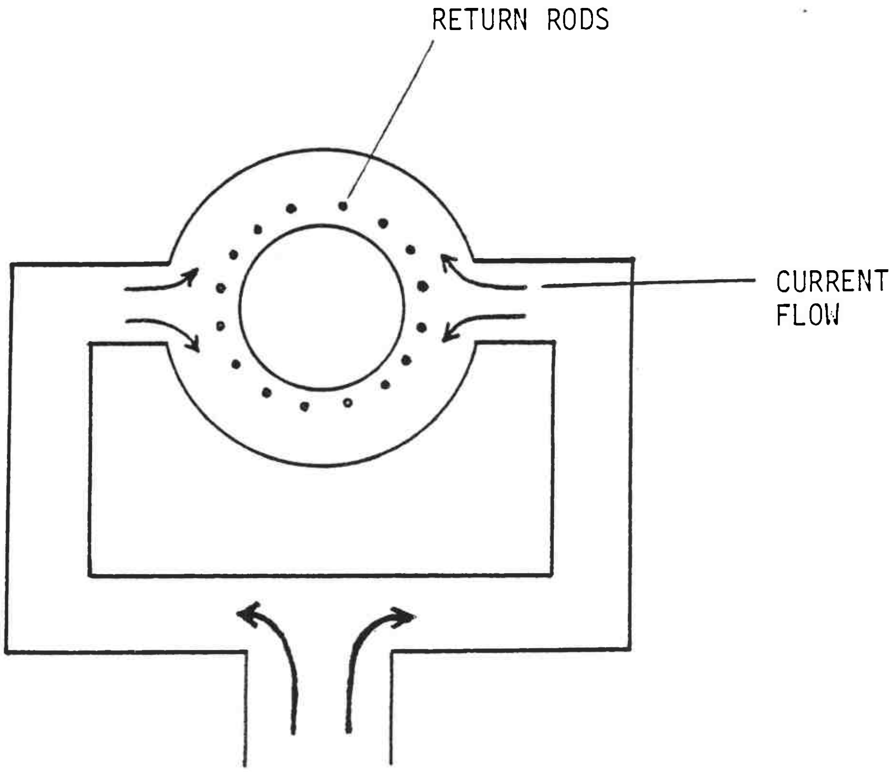

Fig 3.6c: Modified strip feed configuration showing symmetric current flow.

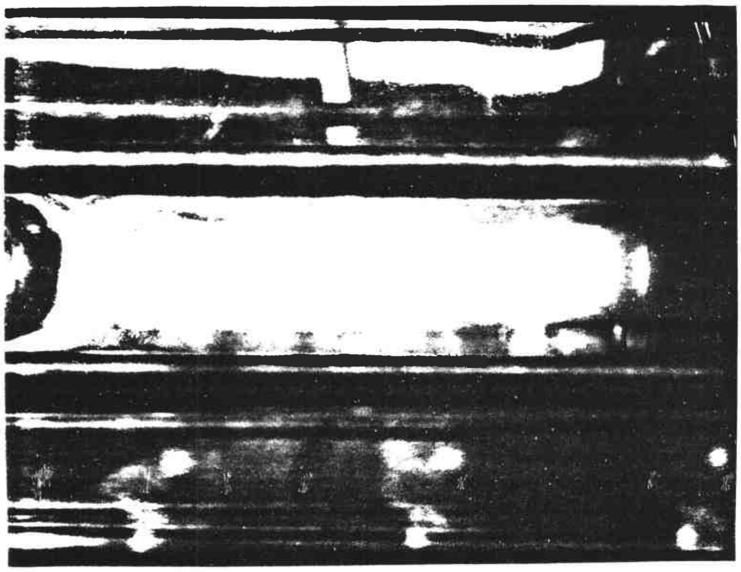

Fig 3.6d: Side on pinch emission showing undeflected plasma following strip feed modification.

Also seen in the polaroid photographs were regions of diminished pinch emission near the electrodes. These were examined with a fast, linear photodiode and the normalised emission levels recorded in Figure 3.7 for a 5 kV bank voltage and 1 torr filling pressure. The emission is corrected for transmission through the pyrex tube which was measured by placing a thermaline lamp along the pinch axis. Since the photodiode had a broadband response in the visible, both mercury and neon thermaline sources were used, and both gave the same transmitted intensity. The presence of "end zones" (Folkierski et al., 1962) in the plasma column is clearly indicated in Figure 3.7. The zones also correspond to the approximate start of the emission in the polaroid photographs (at around 8-10 mm from the electrode). The gradients in the plasma conditions indicated by the end zones may limit the usefulness of the z-pinch plasma for end-on spectroscopic studies.

3.7 Time Resolved Broadband Emission Studies

The fast photodiode was employed to carry out a detailed time resolved examination of the broadband pinch emission under various conditions. Figure 3.8a shows three superimposed emission traces taken at the region of maximum emission on the pinch axis for 5 kV and 1 torr. The current trace is also included. Peak emission (corresponding to peak compression) was observed to occur later in the current trace at higher filling pressures due to greater inertia in the gas compression. Earlier emission occurred with higher bank voltages, and the emission intensity increased with bank voltage until a limiting voltage was reached. Above this voltage no increase in emission occurred and a second, broader and less reproducible peak was observed following the first pinch (Figure 3.8b).

Again these results can be explained by inertia of the current sheet under the snowplough/piston model. Earlier pinching at higher bank voltages occurs because greater pinching force from the higher current

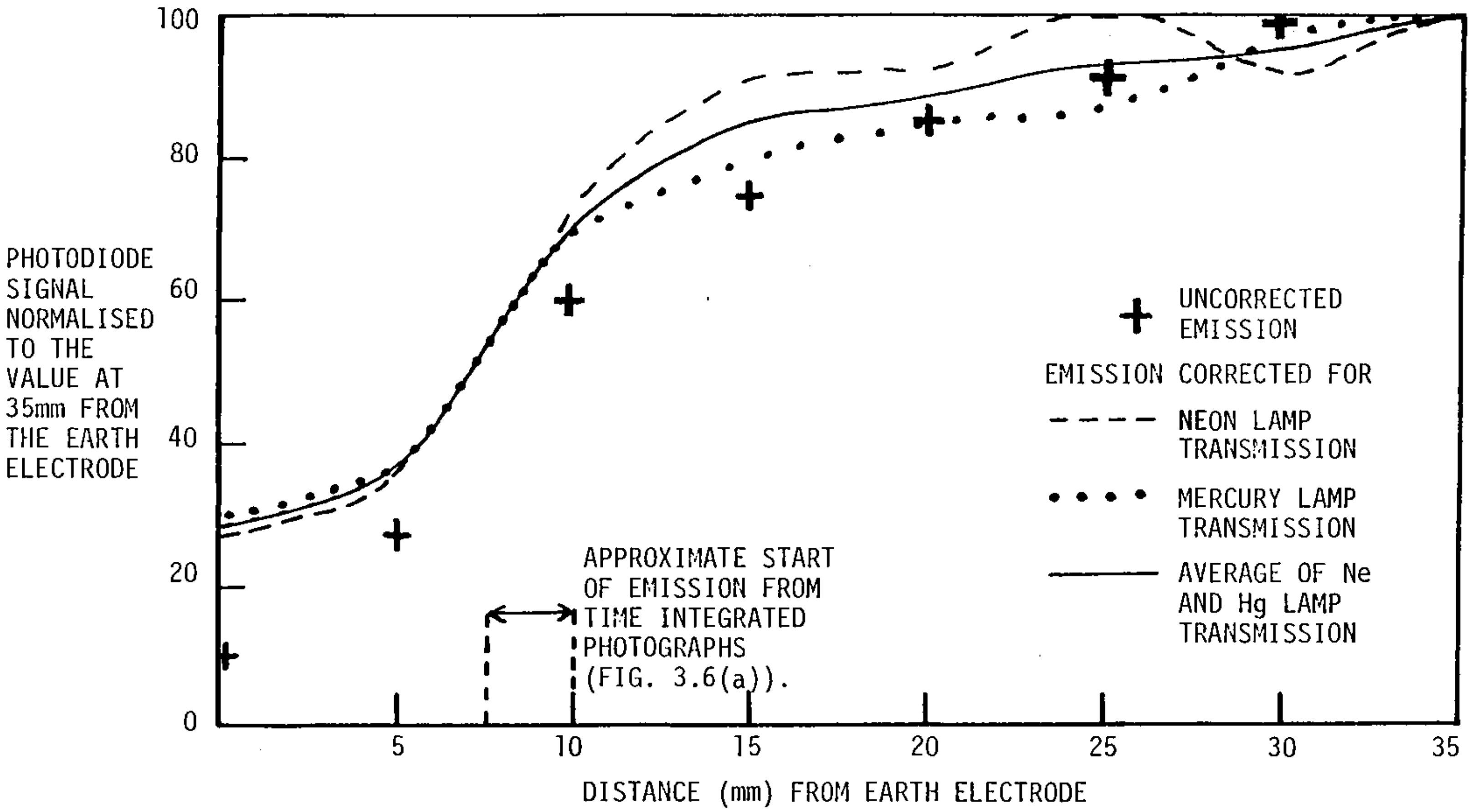

Figure 3.7: Normalised emission at peak compression as a function of distance along the pinch axis from the earth electrode, showing the occurrence of end effects in the plasma column.

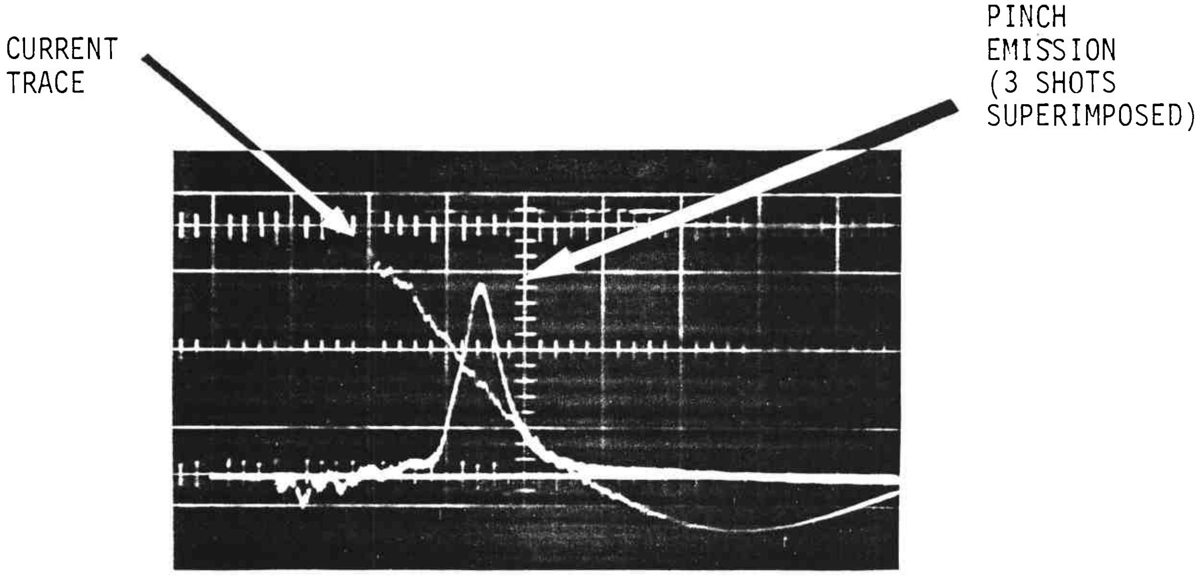

Fig 3.8a: Pinch emission and current trace at 5kV and 1 torr showing 3 shot reproducibility (2μS/DIV).

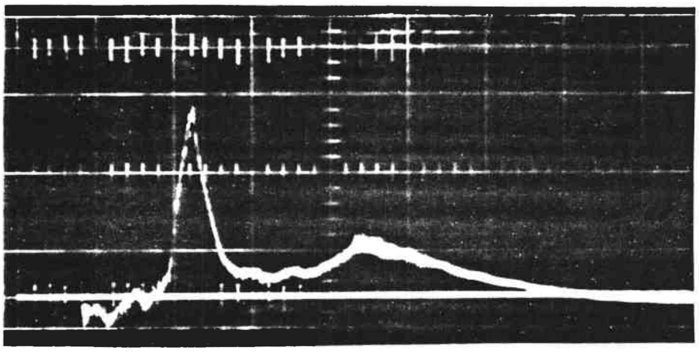

Fig 3.8b: Three shot emission trace at higher bank voltage (9kV, 1 torr) showing the emergence of a second, less reproducible emission peak, and an earlier initial pinch (2μS/DIV).

is applied to the same mass of gas at constant filling pressure. The current ringing time is a constant of the system under these conditions so the peak emission occurs closer to the time of peak current at higher bank voltages. Continuation of the current (albeit reversed in this underdamped circuit) then initiates a second pinch which only becomes apparent

a) if the current is sufficiently large and
b) if the current overswing does not coincide with the inertially-delayed incoming current sheet.

This explains why secondary emission peaks are not seen at lower bank voltages.

The reproducibility of the first pinch set the main limits to the operating conditions of the discharge (Figure 3.9). Below a certain value of the bank voltage (which decreased with decreasing filling pressure) the broadband emission became irreproducible (>±5%) due to conditions being too close to the breakdown voltage of the pinch. At low filling pressures the emission became irreproducible at any bank voltage. The high pressure limit was set by consideration of the peak emission characteristics. Since the amount of emission is a likely indication of peak compression (as continuum emission $\alpha\, n_e^2$), the voltage at which the emission maximised indicated the optimum compression at a given filling pressure. This voltage V_m is also shown in Figure 3.9 (upper solid line) from which it can be seen that for pressures greater than 10 torr, the optimum bank voltage was above the limit set by the capacitor voltage rating.

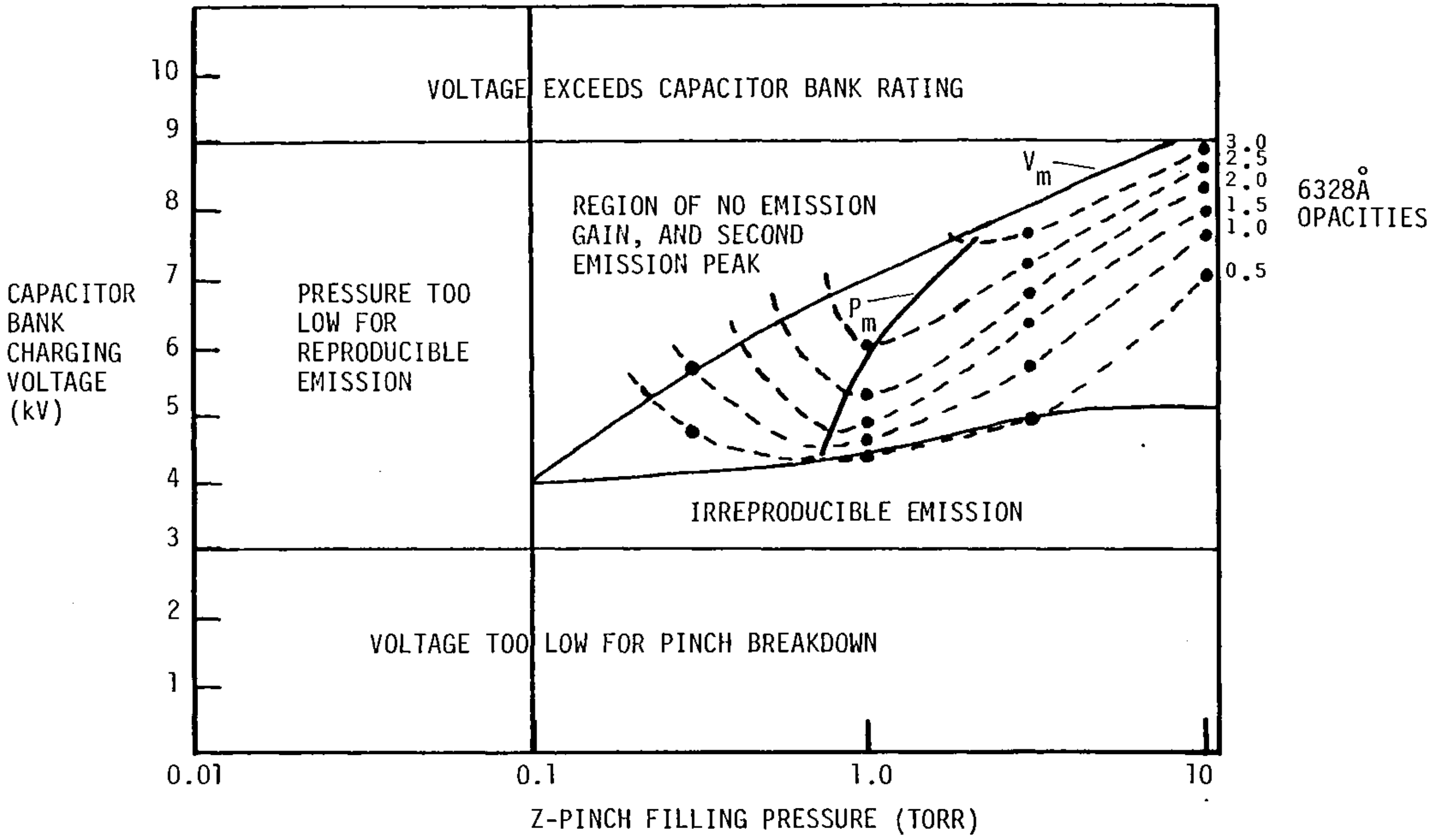

Figure 3.9: Z-pinch operating conditions and 6328Å opacities. Shown are the voltage V_m for a given pressure at which the emission maximised, and the pressure P_m for a given voltage at which the 6328Å opacity maximised.

3.8 Spectrographic Survey

As a first step in the spectroscopic diagnosis of the pinch, a survey was carried out of line emission in the visible and ultraviolet (from 6300 to 2000Å). This had three purposes:

1) to identify the ion and impurity species present in the pinch
2) to locate regions free from line emission for interferometric and continuum studies
3) and to identify lines which might be useful for diagnostic purposes.

The visible survey was carried out using a f12 Hilger-Watts medium glass spectrograph into which light was focussed from the pinch axis. Plates were taken both end on and side on to the pinch, and calibration was achieved using a mercury lamp source. Around 150 emission lines were observed from the following species; Ar I and II, H, Cu I and II, Si I and II, Zn I. Absorption was also seen from the sodium D lines. Since the impurities appeared both in the side on and end on observations, time resolved measurements were necessary to determine whether these arose from emission over long timescales following the pinch (as would be the case for migration from the walls or electrodes), or whether indeed such impurities were present at peak compression. A Pockel cell and analyser were therefore placed between the pinch side-arm and the spectrograph, and the Pockels cell was triggered closed immediately following peak emission (as measured by a linear photodiode). No impurity lines were visible in the plates taken by this method. Since the distance from the electrodes to the side-arm ports was 0.1m and the time to peak compression under the conditions used (5 kV, 1 torr) was $\sim 7\mu s$, this placed a maximum velocity on the Cu/Zn ions of $\sim 10^4$ m/s (corresponding to a maximum ion temperature of ~ 20eV).

Since the emission lines of the higher ion stages lie at shorter wavelengths, a UV survey was also carried out using a medium quartz spectrograph. Several plates were taken side on to the plasma at different combinations of 1 torr and 5 torr filling pressure, and 5 kV and 7 kV bank voltages. Due to the poor transmission of the Pockels cell in the UV it was not used for these spectra. Hence there was some contribution to the spectra from emission in the cooler, less dense recombination phase following peak compression. However, the UV lines appearing at the compression peak are less likely to be affected by the continuum opacity in the UV (Figure 3.1) and hence are more likely to appear in the spectra than are visible lines at peak compression.

Several hundred lines between 4000 and 2000Å were identified and were attributed to the same elements as for the visible survey, but included higher ionization stages. These are listed together with their ionization potentials in Table 3.1. It was noticeable that the lines from higher ionization stages only appeared at conditions expected to produce higher temperatures (high bank voltage, low pressures). Because of the long timescale of the exposure the lower ionization stages were usually present under all conditions. The ion distributions are illustrated in Figure 3.10 where the number of argon lines of a given ionization stage observed under a particular condition are shown as a percentage of all lines seen from that stage under all conditions. The appearance of higher ionization stages is only an approximate indication of the relative temperatures of the various conditions, since the electron density must be taken into account via the Saha equation (this is considered more fully in Section 3.12 following the interferometric density measurements). However given that the incease in filling pressure is likely to decrease the temperature at a given bank voltage, the pinch conditions from left to right in Figure 3.10 appear to be listed in order of increasing temperature. There is even evidence of the ArI stage being

Table 3.1: UV emission lines observed in the spectrographic survey and grouped by ion species. Also shown is the ion species ionization potential in eV.

SPECIES	I.P.	NO.	SPECIES	I.P.	NO.	SPECIES	I.P.	NO.	SPECIES	I.P.	NO.
ArI	15.8	11	CuI	7.7	37	ZnI	9.4	9	SiI	8.2	14
II	27.6	53	II	20.3	41	II	17.9	5	II	16.3	4
III	40.9	22	III	36.8	1	III	40.0	-	III	33.4	1
IV	59.8	4	IV	55.2	-	IV	63	-	IV	45.1	-

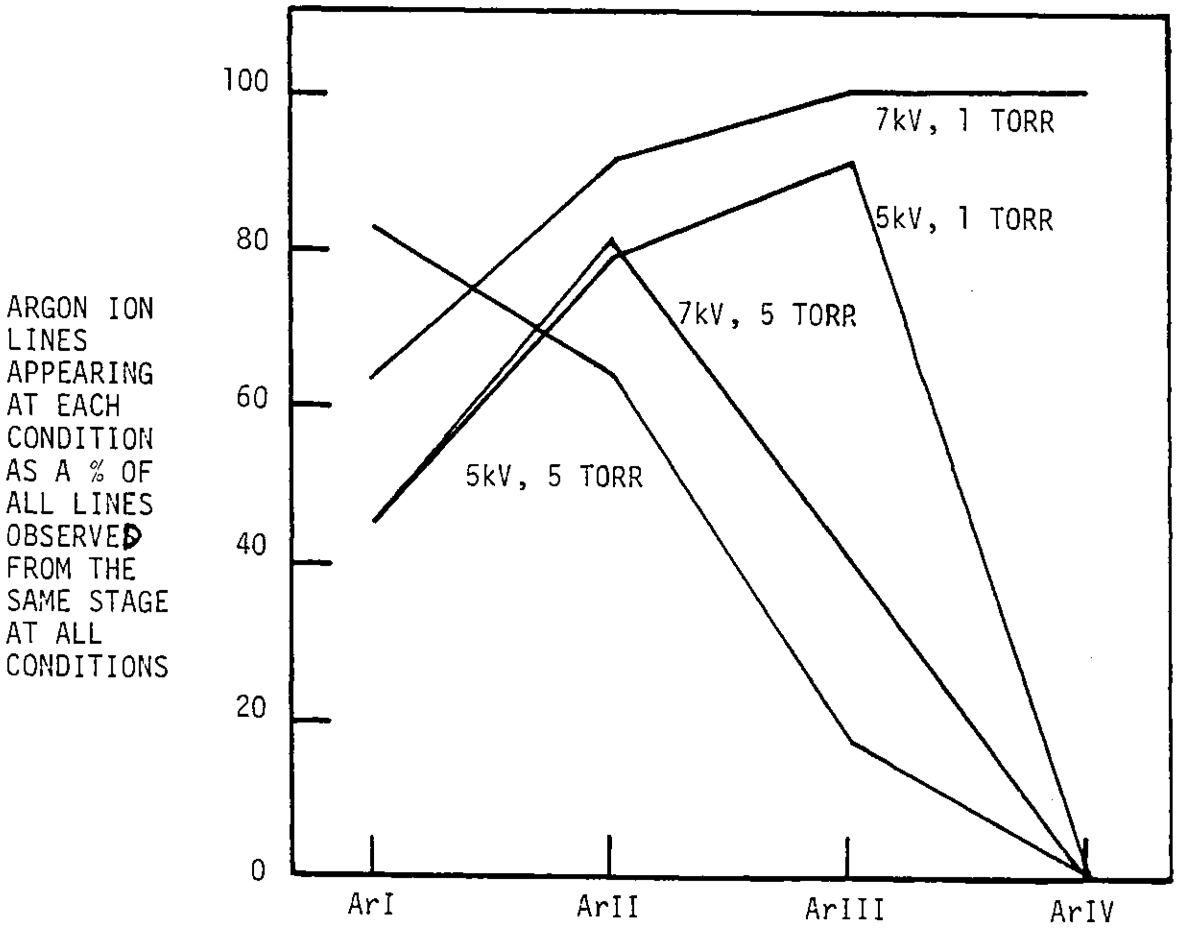

Figure 3.10: Distribution of lines from Argon ion species as a function of z-pinch operating conditions.

"burnt through" for three of the conditions as some ArI lines appear only at 5 kV and 5 torr. The absence of any higher ion states in the impurity species (despite the similarity in their ionization potentials to the argon ions) supports the evidence from the visible survey that the impurities arrive only in the cooler recombination phase following peak compression.

3.9 Measurement of the Continuum Opacity

The visible region spectra discussed in the previous section revealed several regions of continuum emission that were relatively free of argon and impurity lines, most notably between 5700 and 6400Å. In order to study the usefulness of this line-free region for interferometric measurements, continuum absorption studies using cw lasers were carried out to determine the opacity of the plasma.

Initially a He-Ne laser of around 10 mW power was employed in the configuration shown in Figure 3.11a. A lens was used to gather any light deflected by spatial variations of the plasma density and hence of the plasma refractive index. Significant refraction of the beam by the plasma was observed since the transmitted intensity decreased to zero when the lens was removed. A variable aperture was placed between the z-pinch and the lens, and the aperture was increased until no change in the transmitted intensity was observed.

A typical absorption trace is shown in Figure 3.11b where two aperture stops (7mm and 32mm) were employed. The two top traces represent the laser transmission at the different apertures, while the lower traces show the pinch emission levels without the laser (again at 7 and 32mm apertures). The deeper absorption and almost zero emission traces were obtained using the smaller aperture. Although the transmission trace for the largest aperture shows less apparent absorption, this must be corrected for the greater level of emission (i.e. by subtracting the emission peak directly below the absorption dip). The minimum in the

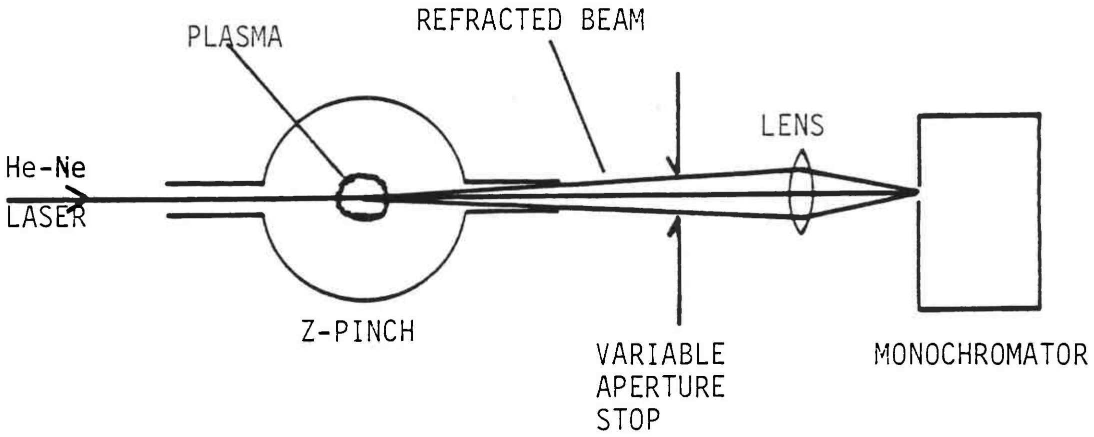

Figure 3.11(a): Continuum absorption experiment.

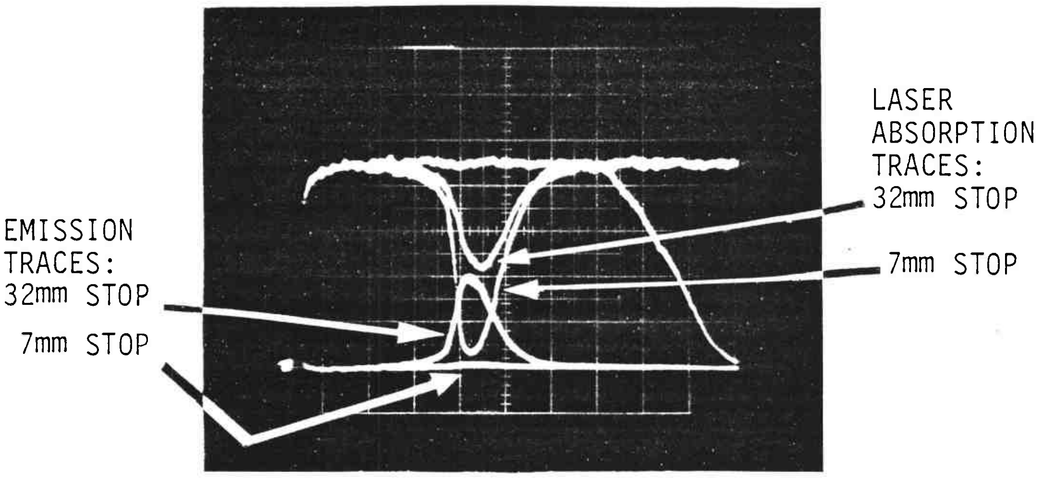

Figure 3.11(b): Continuum absorption and pinch emission traces taken on separate shots using two aperture stops (no emission was visible in the trace for the 7mm stop).

Optical depths at 7kV, 3 torr:

7mm stop $\tau \sim 2.6$

32mm stop $\tau \sim 2.3$

absorption trace only appears to be slightly later than the emission peak simply because the emission level is falling following the peak - the difference between the curves isstill minimized at the emission peak. The falling absorption trace on the right is the gated photomultiplier circuit being turned off (to avoid depletion of the dynode chain capacitors which would affect the circuit linearity). As shown in Figure 3.11b there is very little variation in the plasma opacity for a 20 fold change in the collection area using the two different apertures. This indicates that the transmission trace was a true measure of the continuum absorption and did not include effects due to refraction.

Absorption measurements were made side on and at the centre of the pinch axis for the various conditions shown in Figure 3.12. Both size apertures were employed to ensure that beam refraction was not responsible for the absorption. The optical depths shown in Figure 3.12 were taken from the larger 32 mm aperture setting which in all cases gave only slightly smaller values of the optical depth than the 7mm aperture. Greater uncertainty arose when measuring larger optical depths as is shown by the error bars for the 3 torr results, the maximum measurable optical depth being 4 (corresponding to 2% transmission or one trace width).

3.9.1 Relation of the opacity variation to the z-pinch dynamic behaviour

The results of the continuum opacity measurements for various conditions are also shown in Figure 3.9. They indicate that for a given bank voltage, the opacity (and hence electron density) maximised at a particular filling pressure (P_m) which varied with bank voltage. Maximization of the electron density was also found to occur for a critical filling pressure by Burgess et al. (1967) and Burgess (1965) on two completely different z-pinch discharges (critically damped and overdamped respectively). Roberts (1972) observed a similar effect and explained

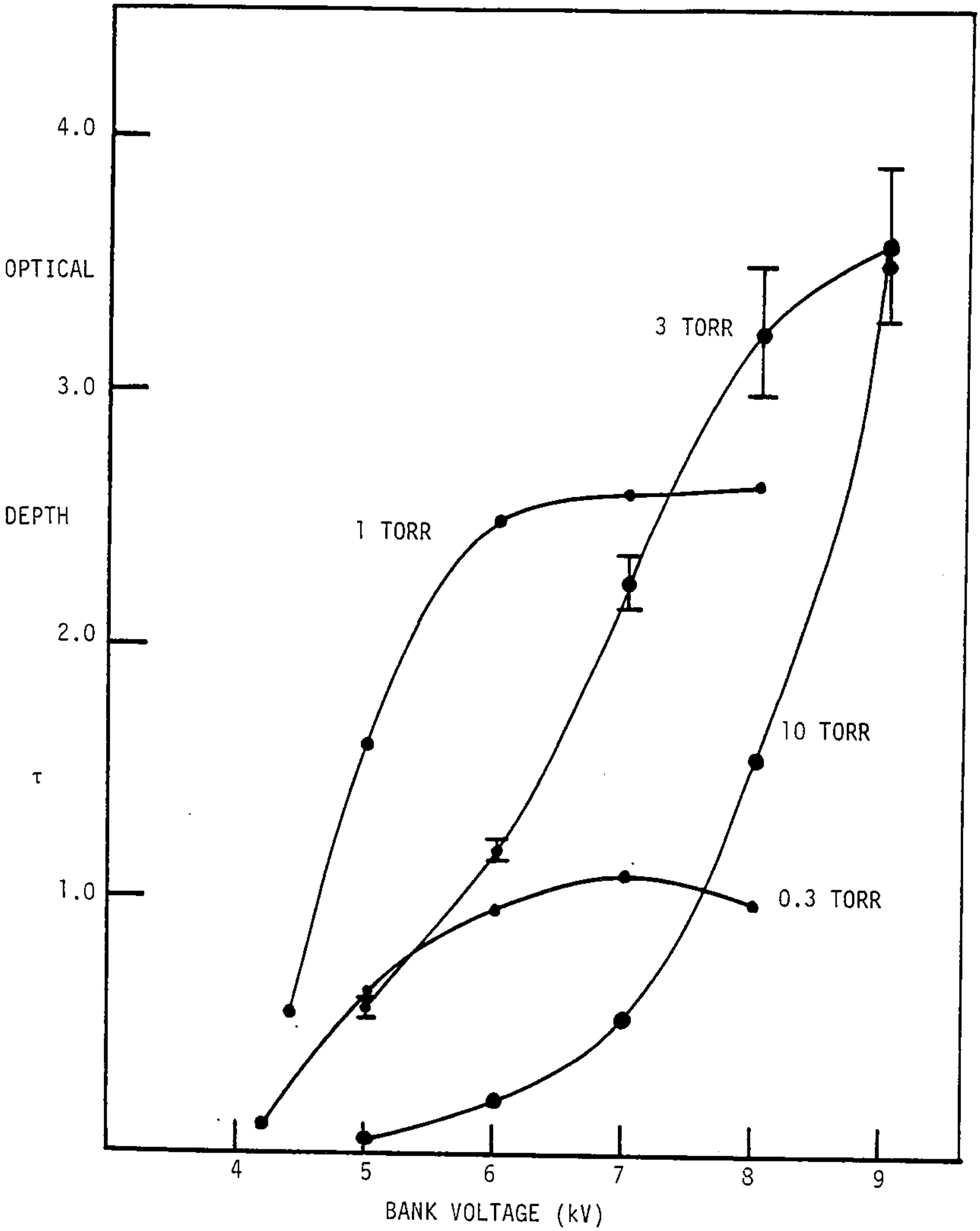

Figure 3.12: Variation of continuum absorption at peak compression with initial pinch conditions.

the behaviour in terms of the shock-piston separation mentioned previously.

In this model the inward moving current sheet acts as a piston, sending ahead of it a shock wave which on reaching the pinch axis is reflected, thereby heating the gas on axis. When the current sheet reaches this region it is impeded by the kinetic pressure of the shock-heated gas, and this determines the size of the pinch region at peak compression. A cooler expansion phase then follows. For filling pressures less than the critical pressure P_m, the separation between shock and piston is distinct, but not too great, so that the pinch axis is relatively small when the current sheet meets the reflected shock. Roberts showed that in this regime the peak electron density is a function of filling pressure P_o and bank voltage V_o as follows

$$n_e \propto P_o V_o^2 \tag{3.10}$$

provided that one ion species is dominant (for Roberts this was ArIII). Further increasing the filling pressure reduces the plasma temperature, causing the plasma to revert to the next lowest ionization stage. This causes the slope of n_e vs P_o to decrease. Above a certain critical pressure P_m, however, the density then falls. This is a result of the fact that the regions defined by the shock and the current piston are no longer distinct. Heating by the shock causes some ionization with up to 10% of the current flowing between the shock and the main piston. This leads to Joule heating and further ionization behind the shock, which inhibits the on-axis compression by the incoming current sheet.

The maximization of the opacities at a particular pressure for a given bank voltage in this experiment can then be understood in terms of this model. As shown in Figure 3.9, the value of the critical pressure P_m increases with increasing bank voltage in accordance with the observations of Roberts (1972). The identification of the critical pressures was an important step in the optimisation of plasma densities achievable in the present pinch.

3.9.2 Wavelength variation of continuum opacity

Since the plasma densities at peak compression produced a significant opacity at 6328Å, further absorption measurements were carried out in the apparently line-free 5600-6000Å region to determine whether this would be suitable for interferometric studies. A cw ring dye laser using Rhodamine 6G was employed to measure the absorption in this region. The laser spot (∿10mm in diameter) was reduced using a ½ mm horizontal slit to enable resolution of the densest region on the pinch axis. At 5kV and 1 torr the optical depth was measured at 2.3±0.2 with no variation outside the error limits over the wavelength region. This constancy with wavelength indicates that the absorption was due to continuum rather than line opacity. Hence this region would probably be of use for interferometry despite the amount of laser absorption.

The absorption experiment was later repeated using the He-Ne laser projected through the slit, and the same optical depth (∿ 2.3) was obtained within the error limits. To test for greater variation in the continuum opacity over a larger wavelength range (as would be expected from Section 3.2.1), a further absorption study was made at a significantly different wavelength (3371Å) using a nitrogen laser system.

The experimental arrangement is shown in Figure 3.13. Since the nitrogen laser pulse was of short duration (∿5ns) careful timing was required to ensure that the pulse arrived at the pinch peak. This was achieved by triggering the laser from the rising edge of the broadband pinch emission as measured by a photodiode. Several delay settings were used very near to the emission peak, and at 5 kV and 1 torr all gave optical depths of about 1, the peak being 1.2±0.2. The ratio of this result to the 5830Å opacity is ∿0.5. This ratio is considerably more than predicted by the calculated ratio of ∿0.25 (see Figure 3.1, assuming T_e is

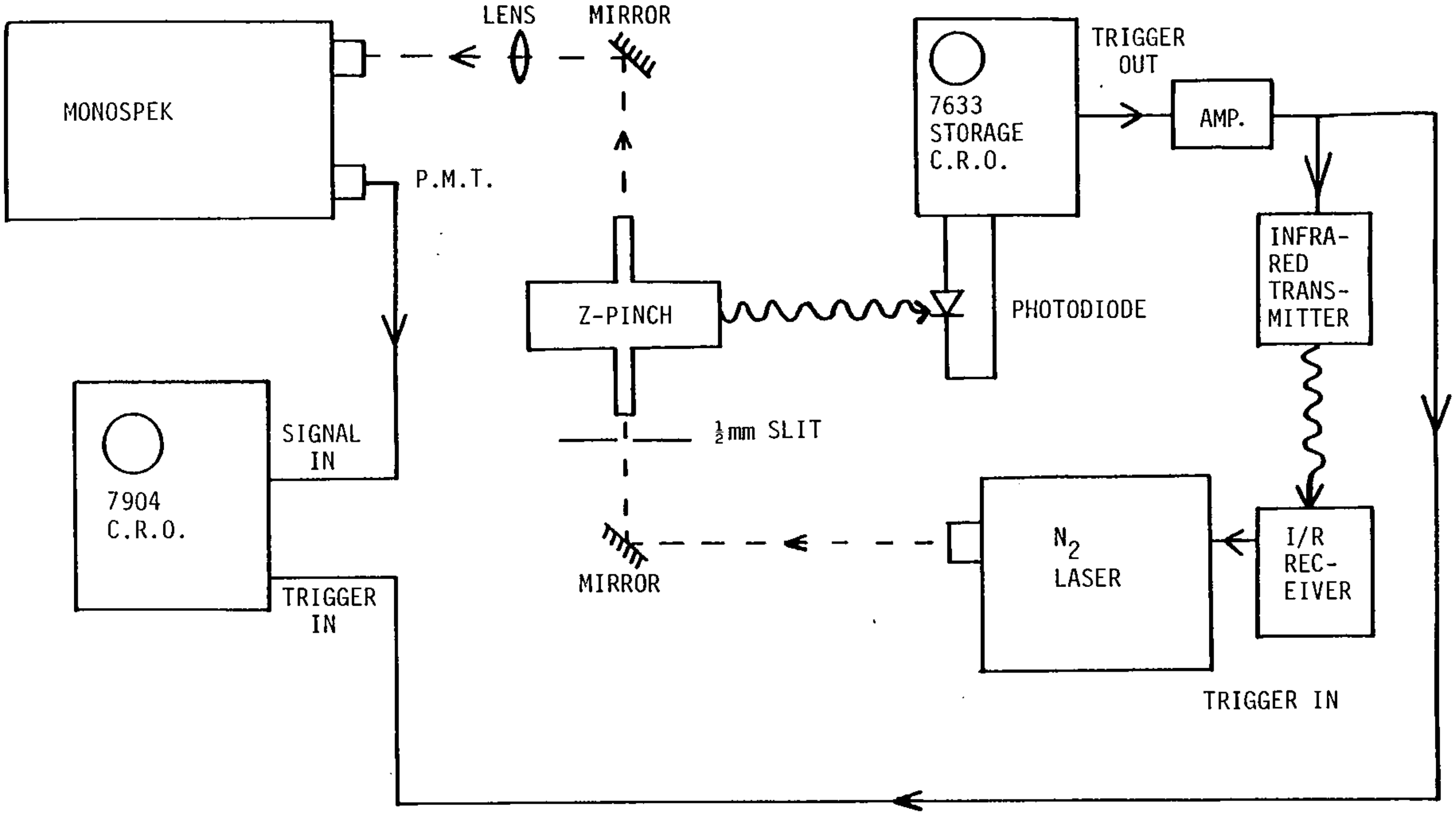

Figure 3.13: Nitrogen laser (3371Å) absorption experiment.

of the order of 3eV). This is probably a result of the neglect of the $\xi(\lambda, T)$ variation with temperature (Equation 3.3), particularly since the results presented by Hofsaess show an increase in the ξ factor with temperature at short (U.V.) wavelengths, but not in the visible. However the general trend to less optical depths at longer wavelengths was still apparent.

3.9.3 Effect of the continuum opacity on lineshape studies

The results of the opacity studies presented in sections 3.9 – 3.9.2 have significant consequences for diagnostic and line profile studies on this plasma source. Since the optical depth in the visible and near UV was significant side-on to the plasma, end-on studies in these wavelength regions were impossible over the much greater length of plasma column (200 mm compared with only ∿ 5mm side on). More importantly, the high opacity precluded any near UV or visible lineshape studies side-on to the plasma, due to the additional complications of radial gradients both in density and temperature.

The usual justification for ignoring the effects of gradients on side-on line profiles is that the regions which contribute most to the line width occur at the dense core of the pinch (which is often also the region of strongest emission). However, since this emission is now discriminated against by the high continuum opacity of the dense pinch core, emission from the outer, less dense regions becomes more important and prejudices the interpretation of line profiles. Furthermore, in plasmas of high opacity at longer wavelengths, the approach of the continuum emission to the blackbody level may prevent the observation of emission lines altogether.

3.10 Choice of Interferometry as a Density Diagnostic

The limitations placed on interpretation of line spectra by the high continuum opacity prevented the use of linewidths and shapes as a measure of electron density. The presence of numerous lines (many of which were very broad) also made measurements of the continuum emission over a large wavelength range (e.g. Finken et al., 1978) impractical as a diagnostic. Thomson scattering had previously been eliminated as a feasible technique (at least with only visible lasers available). Hence interferometry remained the only other choice of density diagnostic, although as described in the following sections this was limited ultimately by loss of fringe visibility due to fast changing fringes and continuum absorption. However, so long as the interferometric measurements were made side-on and correctly Abel inverted (Section 3.10.4), interferometry provided the only unambiguous and spatially resolved measure of the electron density available over the wide range of conditions required.

3.10.1 Contributions to the plasma refractive index

Interferometric measurements at a wavelength λ relate the number of fringe shifts observed (m) to the change in the refractive index (ΔN) over a plasma length (L) via the equation

$$m = \frac{1}{\lambda} \int_0^L \Delta N(x)\, dx \tag{3.11}$$

The refractive index is partly comprised of contributions from the bound-bound transitions of atoms or ions, the magnitude being given by (Thorne, 1974)

$$N-1 = \frac{e^2}{8\pi^2\varepsilon_0 mc^2} \sum_j \frac{n_j f_j \lambda^2{}_j \lambda^2}{(\lambda^2-\lambda^2{}_j)} \tag{3.12}$$

Here the sum is over the transitions j of wavelength λ_j and oscillator strength f_j, while n_j represents the population of the lower level of the transition. Usually the largest contribution to the bound electron refractive index comes (as will be shown) from the resonance lines. Equation 3.12 can then be re-written in terms of the ground state atom population n_o (or n_i for ion stage i) viz.

$$N-1 = n_{o,i}\, N^S_{o,i} = n_{o,i} \frac{e^2}{8\pi^2\varepsilon_o mc^2} \sum_j \frac{f_j\lambda_j{}^2\lambda^2}{(\lambda^2-\lambda_j^2)} \qquad (3.12a)$$

where $N^S_{o,i}$ is the specific refractive index per atom (or ion) and the sum is over the resonance lines.

The refractive index contribution of the free electrons is given by (Thorne, 1974)

$$N-1 = \frac{e^2\lambda^2}{8\pi^2 m_e\varepsilon_o c^2}\, n_e = N^S_e\, n_e \qquad (3.13)$$

where N^S_e is the electron specific refractive index. For a single ionizing event the change in refractive index is simply the difference between N^S_o and $N^S_e+N^S_i$. Hence the usefulness of the fringe shift as a measure of the electron density is dependent on the validity of ignoring $N^S_o-N^S_i$ compared to N^S_e, as will be discussed in this section.

The region around 5830Å was chosen for interferometric measurements both for being relatively line free and because the cw laser employed in the absorption studies could be used at its maximum intensity to overcome the high continuum opacity. At 5830Å the electron specific refractive index is 1.53×10^{-28} m^{-3}, for which one fringe shift corresponds to a density-length product of $3.82 \times 10^{21} m^{-2}$. The contribution due to ground state atomic argon is obtained from the refractive index of argon at S.T.P. (1.000281 - Weast, 1974). This yields a specific refractive index of 1.05 x $10^{-29} m^{-3}$ which is much smaller than that above for an electron.

The contribution to the refractive index from lines of excited argon atoms is negligible compared to the ground state atom value due to the much smaller population of the excited levels (even though the lines may be very near the laser wavelength). For example the nearest line here is the 4p-5d line at 5834Å, with a lower state energy of 13.2eV andan f value of 0.0026. This compares with the 3p-4s resonance line at 1048Å which has an f value of 0.254. Assuming a temperature of ∿1eV (above this temperature most of the argon atoms are ionized) yields an excited state/ground state ratio of $\sim 10^{-5}$. When substituted into Equation(3.12) this ratio gives a refractive index contribution relative to the resonance line of $\sim 4 \times 10^{-4}$. Hence the contribution of excited argon atoms to the overall refractive index is negligible.

The magnitude of the argon specific refractive index N_0^S represents an upper bound on the error produced by equating the electron specific refractive index with the total change of refractive index in an ionizing event. The ion specific refractive index N_i^S must be subtracted from the neutral value, and in general this yields an even smaller error since the ion resonance line wavelengths are shorter (thereby making $N_i^S < N_0^S$). Therefore as ionization proceeeds the bound electron contribution to the refractive index will not be strictly constant, although the magnitude of the bound contribution will be small compared to the electron specific refractive index. Even if the effect of higher ionization stages is ignored completely, the neutral argon specific refractive index is small enough (∿ 6% compared to that of the electrons) to be neglected.

In the case of hydrogen, there is no ameliorating effect due to the presence of a higher ion state. However, Allen (1955) gives the hydrogen polarizability ($\frac{1}{2\pi}$ times the specific refractive index) as $6.7\times10^{-31}m^{-3}$, which together with the low hydrogen concentration (∿ 1%) makes this contribution unimportant. Molecular hydrogen is also present in negligible concentrations. Using the calculations of Tatum (1967) for the H_2 dissociation equilibrium constants, at densities of $\sim10^{22}$ ($\sim \frac{1}{100}$ of Baker's measured electron density) molecular hydrogen is almost completely dissociated at temperatures above 3000K. In any event the H_2 specific refractive index ($5.0\times10^{-30}m^{-3}$) is less than that of argon.

It is therefore evident that the dominant contribution to the plasma refractive index comes from the electrons. Hence measurement of the fringe shift using the cw laser at ∿5830Å provided a measure of the electron density accurate to better than 6%. Subsequent tuning of the laser some tens of Ångstroms from this wavelength showed no variation in the fringe count, thus indicating that at least for nearby lines (where N changes rapidly), the contribution of bound electrons was negligible.

3.10.2 The interferometry experiment

The experimental arrangement for the interferometric studies is shown in Figure 3.14. The cw laser beam was split in a Mach-Zehnder configuration, using partially reflecting mirrors to divert a small fraction of the probe beam into the reference arm. A pair of parallel prisms were placed before the first mirror to allow variation of the beam height above the pinch axis. The precise height was defined by a ½mm slit placed on a vertical travelling mount, with a corresponding slit on the other side of the pinch which was used to align the beam prior to each shot. The second slit was removed when the interferometric trace was taken so as not to block light refracted by the plasma. After rejoining the reference beam the probe beam was reflected through

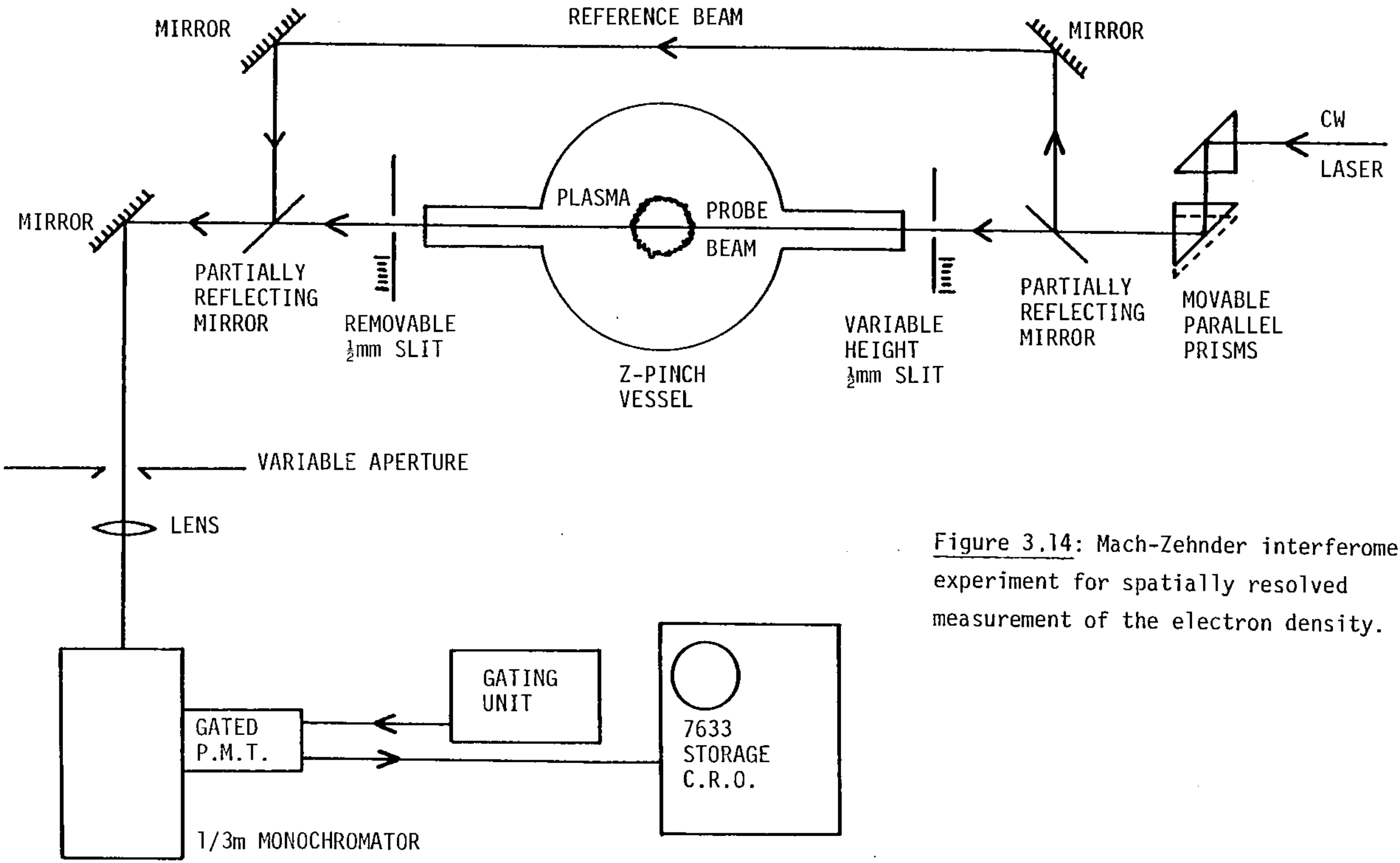

Figure 3.14: Mach-Zehnder interferometry experiment for spatially resolved measurement of the electron density.

a variable aperture, collected by a long focal length lens and focussed onto the entrance slit of a $\frac{1}{3}$m monochromator. The variable aperture was used (together with the monochromator) to discriminate against the strong background pinch emission. The aperture could also be opened to allow a trace to be taken of the pinch emission alone, which could then be used as a timing reference for the interferometry traces.

Two such timing traces were taken at each off-axis height, one before and one after the interferometric measurements. Three interferometric traces were taken as a check of the density reproducibility, and were registered (along with the emission traces) on a storage oscilloscope which was triggered simultaneously with the z-pinch circuitry. Measurements at heights up to 7mm above the pinch axis were possible through the diagnostic ports in steps as small as ½ mm. Traces were also taken at positions either side of the height at which maximum fringe shift occurred, in order to determine accurately the position of the pinch axis for the purposes of Abel inversion. A typical set of traces is shown in Figure 3.15a taken at 6 kV and 5 torr near the pinch axis, together with a trace in Figure 3.15b under the same conditions on a longer timescale.

3.10.3 Interpretation of interferometry traces

The complexity of the interferometry traces shown in Figure 3.15 necessitates caution in their interpretation if a correct estimate of the electron density is to be derived. Three regions in the traces can be identified.

The first (times 0 to 1), precedes the peak compression which is identified both by the emission peak and the change in the fringe direction at time 1. Fringe amplitude is considerably reduced near peak compression where the fringes are also very fast. Prior to the final

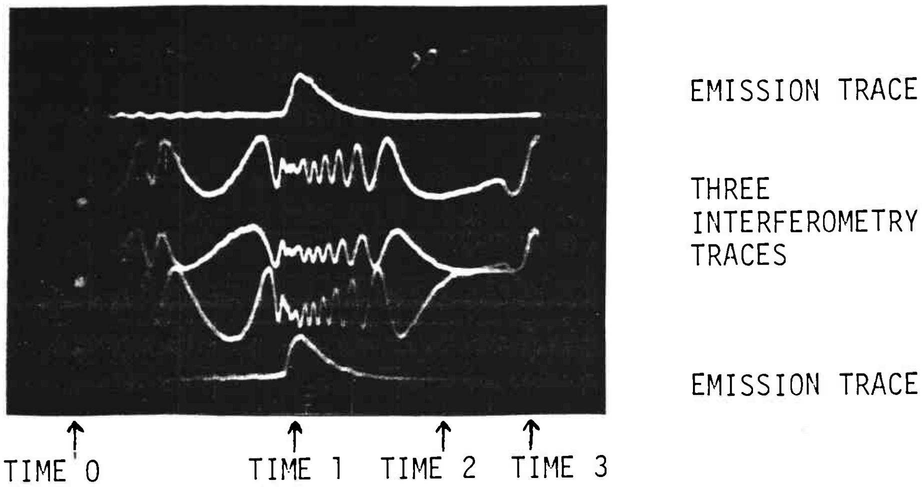

Fig 3.15a: Interferometric fringes and emission timing traces at 6 kV, 5 torr.

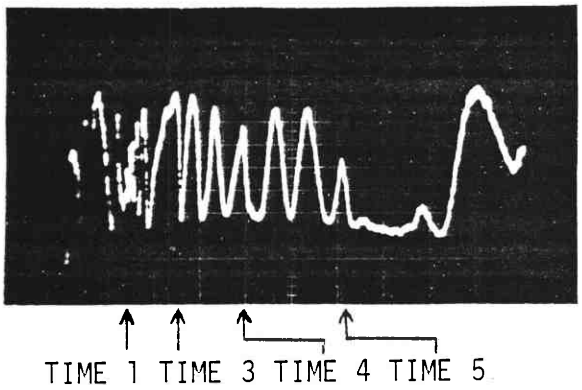

Fig 3.15b: Interferometry trace at 6 kV, 5 torr on longer timescale (10μS/DIV).

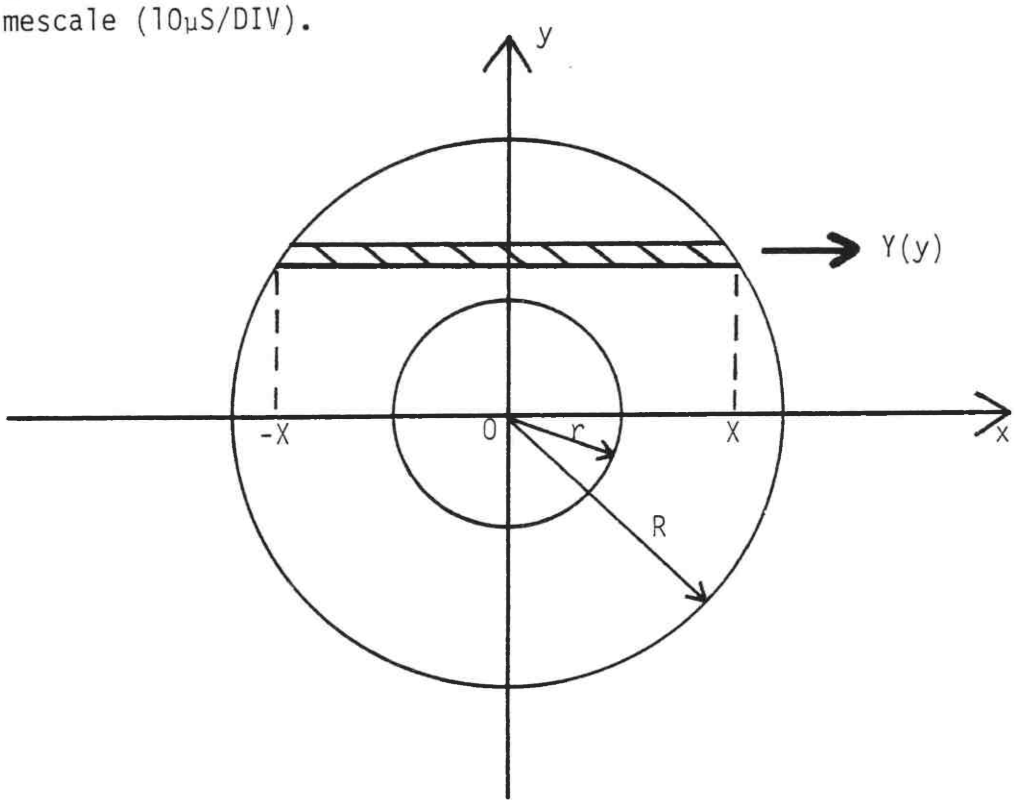

Fig 3.16: Coordinate geometry of the Abel inversion measurements. 0 represents the pinch axis, and Y(y) the fringe shift measured at height y above the pinch axis.

compression the fringes change direction several times. This behaviour is probably due to heating and ionization of the gas by the passage of the shock front, which on reflection from the axis produces fluctuations in the electron density before the arrival of the current ~~positon~~ piston in the final fast compression. The resulting complicated fringe pattern makes it difficult to count the fringe shift prior to the compression peak.

The second region (times 1 to 2) is a period of expansion as the plasma moves outwards after being reflected from the shock-heated core at peak compression. The third region (time 2 onwards) is characterised by a flat plateau (times 2 to 3) during which there is no change in the refractive index at all. This plateau occurs well after the emission and current traces have disappeared, and is followed by a series of fluctuations over longer timescales. As far as could be determined these fluctuations altered direction (time 4) and then cancelled one another e.g. 3-4 and 4-5, leaving no net contribution to the electron density. An exactly similar behaviour was observed by Burgess et al. (1967) for discharges in various gases at filling pressures greater than P_m (the pressure at which maximum electron density occurred). This behaviour was attributed to penetration of the incoming current sheet by the outward moving shock, which was not fully absorbed and which then proceeded to bounce off the pinch wall and return to the pinch axis. Since the densities measured in this experiment were at conditions around or above the apparent P_m shown in Figure 3.9, the interferometric traces after time 3 can be interpreted in terms of this behaviour.

An upper bound on the temperature in the expansion phase can be determined from the bounce time in Figure 3.15b of $\sim$35 μs (times 3 to 5). The shock speed will be greater than the neutral sound speed, given by

$$c_s = \sqrt{\frac{\gamma kT}{M}} \qquad (3.14)$$

where $\gamma = 1.67$ is the ratio of specific heats for a monatomic gas and M is the atomic mass of argon. Since the z-pinch tube diameter is 9×10^{-2} m, this gives a maximum temperature of ∿19,000K in the pinch afterglow.

From the analysis of the fringe behaviour presented in this section, the electron density was measured by counting the fringes from peak compression (marked by the change in direction at time 1) to the plateau region of no fringe change (time 2). The net fringe change following the plateau is in any event negligible compared to the number of fringes observed in the initial expansion phase. In addition, the later fringe changes occur well into the recombination phase of the discharge when the electron density is distributed more evenly over the whole pinch volume. The length of plasma probed is then greater and hence the electron density is smaller per fringe shift ($\alpha\ n_e \perp$). The neglect of these later fringes is justified by the results presented in the following section, where one fringe was added to the measured shift at all heights above the axis (simulating the case when the plasma fills the whole pinch volume). The results showed little alteration in the Abel-inverted peak axial density (< 10% - see Figure 3.17d). Hence counting of the fringe shifts between peak compression, and the region of constant density following the initial expansion phase, was considered a sufficiently accurate measure of the electron density.

3.10.4 Analysis of interferometry data by Abel inversion

The fringe shifts obtained at the off axis points were converted into radial electron density profiles using a Fortran Abel inversion routine (Fleurier and Chapelle,1974). This program employed a polynomial fitting procedure to produce a smooth fit to the uninverted experimental data. An interpolation subroutine increased the number of points by a factor of four using the fitting polynomial, in order that a better determination of the fringe gradient could be made for profiles where the density varied quickly. The program was modified to include measurements falling on either side of the maximum fringe shift, and also calculated the interpolated point at which the maximum fringe shift occurred. This point was then used to define the pinch axis from which the Abel inversion routine was initiated.

The process of Abel inversion (as applied to systems of cylindrical symmetry) deconvolves the incremental addition of refractive index changes to the line-of-sight fringe shift as the height above the symmetry axis is altered. The diagram in Figure 3.16 defines the coordinate geometry of the cylindrical system with the chord along the line-of-sight being given by the shaded region. If F(r) is the fringe shift of the plasma at radius r then the total fringe shift along the line-of-sight is

$$Y(y) = \int_{-X}^{+X} F(r)\,dx \qquad (3.15)$$

which after a suitable change of variable becomes

$$Y(y) = 2\int_{y}^{R} rF(r)(r^2-y^2)^{-\frac{1}{2}}dr \qquad (3.16)$$

From this F(r) can be obtained using the inverse formula

$$F(r) = -\frac{1}{\pi}\int_{r}^{R} \frac{dY(y)}{dy}(y^2-r^2)^{-\frac{1}{2}}\,dy \qquad (3.17)$$

The term in parentheses in Equation(3.17) indicates that the electron density at a given radius r will be determined primarily by the gradient of the fringe shift at heights y near r. This is because as the height y=r is approached from above, the increment in the fringe shift along the line-of-sight arises from the additional refractive index contribution of the electron density at radius r. Therefore the statement by Baker

(1977) that "the core density given by an Abel inversion procedure is heavily weighted in favour of the wings of the fringe distribution" is not, in general, correct. The statement will only be true when the fringe gradient near the pinch axis is zero or is significantly less than the gradient in the wings. In this experiment the fringe gradient was if anything steeper within a few millimetres of the pinch axis (Figure 3.17a), and it was therefore important to accurately measure the fringe shifts near the pinch core. For this reason the Abel inversion routine was altered to precisely determine the position of maximum fringe shift, and it was also not necessary to extend the interferometric measurements further than 7mm from the pinch axis.

The evidence for the importance of near axis measurements to the pinch core density in this experiment is shown in Figures 3.17 a-c. The uninverted experimental data is shown in Figure 3.17a, with various asymptotic wings at larger off-axis heights corresponding to a smooth extension of the available data, a sharp cut off, and a plateau region to the end of the smooth extension. The Abel inverted density profiles for the three cases are shown in Figure 3.17b. There is no effect whatever on the peak axial density, although the wings have been affected to varying degrees as would be expected from fringe gradients in the wings. The justification for ignoring the fringe shifts at large axial separations is then evident.

The effect of near axis variations is, however, much more significant. The error bars in Figure 3.17a show the standard deviation of the three interferometric fringe shift traces (or the ±¼ fringe accuracy, whichever is the greater). By taking the upper error bar limit for one point and the lower for the other, the resultant inverted densities are shown in Figure 3.17c. The differences in the peak densities are quite marked, varying by a factor of two for only a ±7% variation in the two fringe measurements.

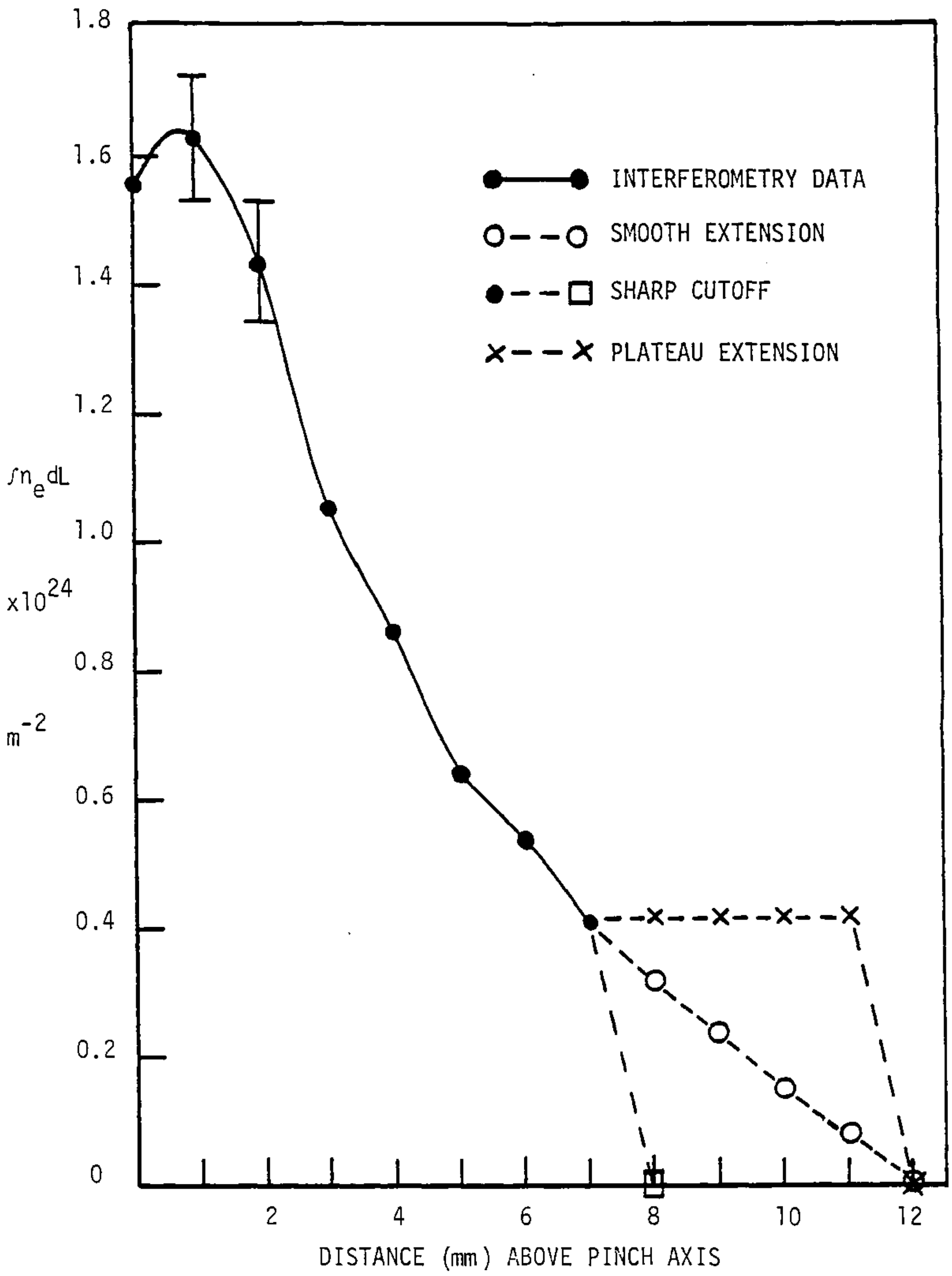

Figure 3.17(a): Fringe shift measurements for 10 torr, 7kV (1 fringe = 3.82 x $10^{21} m^{-2} = \int n_e dL$). Also shown are various extensions of the experimental data beyond the region visible through the side-arm ports.

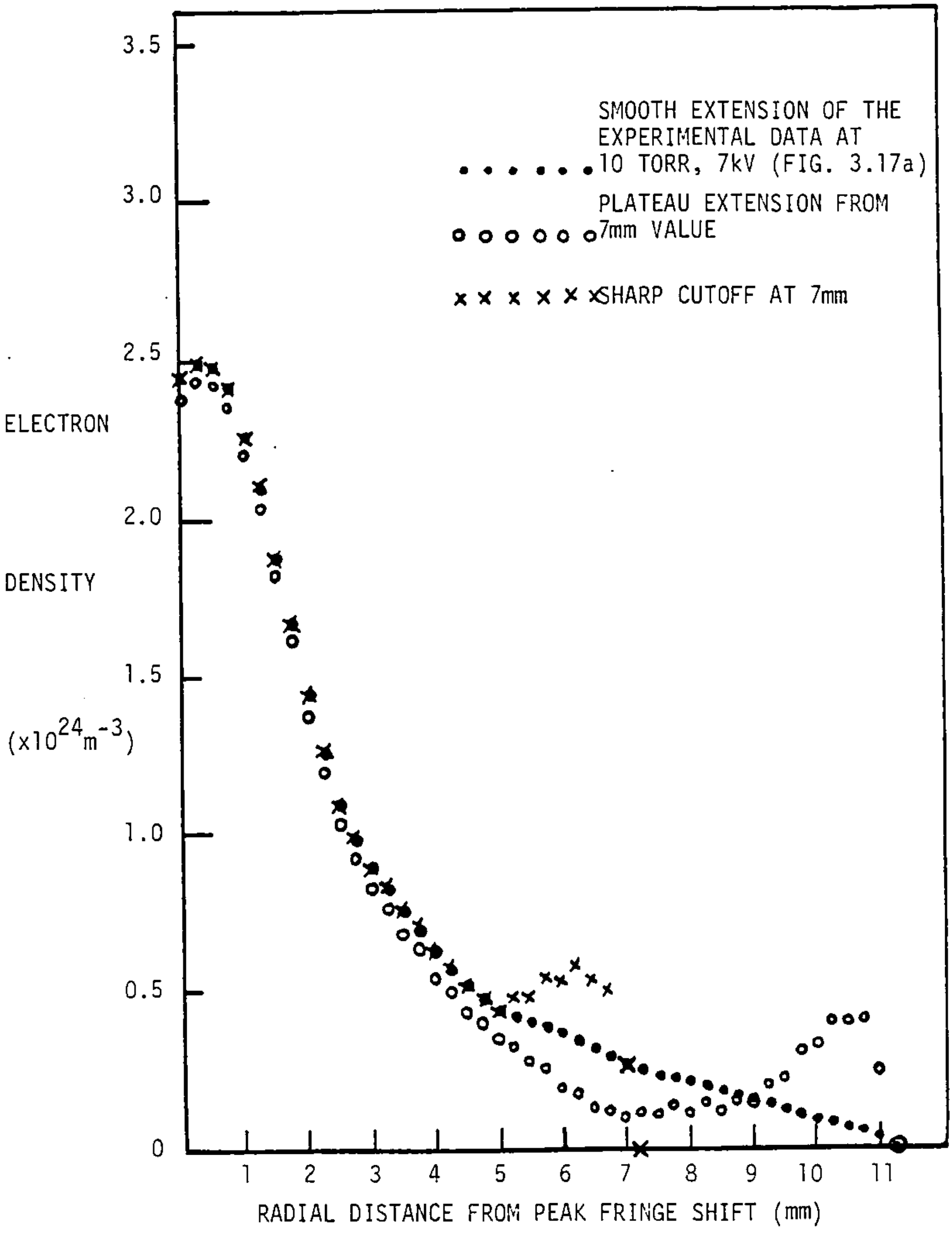

Figure 3.17(b): Abel inverted electron density showing the effect of various cutoffs in the fringe measurements at large separations from the pinch axis.

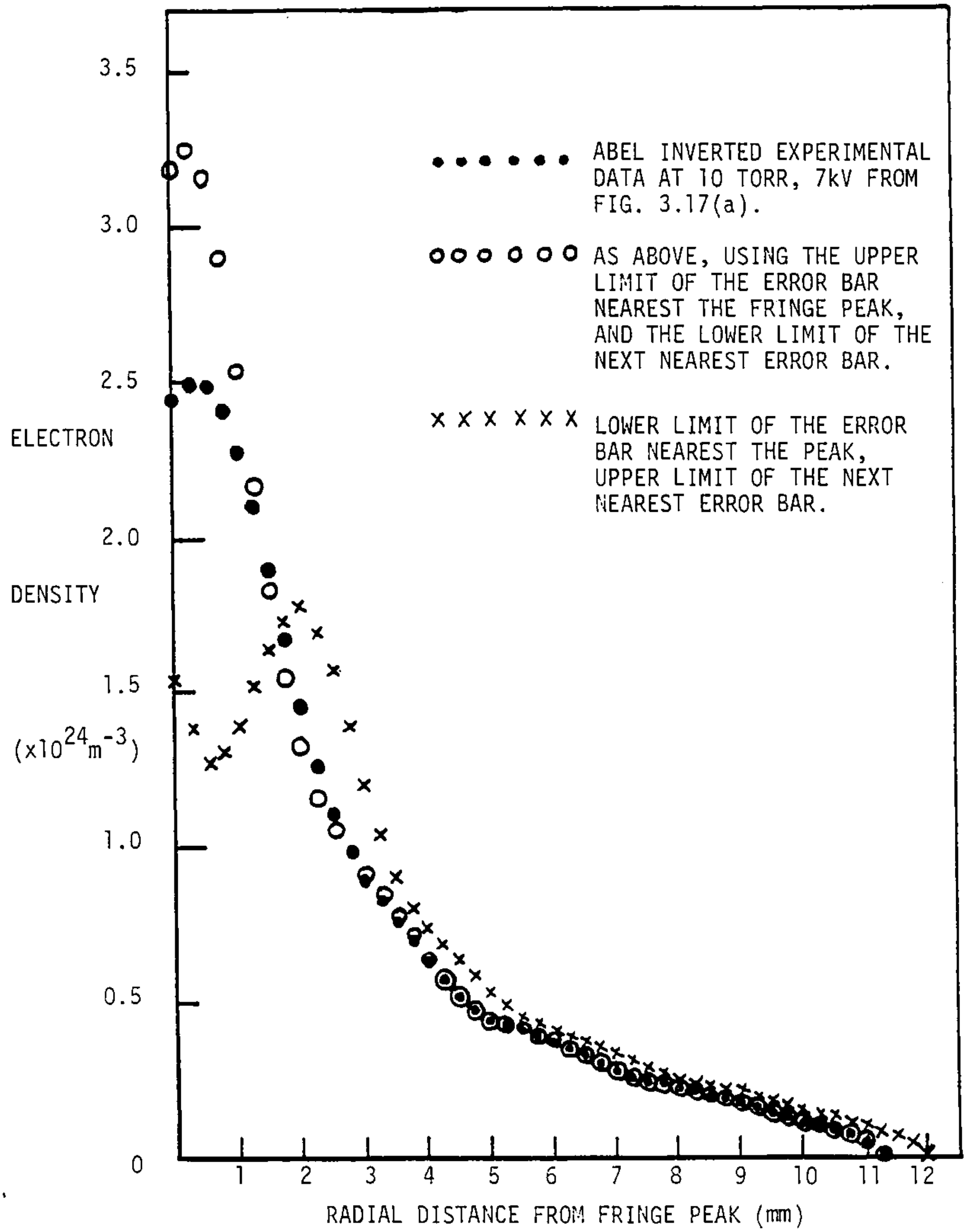

Figure 3.17(c): Abel inverted electron density showing the effect of fluctuations in fringe measurements near the pinch axis.

It is difficult though to place error limits on the peak densities obtained by Abel inversion since various combinations of error bar limits produce a wide range of possible peak densities. The analysis of Figure 3.17c can, however, be assumed to represent a worst case (since it involves the most disadvantageous combination of the error limits). For the purposes of error estimation it was therefore decided to use one half the maximum uncertainty given by such an analysis.

It remains to consider the effect of ignoring the fringe shifts when, following the initial expansion phase, the plasma fills the pinch volume uniformly and gradually recombines. To simulate this, one fringe was added to the measured shift at each height above the axis for the lowest density condition (10 torr, 6 kV). At this condition, the largest number of fringes observed was only 1¾. The resultant Abel inverted density profile is shown in Figure 3.17d and is compared with the inverted profile using the original data. For more than a 50% increase in the fringe shift the peak density alters by less than 10%. This was therefore a negligible source of systematic error in view of the uncertainty due to fluctuations in the near axis fringe shifts treated above.

3.10.5 Interferometric electron densities

The results of the Abel inverted interferometric data, together with the plasma diameter at half maximum density, are shown in Figure 3.18 for the various conditions analysed. The density error bars were determined by the methods of the previous section. The smaller percentage error bars occurred for the higher densities (larger fringe numbers) as expected, with the exception of the 5 torr, 6 kV result for which the fringe peak was unusually poorly defined.

The upper limit on the diagnosed densities ($n_e \sim 10^{25} m^{-3}$) was imposed by continuum absorption which reduced the fringe amplitude (simultaneously with the occurrence of very fast fringes that also made

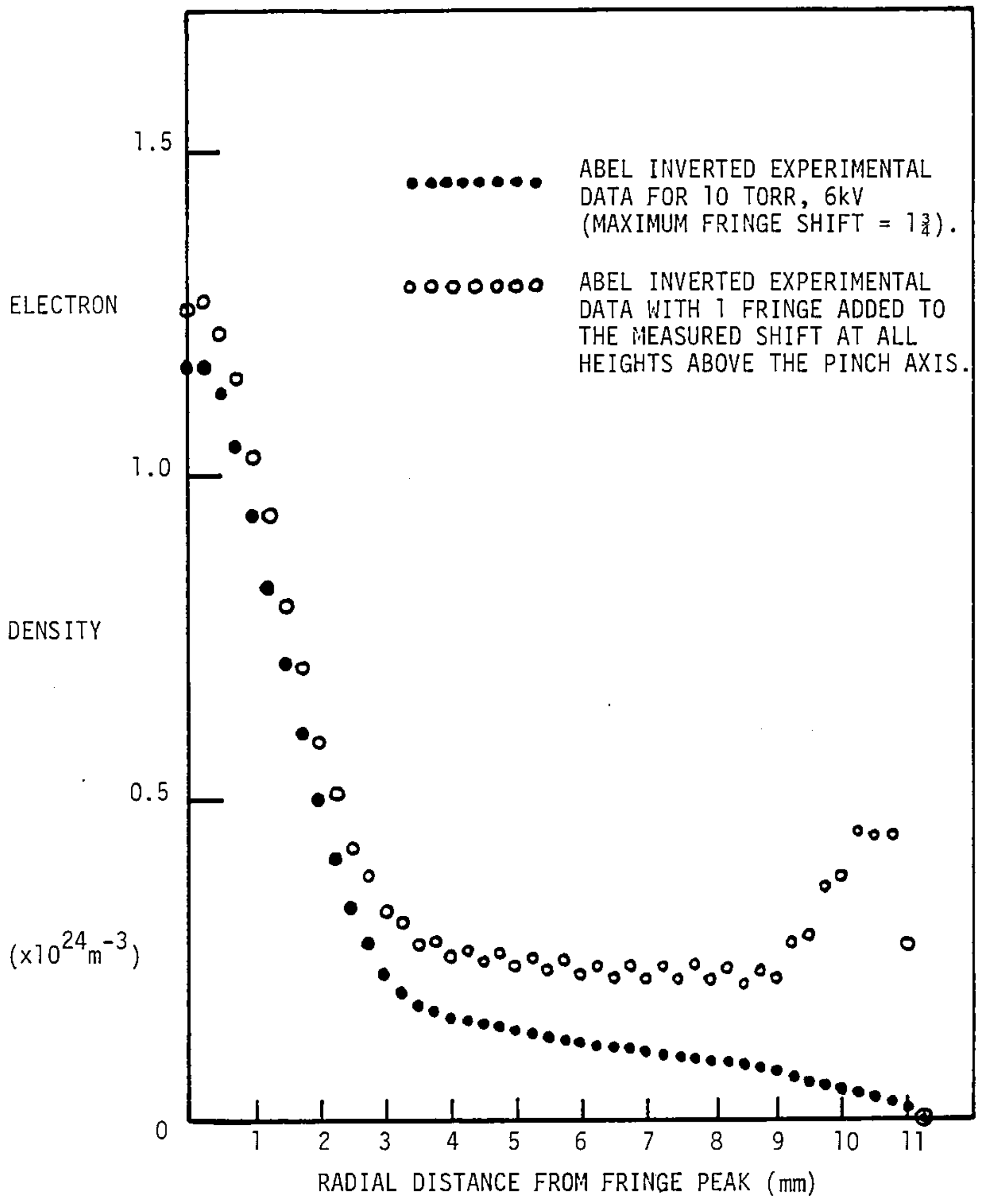

Figure 3.17(d): Abel inverted electron density, showing the effect of adding one fringe to the measured shift at all heights above the pinch axis for the lowest density condition (10 torr, 6kV).

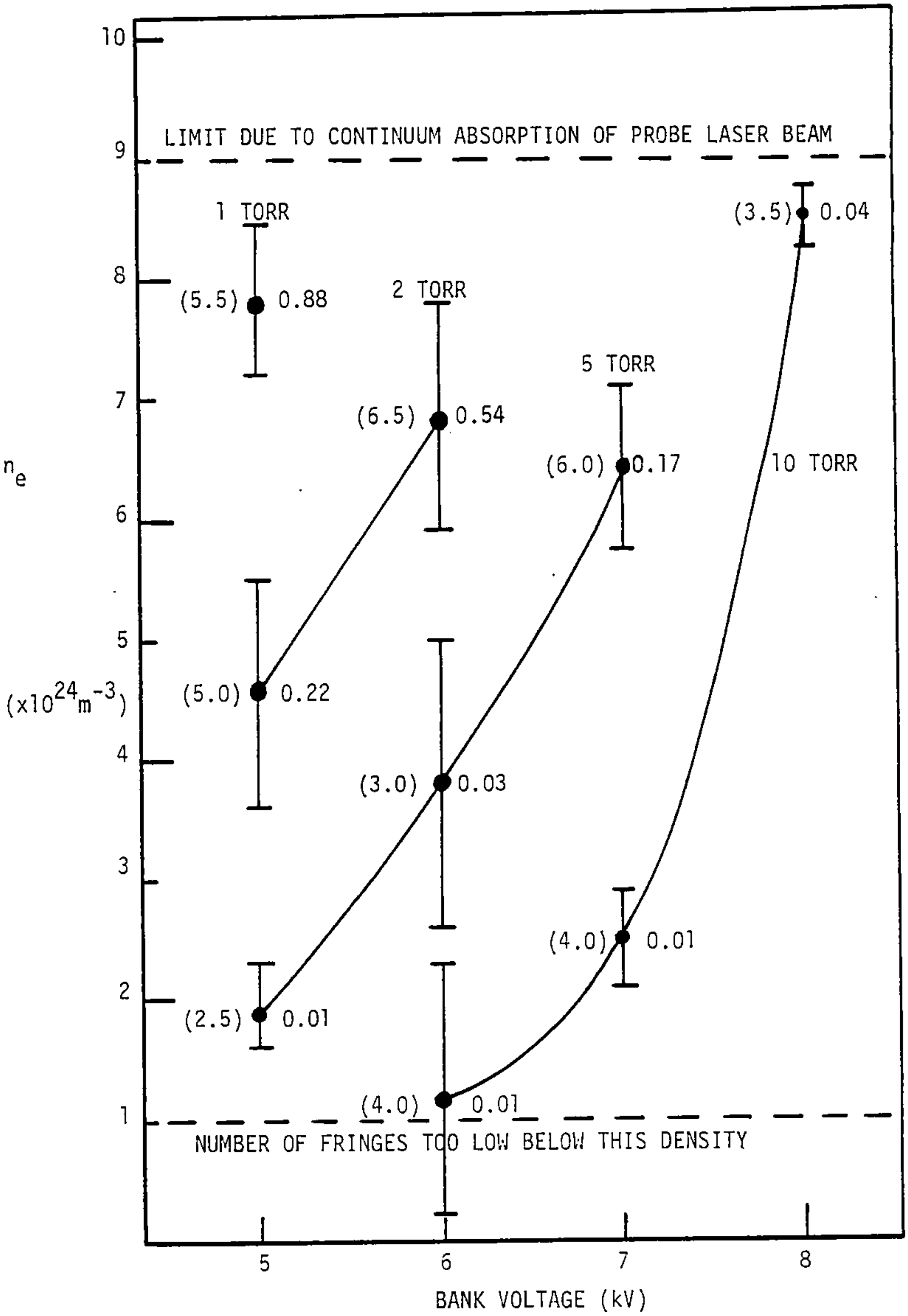

Figure 3.18: Electron density and FWHM pinch diameter (d) in mm at peak compression, as a function of bank voltage and filling pressure. Also shown is the trapping ratio $d^2 n_e \div D^2 n_o$ (D is the pinch vessel diameter and n_o the filling gas number density).

measurement of the fringe shift difficult). The lower density limit was set by the occurrence of too few, ill-defined fringes below $n_e \sim 10^{24} m^{-3}$.

The Abel inverted density profiles can be compared with the densities expected by compressing all the available filling gas into a cylinder of diameter equal to that of the plasma column (and assuming single ionization). For the low pressure conditions the agreement is quite good e.g. for 1 torr, Figure 3.18 indicates that ∿90% of the original gas is trapped in the pinch core at peak compression. However for high filling pressures the agreement is much worse, approaching trapping ratios of a few percent at the highest pressures. A decrease in trapping efficiency with a decrease in bank voltage was also observed at constant pressure. These lower trapping efficiencies may result from a lower proportion of the gas being ionized when the z-pinch first breaks down. When this occurs the neutral gas in the outer regions of the pinch vessel may not be trapped in the initial states of the discharge collapse. Only when the current density rises to a sufficiently high value closer to the pinch axis can the current sheet then efficiently snowplough the remaining gas into the pinch core.

The interferometric results of Figure 3.18 indicate a considerable extension of the range of peak densities obtainable with the present pinch in comparison with the densities obtained by Baker ($n_e \sim 1\text{-}3 \times 10^{24} m^{-3}$). The maximum electron density in the present experiment was in fact limited not by the source but by the lack of available diagnostics to measure densities greater than $\sim 10^{25} m^{-3}$. However, the order of magnitude density variation should enable testing of the density dependence of the Lyman-α satellite features with which this project is primarily concerned.

3.11 Validity of Local Thermodynamic Equilibrium

The high electron densities determined by interferometry suggest that the plasma may attain local thermodynamic equilibrium at peak compression provided (as will be shown) that the electron temperature is not too great. The criterion for L.T.E. - that collisional rates greatly exceed the radiative rates - has been expressed by Griem (1963) for all states down to the ground state as being satisfied when

$$n_e \gtrsim 9.2 \times 10^{23} Z^{*7} \left(\frac{kT}{E_H^Z} \right)^{\frac{1}{2}} \left(\frac{E_2 - E_1}{E_H^Z} \right)^3 \quad m^{-3} \qquad (3.18)$$

where Z* is the charge acting on the optical electron (Z*=1 for neutrals), E_H^Z is the ionization energy of the hydrogen-like ion, and E_2-E_1 is the energy of the resonance line transition. Other authors such as McWhirter (in Huddlestone and Leonard, 1965) yield similar results within a numerical factor of 2 from the above. While this criterion is strictly valid only for hydrogenic ions (or near Rydberg states of other ions) it has been applied here as an approximation to determine the conditions required for L.T.E. in an argon plasma. For optically thick resonance lines the above criterion can be relaxed by an order of magnitude as the net radiative decay rate is reduced due to reabsorption (Griem, 1963). Using this assumption for the resonance lines, the minimum electron density required for L.T.E. to exist down to the ground state is shown in Table 3.2 as a function of ion stage and temperature. Also given are the resonance line energies (E_2-E_1) and ionization potential (I.P.) for each ion stage (of charge Z* on the optical electron).

The results indicate that Ar I and II will be in L.T.E. down to the ground state over the range of densities diagnosed (10^{24}-$10^{25}m^{-3}$). However, Ar III will be in L.T.E. only for densities greater than 4-6 x $10^{24}m^{-3}$, with higher temperatures requiring higher densities for L.T.E. to hold. For Ar IV and V, L.T.E. will not exist down to the ground state at any of the diagnosed densities. However, the first excited state energies of Ar IV and V are some 30eV above the ground state (c.f. ionization energies of 60 and 75eV) and hence it is likely that most levels above the ground state will be in L.T.E.

	T (eV)		ArI	ArII	ArIII	ArIV	ArV
		E_1-E_2 (eV)	11.55	16.41	17.96	31.02	26.98
		I.P. (eV)	15.76	27.62	40.90	59.79	75.0
		Z*	1	2	3	4	5
(a)	2	n_e (m^{-3})	1.29×10^{22}	6.70×10^{23}	3.77×10^{24}	3.85×10^{25}	5.46×10^{25}
	3	FOR	1.58×10^{22}	8.12×10^{23}	4.61×10^{24}	4.72×10^{25}	6.69×10^{25}
	4	L.T.E. to	1.82×10^{22}	9.41×10^{23}	5.33×10^{24}	5.44×10^{25}	7.73×10^{25}
	5	GROUND-STATE	2.04×10^{22}	1.05×10^{24}	5.96×10^{24}	6.09×10^{25}	8.64×10^{25}
(b)	2	τ(ns)	10	540	2400	4×10^6	6×10^5
	3	FOR FIRST EXCITED	2	43	150	3×10^4	8000
	4	STATE	0.7	13	38	2300	1000
	5	EQUILIBRATION	0.5	6	17	550	300

Table 3.2 (a) Electron density required for L.T.E. to exist down to the ground state (assuming optically deep resonance lines)

(b) Time required for the first excited state to attain L.T.E. Note that, in addition to Eqn. 3.19, it is also necessary to ensure that the equilibration time is shorter than the radiative lifetime of the first excited state.

A further criterion for L.T.E. is that the plasma duration, of the order of a microsecond at peak compression, exceeds the time required to bring the resonance line states into L.T.E. The latter time is given by the product of the inverse ground state excitation rate and the fraction of atoms or ions to be excited i.e. (Griem, 1963)

$$\tau = \frac{1.15\times10^{13} Z^{3}}{f_{21} n_e} \left[\frac{N^+}{N^+ + N}\right] \left(\frac{E_2-E_1}{E_H^Z}\right) \left(\frac{kT}{E_H^Z}\right)^{\frac{1}{2}} \exp\left(\frac{E_2-E_1}{kT}\right) \text{ sec} \qquad (3.19)$$

Here f_{21} is the resonance line strength and the ratio in square brackets the fraction of atoms or ions to be excited. Since this ratio is at most 1 and using $f_{21} \sim 0.1$, the lowest density diagnosed ($n_e = 10^{24} m^{-3}$) gives the τ values shown in Table 3.2b. As can be seen, this temporal criterion breaks down for roughly the same ionization stage (ArIV) as the density criterion used previously.

Finally, there is the criterion of spatial homogeneity which requires that atoms or ions do not diffuse over spatial gradients during times faster than the equilibration time τ above. Griem's condition is that the gradients should occur over distances less than

$$d = \frac{7 \times 10^{18}}{A^{\frac{1}{4}}} \left(\frac{kT}{E_H} \right)^{\frac{1}{2}} \left(\frac{E_2 - E_1}{f_{21} E_H} \right)^{\frac{1}{2}} \exp\left(\frac{E_2 - E_1}{2kT} \right)$$

$$\times \left[(N + 10N^+)(N + N^+) \right]^{-\frac{1}{2}} \quad m \tag{3.20}$$

where A is the atomic weight (40 for argon). Assuming that the quantity in brackets is of the order of 2 n_e (if N and N^+ are the dominant ion stages), then given the greatest resonance line energy and the lowest temperature, the largest characteristic distance is $\sim$0.05mm. This is much smaller than the plasma diameter at peak compression which is typically 5mm.

It is therefore apparent that at temperatures $<$ 5eV, the L.T.E. validity criteria are satisfied for argon stages I and II at all the diagnoseddensities, while L.T.E. exists down to the ground state of ArIII only for the higher densities. Although Ar IV and V are not in L.T.E. down to the ground state at any density $< 10^{25} m^{-3}$, their higher lying states will probably be thermalised.

3.12 Calculation of the Ionization Balance in a Dense, non-Debye, Argon Plasma

The assumption of L.T.E. allows calculation of the plasma composition using the Saha equation over the range of temperatures and ion stages inTable 3.2 for which L.T.E. is valid. However, in dense, strongly coupled plasmas the depression of the ionization potential becomes important and must also be included in any calculation of the ionization balance.

Firstly, for an n-times ionized plasma there are n-1 Saha equations relating the densities of adjacent ionization stages,

$$\frac{n_{r+1}n_e}{n_r} = 2\,\frac{u_{r+1}(T,\Delta E_{r+1})}{u_r(T,\Delta E_r)}\;\frac{(2\pi m_e kT)^{3/2}}{h^3}\exp-\left(\frac{E_r-\Delta E_r}{kT}\right) \tag{3.21}$$

Here u_r represents the partition function, E_r the ionization energy,and ΔE_r the ionization potential depressionfor the lower ionization stage. These equations, together with the condition for overall charge neutrality

$$n_e = \sum_i n_i Z_i \tag{3.22}$$

enable the plasma composition to be determined for a given temperature and electron density.

However, the ionization potential depression is not known a priori, since it may itself depend upon a knowledge of the plasma composition. This is true if a Debye potential is assumed, for which the I.P. depression is a function of the mean plasma charge <Z> via the Debye length (Equation 1.21). However an initial estimate for the I.P. depression can be achieved by using the ion-sphere result (Equation 1.22) which depends only on the mean interparticle separation R_0. Using this value for the I.P. depression yields a first estimate of the ionization balance which can then be used to determine the value of the

Debye depression. The ion distribution is then re-calculated in an iterative process. This method was employed here and found to converge rapidly for the range of conditions evaluated (n_e=10^{24}-10^{25}, T_e=2-5eV). For these conditions (where $R_o \sim \lambda_D$) the ion-sphere and Debye depression values are similar and the rapid convergence is to be expected.

The ionization balance was calculated using partition functions taken from the tables of Drawin and Felenbok (1965). The argon stages I-V were included, although as shown in the previous section only stages I-III can be in L.T.E., with IV and V being thermalized only in the upper states. The hydrogen concentration was much lower (∼ 1%) and its contribution to the electron density was therefore neglected, particularly since the proton partition function (=2) is small compared to that for the argon ions. The results of the ionization balance calculations are shown in Table 3.3, along with the mean ion charge <Z> (Equation 1.19) to which the ionization balance calculations were found to converge.

The density of each ion stage is also expressed as a percentage of the total ion/atom number density in Figures 3.19 a-d. Note that ArIV and V only appear in appreciable concentrations at the higher temperatures (4 and 5eV), and then (for Argon V at least) only at lower densities. Neglect of even higher stages in the calculations is therefore probably justified, and data for their partition functions was not in any case available.

$n_e(m^{-3})$	T(K)	Ar(I)	Ar(II)	Ar(III)	Ar(IV)	Ar(V)	<Z>
10^{24}	23,200	5.27/22	9.28/23	3.60/22	7.27/17	-	1.07
	34,800	1.10/21	7.61/22	4.37/23	1.69/22	1.84/18	1.98
	46,400	4.74/18	3.77/21	1.37/23	2.34/23	4.83/21	2.74
	58,000	-	9.70/19	1.32/22	2.00/23	9.36/22	3.35
$2x10^{24}$	23,200	1.67/23	1.92/24	4.03/22	4.60/17	-	1.04
	34,800	4.09/21	2.70/23	8.40/23	1.66/22	9.37/17	1.89
	46,400	4.35/19	1.83/22	4.23/23	3.73/23	3.88/21	2.56
	58,000	-	8.73/20	5.84/22	4.72/23	1.17/23	3.18
$4x10^{24}$	23,200	5.19/23	3.91/24	4.61/22	3.12/17	-	1.02
	34,800	2.11/22	8.97/23	1.53/24	1.71/22	5.62/17	1.79
	46,400	3.64/20	8.48/22	1.14/24	5.43/23	3.12/21	2.40
	58,000	-	6.68/21	2.30/23	1.00/24	1.34/23	3.02
$6x10^{24}$	23,200	1.03/24	5.90/24	5.05/22	2.59/17	-	1.02
	34,800	4.68/22	1.73/24	2.11/24	1.68/22	4.10/17	1.72
	46,400	1.24/21	1.94/23	1.93/24	6.46/23	2.67/21	2.30
	58,000	-	1.65/22	4.87/23	1.48/24	1.41/23	2.92
$8x10^{24}$	23,200	1.71/24	7.89/24	5.47/22	2.35/17	-	1.01
	34,800	8.08/22	2.74/24	2.63/24	1.67/22	3.30/17	1.68
	46,400	2.64/21	3.33/23	2.74/24	7.28/23	2.41/21	2.24
	58,000	-	3.22/22	8.01/23	1.93/24	1.44/23	2.86
10^{25}	23,200	2.55/24	9.88/24	5.85/22	2.21/17	-	1.01
	34,800	1.33/23	3.82/24	3.07/24	1.65/22	2.84/17	1.62
	46,400	4.79/21	5.19/23	3.56/24	7.86/23	2.18/21	2.19
	58,000	-	5.42/22	1.17/24	2.34/24	1.46/23	2.81

Table 3.3 Ion stage densities ($A/B = Ax10^{B}m^{-3}$) in L.T.E. calculated from the Saha equation (including the effects of ionization potential depression). Also shown is the mean ion charge <Z>.

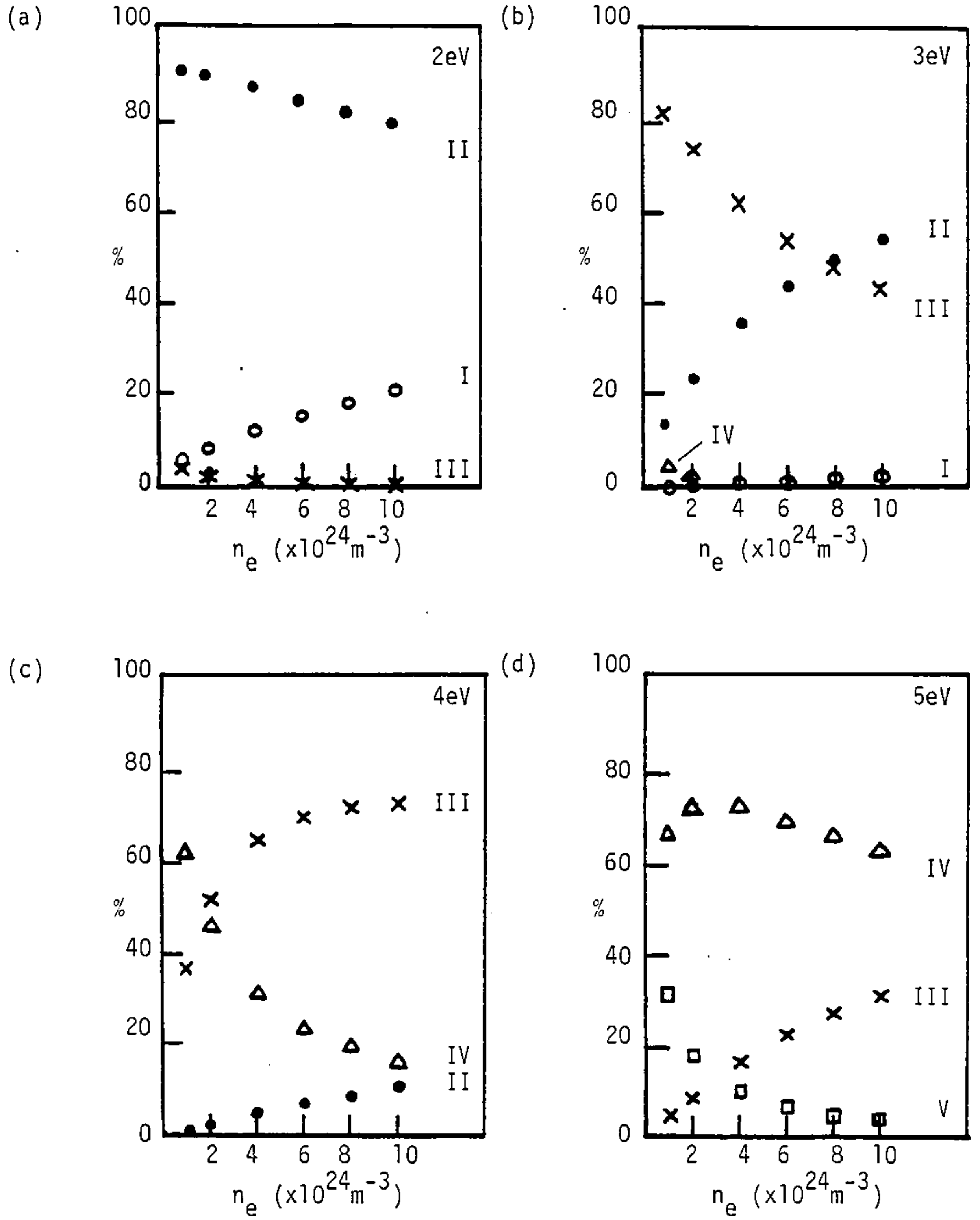

Figure 3.19: The L.T.E. abundance of argon ion stages I-V as a function of density and temperature. The number of ions in each stage is expressed as a percentage of the total number of argon ions.

3.13 Choice of a Temperature Diagnostic

The ionization balance in the z-pinch plasma can be obtained from the calculations of the previous section provided that the electron temperature can be determined. (The electron and ion temperatures will be equal at the $> 10^{24}\mathrm{m}^{-3}$ electron densities considered here, since the electron-ion equilibration time given by Griem (1964, p.155),

$$\tau^{Z}_{e-i} \sim \left[3\times10^{-13}\left(\frac{Z^2 13.6}{T(\mathrm{eV})}\right)^{3/2} n_e(\mathrm{m}^{-3})\right]^{-1} Z\ \frac{m_{ion}}{m_e} \qquad (3.23)$$

is ~ 30 ns, and therefore much less than the $\sim 1\,\mu$s risetime of the peak compression). The following temperature diagnostics were considered:

1) Line intensity and line-to-continuum ratios: The high continuum opacity again made interpretation of emission intensities difficult in the visible and near UV, while no accurate quantitative information was available for argon line strengths in the VUV.

2) Continuum slopes: Measurement of the argon recombination continua for all ion stages was complicated by the presence of many overlying lines from higher ion stages.

3) Thomson scattering: At the densities considered here the α value (Equation 1.49) was large for temperatures of a few eV, and hence the Doppler width of the (argon) ion feature would give the only indication of the plasma temperature. Even at a temperature of 5eV this width would be too small ($\sim$0.1Å at the 6943Å ruby laser wavelength) to be resolved. In any event, the scattered signal level for visible lasers would be too low relative to the fluctuations in the background continuum emission (as discussed previously in Section 3.2).

4) Absorption of resonant laser radiation: A temperature diagnostic proposed by Burgess and Cooper (1965) and calculated for the argon 4880Å line by Wheeler and Troughton (1969) involves measurement of the absorption coefficient of argon II lines using resonant laser radiation. Since

both the electron impact linewidth and the ArII number density increase linearly with the electron density, the absorption coefficient is nearly density independent and is only dependent on temperature. This property was used as a temperature diagnostic by Baker (1977) who measured the absorption coefficient of the ArII 4880Å line using a cw argon ion laser.

However Baker did not take into account the effects of the continuum opacity. The calculations of Wheeler and Troughton (1969) show that over a 5mm plasma length at $n_e=10^{24}m^{-3}$ and $10^{25}m^{-3}$, the maximum possible optical depths for the 4880Å line are ~1 and ~2.7 respectively. The maximum optical depths occur at T_e=30,000K, and a temperature variation from this value of ±5,000K decreases the line opacity by more than half. By comparison, the continuum opacities measured in Figure 3.9 (albeit at a somewhat longer wavelength - 6328Å) can be comparable to the calculated absorption line opacities. However, since the argon ion laser was not tunable, it was not possible to correct for the continuum contribution to the 4880Å opacity.

5) Observation of lines from argon ion stages: The presence of line emission from various ion stages can be combined with the ionization balance calculation of Section 3.12 to provide an estimate of the plasma temperature (given that the plasma was in L.T.E.). This can only be a crude estimate due to the number of variables that determine the presence of emission lines (other than density and temperature). These variables include timescale of emission, length of the line-of-sight emitting region, line strength and film sensitivity.

However, given the considerable limitations of the other temperature diagnostics above, the relative argon ion line abundance from Figure 3.10 was therefore used in combination with the relative argon ion distributions of Figures 3.19 a-d to infer an approximate electron temperature. Only the UV lines were considered (since the effects of continuum absorption on the observation of lines at peak compression was less than in the visible), and the results are discussed in the following section.

3.13.1 A temperature estimate from the presence of higher ion stages

The UV (2000-4000Å) lines observed in Section 3.8 were compared with the strong argon ion lines tabulated for this region by Striganov and Sventitskii (1968, pp.34-36). The proportion of tabulated lines that were observed at each condition was used as an indication of the population of the highest ion stage (and hence of the highest plasma temperature) at peak compression. Also used was the proportion of lines (both weak and strong) of a given ion stage observed at one condition, relative to the total number of lines of that stage observed from all conditions (Figure 3.10).

The appearance of ArIV lines solely at 1 torr and 7 kV ($n_e \gtrsim 10^{25} m^{-3}$) indicated that this was the highest temperature condition. In that spectrum all the ArIII lines also appeared, which from the relative ion populations of Figure 3.19b suggested a temperature greater than 3eV, but probably less than 4eV since few of the possible ArIV lines were present. At 1 torr, 5kV ($n_e \sim 7.8 \times 10^{24} m^{-3}$) most of the ArIII but none of the ArIV lines were present, thereby indicating a temperature of 3eV. The preponderence of ArII lines over ArIII lines at 5 torr and 7 kV suggested a lower temperature (say 2.5eV). The temperature was greater than 2eV, since at 2eV and $n_e \sim 6.4 \times 10^{24} m^{-3}$ a significant number of ArIII ions would not be present. A temperature of 2eV would be more applicable to the result at 5 torr and 5kV ($n_e \sim 1.9 \times 10^{24} m^{-3}$) which showed more ArI lines than any other condition, and which had fewer ArII and ArIII lines present. Using this analysis, the temperatures ascribed above can only be estimated to within ±0.5eV.

The conditions produced in this pinch thus showed a temperature range of 2-3.5±0.5eV, with a trend to increased temperatures at higher bank voltages and at lower filling pressures. The temperature conditions included and extended the range achieved by Baker (2-2.5eV) using the same discharge energies.

3.14 Summary

By optimising the z-pinch operating conditions and increasing the discharge current, the range of electron densities accessible in a physically identical z-pinch to Baker's was significantly increased. The maximum density diagnosed by interferometric methods was $\sim 8.5 \times 10^{24} m^{-3}$; but this did not represent the maximum density achievable in the present device since the diagnostics were limited by continuum absorption and fast fringe speed at higher densites. The density range obtained ($1.2\text{-}8.5 \times 10^{24} m^{-3}$) overlaps the densities achieved by Baker and should enable a test of the density dependence of the Lyman-α features which were the chief concern of this study.

Temperature diagnostics were also severely limited, again principally by the continuum opacity. However, as the temperature was of secondary importance in determining the behaviour of the satellite features, a rough estimate from ion species abundance (accurate to ±0.5eV) was considered sufficient over the wide temperature range achieved (2-3.5eV). When combined with the measured densities, the number of particles per Debye sphere N_D is shown in Figure 3.20. The present experiment is compared with the N_D value obtained by Baker for the same bank voltage. Also shown is the N_D value of Landen and Winfield (1983, private communication) who have performed a sodium vapour ionization experiment (also in this laboratory). Their scheme used resonantly pumped laser ionization of sodium, and their low value of N_D is fairly typical of other workers

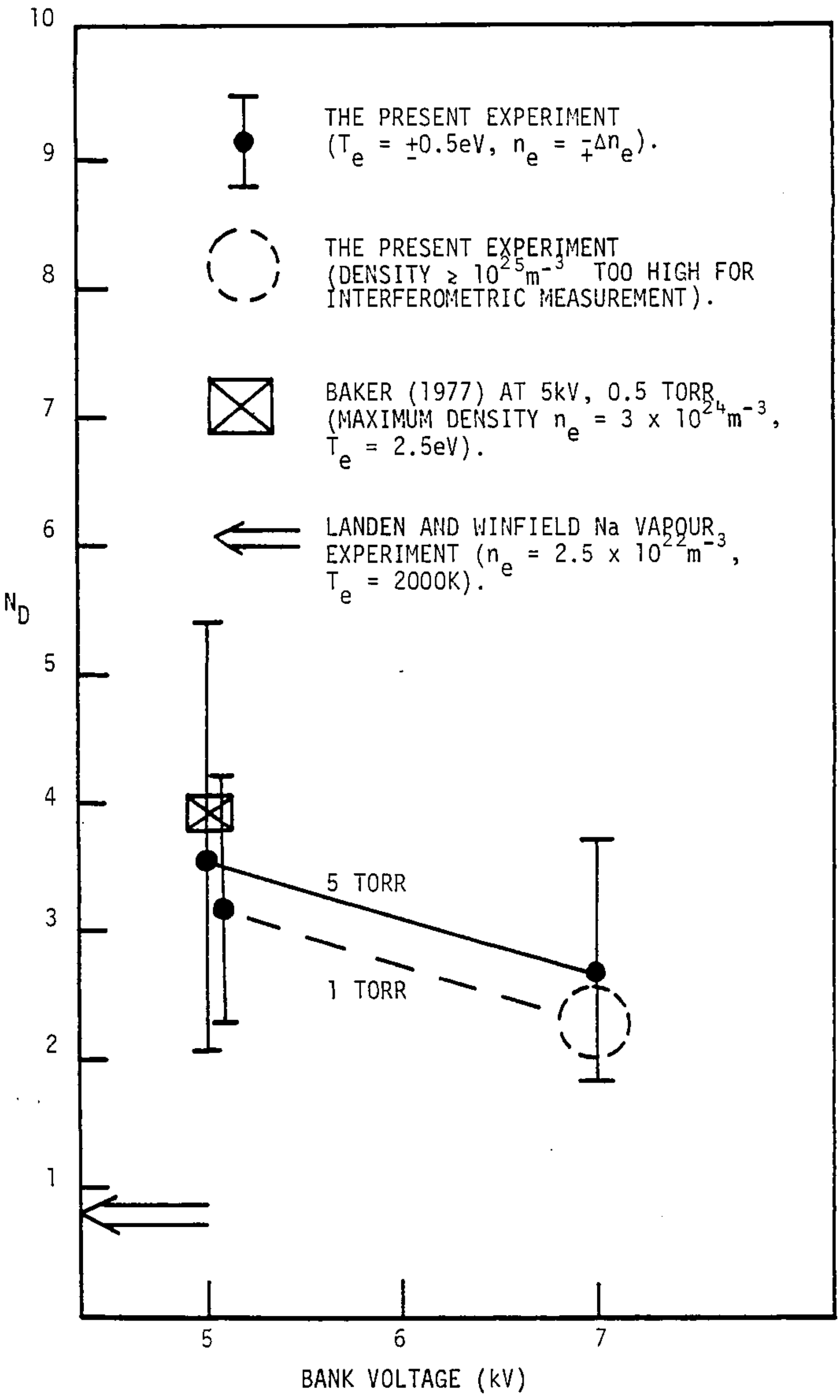

Figure 3.20: Number of particles per Debye sphere ($N_D = \frac{4\pi}{3} \lambda_{De}^3 n_e$) as a function of initial pinch conditions.

in their field as is shown earlier in Figure 1.1 (see Sechenov et al. and others in Tepl. Vys. Temp. 15, 1977).

The significantly lower N_D value of Landen and Winfield was probably due to the faster initiation of the ionization (by a 15 ns laser pulse) which produced a short-lived (<200 ns) non-Debye plasma. Similarly, the shock tube experiments in Figure 1.1 produce low N_D values using a fast, non-equilibrium onset of the plasma (by shocks travelling at $\gtrsim 10^4$m/s and with submillimetre shock thicknesses). This sudden, non-equilibrium plasma creation is in contrast to the much more slowly increasing z-pinch plasma densities created here (on microsecond timescales). While incomplete shock-piston separation was kept to a minimum in order to maximise n_e, some current inevitably flowed between the shock and the main current sheet. The resulting increase in plasma density was thus gradual and continuously in equilibrium. Achievement of even fewer particles per Debye sphere was then prevented by the tendency of the gradually developing, cold, dense plasma to recombine. This hypothesis is supported by the fact that although the range of densities achievable in the present pinch was increased by a factor of $\sim$ 3 compared with Baker, the number of particles per Debye sphere was maintained at or just below the same level.

CHAPTER 4

THE COHERENT LYMAN-α SOURCE

4.1 Introduction

Recent advances in the frequency upconversion of laser radiation have extended the range of coherent radiation sources into the VUV (e.g. Vidal, 1980). In particular, frequency tripling of dye laser radiation has produced Lyman-α output powers of ∿ 10W or ∿ 5x10^{10} photons/pulse (e.g. Mahon et al., 1978; Cotter, 1979; Langer et al., 1980; Hilbig and Wallenstein, 1981). Krypton was the non-linear medium used in the tripling process, and the VUV output was tunable between 1203 and 1236Å. Narrow bandwidths (< 1GHz) have also been obtained, limited either by the bandwidth of the dye laser or (ultimately) by the Fourier transform of the laser pulse length ($\Delta\nu^{-1} \sim \tau \sim 10^{-9}$s).

Such tunable, narrowband coherent radiation sources have enabled high resolution spectroscopy in the VUV (e.g. Stoicheff et al., 1982). However, to date there have been few applications to plasma spectroscopy (see, however, the fluorescence studies of Dreyfus et al., 1982). One of the aims of the present project was the construction of a tunable, coherent Lyman-α source in order to obtain detailed absorption lineshapes of the Lyman-α satellites, and to measure the Lyman-α wing opacity.

This chapter first outlines the principles of third harmonic generation. The various schemes employed elsewhere for coherent Lyman-α generation are then considered, and the system developed here for the production of coherent Lyman-α radiation is described.

4.2 Theory of Third Harmonic Generation

This section briefly summarizes the principles of frequency tripling, and follows the treatment and nomenclature used by Bjorklund (1975). The process considered here is degenerate three-photon absorption to a virtual state in a rare gas (krypton), followed by emission of a Lyman-α photon at the sum frequency of the fundamental radiation components.

Bjorklund derives the following expression for the power radiated at the third harmonic frequency

$$P \propto (3\lambda)^{-4} [\chi_3(\lambda)]^2 \, n_o^2 \, P_1^3 \, F_1(b\,\Delta k, \frac{b}{L}, \frac{f}{L}) \qquad (4.1)$$

where

3λ	is the wavelength of the fundamental radiation
$\chi_3(\lambda)$	is the third order susceptibility per atom at the third harmonic
n_o	is the krypton number density
P_1	is the fundamental laser power
F_1	is a geometric factor to be defined.

The third harmonic power is proportional to the cube of the fundamental input power, since the nonlinear process requires the simultaneous absorption of three photons. Efficient third harmonic generation is dependent on the non-linear medium possessing a significant third order susceptibility at the third harmonic.

The properties of the medium also affect the tripling process via the geometric factor. In general, the fundamental and harmonic waves will become out of phase when passing through the medium, due to the different refractive indices (N) at λ and 3λ. In order to achieve effective tripling, the geometric factor must be optimised so that third harmonic contributions from different regions in the medium are correctly phase-matched to give constructive interference.

The mis-match between the third harmonic and fundamental wave vectors is given by

$$\begin{aligned} \Delta\vec{k} &= \vec{k}_3 - 3\vec{k}_1 \\ &= \frac{2\pi}{\lambda}(N_3 - N_1) \end{aligned} \qquad (4.2)$$

For the case of tight focussing into a tripling cell (of length L), the geometric factor is

$$F_1 = (\pi b \Delta\vec{k})^2 e^{\,b\Delta k} \qquad (4.3)$$

Here b is the confocal beam parameter ($b \ll L$ for the tight focussing case) defined by

$$b = \frac{2\pi W_0^2 N_1}{3\lambda} \sim \frac{2\pi (f\theta)^2 N_1}{3\lambda} \qquad (4.4)$$

where f is the lens focal length, θ is the half-angle fundamental beam divergence and W_0 is the beam waist radius of the focal spot. The geometric factor is maximised for

$$b\Delta\vec{k} = -2 \qquad (4.5)$$

which can be achieved by altering b (changing the focus) or by altering $\Delta\vec{k}$.

For a fixed focus, $\Delta\vec{k}$ can be adjusted by changing the dispersion $(N_3 - N_1)$ of the non-linear medium i.e. by altering the gas pressure.

Krypton is negatively dispersive between 1203-1236Å due to the 4p-5s resonance line at 1236Å (Mahon et al., 1979b). However, another gas of positive dispersion and negligible third order susceptibility (e.g. argon) can be mixed with the krypton. The mixture of gases has the advantage that the krypton gas can be kept at a high pressure to take advantage of the n_0^2 dependence of the third harmonic power, while the phase matching can be achieved by varying the argon pressure. In reality the output power is limited by gas breakdown at high pressures and by VUV absorption. The more important limitation as far as the present experiment is concerned is that the rapid change in refractive index with wavelength near the resonance line greatly limits the pressure tuning range of the two gas system (Mahon et al., 1979b).

In order to tune the VUV radiation over the complete wavelength range for which krypton is negatively dispersive (1203-1236Å), a single gas system is used in which phase-matching is achieved by varing the krypton pressure. However the optimum phase matching criterion is different, since the n_0^2 dependence of the output power must be included in the geometric factor (as $\Delta k \propto (N_3 - N_1) \propto n_0$). The new quantity to be optimised is then

$$\begin{aligned} G_1\left(b\Delta k, \frac{b}{L}, \frac{f}{L}\right) &= (b\Delta k)^2 \, F_1\left(b\Delta k, \frac{b}{L}, \frac{f}{L}\right) \\ &= (b\Delta k)^2 \, (\pi b\Delta k)^2 \, e^{b\Delta k} \qquad (4.6) \end{aligned}$$

which maximises for

$$b\Delta k = bA(\lambda)\, n_0 = -4 \qquad (4.7)$$

where $A(\lambda)$ is the ratio $\frac{\Delta k}{n_0}$. Hence as the fundamental wavelength is altered, the phase matching is optimised simplying by varying the krypton density.

An example of such a pressure tuning curve is shown in Figure 4.1a for a 50mm focussing lens at 1232Å (from Cotter, 1979). Also shown (in Figure 4.1b) is the optimum phase-matching pressure as a function of third harmonic wavelength. The full tuning range indicated in Figure 4.1b was required to observe satellites up to 20 Å into the wings of Lyman-α. Therefore the single gas phase-matching scheme was used in the present experiment.

The analysis presented above assumes a TEM_{00} Gaussian beam profile. However Yiu et al. (1979) have shown that the phase-matching criteria may vary when the beam profile deviates from this form. For example a TEM_{pm} mode is predicted to produce several maxima for F_1. The maximum power is expected to increase with p for a single gas medium, and to decrease with increasing p for a two gas medium. Occurrence of a number of modes was also predicted to cause severe fluctuations in the output power. Therefore control of the quality of the fundamental beam profile is important in determining the ultimate harmonic power.

4.3 Previous Schemes for Coherent Lyman-α Generation

Third harmonic generation at Lyman-α has been achieved by a number of workers using either the single or the two gas phase-matching methods. Table 4.1 lists four schemes which illustrate the range of techniques employed, both in the production of the fundamental dye laser radiation and in the frequency conversion process.

Two types of dye laser pumping schemes are employed. The first is longitudinal pumping, in which the pump laser beam is directed along or near the axis of the dye laser output. Longitudinal pumping minimises the energy density in the dye cell by pumping a large volume of dye, which requires a low dye concentration to prevent absorption

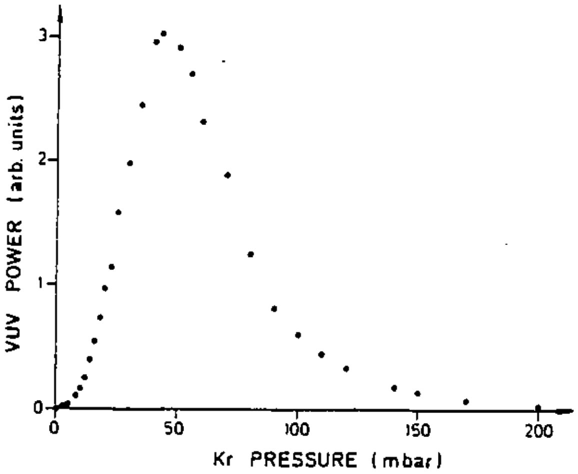

Fig. 4.1a: Lyman-α output at 1232Å as a function of tripling cell krypton pressure, using a 50mm focal length lens (Cotter, 1979).

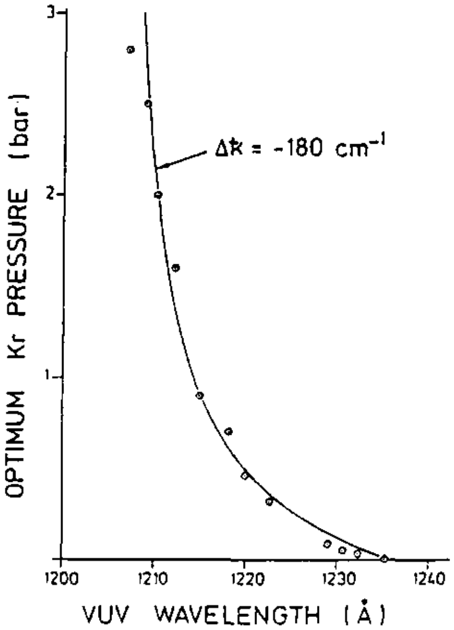

Fig. 4.1b: Krypton pressure for optimum VUV output as a function of wavelength, using a 50mm focal length lens (Cotter, 1979). Also shown is the value of Δk derived from this plot.

REF.	MAIN PUMP LASER	DYE LASER WAVE-LENGTH (Å)	DYE LASER BANDWIDTH (GHz)	PULSE LENGTH (nS)	PEAK DYE LASER POWER (MW)	TRIPLING MEDIUM	OUTPUT AT 1216Å (W)	CON-VERSION EFFIC-IENCY
(1)	Ruby	7296	170	15	10	Kr	60	$6x10^{-6}$
(2)	Excimer	3648	3	7	1	Kr	5	$5x10^{-6}$
(3)	Ruby	7296	12	10	NOT GIVEN	Kr/Ar	NOT GIVEN	10^{-4}
(4)	Nd:Yag DOUBLED	7296	0.26	6	1.5	Kr/Ar	16	10^{-5}

Table 4.1: Comparison of Lyman-α generation schemes

(1) Mahon et al. (1978): Flashlamp pumped, etalon tuned oscillator; five longitudinally pumped amplifiers followed by a frequency doubling crystal.

(2) Cotter, (1979): Grating tuned oscillator; one amplifier (also transversely pumped).

(3) Langer et al., (1980): Longitudinally pumped, etalon tuned oscillator; four transversely pumped amplifiers followed by frequency doubling crystal.

(4) Hilbig and Wallenstein (1981): Grating and etalon tuned oscillator; three amplifiers (also transversely pumped) and a doubling crystal.

of the pump beam over a small region. However, a high quality beam profile is required for the pump laser, as the output beam profile is directly determined by the pump beam profile (Mahon et al., 1979).

The second type of dye laser pumping is the transverse system, which is employed for low (< 100mJ) pump energies. The pump radiation is focussed by a cylindrical lens into a line just behind the dye cell window. The radiation is absorbed over a small (few hundred μm) distance due to the high dye concentration. A high gain region is thereby produced along the line focus, which then defines the dye laser axis. The small diameter of the line focus acts as a spatial filter in the dye laser cavity, thereby enchancing the beam quality and making the dye laser profile less dependent on the pump laser beam quality (Hansch, 1972).

The pump laser pulse length is usually short (typically 10 ns) since for a constant pump energy, the dye output power (and hence the harmonic output power $\propto P_1^3$) is greater. The pulse length also determines the minimum possible bandwidth, the transform limit being ∿100 MHz for a 10 ns pulse. All the schemes shown have a greater bandwidth, which is determined by the bandwidth of the tuning element (usually a grating) which provides selective feedback into the oscillator cavity. The Lyman-α bandwidth (in Hz) will be the same as for the dye laser, since although the bandwidths of the three fundamental waves add, the P_1^3 dependence of the Lyman-α power reduces the summed bandwidths by a factor of three. (This can be seen by considering the half-intensity width of the fundamental spectral profile, which on tripling becomes the $\frac{1}{8}$th-intensity width.)

The dye laser outputs of the systems shown in Table 4.1 were focussed into the respective non-linear media using focal lengths of between 50 and 250 mm (depending on gas breakdown limitations). The conversion efficiency (listed at 1216Å for comparison) was significantly improved when phase-matching by the two gas system was employed. However the maximum output power achieved was of the same order as in the single gas systems due to the limitations of gas breakdown and VUV absorption. Tuning was possible in the single gas systems over the full range of wavelengths for which krypton is negatively dispersive (1203-1236 Å). The tuning range shown in Figure 4.2 (from Cotter, 1979) indicates that the Lyman-α output was constant over most of the tuning range (within a factor of 3), except at the limits to the negatively dispersive region where the VUV output decreased rapidly.

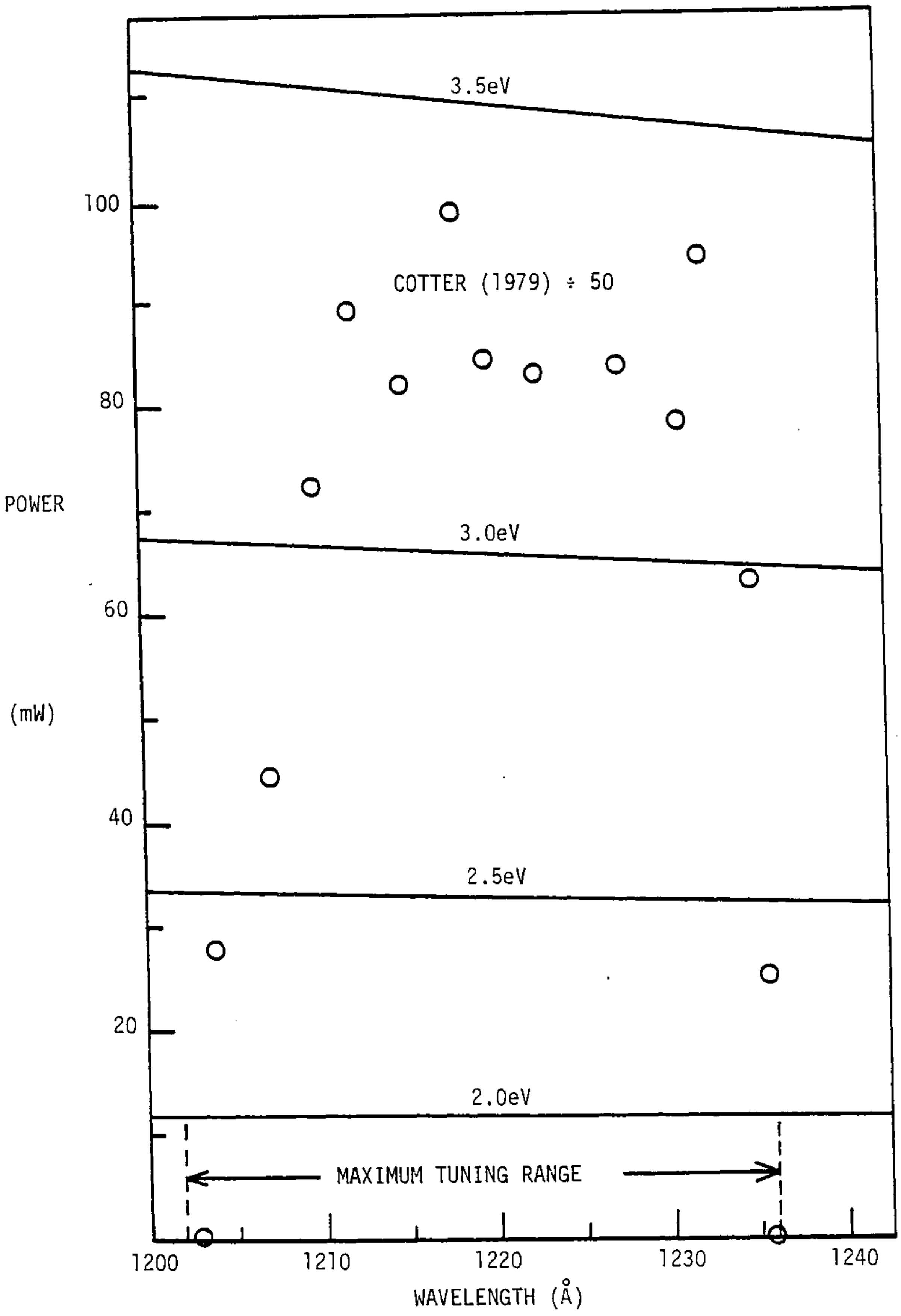

Figure 4.2: Black body power radiated from the z-pinch plasma into the beam area of the coherent Lyman-α source at the detector. Also shown is 1/50th the power achieved by Cotter (1979).

4.4 Estimate of the Lyman-α Power Required for the Present Absorption Experiment

Intensity fluctuations due to random noise in the pinch emission were expected to provide the major limitation to the visibility of the transmitted Lyman-α beam in an absorption experiment. The intensity of the pinch emission can be estimated to be (at most) equivalent to the black body emission level at the plasma temperature (2-3.5eV). The power radiated by a black body per unit wavelength interval, per unit area, per steradian is (Thorne, 1974)

$$B_o(\lambda,\ T)d\lambda \ = \ \frac{2hc^2}{\lambda^5}\ \frac{1}{e^{hc/\lambda kT}-1}\quad d\lambda Wm^{-2}ster^{-1} \qquad (4.8)$$

To estimate the power required for the coherent Lyman-α source the Lyman-α beam is assumed to be collimated by a lens. The lens is placed so that the beam waist of the fundamental (focussed into the tripling cell) is at a distance equal to the focal length of the collimating lens at 1216Å. The finite size of the beam waist is due to the divergence of the fundamental beam, and causes the collimated harmonic beam also to be divergent. (This is because radiation which is emitted e.g. from the beam waist radius passes through the centre of the lens to form a divergent cone.) The divergence of the output beam is therefore related to the input beam divergence by the ratio of (a) the distance from the beam waist to the collimating lens, to (b) the focal length of the initial focussing lens. A collimated Lyman-α output beam of θ=2 milliradians divergence is assumed, together with a 5 mm beam diameter at the plasma and a 0.2Å bandwidth for the monochromator detection system. (The monochromator is necessary not only to discriminate against the background pinch emission, but also to reject radiation from the fundamental beam.) These assumptions yield the following black body power radiated into the solid angle $\pi\theta^2$

in the far field:

$$P_B^{\infty} = B_o(\lambda,T)\ d\lambda \times \frac{\pi d^2}{4} \times \pi\theta^2$$
$$= 4.9\text{x}10^{-21}\ B_o(\lambda,T)\ \text{Wm}^{-2} \qquad (4.9)$$

However, the difficulties of aligning a laser beam in the VUV means that in practice the detection system is located close to the tripling cell. To estimate the maximum power required for the Lyman-α source, the minimum possible distance from the pinch axis to the monochromator (0.26m) is therefore assumed. The side-arm ports restrict the area of the pinch axis that is visible at the detector to a region that lies within the acceptance angle of the f10 monochromator - a region ∿ 15mm long by 5mm high (∿ the pinch diameter at peak compression). This area could be further reduced (to the area of the Lyman-α beam) by introducing baffles into the pinch vessel, but this may affect the pinch characteristics and introduce impurities. If the Lyman-α beam diameter at the slits is ∿ 5mm, then the black body radiation into the same beam area is

$$P_B^{0.26} = 4.3 \times 10^{-19} B_o(\lambda,\ T)\ \text{Wm}^{-2} \qquad (4.10)$$

i.e.approximately a factor of 100 greater than in the far field. The power required could be reduced further by focussing the Lyman-α beam onto the slits, although the spot diameter at f∿ 0.5m from the focussing lens would be $2f\theta \sim 2$mm. The power required is then reduced by a factor of only ∿ 2.5 (since the slit widths remain constant), and the 2mm acceptance height would make alignment of the VUV beam even more difficult.

Equation (4.10) was therefore used as an upper bound on the expected level of background pinch emission, and the results are plotted as a function of wavelength and temperature in Figure 4.2. When compared to the Lyman-α power achieved by Cotter (1979), the blackbody levels indicate that the coherent Lyman-α radiation should be visible above the background pinch emission at all the conditions shown (2-3.5eV).

Finally it is interesting to consider the VUV power needed to saturate the Lyman-α transition over the whole beam area (neglecting the effects of collisional de-excitation). The flux required is given by the ratio of the Einstein A_{21} and B_{21} coefficients (respresenting spontaneous emission and absorption respectively) i.e. (Thorne, 1974)

$$I(\mathrm{Wm}^{-2})\ d\lambda = \frac{A_{21}}{B_{21}} = \frac{8\pi hc^2}{\lambda^5}\ d\lambda \tag{4.11}$$

Assuming a Stark broadened Lyman-α full width of $\sim 3\text{Å}$ and using the 5mm beam diameter above yields a saturation power of more than 300 kW, which greatly exceeds any of the coherent Lyman-α powers generated to date.

4.5 The Ruby Pump Laser and the Choice of Dye Laser System

The scheme used to generate the fundamental beam was determined mainly by the type of laser available to pump the dye laser system (as discussion in Section 4.3). In the present experiment, the only short pulse laser available with sufficient power to efficiently pump an amplifier chain was a 1.5 Joule ruby laser (manufactured by J.K. Lasers). The ruby laser and its effect on the choice of dye laser operation are described in this section.

The ruby laser consisted of a single oscillator rod in a 0.5 m cavity (formed by a concave rear mirror and a plane, 30% transmitting front mirror). The 6943Å output was Q-switched by a krytron-triggered Pockels cell, and the measured energy could be varied between 0.8-1.5J in 30-20 ns pulses respectively (27-75 MW). The output could also be frequency doubled using an ADP crystal, which was tuned for maximum efficiency by altering the incidence angle of the ruby beam. Conversion efficiences of around 6% were obtained, giving 3471Å energies of up to 100 mJ in pulses only some 5% shorter than the fundamental beam.

The laser beam quality was poor and exhibited a multimode structure, both for the fundamental and the doubled beams. An example of the 3471Å burn pattern (produced on Polaroid film at low power to reveal the structure) is shown later in Figure 4.3. The profile was of too poor quality to employ the ruby laser in a longitudinal pumping configuration, for which a uniform beam profile was required(Mahon et al., 1979a).

Consequently it was necessary to transversely pump the dye laser system, and this restricted the choice of pump beam to the frequency doubled (3471Å) radiation since the energy density of the focussed 6943Å radiation would be too great. In any event, no frequency doubling crystal was available for use with a 7296Å dye laser system, and because of the non-linearity of the frequency doubling process, doubling of the higher intensity ruby laser radiation would be more efficient.

However, the PBD type dye that is normally used to generate 3x Lyman-α radiation (Cotter, 1979) did not have a sufficiently strong absorption band at the doubled-ruby wavelength (3471Å). When measured with a Beckman spectrophotometer, the absorption coefficients K_λ of a 4.5×10^{-3} molar solution of PBD dye (molecular weight 298) were obtained for the wavelengths shown in Table 4.2.

PBD is compared with another dye (PPF, MW 220) at the same concentration (4.5×10^{-3}M or 1 g/l). The values obtained agreed with the dye absorption spectra of Berlman (1971) to within 20%.

	K_λPBD (m^{-1})	PPF (m^{-1})
3371 Å (N_2 laser)	3400	9000
3471 Å (2xRuby)	160	4000
3648 Å (3xLyman-α)	10	15

Table 4.2: Wavelength variation of the absorption coefficient K_λ for PPF and PBD dyes

Since transversely pumped dye lasers require a narrow diameter pumped region within several hundred microns of the dye cell window (e.g. Wallenstein and Zacharias, 1980), absorption coefficients of the order of 4000 m^{-1} are required if the pump energy is to be absorbed over such distances. Table 4.2 indicates that PBD has an absorption coefficient of this magnitude only at the nitrogen laser wavelength (3371Å), while PPF dye absorbs efficiently at the double ruby wavelength (3471Å). Both dyes have low absorption at 3xLyman-α (∿ 3648Å).

PPF dye was therefore chosen for use with the doubled ruby system, there being no other dyes with efficient absorption bands at 3471Å that emit in the 3xLyman-α region (Berlman, 1971). The following sections briefly summarise the dye laser development, during which a large variety of techniques and configurations were attempted before arriving at the final system.

Figure 4.3: Pattern produced by the frequency doubled ruby laser beam when incident on polaroid film. A multimode structure is indicated by the uneven intensity and the presence of two side lobes.

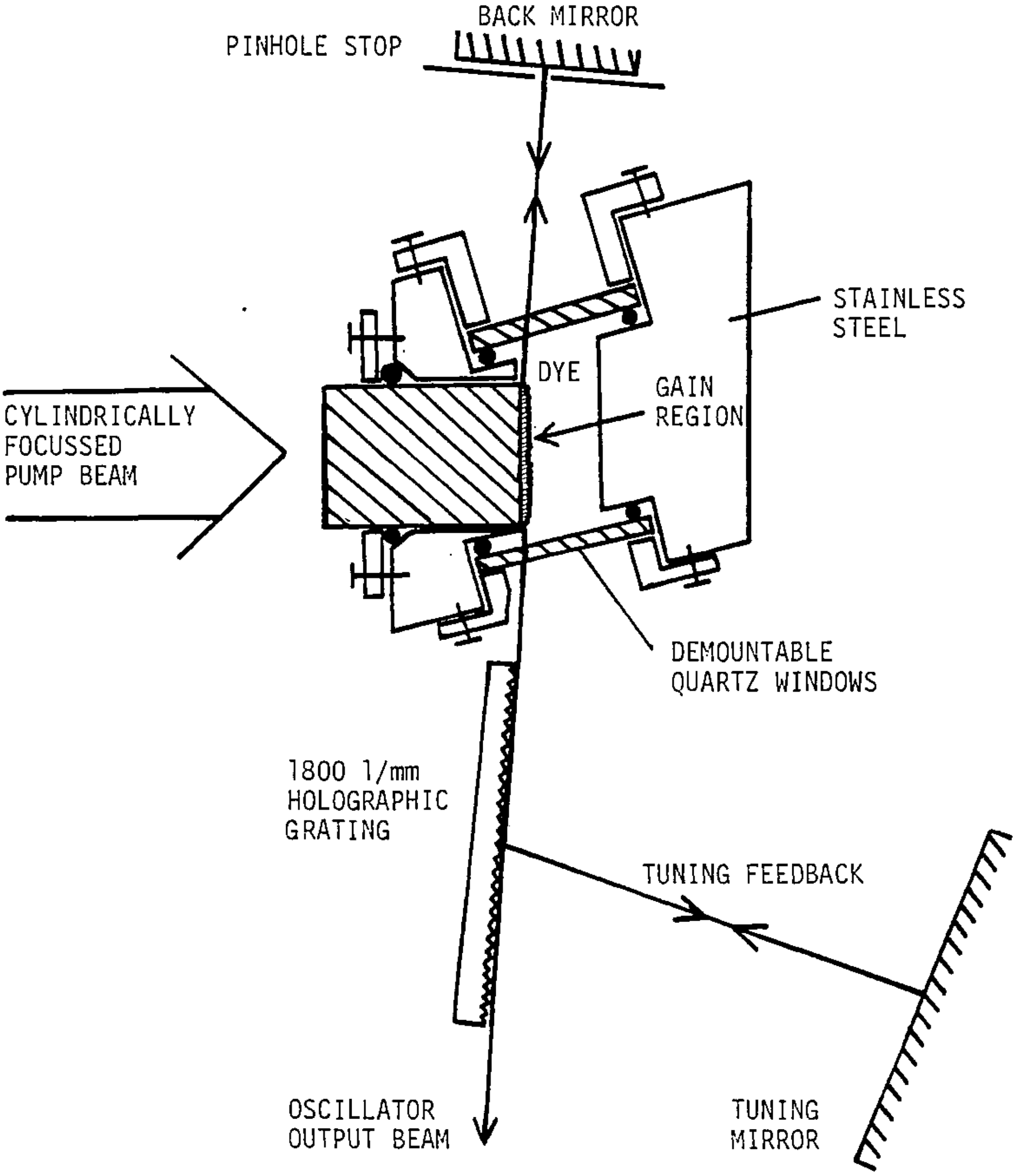

Figure 4.4: The Littman configuration dye oscillator system, employing dispersive selective feedback using a holographic grating.

4.6 The Dye Laser Oscillator

The UV dye laser oscillator was constructed in a Littman configuration (Littman and Metcalf, 1978), and was similar to other oscillators constructed in this laboratory for use in the visible (e.g. Bowen, 1982). The oscillator is shown schematically in Figure 4.4, and was based on a transversely pumped dye cell system. The pump beam was focussed into a line just behind the dye cell front window using a 150mm focal length cylindrical lens. The narrow diameter gain axis thereby produced was situated in a cavity formed by a 100% reflecting back mirror and a 100% ($\lambda/10$ flatness) tuning mirror. The dye radiation was diffracted onto the tuning mirror using an 1800 lines/mm holographic grating. The selective feedback from the grating/mirror system provided the dispersion necessary to operate the oscillator in a narrowband mode (Bandwidths of 2×10^{-2} Å were obtained by Bowen, 1982 at 5535Å). The chief advantage of the Littman system is that tuning is achieved simply by rotating the tuning mirror. The direction of the output beam (the zero order grating diffraction) then remains unchanged.

The dye cells used both for the oscillator and amplifiers were constructed of stainless steel and employed quartz windows in a demountable configuration. Teflon o-rings were used to avoid contamination since nitrile o-rings were found to release UV-absorbing impurities. The window glues employed in a non-demountable construction were found to dissolve in some solvents (e.g. toluene), and furthermore prevented regular cleaning of the windows to stop absorption of pump radiation by impurity deposits (which also caused burn marks on the front windows). The end windows were angled to avoid reflections (which may have caused unwanted feedback), and were recessed to minimise the length of the unpumped, UV-absorbing dye region.

4.6.1 The Doubled-Ruby Pumped Oscillator

The dye oscillator was initially pumped using only a small fraction of the doubled ruby beam (<5mJ) which was split from the main beam using a single reflection from a quartz prism. Lasing action was observed and the output optimised at a dye concentration of ∿1 g/l PPF in ethanol.

The tuning range of the dye oscillator was measured using a Monospek spectrograph with a reciprocal dispersion of 8.3Å/mm, and the result is shown photographically in Figure 4.5a. The longer lines shown are from the mercury calibration spectrum (at 3650.1, 3654.8 and 3663.3Å) while the shorter lines are from oscillator pulses taken at ∿13Å intervals. The tuning range was from 3638 to 3692Å, corresponding to 1213 to 1231Å at Lyman-α. Hence much of the short wavelength region in the possible tripling range (1203-1236Å) was not accessible with PPF dye. The restricted range of the PPF fluorescence is shown in the longer exposure of Figure 4.5b, in which broadband radiation due to amplified spontaneous emission was observed. A.S.E. is inherent in such high gain systems (e.g. McKee et al., 1982), and Figure 4.5b shows that the A.S.E. peak also lies on the long wavelength side of the 3xLyman wavelength (which is near the Hg 3650Å line).

Although lasing action was demonstrated using doubled ruby pump radiation, the oscillator beam quality was found to be very poor, exhibiting a vertical, two-lobe structure that was rapidly divergent. Numerous methods were employed in an attempt to improve the beam quality e.g. by altering the pump beam focus, the input energy, and the dye concentration. However no improvement was obtained, and it was concluded that the poor quality of the pump beam was contributing to the poor output beam quality.

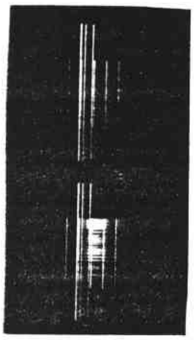

Fig 4.5 (a) Oscillator tuning range (3638-3692Å), with shots at 13Å intervals using doubled-ruby pumped PPF dye (short lines).

(b) Longer exposure showing broad band A.S.E.

Also shown is the Hg calibration spectrum (long lines, L-R: 3650, 3654, 3663Å)
Reciprocal dispersion: 8.3Å/mm
A 25% transmission filter covers the lower half of the spectra.

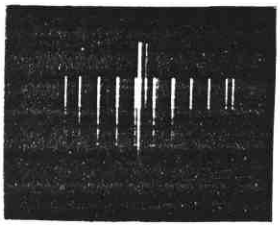

Fig 4.6 (a) Oscillator tuning range (3600-3716Å) of nitrogen-laser pumped PBD dye (reciprocal dispersion 5.5Å/mm).

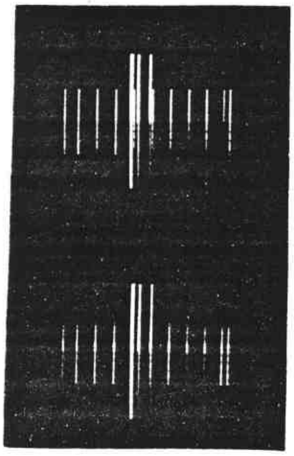

Fig 4.6 (b) Enhancement of tuned radiation due to tilting of the grating about its normal -

(c) compared to the weaker lines produced when the grating rulings are perpendicular to the laser axis.

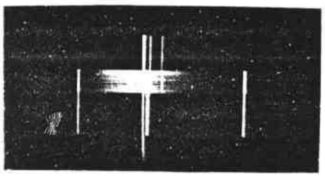

Fig 4.6 (d) Oscillator output at 3 wavelengths without the 400μm pinhole over the back mirror -

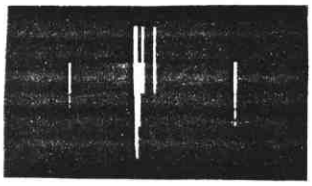

(e) and with the pinhole centred on the back mirror beam spot, showing a significant reduction in A.S.E.

Since a poor, rapidly divergent oscillator beam would made amplification difficult, and since the tripling efficiency was dependent on good beam quality, use of the frequency doubled ruby laser as an oscillator pump source was abandoned. The impossibility of using this particular doubled ruby laser to pump an oscillator/amplifier system has since been verified in the visible (at 4600Å - Drinkwater, private communication).

4.6.2 The Nitrogen Laser Pumped Oscillator

A low power nitrogen laser (0.5 mJ in 5 ns) was therefore employed to pump the oscillator, and a significant improvement was observed in the beam quality. A main "D" shaped spot was produced (along with several diffraction side lobes of much lower intensity). Use of the more efficient PBD dye was also possible at the nitrogen laser pump wavelength (3371Å). A number of solvents and dye concentrations were employed, and the maximum output of 40-50μJ (8-10% efficiency) was produced by a 1 g/1 solution of PBD in a 1:1 mixture of ethanol/toluene. By comparison, the PPF dye was only 2-3% efficient. Furthermore, the PBD dye was tunable over a much wider wavelength range (3600-3716Å) as shown in Figure 4.6a, and was limited only by the adjustment range of the tuning mirror.

Also present in the oscillator spectra was a band of A.S.E. (e.g. Figure 4.6d), which peaked at shorter wavelengths than the A.S.E. produced by PPF (Figure 4.5b). Measurements were made of the pulse energy from the oscillator, and it was found that when the tuning mirror was blocked, the pulse energy fell by only 50%. This result indicated that as much as half the output radiation may have been in A.S.E. (although the A.S.E. was apparently less visible than the tuned radiation in the spectra due to the greater A.S.E. bandwidth).

Blocking the tuning mirror may not have been a completely fair test of the A.S.E. level since tuned radiation would have reduced the gain available for A.S.E. when the mirror was not blocked. Nevertheless the possible high level of A.S.E. could have considerably reduced the efficiency of the dye laser system. Any A.S.E. produced early in the oscillator pulse could have depleted the amplifier gain available to tuned radiation (since the tuned radiation was multi-passed through the oscillator and hence arrived later in the pulse). Therefore a number of precautions were taken to reduce the level of A.S.E. in the oscillator output.

4.6.3 A.S.E. Reduction in the Dye Oscillator

The first measure in limiting the A.S.E. level was to ensure that the gain region was not overpumped, which meant reducing the pump power to just above the operating threshold (Wallenstein and Zacharias, 1980). This condition was automatically satisfied by the low power nitrogen laser since the pump power was within a factor of two of threshold.

The second measure taken was the elimination of surfaces that may have reflected radiation back into the gain region (the dye cell windows were angled for this reason). A less obvious source of reflections were the rulings of the holographic grating which also produced multiple reflections from the tuning mirror (Littman and Metcalf, 1978). Grating reflections were avoided by ensuring that the grating rulings were not perpendicular to the laser axis (i.e. by rotating the grating surface about its normal). The enhancement that this method produced in the tuned radiation (at the expense of A.S.E.) is shown in Figures 4.6b and c.

Another source of reflection was the back mirror itself, since the diameter of the gain region was finite and could sustain a number of off axis modes (corresponding to different wavelengths). Therefore a 400 μm pinhole was placed in front of the back mirror (Figure 4.4) so that the central laser spot remained unobstructed. The considerable reduction in the level of A.S.E. upon introduction of the pinhole is shown in Figures 4.6d and e.

A.S.E. can also be reduced by removing the back mirror and replacing it with an uncoated quartz flat, which allows the radiation to be coupled out of the oscillator through the quartz window (Littman and Metcalf, 1978). This scheme has the advantage that the A.S.E. only passes through the gain region once, whereas taking the output beam from the zero order diffraction allows the A.S.E. to pass through the dye cell twice. However it was found in practice that the reduced feedback from the quartz flat decreased the multipass gain in the present oscillator system, resulting in insignificant tuned output through the quartz flat. Consequently the back mirror was reinstated and the oscillator output was taken from the tuning grating.

Polarization of the output beam by the grating can sometimes be used to discriminate between A.S.E. and tuned radiation, since greater polarization would be expected for the tuned radiation (which was diffracted by the grating several times). However there appeared to be little difference between the polarization ratios in the vertical and horizontal directions (∿ 3:1), either when the tuning mirror was covered (A.S.E.), or uncovered (tuned). Hence use of a polarizer to eliminate A.S.E. was not possible in the present experiment.

All methods aimed at reducing the A.S.E. having been exhausted, the ratio of tuned radiation to A.S.E. was measured using a Monospek to disperse the radiation. With the exit slit jaws completely open and with the tuned line just covered by the jaws, the A.S.E. on either side of the tuned radiation was measured, and compared to the amount of tuned radiation obtained with the slits almost closed. Less than 20% of the total output was measured in the form of A.S.E. However, Figures 4.5 and 4.6 indicated that most of the PBD A.S.E. fell outside the fluorescent bandwidth of the PPF dye used in the amplifier stages. Hence most of the PBD A.S.E. would not have been amplified and the A.S.E. reduction was thus considered sufficient to proceed with amplification.

4.7 The Doubled-Ruby Pumped Amplifier System

The low power of the nitrogen laser meant that the doubled ruby laser was required to pump the dye amplifier system (despite the poor ruby beam quality). However the amplifiers were operated in a single pass mode whereas the oscillator was inherently a multipass system in which spatial inhomogeneities in the gain profile quickly multiplied. Hence the poor ruby laser beam profile was expected to be less detrimental to the final output beam when employed for amplifier (rather than oscillator) pumping.

The pulse length difference between the ruby laser (∿ 20 ns) and the oscillator (∿ 3 ns) resulted in a considerable reduction in the total pulse energy possible from the system. However, the peak amplified power would remain the same provided that the two pump pulses were synchronized at the ruby laser peak (hence the tripling efficiency would also remain the same). The timing of the two pulses was achieved electronically, using a delay unit to fire the nitrogen laser simultaneously with the opening of the ruby laser Pockels cell.

One difficulty that arose with this sytem was the different repetition rates for the two lasers. In order to achieve reproducible pulse energies and delay times from the nitrogen laser, it was necessary to operate at a repetition rate of 3-5 Hz. However, the maximum repetition rate of the ruby laser at peak power was only ∿ 1 shot every ten seconds (to avoid damage to the optical components). Since jitter considerably reduced the number of successfully synchronized shots, the alignment and development of the oscillator/amplifier system was considerably hindered.

4.7.1 Synchronization of Oscillator and Amplifier Pulses

A severe problem was therefore the accurate timing of oscillator and amplifer pulses so that the tuned radiation arrived at the peak of the amplifier population inversion. The importance of pulse coordination was shown by McKee et al. (1982), who found that mistiming of the pulses caused a deterioration in the spectral purity of the amplified output. If the oscillator pulse arrived too late, the A.S.E. inevitably present in the leading edge would deplete the amplifier gain prior to the arrival of the multipass tuned radiation. Arrival too early would result in the oscillator pulse missing the gain peak altogether. Since pulse coordination due to jitter in this system was found to be difficult, much effort was spent on pulse synchronisation (to ensure spectral purity) as is described below.

4.7.1.1 Identification of the Population Inversion Peak

The first requirement was the determination of the peak in the amplifier population inversion. Figure 4.7 shows the time history of the frequency doubled ruby laser pulse, and the fluorescence pulse produced by focussing the pump pulse into the amplifier dye. The sum of these two pulses when simultaneously incident on the fast photodiode detector is also shown.

The fluorescence pulse was observed to be shorter and to peak just before the peak of the pump radiation. This behaviour can be explained as a result of the rapid build up in the population inversion in the initial stages of the pulse. Spontaneous emission then occurred (the dye lifetime was $\sim$ 1.6 ns), and stray reflections along off-axis modes through the high gain region are thought to have caused the population inversion to be rapidly depleted. Pumping of the dye still continued and although a steady state may have been reached (e.g. the plateau region later in the fluorescence pulse), the amplifier gain remained low. This behaviour was verified

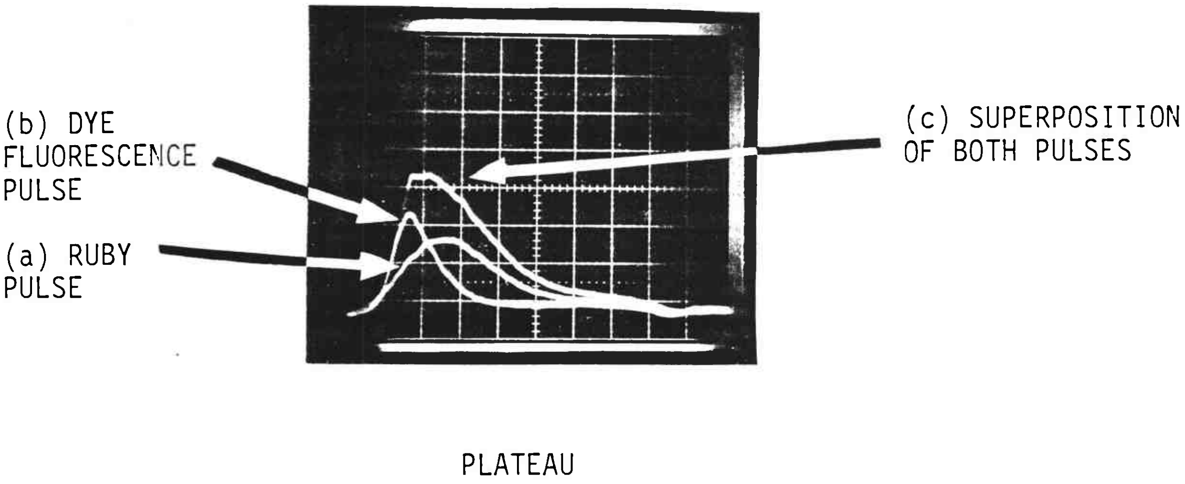

Fig 4.7 (a): Frequency doubled ruby laser pump pulse (10nS/DIV).
(b): Dye amplifier fluorescent output.
(c): (a) and (b) superimposed, indicating gain depletion by A.S.E. during the later part of the pump pulse.

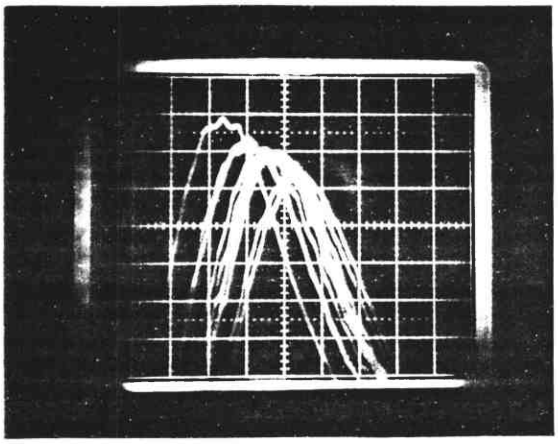

Fig 4.8: Jitter in the ruby laser pulse over 10 shots revealing the relation of the delay to the pulse intensity (10nS/DIV).

experimentally since it was found that the maximum amplification occurred only when the oscillator pulse arrived at the fluorescence peak.

Depletion of the gain by A.S.E. was reduced by decreasing the power density in the dye cell and hence the gain per unit length. The power density was decreased firstly by softening the focus of the pump beam to increase the height of the pumped region, and secondly by simultaneously decreasing the dye concentration to allow a greater penetration depth of the pump radiation into the dye cell. The increased volume of the gain region was then matched by an increase in the area of the beam from the oscillator. This was achieved by placing the amplifier ∿ 0.5 m from the oscillator, thereby using the inherent beam divergence to expand the beam area to ∿ 1 mm.

The defocussing of the doubled ruby beam was however limited by the height of the pump beam (itself only a few millimetres). Optimum results were then achieved using a PPF dye concentration of 1/3 g/l in ethanol. The maximum output of ∿ 0.3 mJ in ∿ 3 ns (100 kW) represented an amplifier gain of ∿ 6-8. This result was roughly consistent with the PPF pumping efficiency of ∿ 2% and with the energy loss due to the pulse length mismatch.

4.7.1.2 Elimination of Jitter between Oscillator and Amplifier Pulses

However, the dye laser output fluctuated widely, with only about 20% of shots attaining the maximum value. This fluctuation occurred despite efforts to reduce the jitter in the two pump laser pulses e.g. by triggering the Pockels cell krytron tube directly from the delay unit. There was an inherent jitter of ± 3 ns in the nitrogen laser, but the jitter in the ruby laser pulse was much greater (± 10 ns). This was found to be a characteristic of the Q-switched operation, for although the Pockels cell opened reproducibly, the higher intensity ruby pulses were emitted more quickly (perhaps due to the higher gain present in the rod). This behaviour is clearly shown in Figure 4.8

where, over ten shots, a greater delay was observed for the less intense pulses.

The ruby laser system was then run at its highest possible power as this was found to produce the minimum jitter. However degradation of the ruby output power then occurred due to heating of the rod, and hence a low repetition rate was necessary (∿ 0.1 Hz). Even under these conditions the total ruby and nitrogen laser jitter was greater than 10 ns. This reduced the fraction of successfully synchronized shots to ∿ 20%. Hence the interval between dye laser pulses was around one minute, which greatly hindered the alignment and optimisation of the system. The limitations imposed by the low repetition rate on the development of the Lyman-α source can be realised when a comparison is made with the repetition rate of the excimer system used by Cotter (∿ 10 Hz) - some 10^3 times faster.

4.7.2 Amplifier Saturation and Single Amplifer Operation

With the jitter between the oscillator and pump laser thus minimized, the entire doubled ruby laser output was used to pump one amplifier. It was found that the amplifier-gain was saturated i.e. a fractional reduction in the oscillator output did not produce a corresponding reduction in the amplified output. The occurrence of saturation was verified by spectra taken of the amplified output, which showed that many apparently successful shots consisted primarily of A.S.E.. This indicated that even the low ($<$ 20%) level of A.S.E. present in the pre-pulse was saturating the amplifier. To ensure that only the larger proportion of tuned radiation in the main pulse caused the amplifer to saturate, a 12% transmission filter was placed between oscillator and amplifier. The result was the production of tuned pulses with energies still of ∿ 0.3 mJ (∿100 kW). However, the influence of the poor pump beam quality on the output beam was still apparent, with distortion of the oscillator beam occurring despite alteration a large

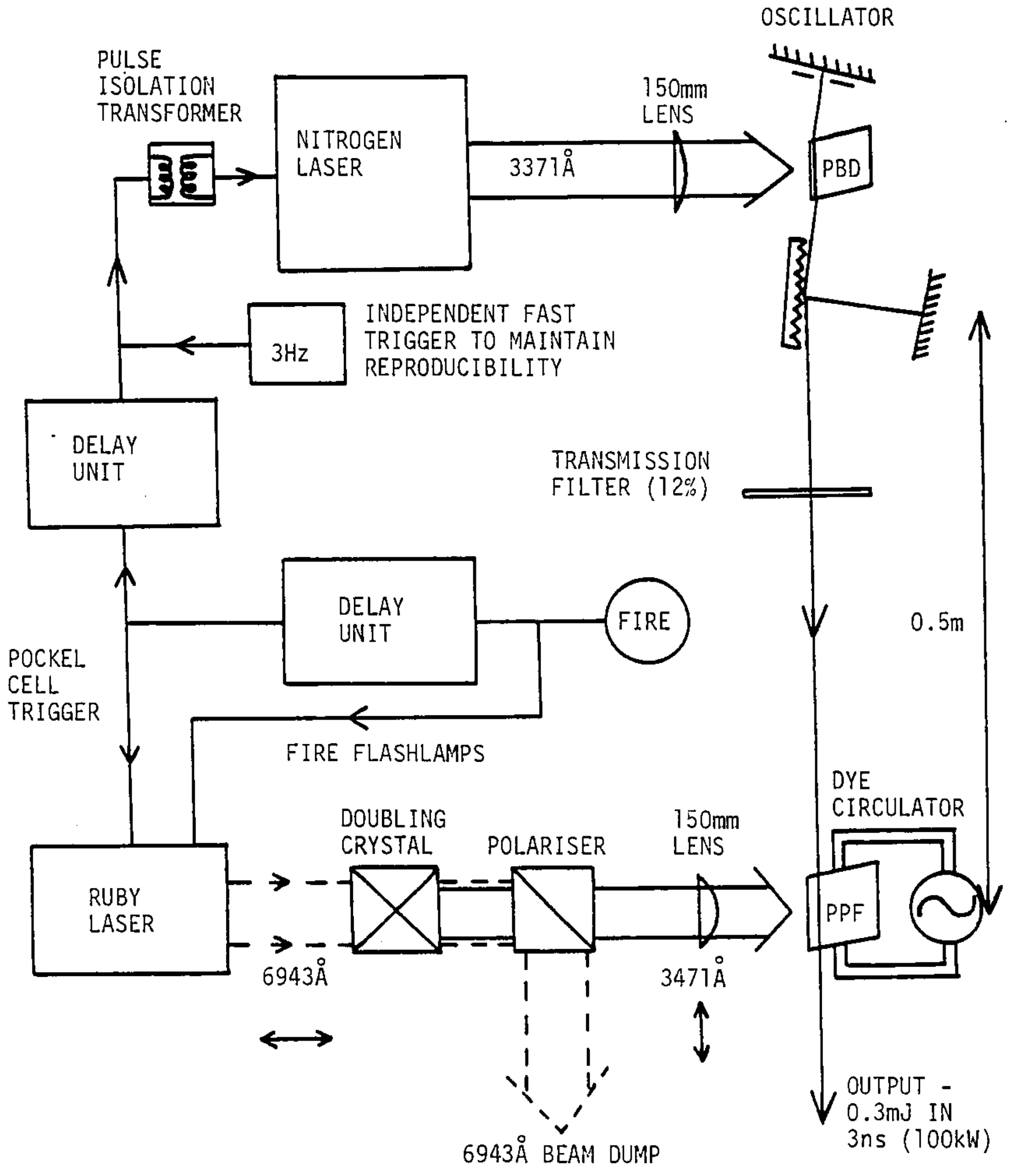

TUNING RANGE OF DYE LASER 3620-3700Å (5.5Å/mm)

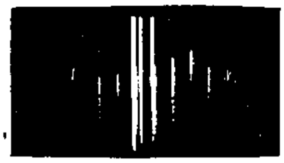

Figure 4.9: Final configuration of the dye laser system, showing the trigger circuit for the synchronisation of the two pump laser beams.

number of parameters (such as pump beam focussing, pulse delay, dye concentration and distance between oscillator and amplifier).

Since the gain was saturated using the full pump power of the doubled ruby laser, no advantage was to be gained by splitting the pump laser output into two amplifiers. (However the high energy deposition necessitated circulation of the amplifier dye to prevent dye degradation and beam refraction due to the heating of the dye.) Therefore a single amplifier stage was employed in the final dye laser system, which is shown schematically in Figure 4.9.

4.8 Generation of Lyman-α Radiation

The achievement of even 100 kW of UV dye laser power suggested that detectable levels of Lyman-α radiation could be produced by frequency tripling. Using similar UV powers, Cotter (1979) produced a Lyman-α output of ∿ 10^7 photons (or 4 mW) per pulse, which was readily detected by a monochromator/photomultiplier system.

4.8.1 The Krypton Tripling Cell

In order to carry out a frequency tripling experiment, the krypton cell in Figure 4.10 was constructed. It consisted of a 200 mm glass cell with aluminium mounts at each end to position the focussing optics. A 50 mm quartz lens was used (similarly to Cotter, 1979) to focus the dye laser radiation. The lens was located on a sliding tube to allow alteration of the focus. The tripled radiation was collimiated by a MgF_2 lens of 102 mm focal length (measured by Harris, private communiction). A pumping port allowed evacuation to below 10^{-5} torr, and the krypton pressure was monitored using capsule dial gauges.

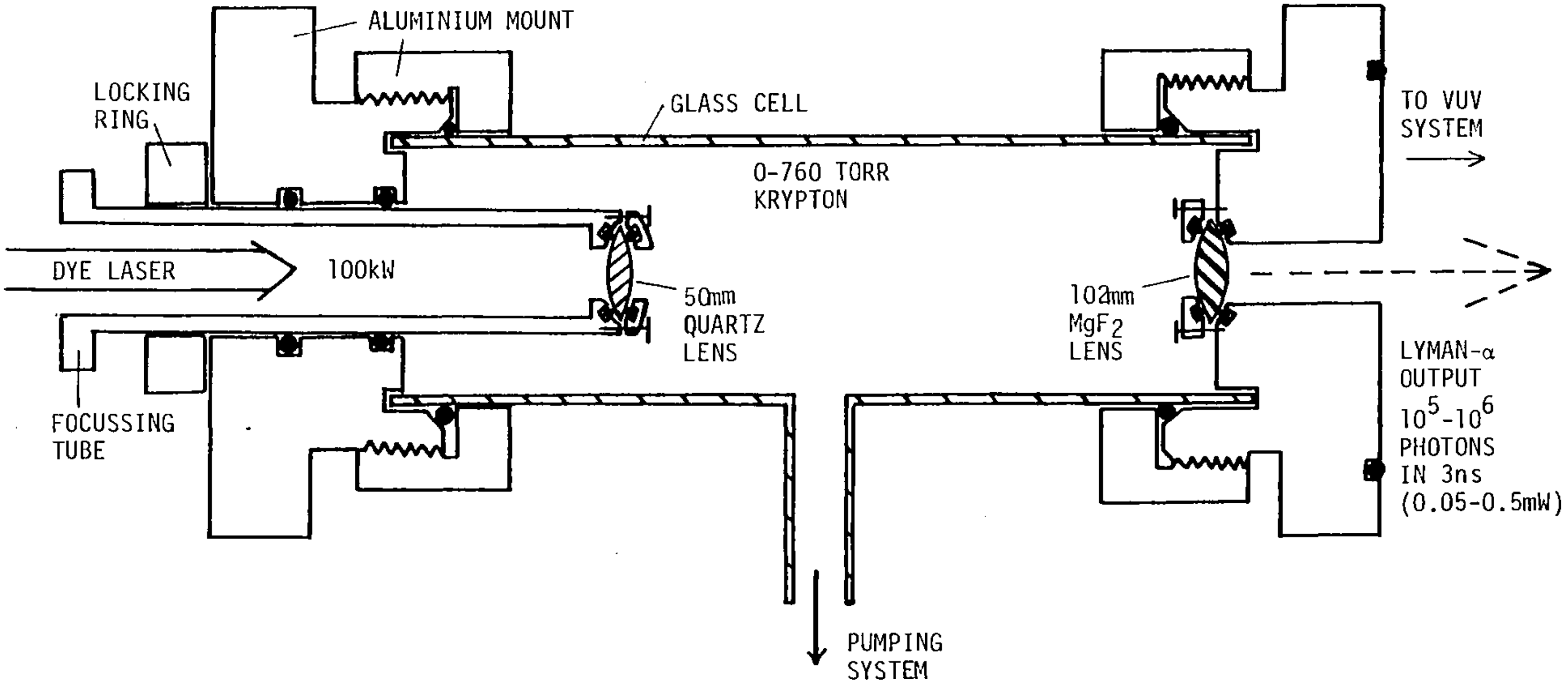

Figure 4.10: Krypton filled tripling cell for frequency conversion of the UV dye laser radiation to Lyman-α wavelengths.

4.8.2 Windows for VUV Transmission

Consideration was also given to the way in which the VUV radiation could be introduced into the pinch discharge vessel (which was itself at a pressure of several torr). A number of schemes were considered.

4.8.2.1 Crystal windows

MgF_2 and LiF are the only solid materials that transmit efficiently at Lyman-α, with efficiences of at least 50% guaranteed by the manufacturer (Harshaw) for windows of 2mm thickness. However LiF suffers from hygroscopic degradation, and there was also the risk of further contamination to both types of windows by impurities from the pinch discharge.

4.8.2.2 Capillary Arrays

Multichannel glass capillary arrays (of up to 50% open area) have been used previously for VUV measurements of extended sources (Lucatorto et al., 1979), and can be differentially pumped to produce an evacuated region between source and detector. However, capillary arrays have not been applied to small (several mm) diameter laser probe beams. A limitation therefore not mentioned by Lucatorto et al. is that significant diffraction of the transmitted light occurs from the capillary array. An example is given in Figure 4.11 for an array of 50μm diameter capillaries (2 mm long) illuminated by an argon ion laser, the pattern shown occurring at a distance of 1 m from the array. The first ring of six diffraction spots from the centre of the pattern corresponds to a divergence of 2 mrad at Lyman-α wavelengths, which greatly increases the overall laser divergence. Considerable energy is also diffracted into the further spots, each of which would be diffracted in turn by the array on the output side of the pinch. The loss in energy and in spatial resolution, combined

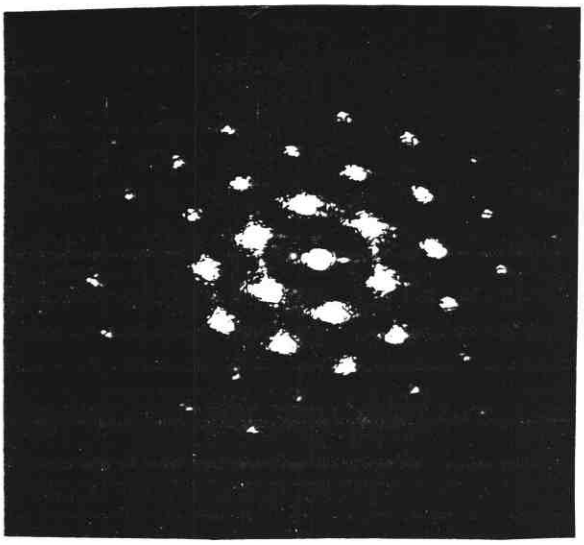

Figure 4.11: Diffraction pattern produced 1 metre from an array of 50μm diameter, 2mm long capillaries illuminated by a 4880Å cw argon ion laser.

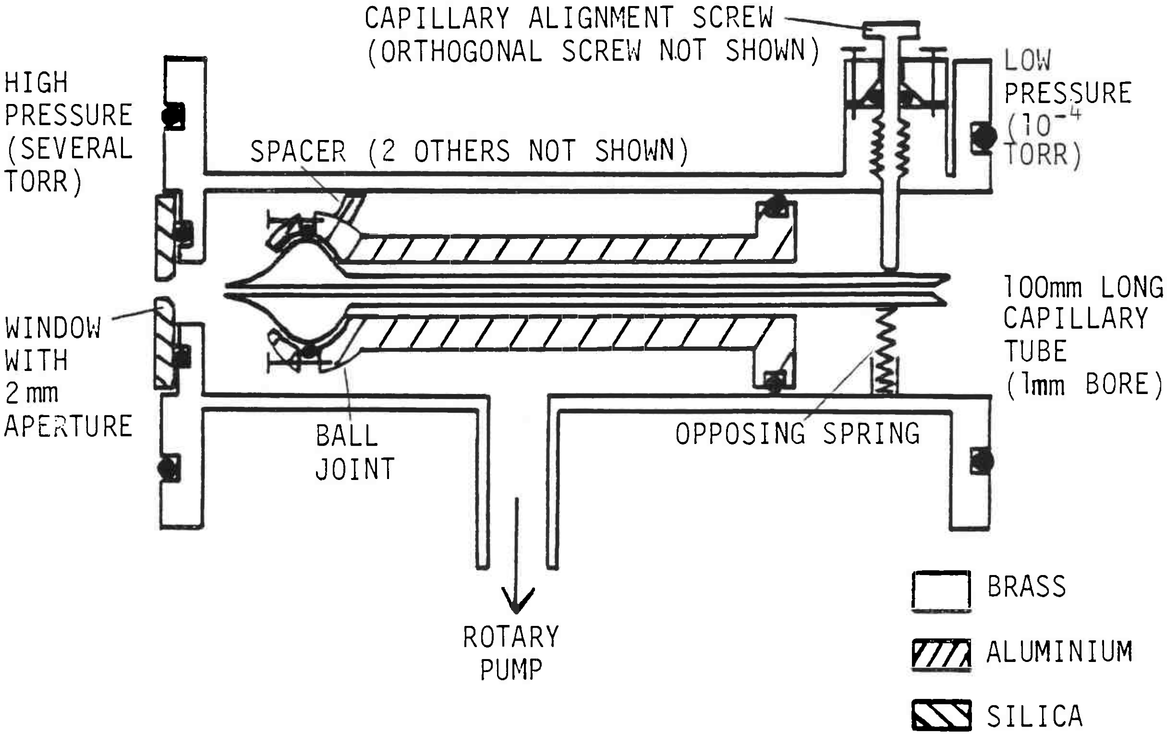

Figure 4.12: Single capillary differential pumping system for use with the coherent Lyman-α source, including adjustment for aligning the VUV beam path.

with the possible damage to the micropore structure by the discharge, made application of multiple capillary arrays impractical in the present experiment.

4.8.2.3 Single Capillary, Differential Pumping System

Consequently, a single capillary differential pumping system was designed as a VUV input port for the pinch discharge vessel (the output from the pinch was intended to pass through the differentially pumped slits of the VUV monochromator described in more detail in Chapter 5). The design finally evolved for the input port is shown in Figure 4.12, and was constructed to fit directly onto the tripling cell. The pressure differential was maintained by the 1 mm bore capillary tube, whose 100 mm length was sufficient to hold off a filling pressure of 2 torr while maintaining 4×10^{-4} torr at the high vacuum end (evacuated using a diffusion pump). Since the capillary conductance was proportional to the fourth power of the capillary bore, it was important to keep the bore as small as possible. Optical alignment was then difficult, so the capillary was mounted on a ball joint at the z-pinch end of the tube, with screws allowing for fine adjustment at the other end.

4.8.3 The Lyman-α Detection System

For the initial Lyman-α testing however, the tripling cell was mounted directly onto the entrance slit of the VUV monochromator. The monochromator was employed to provide an estimated 10^{-4} - 10^{-5} rejection factor for the 3648Å signal from the Lyman-α radiation. Further rejection was achieved using the solar blind photomultiplier described in Chapter 5, which had a specified 20% quantum efficiency at Lyman-α and a 10^{-2}% quantum efficiency at 3648Å. The 5×10^{-4} photomultiplier rejection factor was supplemented by use of an Acton research Lyman-α filter, with a guaranteed 10% transmission at Lyman-α and a measured transmission of 5×10^{-2}% at 3648Å. The total rejection of 10^{-9} to 10^{-10} was therefore sufficient to discriminate between the 3648Å and 1216Å signals, given the expected tripling efficiency of ∿ 6×10^{-8} (scaled from Cotter's results and the P_1 dependence of the Lyman-α power).

4.8.4 Tests for VUV Generation near Lyman-α

The following tests were used to demonstrate the generation of VUV radiation near Lyman-α:

1) The krypton cell was evacuated and the monochromator slits were completely opened. No signal from the 3654Å dye laser was detected.

2) Krypton was introduced gradually into the tripling cell. At a pressure of ∿300 torr, a signal was detected (simultaneously with firing of the dye laser) from the monochromator/photomultiplier system centred at around 1218Å. No gas breakdown was observed.

3) The signal disappared when the monochromator was tuned away from the Lyman-α region.

4) The signal also disappeared when a glass slide (measured be to transparent to 3 x Lyman-α radiation) was introduced between the monochromator entrance slit and the grating.

The above tests therefore proved that VUV radiation had been generated near Lyman-α using the dye laser/tripling cell system. However, the signal was extremely irreproducible, with only ∿ 10% of the laser shots producing measurable signals. The reproducibility was therefore less than for the successful generation of synchronized dye laser pulses (∿ 20%), although greater fluctuation in the tripled output was expected due to the non-linearity of the frequency conversion process.

4.8.5 Estimate of the Lyman-α Flux

The Lyman-α radiation pulses produced a considerable variation in the measured photomultiplier signals, with up to 200 mV being recorded using 100 μm slits, while the majority of signals were between 20 and 50 mV. With a knowledge of the photomultiplier gain (specified at $6\text{x}10^6$) and an estimate of the losses in the system, the total Lyman-α flux could then be approximately determined.

The 200 mV maximum voltage was observed using a 50Ω terminator, and the 4 ns pulse length therefore gave a total collected charge of 1.6×10^{-11}C at the anode. The photomultiplier gain of $6\text{x}10^6$ implied that 20 photoelectrons were produced at the photocathode, which with 20% quantum efficiency, 50% MgF_2 side-window transmission and 10% Lyman-α filter transmission represented 2000 photons through the exit slit. Since the grating was blazed at Lyman-α the grating efficiency may have been as high as 50%, giving 4000 photons through the 100 μm entrance slits. Assuming that the VUV beam diameter was of the same order as the beam diameter of the dye laser ($\sim$ 5mm), the total Lyman-α flux was therefore $\sim 2\text{x}10^5$ photons per pulse. Given the uncertainty in estimating the efficiency of the detection system, an order of magnitude approximation for the flux was thus $10^5 - 10^6$ photons per pulse.

4.8.6 Explanation for the Low Tripling Efficiency

In comparison to the estimated 10^5-10^6 VUV photons/pulse produced in the present experiment, Cotter (1979) achieved $\sim 10^7$ photons/pulse using a dye laser of similar power (100 kW). One immediate explanation for the lower efficiency in the present experiment was the poor beam quality of the dye laser, due to the inhomogeneous pump laser radiation. Cotter, on the other hand, managed to achieve an almost circular, near diffraction limited beam spot.

Alternatively, the 100 kW dye laser output produced in the present experiment may not have consisted entirely of tuned radiation. Although the pressure tuning curves of Figure 4.1 indicate that efficient tripling may occur over a small range of wavelengths, any tripled A.S.E. falling outside this range would not contribute to the VUV output, thus lowering the tripling efficiency.

The VUV output did indeed exhibit a broadband character (some 3-5Å), although with the 100 μm slits the resolution was $\gtrsim$ 1Å. The wavelength of maximum output was observed to decrease at higher pressure, thereby indicating the presence of a tuned component (although the poor reproducibility of the source prevented any quantitative estimate of the tuned fraction). Despite the fact that blocking of the tuning mirror was not a fair test of the A.S.E. level (as mentioned previously), some VUV signal did remain when the mirror was blocked, although at much lower levels ($\sim$20 mV) than with the oscillator tuned.

The above tests thus indicated that some broadband phase-matching had occurred. Hence it was possible that a considerable proportion of the dye laser power was in the form of A.S.E. (although the tuned radiation was more prominent in the amplifier spectrum of Figure 4.9 due to the greater intensity/wavelength interval). Any A.S.E. that was outside the range of wavelengths for which efficient phase-matching was possible would not have contributed to the VUV output. The fractional VUV reduction would have been equal to the cube of the fraction of the dye laser output occurring as unmatched A.S.E. This, together with the poor dye laser beam quality, may explain the low efficiency of the tripling process observed in the present experiment.

4.9 Evaluation of the Coherent Lyman-α Source for an Absorption Experiment

Attempts were made to transmit the Lyman-α beam through the pinch discharge vessel, but without success. Impurity absorption was an unlikely explanation for the lack of transmission since a cold trap and rotary pump were used to evacuate the vessel below 10^{-2} torr.

The Lyman-α beam may not, however, have been correctly centred on the slits, despite use of the dye laser beam for alignment. However, the different refractive index for MgF_2 at 3648Å compared to 1216Å caused the 3648Å beam to diverge, making alignment difficult. Further, the refractive index difference may have caused the VUV beam direction to differ from the dye laser alignment. The extremely poor reproducibility and low frequency of successful Lyman-α pulses made systematic alignment impossible, and random adjustments of the beam were unsuccessful.

In any event, when the 100μm slits employed in the coherent Lyman-α radiation measurements were also employed to measure the pinch emission, the pinch emission completely saturated the photomultiplier. The coherent Lyman-α radiation was therefore unsuitable as an absorption source due to:

1) Insufficient power
2) Poor reproducibility
3) Severe alignment difficulties
4) A.S.E. contributions to broadband output.

However, the use of a tunable UV dye laser, frequency upconverted in a krypton tripling cell to produce coherent Lyman-α radiation, had been successfully demonstrated.

CHAPTER 5

LYMAN-α EMISSION LINESHAPE STUDIES

5.1 Introduction

Since the coherent Lyman-α source was not sufficiently powerful to carry out absorption profile measurements, a study was made of the Lyman-α lineshape in emission. The instrument used was a 1 metre VUV monochromator with a normal incidence, 1200 lines/mm grating blazed at 1200Å. The same system was employed by Baker, but a different photomultiplier detector was used. The present photomultiplier detector was coupled to a Tektronix 7912 AD transient digitizer to allow signal processing of the emission traces. All profiles were taken side-on for direct comparison with Baker's results and to minimise the effects of continuum opacity.

5.2 Monochromator and Detection System

The monochromator was mounted in a vacuum tank which could be evaluated to 5x10^{-6} torr, and was equipped with a cold trap to eliminate volatile, absorbing gases such as H_2O. The exit and entrance slits were located in separate side arms which could be coupled to the photomultiplier detector housing and the z-pinch vessel side-arm tubes respectively.

The z-pinch vessel was isolated from the ~~vacumm~~ Vacuum monochromator by means of a specially constructed differential pumping system (Figure 5.1). The system consisted of an aluminium tube (of 5mm bore) which was threaded on the outside to allow controlled placement of the carefully machined end-face flat against the slits. The tube could then be rotated a known amount to give a 5-10 µm clearance from the slits.

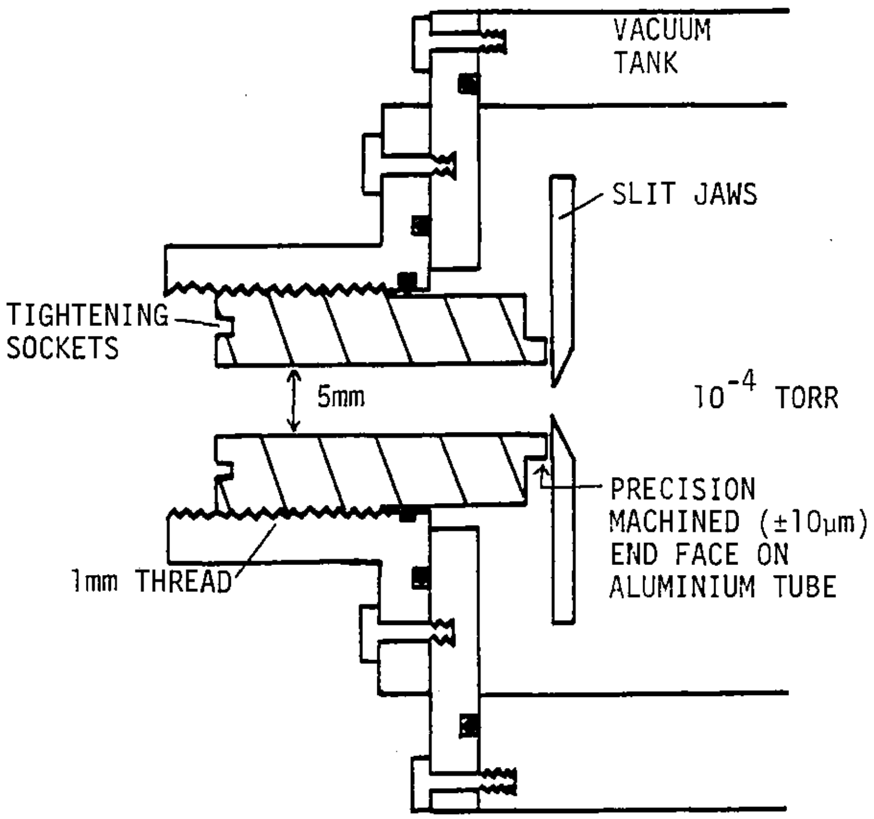

Figure 5.1: Differential pumping system for z-pinch side-arm/ monochromator attachment.

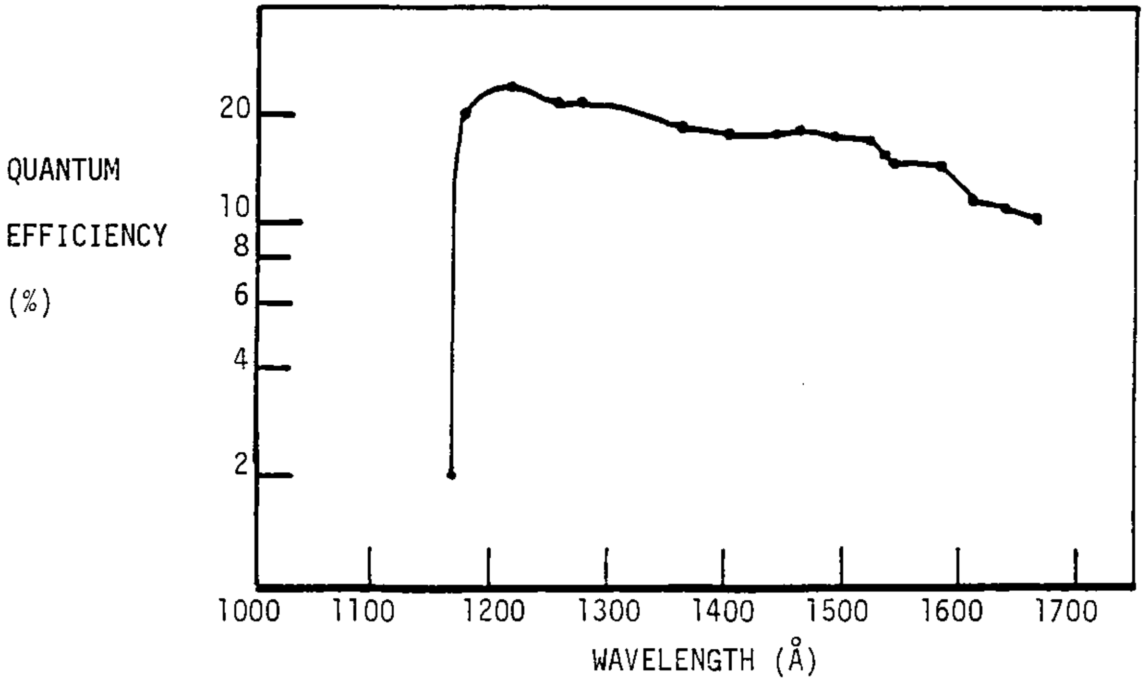

Figure 5.2: R1259 photomultiplier wavelength response (as supplied by Hammamatsu).

This mechanism enabled free movement of the slit jaws and at the same time minimized the flow of gas from the z-pinch discharge vessel to the monochromator. With the vessel evacuated to its base pressure of 10^{-2} torr, the entire monochromator and detector system remained below 10^{-5} torr. At 1 torr Ar/H in the vessel the vacuum tank pressure remained below 4×10^{-5} torr with the slits closed, and below 8×10^{-5}torr with the slits opened to 10 µm (the usual setting). At the highest filling pressure (5 torr) using the largest slit width (25 µm), the tank pressure was just over 10^{-4} torr. This pressure was low enough to allow sufficiently fast exhaust of any gases, thereby preventing absorption of VUV radiation over the 2m path length through the monochromator.

The photomultiplier employed was a Hammamatsu R1259 solar blind side-on type with a CsI photocathode and MgF_2 window. The photocathode had a very high quantum efficiency at Lyman-α (∿ 24%) allowing the use of narrow slit widths to give better resolution. The response curve between 1100 and 1700Å is shown in Figure 5.2 (as supplied by the manufacturer). The photocathode was also blind to longer wavelength radiation (having a quantum efficiency of 10^{-2}% at 3650Å) and was thus able to discriminate against any visible or near UV radiation scattered inside the monochromator. The dark current was very low (measured at 10 pA) when the photomultiplier was mounted in a specially constructed housing attached to the monochromator vacuum system. At the operating dynode voltage of 1.25 kV the current gain was 6×10^{6}. The linearity with respect to pulses as long as the pinch emission was checked by placing a calibrated (32% transmission) wire gauze filter (mesh spacing 100 µm) between the photomultiplier and the exit slit. At the 1.25 kV operating voltage the photomultiplier response was linear up to an output of 500 mV into a 50Ω terminator (10 mA), and saturated completely at 1.5 V output.

The photomultiplier output was fed to a Tektronix 7912 AD transient digitizer using solid-copper shielded coaxial cable to reduce electrical pick up. The noise attenuation of the solid coax was measured at 8 dB better than normal braided coax. The improved noise attenuation was essential since 15 metres of cabling was needed to reach the Tektronix system. The shielding was necessary not only to improve the signal-to-noise ratio of the emission traces, but also to eliminate any noise spikes from the electrical discharge which, it was found, would otherwise interrupt the data handling programmes.

The principle use of this data recording system (apart from conveniently handling large numbers of records) was to reduce uncertainty in the data by signal averaging. Statistical noise was present in the emission traces and in most cases was a greater source of uncertainty than the < 5% shot-to-shot reproducibility of the pinch emission itself. Hence it was advantageous to average the emission traces over a number of shots, thereby reducing random noise fluctuations as well as the shot-to-shot variations. A standard signal averaging programme was modified to allow removal of temporal jitter by horizontal displacement of the emission traces. The traces were matched so that the rising and falling edges of the emission peaks were superimposed. An example of three shots (the usual number taken at each wavelength) is shown in Figure 5.3 a-c, and the signal averaged trace is shown in Figure 5.3d.

5.3 Monochromator Calibration

Following initial alignment in the near UV (performed by optimising the resolution of the mercury 3131Å doublet), the monochromator was focussed in the VUV using emission lines from a water cooled, hollow

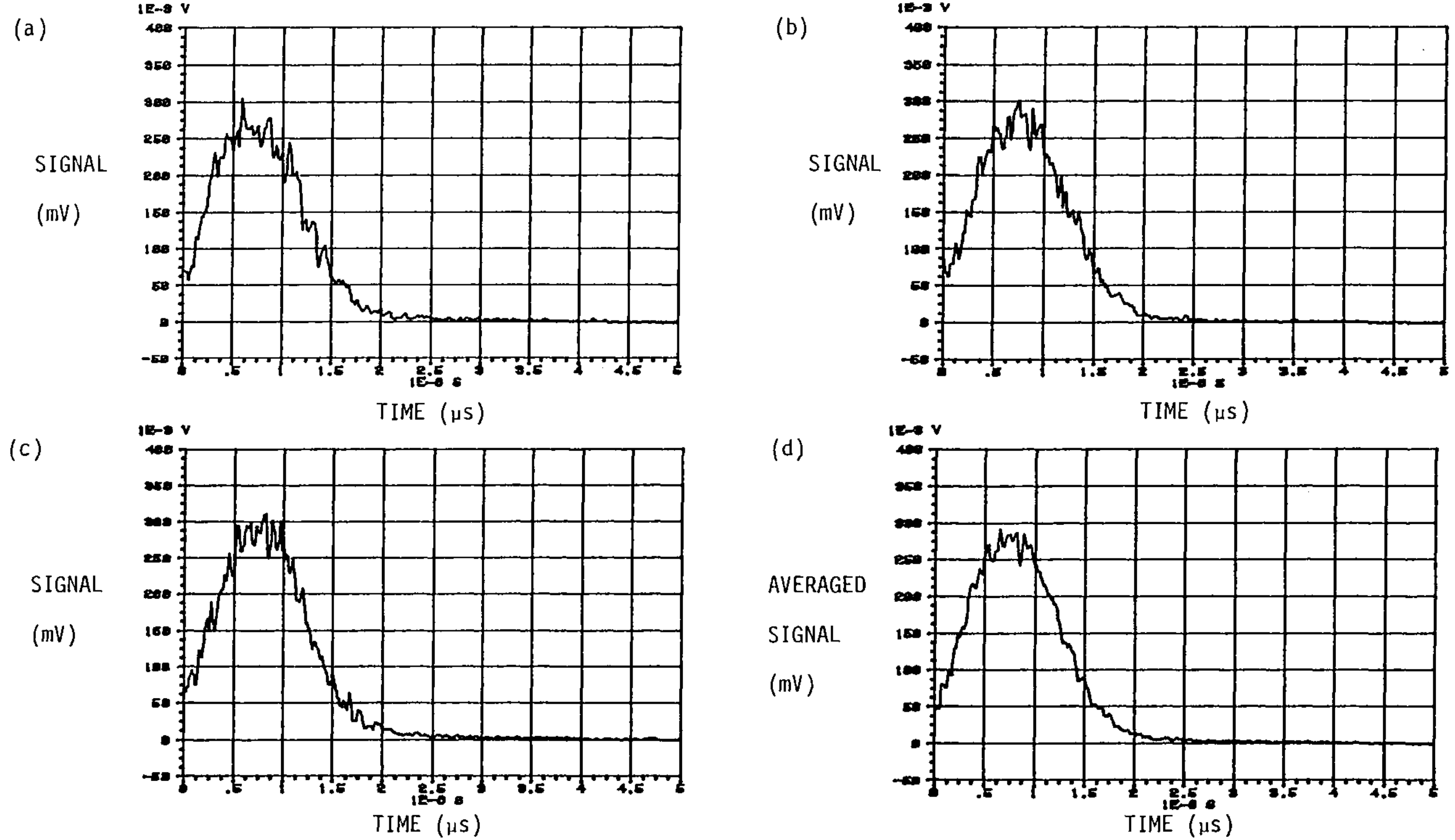

<u>Figure 5.3</u>: (a-c) Digitized emission traces for 5kV, 1 torr at 1250Å and (d) their computed average.

cathode discharge (Sommer, 1982).

The discharge was run in argon at 0.3 torr pressure, although small impurity levels of nitrogen enabled the NI standard lines at 1199.549, 1200.224 and 1200.711Å to be used for calibration. The pressure broadened widths of these lines in the hollow cathode discharge were negligible, and the Doppler widths (<0.01Å for ∿ 1000K) were also unresolvable. Increasing the discharge current from 100 to 250 mA produced no observable effect on the linewidths. The monochromator was then focussed by minimising the widths of these three standard lines. An example of the focussed profile (scanned using a stepper motor drive) is given in Figure 5.4.

The opening positions of the slits were first determined by adjusting the slit jaw micrometer (with the vacuum tank open) until an increase in the transmitted light was observed. This opening position also corresponded to an increase in vacuum tank pressure (with the tank closed), as test gas from the z-pinch vessel entered the monochromator chamber. The slit widths indicated on the micrometer were also verified (to a resolution of 10 μm) using a microscope with a calibrated graticule.

The instrument width for 10 μm slits (as measured from the NI line profiles) was 0.17 ± 0.01Å, while for 20 μm slits the instrument width was 0.23 ± 0.02Å. Since the reciprocal dispersion of the monochromator was 8.4Å/mm, the increase in the instrument width for a 10 μm slit width incease was ∿ 0.08A (assuming no other source of broadening e.g. defocussing), which is within the uncertainty limits above. The measured instrument profiles indicated a further residual instrumental width of ∿ 0.08Å when the slits were fully closed. Increasing the slit widths to 50 μm caused the NI lines to merge, with the result that the instrument width became difficult to resolve.

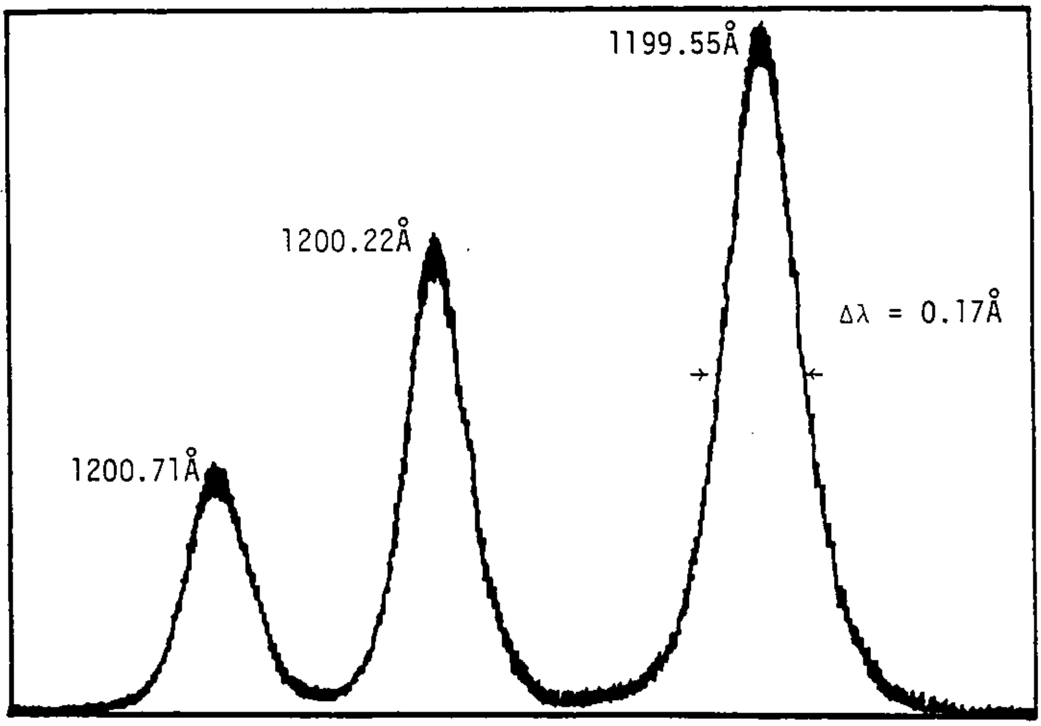

Figure 5.4: Monochromator instrument profile for 10μm slits using the NI standard lines from a hollow cathode discharge.

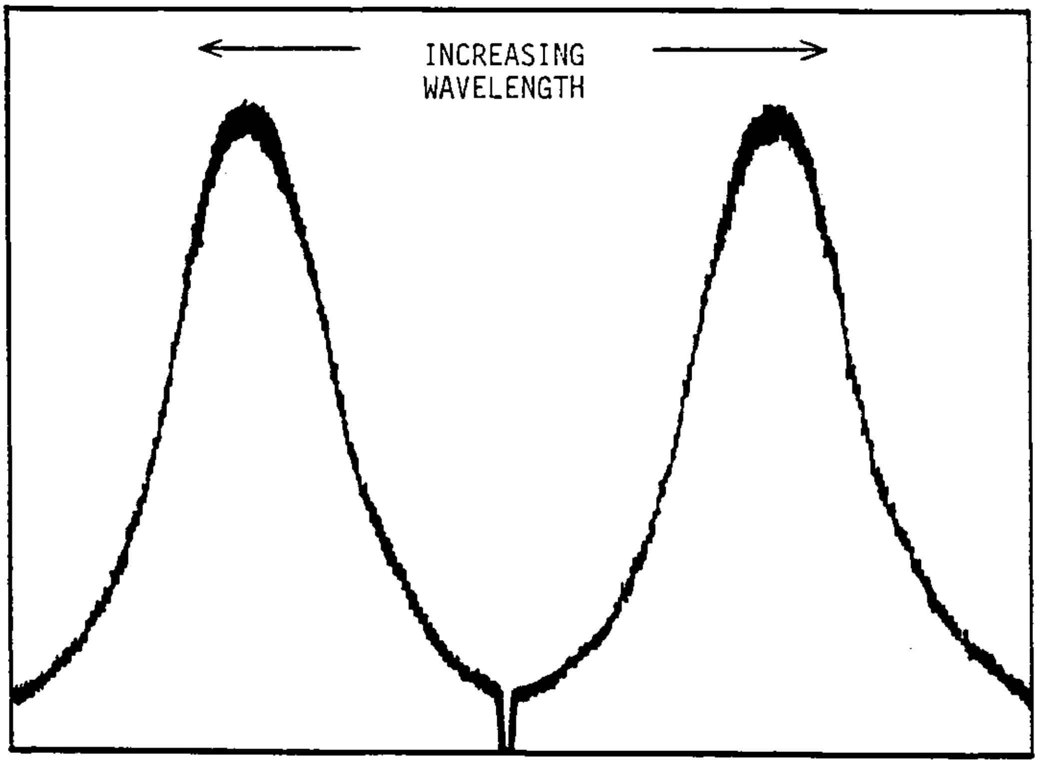

Figure 5.5: Wavelength scans in opposite directions of the Lyman-α line from the hollow cathode discharge.

The monochromator wavelength scale (as measured by a geared counter connected to the grating stepper-motor drive) was calibrated initially using a quartz-envelope mercury lamp in the near UV. This calibration gave a result of 1.053 counter units per Ångstrom, a value which was verified exactly from the position of the nitrogen lines. When moved to 1215.7Å the monochromator also detected a Lyman-α profile due to a residual hydrogen impurity in the argon. With no nearby lines contributing to the Lyman-α lineshape, an exact superposition of scans in the short and long wavelength directions showed that there was no asymmetry in the instrument profile (Figure 5.5).

5.4 Lyman-α Emission Profile Measurements

Emission profile studies were carried out at three conditions, all using the same bank voltage of 5 kV. Included were conditions corresponding (a) to Baker's experiments i.e. n_e=1.9x10^{24}m^{-3} and T_e = 2.0eV (obtained using a filling pressure of 5 torr in the present experiment); (b) to the highest diagnosable densities in the present pinch (7.8x10^{24} m^{-3} and 3.0 eV at 1 torr); and (c) to an intermediate density (4.6x10^{24}m^{-3} at 2 torr for which an intermediate temperature was assumed of ∿2.5eV).

The lineshape at each condition was scanned from shot-to-shot. Three traces were taken for each point at intervals of ∿ 1Å over a region ± 48Å from the 1216Å line centre (which was marked by a strong self absorption dip due to cold hydrogen in the outer side-arms of the pinch). It was found necessary at the beginning of each run to fire cleaning shots with the slits open to avoid depositing debris on the narrowed slits (which would then reduce the amount of light transmitted). When this precaution was taken, no systematic variation in the emission levels occurred over several tens of shots tested at the same wavelength setting. Further, because each profile required some four hundred or so shots with wavelength increments of ∿ 1Å, a monitor of the emission at a given wavelength was taken every 50-100 shots to detect any long term drift in the emission levels over each day-long experiment.

5.4.1 Lyman-α Profiles at the Highest Diagnosed Density (n_e=7.8x10^{24}m^{-3}; T_e = 3.0eV).

A number of profiles were taken at the highest density conditions (using 5 kV and 1 torr), with scans taken in both increasing and decreasing wavelength directions using 10 μm slits. Two extended profiles (measured at peak compression) are shown in Figures 5.6a and 5.6b. The two scans were initiated 0.5Å apart to ensure complete coverage of the spectrum (to ± 48Å from Lyman-α).

The Lyman-α profile was superimposed on a high level of continuum emission. The background continuum intensity was monitored at intervals during the scan using a particular wavelength (usually at ±48Å from Lyman-α) in order to check for any systematic drift in the emission levels or in the detector response. The monitored level is plotted in Figure 5.6 at the wavelength position at which the scan was interrupted for the calibration.

Despite the signal averaging, considerable fluctuations still remained in the emission levels (∿±5% as shown). A slight drift to lower levels with time can also perhaps be discerned in the monitor level of Figure 5.6a (although the percentage drift lies just within the fluctuation limits). Most of the fluctuations appear to be random, with the exception of an absorption feature at ∿1243Å, and an emission feature at ∿1256Å. A much weaker emission feature may also exist at ∿1200Å.

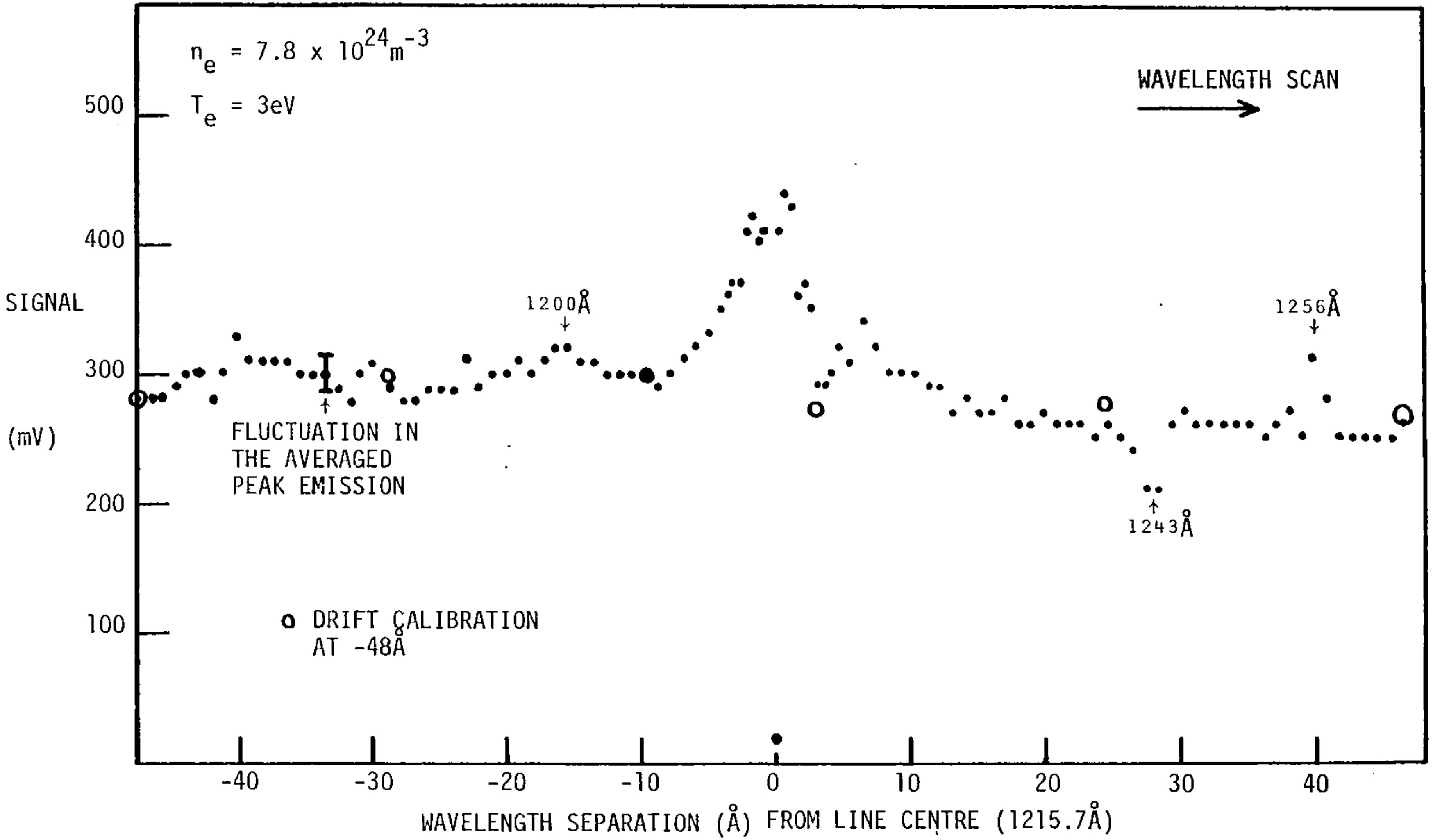

Figure 5.6(a): Lyman-α emission profile at the highest density condition (5kV, 1 torr).

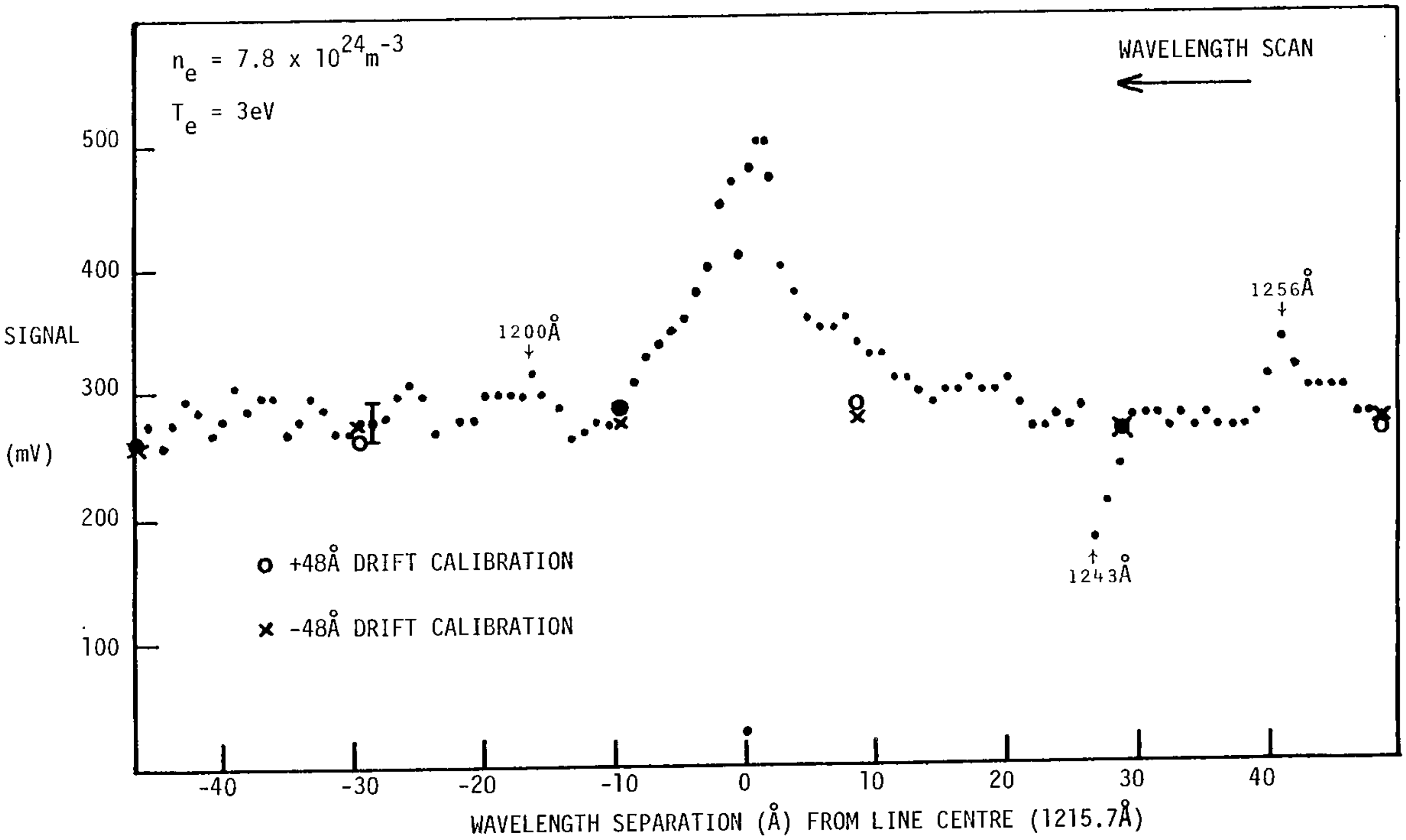

Figure 5.6(b): Lyman-α emission profile at the highest density condition (5kV, 1 torr).

To check whether this structure was due to hydrogen/perturber interactions, the spectrum was retaken using only argon as the filling gas. The same cylinder was used as for the hollow cathode calibration, and the result is shown in Figure 5.7. A small impurity of hydrogen (possibly remaining in the monochromator) produced the Lyman-α absorption feature, while the emission and absorption features observed previously in the Lyman-α wings were also present.

5.4.1.1 An Estimate of the Possible Impurity Species

Since impurity lines may have been responsible for the features observed in the continuum spectrum of Figure 5.7, and since the presence of impurities may also complicate the identification of satellite features in the Lyman-α line wings, an analysis of the possible impurity species present at peak compression was performed.

The impurity elements considered were of three types:

1) Gaseous impurities in the filling lines (which were flushed with filling gas), in the filling gas itself (guaranteed by the manufacturer to contain less than 0.005% impurity gas by volume) or from leaks in the z-pinch vessel vacuum system (which had a base pressure of $< 10^{-2}$ torr). Oxygen and nitrogen were the main possible impurities, although no oxygen or nitrogen lines appeared in the visible or UV spectra of Section 3.8.

2) Metal impurities from the end electrodes and brazing materials, which included copper, zinc, magnesium and aluminium. Although the time-of-flight for these heavy metal ions from the electrodes to the side-arm port was greater than the time to peak compression (Section 3.8), deposits of the electrode material were also observed on the z-pinch vessel near to the ports themselves.

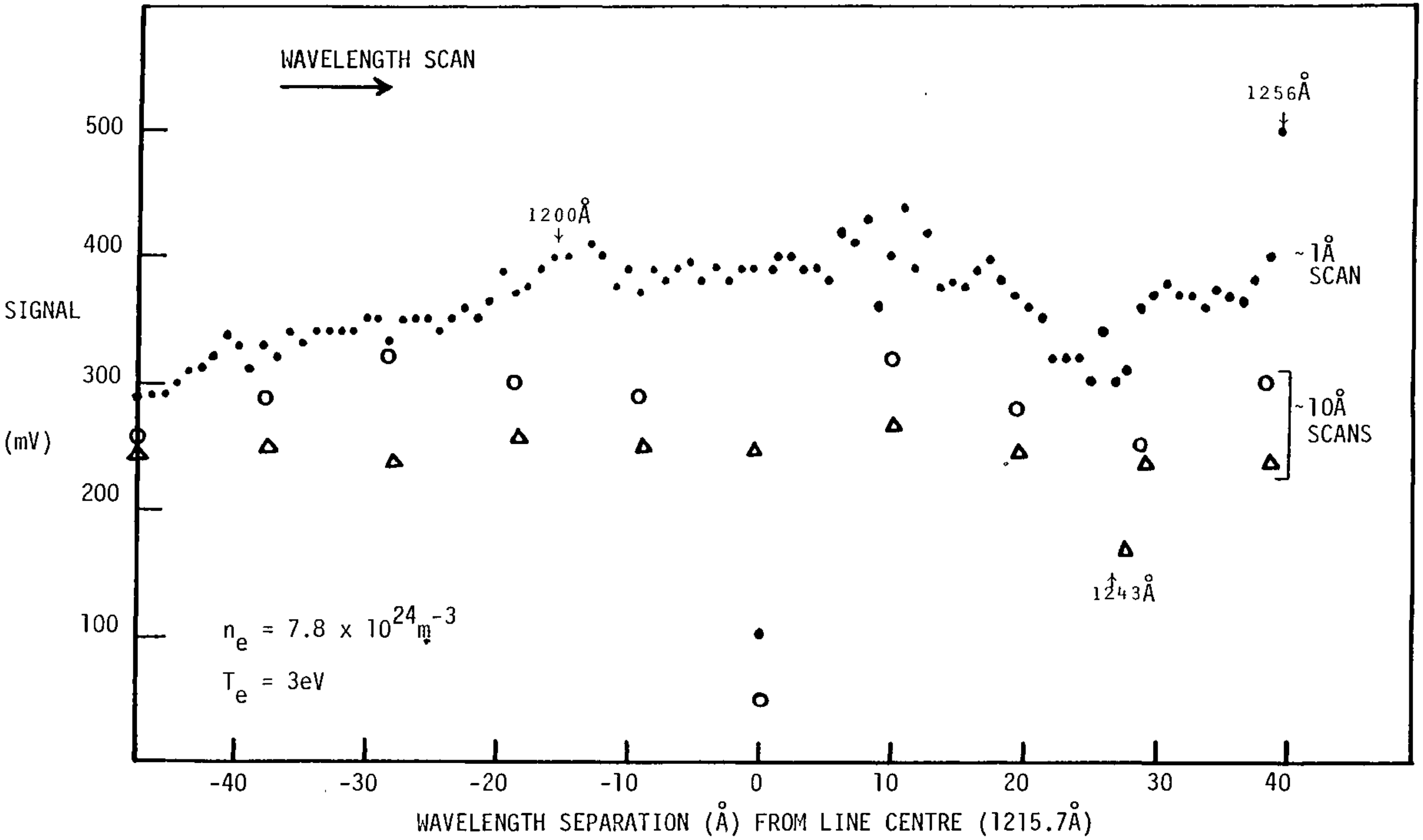

Figure 5.7: Argon (only) emission continuum at the highest density condition (5kV, 1 torr). A detailed (~1Å interval) scan is shown as well as two scans at ~10Å intervals.

3) Impurities from the pyrex z-pinch vessel including silicon, carbon, oxygen and perhaps sodium (the Na D lines were observed in absorption - Section 3.8).

To determine which ion stages of the possible impurity elements may have been present, a calculation of the L.T.E. ionization balance was carried out using the method outlined in Section 3.12. The calculations were performed over the full range of temperatures (1.5-3.5eV) for which the Lyman-α lineshapes were measured, and an electron density of $2\text{x}10^{24}\text{m}^{-3}$ was assumed (corresponding to the densities measured by Baker and to the lowest density condition used for the present Lyman-α measurements). At the highest densities measured in the present experiment the ionization balance would have been slightly different (as was shown by the effect of higher electron density on the argon ionization balance in Figure 3.19). However, a higher electron density causes the proportion of higher ionization stages present in the plasma to decrease, and hence the calculation at $n_e=2\text{x}10^{24}\text{m}^{-3}$ represented an upper bound on the number of ion stages present.

The results of the L.T.E. ionization balance calculations are shown in Figures 5.8a-g for those impurity elements with lines in the 1170-1260Å region. The abundance of the various ion stages for each element are expressed as a percentage of the total number of ions present for that element. All stages I-IV have been included except for ZnIV and CuIV, for which the partition functions were not available. (However Zn and Cu have similar ionization potentials to Si for ionization stages I-III, and hence might be expected to show a similar stage IV abundance.) Most elements have I-IV stage abundances of 1% or greater at some point in the temperature range considered, except for Na which has a very high ionization potential for NaIII (72eV).

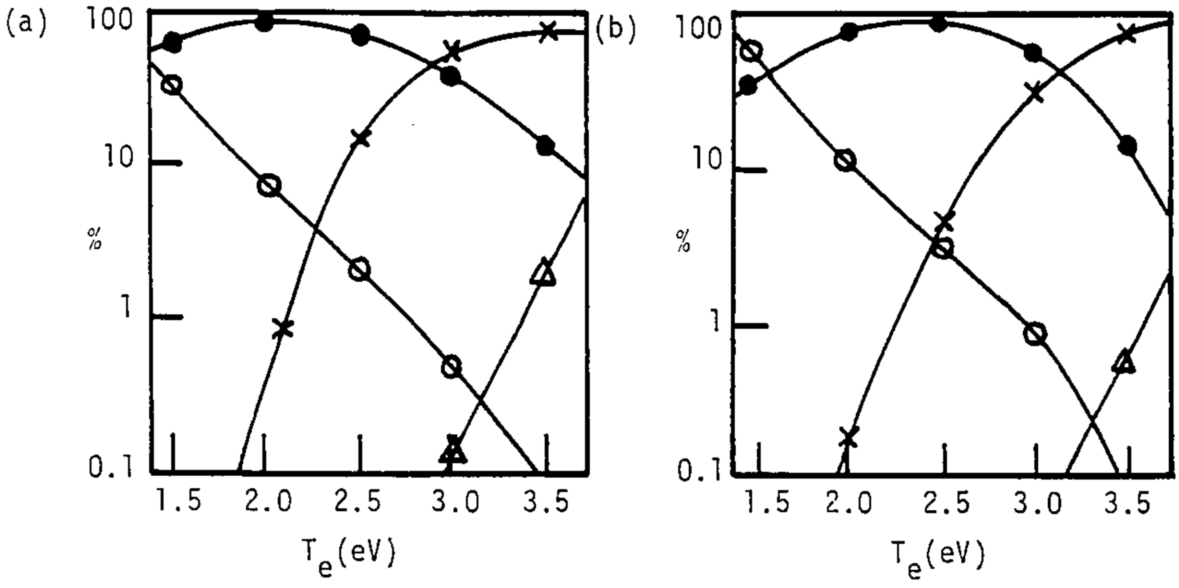

CARBON

NITROGEN

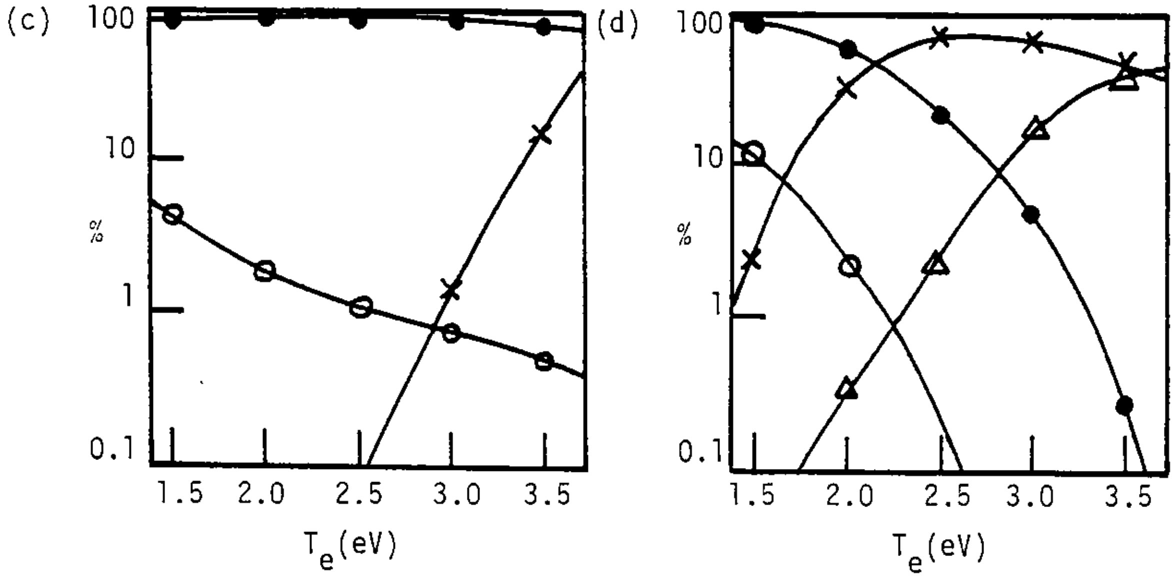

SODIUM

SILICON

Figure 5.8(a-d): Abundances of ion stages as a function of temperature for possible impurity elements, expressed as a percentage of the total number of atoms/ions for that element (n_e assumed = $2 \times 10^{24} m^{-3}$).

KEY: ○ I ● II × III △ IV ION STAGES

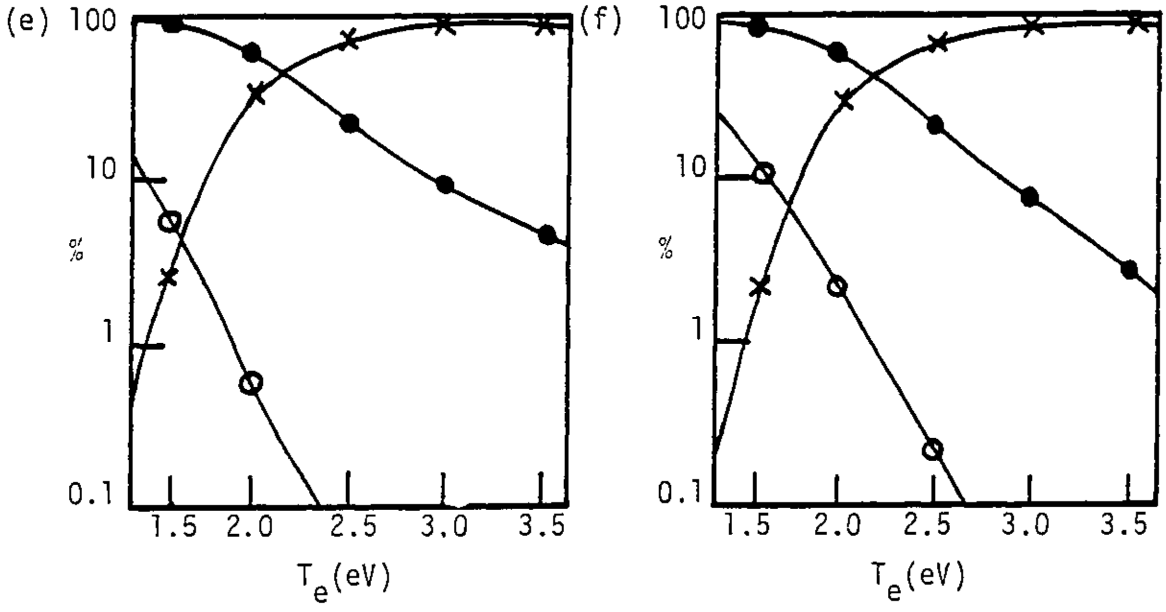

COPPER

ZINC

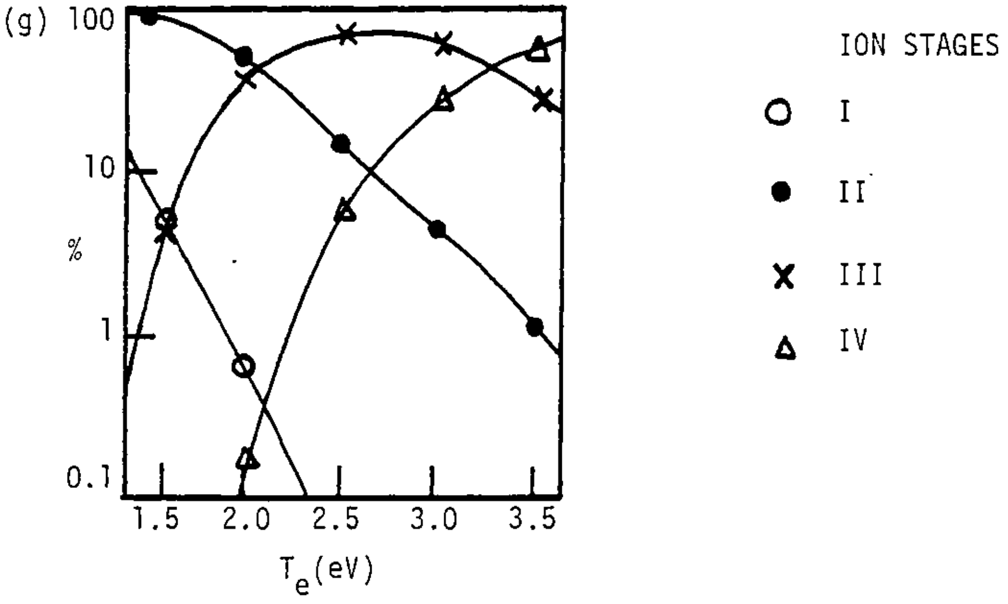

ALUMINIUM

Figure 5.8(e-g): Abundances of ion stages as a function of temperature for possible impurity elements, expressed as a percentage of the total number of atoms/ions for that element (n_e assumed = $2 \times 10^{24} m^{-3}$).

5.4.1.2 Examination of Impurity Lines in the Continuum Spectrum

Table 5.1 lists the possible impurity lines that may account for the features observed in the continuum spectrum of Figure 5.7.

FEATURE	IMPURITY SPECIES	GROUND STATE	λ(Å)	TRANSITION	INTENSITY a, b or (c)	UPPER (LOWER) STATE ENERGY (eV)
1256Å	NaIII	$2p^5(^2P^o_{3/2})$	1256.7	$3p(^2D^o)-3d'(^2D)$	20,1	61.2
	CIII	$2s^2(^1S_0)$	1256.5	-	100d,1	-
	SiI	$3p^2(^3P_0)$	1256.5	$3p^2(^3P)-3p^3(^3S^o)$	40,40	9.9
	"	"	1255.3	"	10,10	"
	CuIII	$3d^9(^2D_{5/2})$	1254.7	$a^2F-x^2F^o$	-,3	18.4
1243Å	CuIII	$3d^9(^2D_{5/2})$	1244.4	$a^4F-y^4D^o$	-,10	(7.7)
	NI	$2p^3(^4S^o_{3/2})$	1243.3	$2p^3(^2D^o)-3s'(^2D)$	400,15	(2.4)
	"	"	1243.2	"	550,20	(2.4)
	CuII	$3d^{10}(^1S_0)$	1242.0	$^4p(^3P^o)-6d(^3D)$	-,2	(8.2)
1200Å	NI	$2p^2(^4S^o_{3/2})$	1200.7	$2p^3(^4S^o)-3s(^4P)$	700,30	10.3
	"	"	1200.2	"	950,20	10.3
	ZnI	$4s^2(^1S_0)$	1200.2	-	(0)	-
	ZnIII	$3d^{10}(^1S_0)$	1199.4	-	(1)	-
	NI	$2p^3(^4S^o_{3/2})$	1199.5	$2p^3(^4S^o)-3s(^4P)$	1000,5	10.3

Table 5.1: Possible impurity lines in the continuum spectrum at 5 kV, 1 torr. Intensities a,b and (c) are taken from: a-Kelly (1968) who used a scale from 0-1000; b-Striganov and Sventitskii (1968) who used a mixture of 10, 100 and 1000 scales; and (c) Kelly (1959) who used a 0-10 scale (with 00 for very weak lines). Filled shells in the ground state configuration have been omitted.

Examination of Table 5.1 in conjunction with Figures 5.8 indicates that for the temperature corresponding to the continuum spectrum conditions (∿3eV), little SiI for example would be expected (even allowing for the fact that the spectrum was taken at a higher electron density than for the ionization calculation). However, emission from lower ionization stages may have occurred in the cooler outer regions of the discharge or in the side-arm port itself. Therefore the lower ionization stages shown in Table 5.1 cannot be eliminated as a source for the impurity lines observed in the continuum spectrum.

The strong emission feature at ∿1255Å may therefore be due to the pair of SiI lines (which may also explain the 1Å apparent width of the features in Figures 5.6a and b). The high lying level (61.2eV) for the NaIII line makes this an unlikely impurity line, while the CuIII line is weak and is further from the observed wavelength. CIII has a possible impurity line but the exact transition levels have not been identified and the line is also listed as "d" (diffuse - Kelly, 1968).

The absorption feature at ∿1243Å was most likely to have been caused by the strong NI lines. The lower state energy (2.4eV) indicates that absorption was not due to cold nitrogen in the monochromator chamber.

Similarly, the strong NI standard lines at 1200.7, 1200.2 and 1199.5Å may account for the possible broad, weak feature at ∿1200Å, although the ±5% fluctuation in the continuum background made the observation of this feature uncertain.

In addition to the features produced by the possible impurity lines, there was also a noticeable decline in the continuum emission level near 1170Å. To check whether this decline was due to decreased photomultiplier sensitivity or to a drift in the experimental measurements, the continuum emission was measured in larger (∿ 10Å) wavelength intervals as shown in Figure 5.7. Two scans were done at different times, with a slight irreproducibility in the slit settings producing the different continuum intensity levels. The scans were initiated at ∿ 1170Å and re-measured afterwards at 1170Å as a check for drift. The 1170Å measurement remained the same, and was found to be lower than the average of the longer wavelength measurements in both scans. This may have been due to decreased photomultiplier sensitivity near the MgF_2 cut-off at ∿1130Å (Figure 5.2).

5.4.1.3 Detailed Examination of the Lyman-α Near Line Wing

The extended Lyman-α profiles of Figures 5.6 together with the continuum spectrum in Figure 5.7 indicate that there were no prominent features that could be attributed to satellites in the far wings of Lyman-α.

However, near line centre it was possible to discern a weak feature ∿+8Å in the red wing of the Lyman-α profile. Therefore a more detailed scan was made of the region near line centre using ~1/3Å increments.

The result is shown in Figure 5.9 with the line centre regions of Figures 5.6a and b also included. From these scans a broad feature can be discerned between 1223 and 1224Å (which may also be the result of a dip in the line wing at 1220-1222Å). The background pure argon intensity in Figure 5.7 also shows a smaller feature which may, however, just be due to noise fluctuations. This background continuum has been scaled in Figure 5.9 to fit the far wing level of the detailed Lyman-α profile. When the background emission is subtracted (inset) the feature is still evident, although the uncertainty due to the root mean square of the noise fluctuations for the two signals is quite large. Nevertheless a comparison of the red and blue wings still indicates a noticeable structure.

To ascertain whether this structure was confined only to the highest density conditions, measurements of the Lyman-α profile were also made at lower densities.

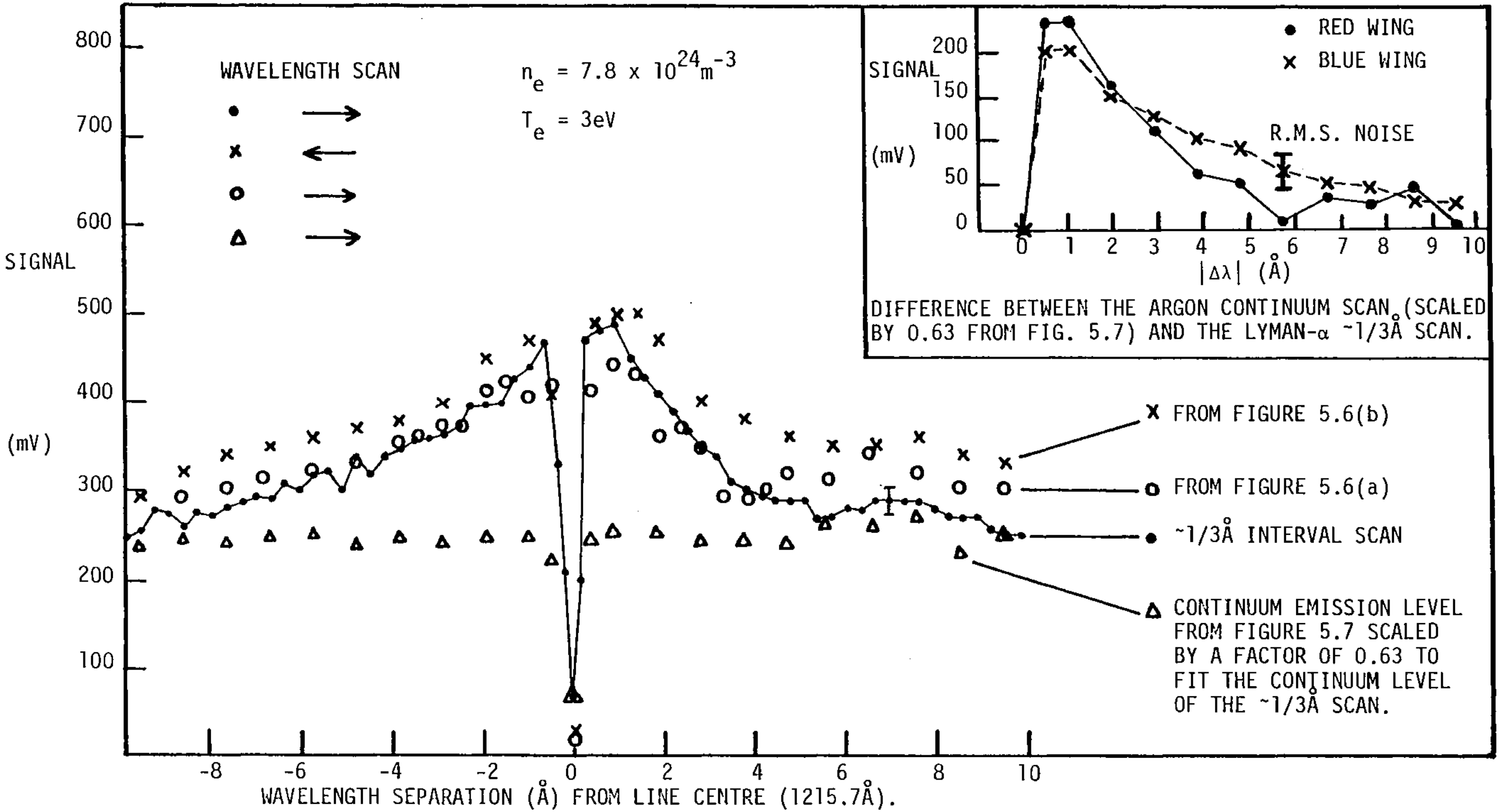

Figure 5.9: Detailed 5kV, 1 torr Lyman-α profile (~1/3Å intervals),and the line centre profiles from Figs. 5.6(a) and (b). The difference between the ~1/3Å scan and the argon continuum level (scaled from Fig.5.7) is shown inset.

5.4.2 Lyman-α Profiles at Intermediate Densities (n_e=4.6x10^{24}m^{-3} ; T_e∿ 2.5eV)

Using a filling pressure of 2 torr and the same bank voltage of 5 kV, emission measurements were carried out with the slits opened to 13 μm. The extended (± 48Å) Lyman-α profile is shown in Figure 5.10, and reveals little structure in the wings apart from the usual 1170Å intensity fall off and the reappearance of the NI absorption feature at ∿1243Å.

In order to check for the presence of the +8Å feature, a further scan was made of the red wing near line centre (this time in the reverse direction). The results of both scans are shown in Figure 5.11, and the difference in intensities may again have been due to inaccuracies in resetting the slit widths (since the experimental runs were done some time apart). It is just possible to discern a small inflexion in the red wing, but this time further out at ∿+10Å (although noise fluctuations make this result much less certain than the +8Å feature observed at the higher density conditions). Otherwise the two intermediate density profiles appear almost identical and are virtually featureless.

5.4.3 Lyman-α Profiles at Densities (n_e = 1.9x10^{24}m^{-3} ; T_e = 2eV) Similar to Baker (1977)

The satellite features observed by Baker occurred in plasmas with densities in the range n_e = 1-3x10^{24}m^{-3} and at temperatures T_e = 20,000-30,000K (two of the spectra are reproduced later in Figures 5.14a and b). In the present z-pinch, similar densities (1.9x10^{24}m^{-3}) were diagnosed interferometrically (in the same manner as Baker) when a filling pressure of 5 torr and a bank voltage of 5 kV were used. A similar temperature of 2 ± 0.5eV (23,200 ± 5,800K)

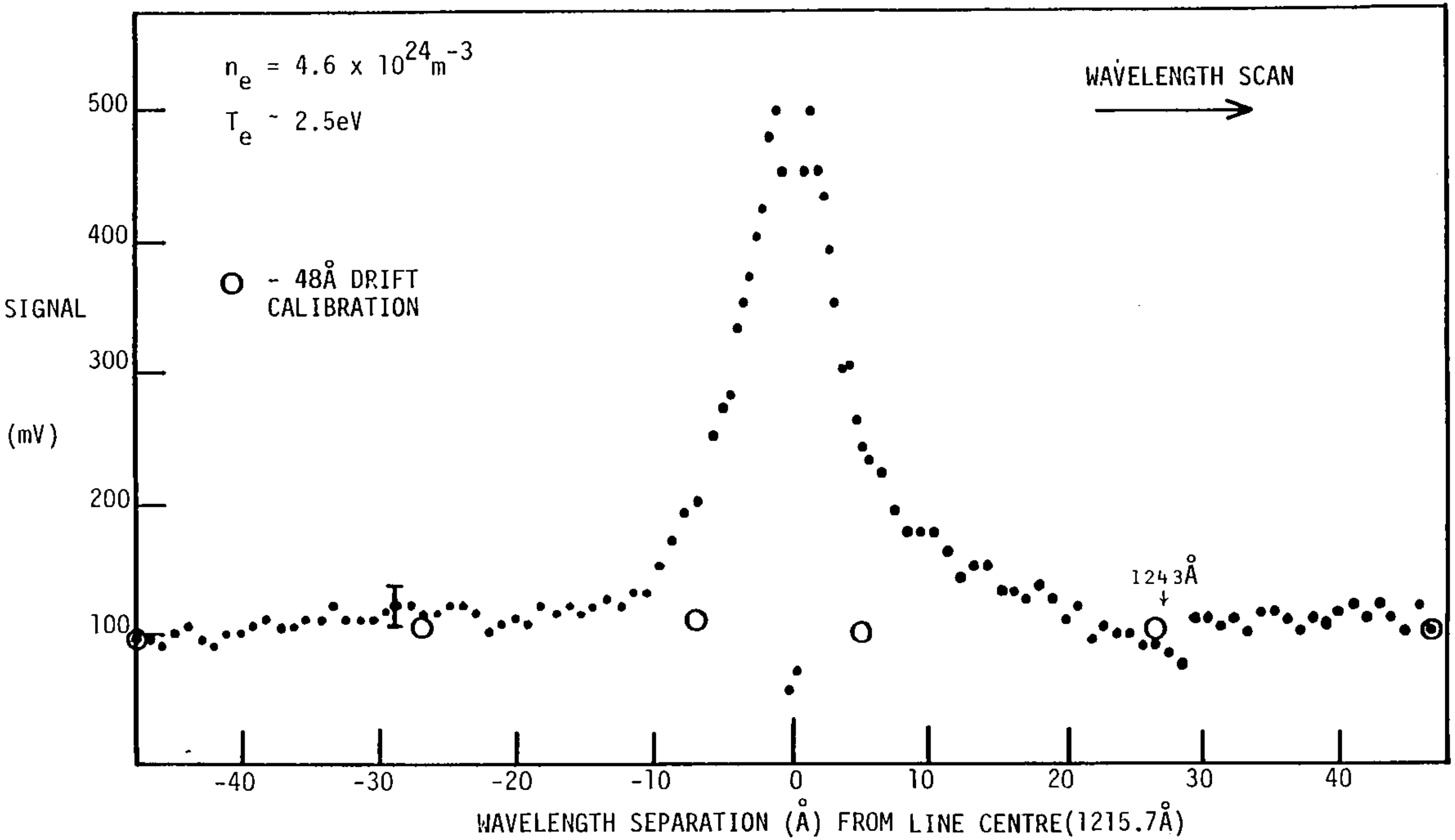

Figure 5.10: Lyman-α profile at the intermediate density condition (5kV, 2 torr).

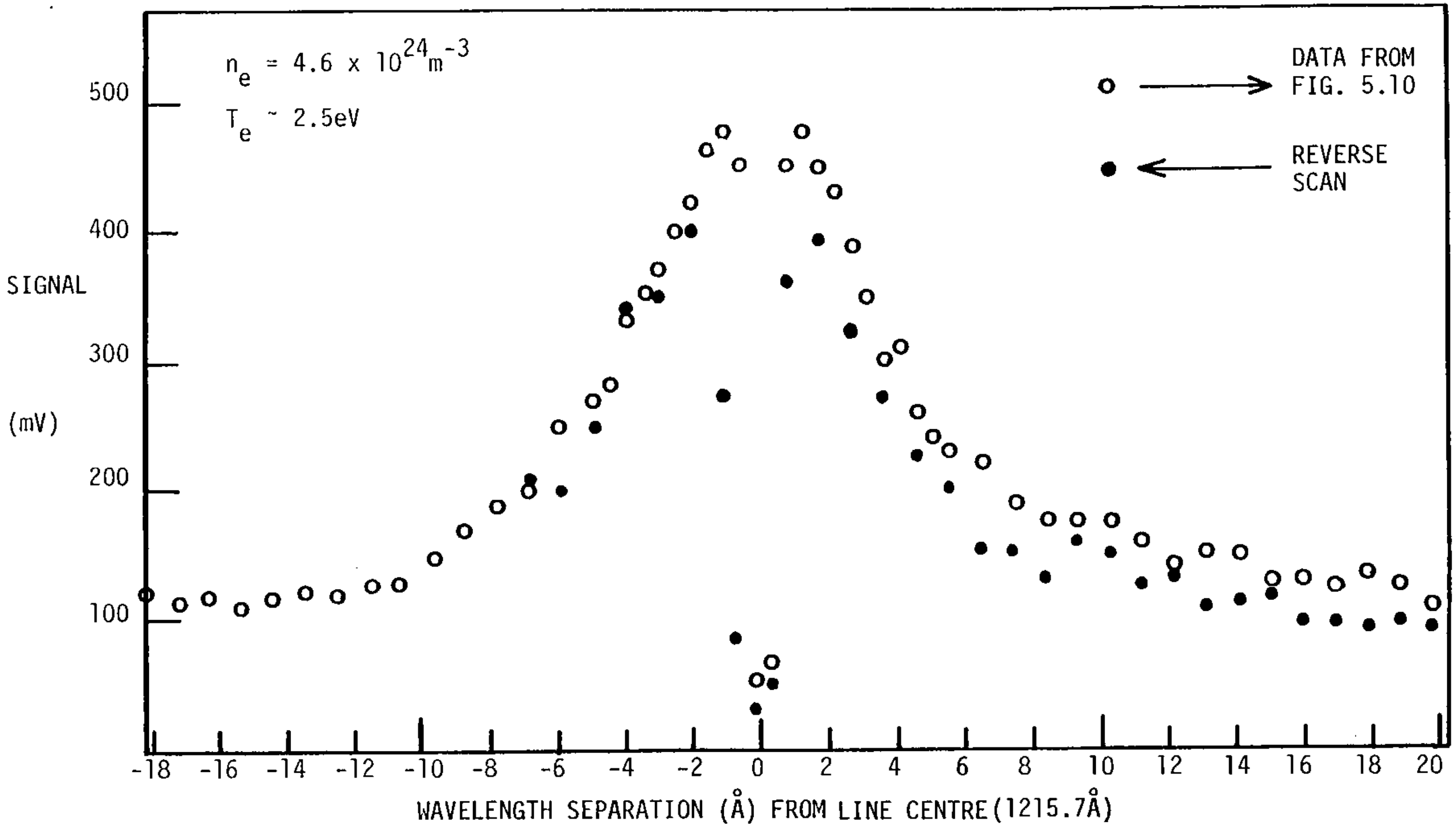

Figure 5.11: Lyman-α profile near line centre at the intermediate density condition (5kV, 2 torr).

was also obtained, although measured using different diagnostics to Baker (as mentioned in Section 3.13). Therefore at 5kV and 5 torr, the plasma conditions in the present experiment were roughly comparable to the plasma conditions at which satellite features were observed by Baker.

Line profile measurements were therefore carried out at 5kV and 5 torr, for which the emission levels were considerably lower than for the previous conditions. Slits of 25 μm width were thus employed, and the 32% transmission wire gauze filter (used for the earlier conditions to reduce the intensity to the linear gain region of the photomultiplier) was removed. The resolution with the 25 μm slits was ∿¼Å (c.f.∿½Å for Baker's measurements).

Two Lyman-α profiles are shown in Figures 5.12a and b (scanned in opposite directions). The latter profile shows greater intensity fluctuations, possibly due to trigger pin deterioration in the spark gap (as the latter profile was taken much later in the experimental programme). Neither profile shows any significant features whatever, and in particular there is no evidence of the +8Å feature seen previously at the highest density condition in the present experiment. The continuum background level in Figures 5.12 is also much lower as expected at the lower density conditions.

Therefore, in contrast to Baker's results, no satellites were observed in the present experiment. The only exception was a possible weak feature at ∿+8Å observed at higher densities than were obtained by Baker.

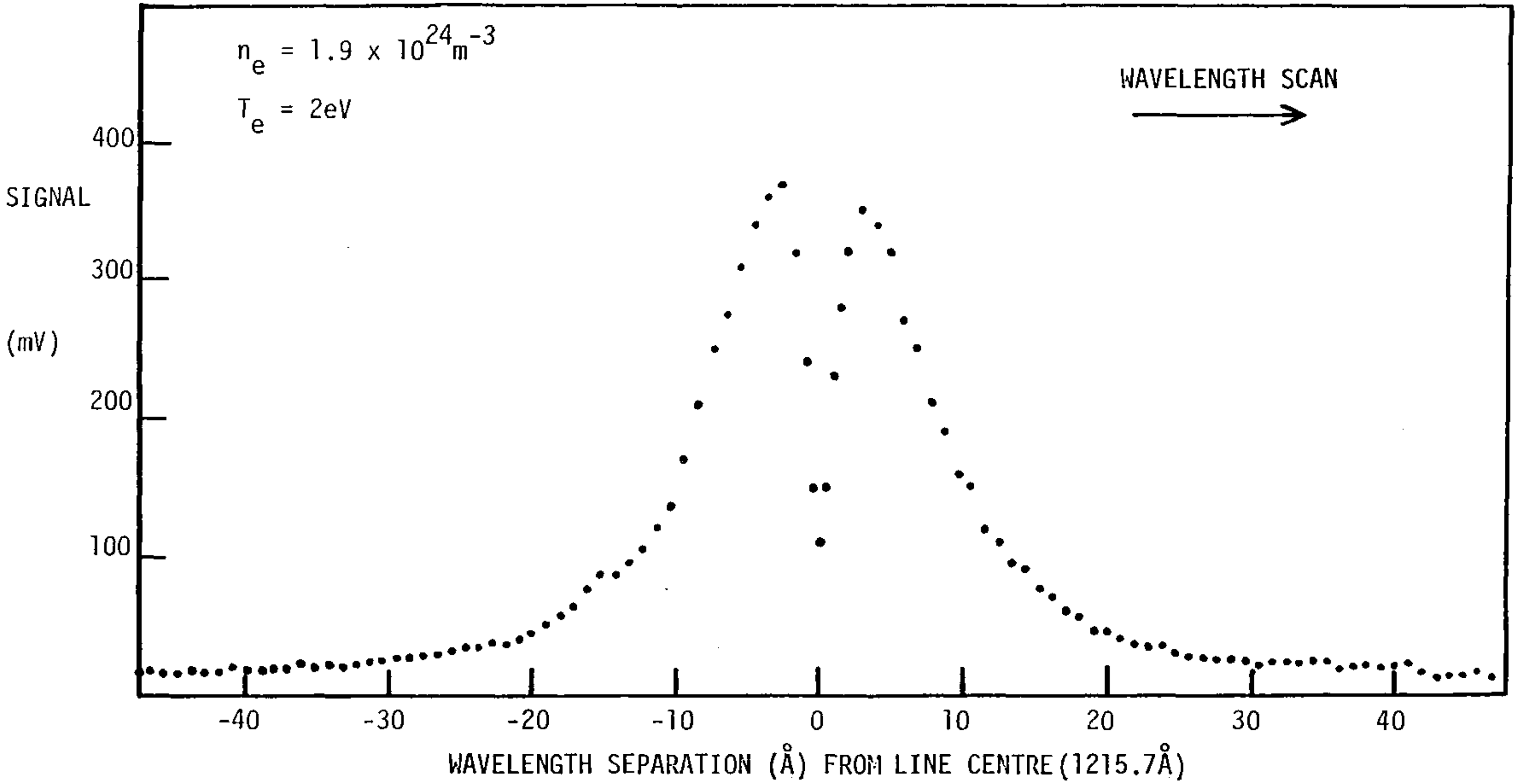

Figure 5.12(a): Lyman-α profile at 5kV, 5 torr. The plasma conditions were comparable to the range diagnosed by Baker (n_e = 1-3x$10^{24}m^{-3}$, T_e = 20,000 - 30,000K) for which Lyman-α satellite features were observed.

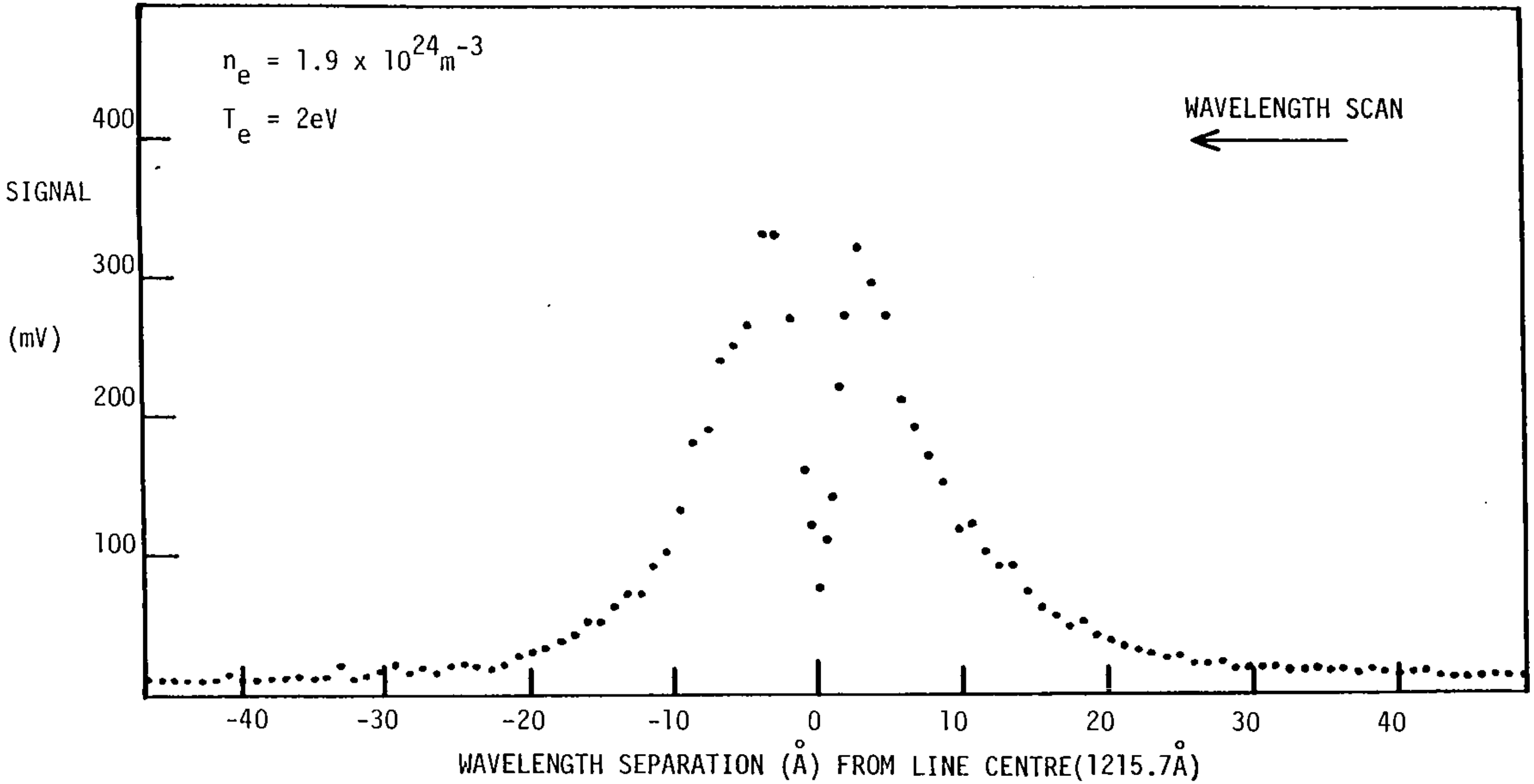

Figure 5.12(b): Reverse scan of the Lyman-α profile at 5kV, 5 torr.

5.5 Explanation of the +8Å Feature

At the highest density condition, the persistence of the structure at ∿+8Å (when correction was made for the background emission) suggests that impurity lines were unlikely to have caused this feature despite the uncertainty produced by fluctuations in the emission levels.

However, impurity line effects on the Lyman-α line wing must be considered a possibility, and as mentioned previously may take the form of an emission feature at ∿+8Å or an absorption feature at ∿+5Å. Table 5.2 lists the likely impurity lines in these regions.

FEATURE	IMPURITY SPECIES	GROUND STATE	λ(Å)	TRANSITION	INTENSITY	UPPER (LOWER) STATE ENERGY (eV)
∿+8A (1223。 -1224A)	SiII	$3p(^4P^0_{1/2})$	1222.3	$3p^2(^4P)$-$3d'(^4P)$	0,-	15.5
	SiII	"	1222.6	"	5,5	"
	ZnIV	$3d^9(^2D_{5/2})$	1223.2	-	(4)	-
	NI	$2p^3(^4S^0_{3/2})$	1223.2	?	-,3	?
	NaIII	$2p^5(^2P^0_{3/2})$	1223.4	$3p(^4D^0)$-$3d'(^2P)$	80d,4	61.2
	NI	$2p^3(^4S^0_{3/2})$	1223.8	?	-,2	?
	SiII	$3p^2(^2P^0_{1/2})$	1223.9	$3p^2(^4P)$-$3d'(^4P^0)$	20,20	15.5
	ZnIV	$3d^9(^2D^0_{5/2})$	1224.1	-	(1)	-
	SiII	$3p^2(^2P^0_{1/2})$	1224.3	$3p^2(^4P)$-$3d'(^4P^0)$	20,20	15.5
	NaIII	$2p^5(^2P^0_{3/2})$	1224.7	$3p(^4D^0)$-$3d'(^2D)$	80,4	61.2
	SiII	$3p^2(^2P^0_{1/2})$	1225.0	$3p^2(^4P)$-$3d'(^4P^0)$	10,10	15.5
	NI	$2p^3(^4S^0)$	1225.0	$2p^3(^3P^0)$-$4d(^2D)$	-,15	13.7
∿+5Å (1220。 -1222A)	AlIV	$2p^6(^1S_0)$	1219.2	$3p(1\frac{1}{2})$-$3d'(1\frac{1}{2})^0$	10,0	(85)
	CuIII	$3d^9(^2D_{5/2})$	1219.3	a^4F-y^4D	-,5	(7.5)
	AlI	$3p(^2P^0_{1/2})$	1220.6	?	10,-	(?)
	NaIII	$2p^5(^2P^0)$	1221.1	$3p(^4D^0)$-$3d'(^2D)$	100,5	(51)

Table 5.2: Impurity lines in the region ∿+8Å and ∿+5Å in the red wing of Lyman-α. Intensities a,b and (c) as for Table 5.1. Energies are measured from the ground state.

Of the emission lines, the five SiII lines arising from the same multiplet are the most likely candidates. The NI and ZnIV lines are weaker while the NaIII lines have such a high upper state energy ($\sim$ 61eV) as to be relatively unpopulated.

The high lying lower levels for the NaIII and AlIV absorption lines also ~~elimates~~ eliminates these lines as a cause of the +5Å dip in the Lyman-α wing. No AlI lines were observed in any of the visible or UV spectra which leaves the CuIII line as the only possible candidate.

Therefore impurity lines do exist which may explain the +8Å feature, although it is impossible to assess the absolute impurity concentrations and hence the expected line intensity. However, the presence of a possible SiI emission line in the continuum spectrum lends support to the existence of the SiII lines at $\sim$+8Å. Furthermore the $\sim$+8Å feature disappears at the lower density (and higher temperature) conditions, with the exception of perhaps a very slight inflexion in the line wing for the 5kV, 2 torr profile. The absence of any feature at lower densities and temperatures may thus indicate a lower population of the impurity line level.

The appearance of a feature at +8.3Å in the spectra of Baker (which were taken at densities of $1\text{-}3\times10^{24}\text{m}^{-3}$) suggests that the feature observed in the present experiment amy alternatively have been the result of close interaction satellite formation. However, the absence of any feature in the present experiment at the densities corresponding to Baker is difficult to explain if the $\sim$+8Å feature observed at the highest density was indeed a satellite. The lower temperature at the lower density condition in the present experiment (5kV, 5 torr) would be expected to enhance the satellite (as discussed in Section 2.5). However, the $\sim$+8Å feature showed decreased visibility with a decrease in temperature in the present experiment.

Further, the feature did not correspond to a multiple of the plasma frequency since $\Delta\lambda_p = 12.4\text{Å}$ at the diagnosed electron density of $7.8\times10^{24}\text{m}^{-3}$ (plasma satellites would not in any case be expected here as will be discussed shortly in Section 5.6.2). Hence, although it cannot be ruled out that the feature at ∿+8Å in the red wing of Lyman-α was due to close interaction satellite formation, the existence of impurity lines at this wavelength was also a possible explanation for the observed feature.

5.6 Explanations for the Appearance of Baker's Satellites

Apart from the single, weak ∿+8A feature just discussed, there was no evidence whatever from the present experiment for the existence of any of the other satellites seen in Baker's study.

A number of possible reasons may account for this discrepancy including:

1) differences in plasma conditions
2) the appearance of plasma frequency satellites
3) the presence of molecular hydrogen lines
4) the presence of impurity lines

Each of these explanations will be examined in the following sections.

5.6.1 Differences in Plasma Conditions

The emission profiles from the present experiment that were discussed in Section 5.4.3 were taken at an electron density of $1.9\pm0.4\times10^{24}\text{m}^{-3}$ (5 kV, 5 torr). This density was in the middle of the range of densities measured by Baker ($1\text{-}3\times10^{24}\text{m}^{-3}$) using identical interferometric methods, and for which Lyman-α satellites were observed.

However, the temperature diagnostic employed by Baker (measurement of the argon-ion laser absorption at the 4880Å ArII line) did not account for the effects of continuum opacity. An alternative temperature diagnostic (the observation of the relative abundance of Ar ion species lines) was therefore employed over the higher density range ($1.6\text{-}8.5\times10^{24}m^{-3}$) produced in the present experiment. At 5kV, 5 torr the temperature was estimated in the present experiment to be 2±0.5 eV which was within the range measured by Baker (20,000-30,000 K) using different diagnostics. It is perhaps possible, however, that the actual plasma temperatures may have been different in the two experiments. If for example the temperature in the present experiment was higher, the lack of visibility of the H-Ar^+ satellites relative to the Lyman-α wing may have been due to the lower Ar^+ population (as well as the greater broadening of the satellites with temperature - Section 2.5).

To examine the effect of an increase in temperature on the Ar^+ population, the L.T.E. ionization balance was calculated for an electron density of $2\times10^{24}m^{-3}$ over the temperature range shown in Figure 5.13. At this fixed electron density, the Ar^+ population is seen to be relatively insensitive to temperature variations within the limits diagnosed in the present experiment (2±0.5eV), changing by less than a factor of 2 over the range 1.5 - 2.5 eV. The temperatures diagnosed by Baker (20,000-30,000K) in fact overlap the upper part of the uncertainty range of the temperatures diagnosed at 5kV and 5 torr for the present experiment. Therefore, even if the temperature in the present experiment was too low by as much as 1eV (i.e. $T_e \sim 3$ eV), the Ar^+ population would still have been within a factor of 3 of the Ar^+ population in Baker's plasma.

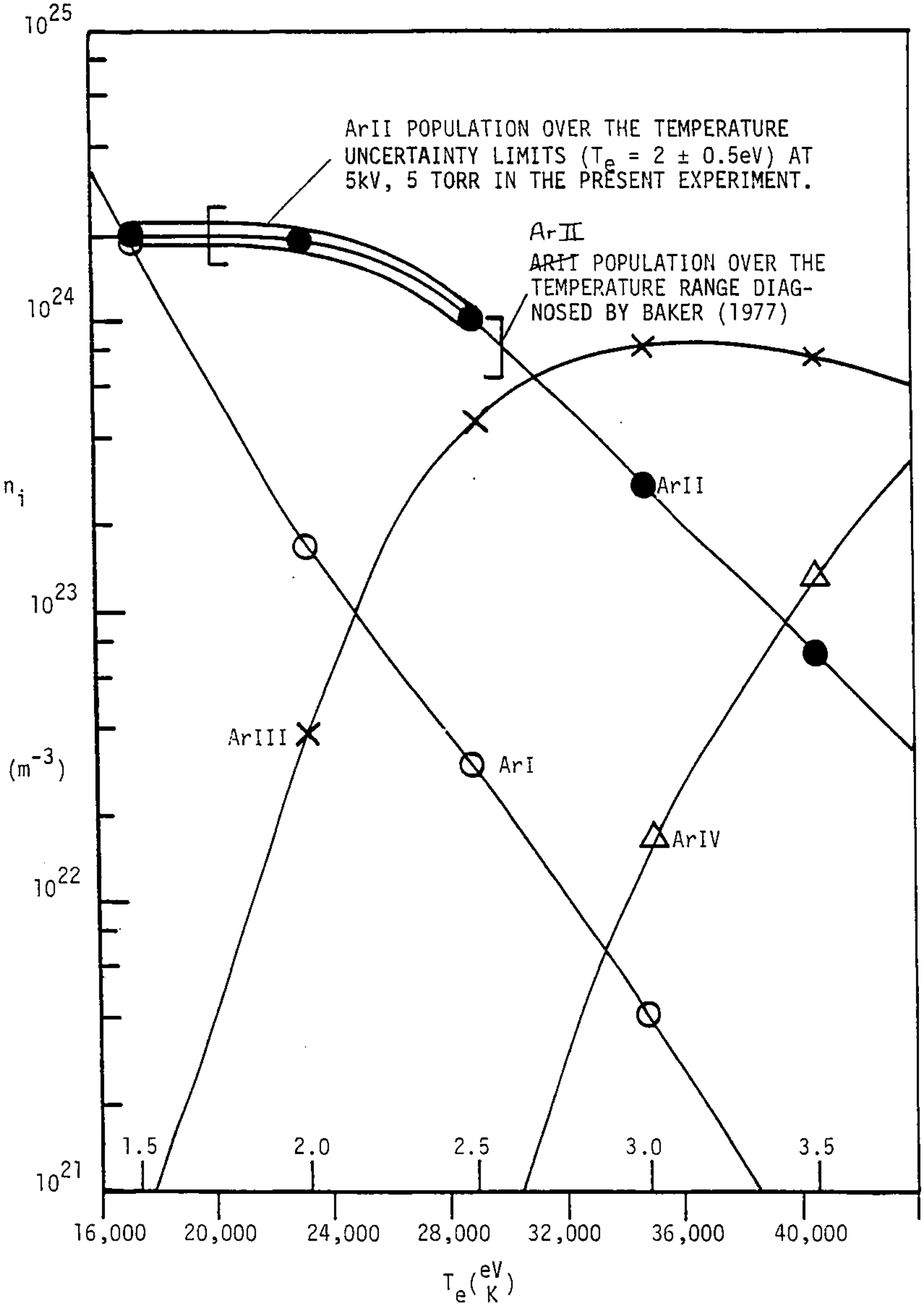

ArII POPULATION OVER THE TEMPERATURE UNCERTAINTY LIMITS (T_e = 2 ± 0.5eV) AT 5kV, 5 TORR IN THE PRESENT EXPERIMENT.

ArII
~~ARII~~ POPULATION OVER THE TEMPERATURE RANGE DIAGNOSED BY BAKER (1977)

Figure 5.13: L.T.E. calculation of the argon ion populations as a function of temperature (with $n_e = 2 \times 10^{24} m^{-3}$). The ArII populations in Baker's z-pinch and in the present experiment are also shown for this density.

However the calculations of Section 3.12 indicate that at $n_e = 2\times10^{24}\,m^{-3}$, the plasma would consist of ~75% ArIII at a temperature of 3eV. In fact only four weak ArIII lines (from the low lying 4p states) were observed at 5kV and 5 torr out of 22 ArIII UV lines observed at all conditions, thus indicating that little ArIII was present (some ArIII emission was also observed by Baker).

Furthermore the large number of ArII lines observed in the present experiment at 5kV and 5 torr indicated the presence of a significant ArII population. It is possible that the ArII lines were emitted in the afterglow following the peak compression, but the fact that the ArI stage appeared to be "burnt through" at the higher temperature conditions suggested that the emission lines probably originated at peak compression (since ArI would be expected in the afterglow at all conditions). Over 60% of the total number of ArII lines were present at 5kV, 5 torr. Of the 60% most were from lower (e.g. 4d) excited states, in comparison with the prominent lines from the 4f and 5d states that were observed only at the higher temperature conditions.

Therefore despite the difference in temperature diagnostics, the Ar^+ population in the present experiment would not appear to have been significantly less than the Ar^+ population observed by Baker. The comparable Ar^+ populations, together with the relatively weak temperature dependence ($\propto T^{\frac{1}{2}}$) of the satellite widths (e.g. Preston, 1977), suggest that temperature differences between the two experiments would not explain the discrepancy in the observation of Lyman-α satellites.

5.6.2 Plasma Satellites to Lyman-α

Due to the degeneracy of the allowed (2p) and forbidden (2s) levels of hydrogen Lyman-α, the occurrence of plasma satellites cannot be described simply using the formalism of Baranger and Mozer (1961).

However it is possible for plasma satellites to hydrogen lines to occur under certain conditions as is described by Cohn et al. (1972), who considered the effect of adding static (low frequency) and dynamic (high frequency ω_p) electric fields. When the two fields are parallel, the plasma frequency field produces satellites at multiples of ω_p from the line centre, with each satellite being symmetrically split (when the static field is introduced) by an amount proportional to the static field. For perpendicular static and dynamic fields satellites also occur at multiples of ω_p, but when the static field is increased the satellites first split and then move back through the original satellite position. The intensities of the various satellites also alter as the static field is increased. Satellites corresponding to this predicted behaviour have been observed by Gallagher and Levine (1973) in a toroidal plasma in which the low frequency field strength was enhanced by plasma turbulence, and the plasma oscillations were induced parallel to the direction of the toroidal field.

However in an equilibrium plasma in which the electric fields have no preferred direction, averages over both the orientation and magnitude of the random electric fields would cause the satellites to become smeared out. Thus plasma satellites to Lyman-α would not be expected in Baker's or the present experiment (furthermore the analyis by Cohn et al. breaks down at high densities, once the quadratic Stark effect becomes significant in comparison to the linear Stark effect - see Section 1.3.2.1). In any event, the satellite features observed by Baker did not correspond to multiples of the plasma frequency and did not show any frequency variation with density.

Therefore plasma satellites can be eliminated as an explanation of the features observed by Baker.

5.6.3 Molecular Hydrogen Lines

Although molecular hydrogen would be completely dissociated at the temperatures (20,000-30,000K) obtained by Baker at peak compression

(Tatum, 1967), it is possible that the satellites could have been caused by molecular emission in the cooler outer regions of the pinch vessel or side-arm ports.

The tables of Dieke and Hopfield (1927) list the hydrogen bands dominating the spectrum below 1250Å. The molecular hydrogen lines from the Werner band that lie within 1Å of the satellite features observed by Baker are shown in Table 5.3.

SATELLITE	WAVELENGTH (Å)	H_2 WERNER BAND LINES (Å)	TRANSITION
S_{3-}	1192.0	1191.5	C_3-A_6
S_{2-}	1199.8	1199.9	C_1-A_7
S_{2+}	1232.6	1231.9	C_3-A_7
S_{3+}	1239.6	1239.5	C_4-A_8

Table 5.3: Hydrogen Werner band lines corresponding to the satellites observed by Baker.

Although a scaling with hydrogen concentration would be expected for the molecular lines, a scaling with Ar^+ would not be expected. Further, since none of the other molecular hydrogen lines appeared in the wavelength range 1257-1175Å studied by Baker, molecular lines are an unlikely explanation for the Lyman-α line wing features.

5.6.4 Impurity Lines

Two of the satellite spectra observed by Baker are given in Figures 5.14a and b (from Figures 7.3 and 7.2 of Baker, 1977). It is possible that some of the satellite features shown were in fact due to impurity emission in the plasma. The wavelengths of the features observed are listed in Table 5.4, together with possible impurity lines

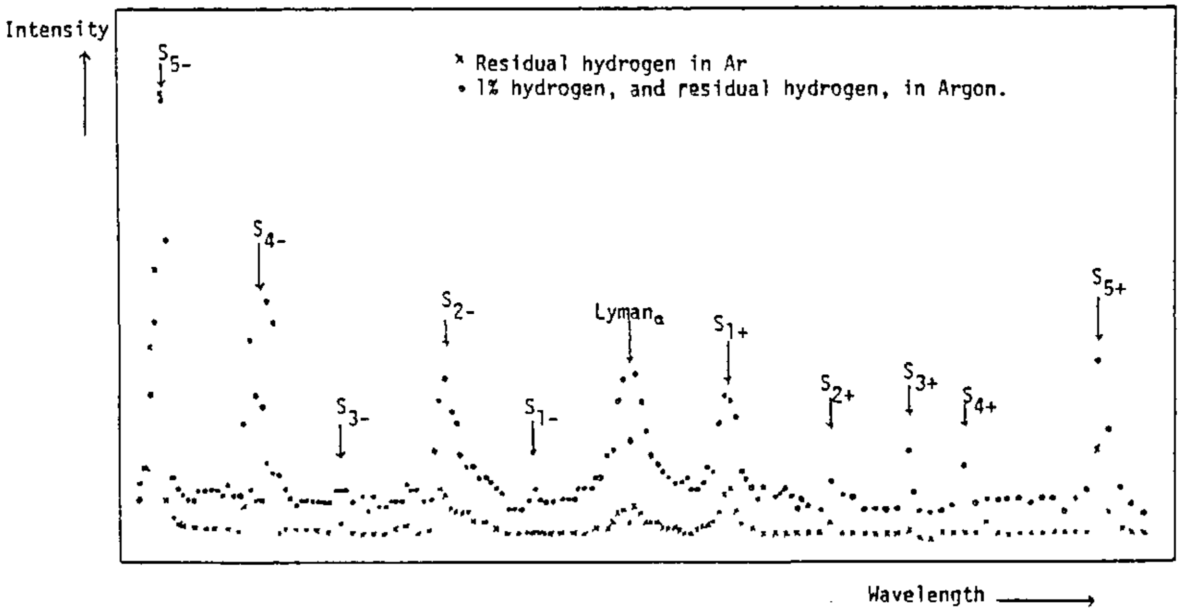

Figure 5.14(a): Lyman-α spectra obtained by Baker (1977, Fig. 7.3) at 5kV, 0.1 torr ($n_e = 1 \times 10^{24}$, T_e = 28,000K). The lower intensity of the features in the residual hydrogen spectra indicate that all but the S_{5-} and S_{3-} satellites scale with the hydrogen concentration.

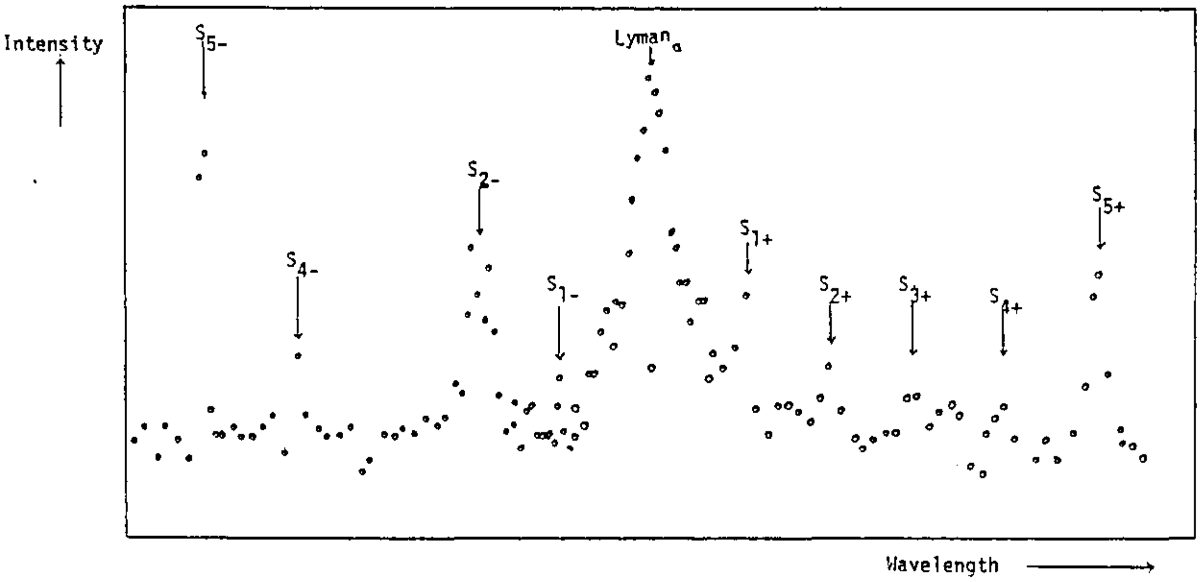

Figure 5.14(b): Spectrum from Baker (1977, Fig. 7.2) at lower temperatures (24,000K, $n_e = 2.8 \times 10^{24} m^{-3}$) using a filling pressure of 0.55 torr at 5kV.

Table 5.4: Comparison of the satellites observed by Baker with nearby impurity lines. Intensities a,b and (c) as for Table 5.1. The asterisked lines were considered as possible impurities by Baker.

SATELLITE WAVELENGTHS (Å)	IMPURITY LINES WITHIN 0.5Å				IMPURITY LINES WITHIN 1-0.5 Å			
	SPECIES	λ(Å)	INTENSITY	TRANSITION	SPECIES	λ(Å)	INTENSITY	TRANSITION
1175.8 (S_{5-})	CIII	1175.3	300,3	$2p(^3P^0)-2p^2(^3P)$	SiIII	1174.4	120,6	$3p^2(^3P)-5p(^3P^0)$
	ZnIV	1175.3	(00)	-	CIII	1174.9	350,3	$2p^3(P^0)-2p^2(^3P)$
	CIII	1175.6	200,2	$2p(^3P^0)-2p^2(^3P)$	CIII	1176.4	350,3	"
	*CIII	1175.7	1000,5	"	NI	1176.5	350,15	$2p^3(^2D^0)-4s(^2P)$
	CIII	1176.0	300,3	"				
1184.1 (S_{4-})	NI	1184.0	20,3	?				
	*NIII	1184.5	400,8	$2p^2(^2P)-2p^3(^2P^0)$				
1192.0 (S_{3-})	*AlII	1191.8	100,5	$3p(^3P^0)-4d(^3D)$	NI	1191.0	-,5	$2p^3(^2P^0)-5d(^2P)$
	CI	1191.8	120,1	$2p^2(^3P)-4d(^1F^0)$	NI	1192.6	-,2	$2p^3(^2P^0)-6s(^4P)$
	ZnI	1191.7	(0)	-	CI	1193.0	700,8	$2p^2(^3P)-4d(^3D^0)$
	NI	1192.0	-,4	$2p^3(^2P^0)-6s(^2P)$				
	*CI	1192.2	70,-	$2p^2(^3P)-5s(^1P^0)$				
	CuII	1192.3	-,2	$4p(^3F^0)-7d(^3G)$				
	*SiIII	1192.3	P,-	3s3d-3p4s				
	CI	1192.5	120,2	$2p^2(^3P)-5s(^1P^0)$				
1199.8 (S_{2-})	*NI	1199.5	1000,50	$2p^3(^4S^0)-3s(^4P)$	NI	1200.7	700,30	$2p^3(^4S^0)-3s(^4P)$
	ZnIII	1199.4	(1)	-				
	ZnI	1200.2	(0)	-				
	NI	1200.2	950,2	$2p^3(^4S^0)-3s(^4P)$				
1207.4 (S_{1-})	*SiIII	1207.5	180,9	$3p^2(^1D)-3d'(^1D^0)$	AlII	1208.4	60,3	$3p(^1P^0)-7d(^1D)$
					SiIII	1206.5	600,30	$3s^2(^1S)-3p\ (^1P^0)$
					ZnIV	1206.5	(1)	-
1224.0 (S_{1+})	NI	1223.8	-,2	?	ZnIV	1223.2	(4)	-
	*SiII	1223.9	20,20	$3p^2(^4P)-3d'(^4P^0)$	NI	1223.2	-,3	?
	ZnIV	1224.1	(1)	-	NaIII	1223.4	80,4	$3p(^4D^0)-3d'(^2P)$
	SiII	1224.3	20,20	$3p^2(^4P)-3d'(^4P^0)$	NaIII	1224.7	80,4	$3p(^4D^0)-3d'(^2D)$
					NI	1225.0	40,15	$2p^3(^2P^0)-4d(^2D)$
1232.6 (S_{2+})					*NI	1231.6	5,1	$2p^3(^2P^0)-5s(^2P)$
					NI	1233.2	-,2	$2p^3(^2P^0)-5s(^4P)$
					SiII	1233.4	50,-	?
1239.6 (S_{3+})	*MgII	1239.9	P,-	$3s(^2S)-4p(^2P^0)$	MgII	1240.4	-,P	$3s(^2S)-4p(^2P^0)$
	ZnIII	1239.6	(1)	-	*AlIV	1240.2	100,2	$3p(1\frac{1}{2})-3d(2\frac{1}{2})$
1244.3 (S_{4+})	CuIII	1244.4	-,10	a^4F-y^4D	NI	1243.3	400,15	$2p^3(^2D^0)-3s'(^2D)$
	ZnI	1244.4	(0)	-	*NIV	1244.9	50,1	2p3d-2s6g
1255.8 (S_{5+})	*SiI	1255.3	10,10	$3p^2(^3P)-3p^3(^3S^0)$	*SiI	1256.5	40,40	$3p^2(^3P)-3p^3(^3S^0)$
					CI	1256.5	200,-	$2p^2(^1D)-10d(^1F^0)$
					CIII	1256.5	100d,1	$3s(^3S)-4p(^3P^0)$

lying within 0.5Å (the resolution of Baker's measurements) and within 1Å of the satellite positions.

Included in Table 5.4 are the impurity lines considered by Baker (asterisked). Baker had eliminated a number of lines originating from electrode impurity species. However, the walls of Baker's z-pinch vessel were heavily coated with electrode material and hence such impurities may have been present in the plasma near the side-arm ports. Some other impurity lines were also discounted because the plasma was too hot, but as mentioned previously some emission may have occurred from lower ionization stages in the cooler outer regions of the plasma.

Therefore the criterion adopted from Section 5.4.1.1 for the inclusion of impurity species in Table 5.4 was that all stages with an abundance >1% (or with higher stages having abundances >1%) were included (for temperatures in the range 20,000-30,000K). Although this criterion was somewhat arbitary, the absolute level of the impurity concentration was unknown and hence only a relative estimate of the impurity ion concentrations was possible. The Mg abundance was not calculated, but the low I.P. for MgI (7.6eV) indicates that significant MgII may have been present at the 2-2.5eV temperatures considered.

The satellites S_{5-} and S_{3-} were identified previously as being due to impurities (probably CIII and SiIII respectively - Baker and Burgess, 1979), since the two satellite intensities did not depend on the hydrogen concentration. The S_{1-} feature did not show any dependence on the argon ion concentration, and was therefore also suspected as an impurity line (possibly SiIII 1207.5 from Table 5.4).

Of the remaining satellites, all but S_{2+} have possible nearby impurity lines within the resolution of the monochromator (Table 5.4), and the NI 1233.2Å line is only +0.6Å from the S_{2+} satellite. Some of the impurity lines may be considered less likely to explain the satellite features observed since other strong lines with similar upper state energies in the same species were not visible i.e. CI 1189.6Å (700), SiII 1229.4Å (200).

5.6.4.1 Scaling of the Satellites Observed by Baker with H/Ar^+ Concentration

Although a number of possible impurity lines may exist at the wavelength of the satellite features, this would not explain the scaling of the satellite intensity with the hydrogen n=2 population. Baker observed a considerable decrease in the satellite intensity when the hydrogen concentration in the filling gas was reduced, although the apparent level of the continuum was also observed to decrease (Figure 5.14a). The decrease in continuum intensity was explained by Baker as being due to the lower Lyman-α line wing intensity (although the continuum intensitydecrease appeared to be uniform over the whole range of wavelengths ±40Å from Lyman-α). However, the fact that the S_{5-} and S_{3-} impurity line intensities remained constant indicated that the satellite intensity decrease was not due to some other systematic effect (e.g. a change in the detector response).

It is possible that for those impurity lines due to nitrogen, the apparent decrease in satellite intensity with a change in the filling gas hydrogen concentration may have been caused by a lower impurity nitrogen concentration in the second filling gas. However, the relative line intensities in Figures 5.14 are not always consistent with the nitrogen line intensities quoted in Table 5.4 e.g. NI 1199.5Å (1000) and 1225.0Å (40) - Kelly (1968).

The satellite features were also observed to scale linearly with the Ar^+ concentration (apart from the S_{4-} satellite which appeared to scale with Ar^{2+}). It is conceivable, however, that the impurity ion concentration could also scale in the same manner as the argon ion concentration. Further, Baker observed that the satellite intensities dropped dramatically when the temperatures were lower (i.e. for $T_e \sim$ 23,000-24,000K). Such a behaviour would also be indicative of emission from the excited states of impurity atoms or ions.

5.6.4.2 Absence of Impurity Lines in the Present Experiment

Having considered the possibility of impurity emission as a cause of the satellite features in Baker's pinch, the absence of such features in the present experiment must also be explained (since the plasma conditions and z-pinch design were similar).

The nitrogen lines which appear near all but the S_{3+} and S_{5+} satellites in Table 5.4 may have been less evident in the present experiment due to the considerable care taken to flush the filling lines and to prevent vacuum leaks in the design of the z-pinch vessel. Some possible NI lines were seen only in the spectra taken at the highest densities in the present experiment (notably at $\sim$ 1200Å corresponding to Baker 's S_{2-} satellite).

The difference in the presence of electrode and z-pinch vessel impurities between Baker's experiment and the present experiment is more difficult to explain (although the possible 1256Å SiI impurity line observed in the present experiment at the highest density condition did correspond to the same position as Baker's S_{5+} satellite). The carbon concentrations may have differed e.g. due to the different positioning of the o-ring seals. The silicon and metal impurities, however, would have been expected to possess similar concentrations in the two experiments.

A possible explanation may arise from the way in which the discharge was initiated in the z-pinch vessel, since the different filling pressures and trigger circuits may have caused the initial breakdown to occur in different places. If the discharge had initially broken down along the walls of the vessel in Baker's experiment, this may have produced the ionized impurity species (e.g. SiIII) observed in Baker's spectra. If the discharge broke down through the filling gas in the present experiment, the concentration of impurity elements from the coated walls of the discharge vessel may conceivably have been lower.

In conclusion then, it is possible that impurity lines may have accounted for the satellite features observed by Baker, although no features (either impurity lines or satellites) were seen at comparable plasma conditions in the present experiment. However, the scaling of the features observed by Baker with the hydrogen concentration was a significant indication that the features were due to hydrogen/perturber interactions.

5.7 Lineshape Asymmetry Results

Closer inspection of the spectra revealed what appeared to be asymmetries in the shape of some of the Lyman-α profiles. Caution must however be exercised in the interpretation of line asymmetries due to the high opacity and the self-absorption of Lyman-α under the present conditions. Apparent asymmetries may also result from line shifts for optically thick lines.

Further complications arise from the presence of impurity lines in some spectra, and from the variation of the photomultiplier response with wavelength (Figure 5.2). Examination of Figure 5.2 reveals that the quantum efficiency falls as the wavelength approaches the MgF_2 cut-off, while the decreased efficiency to the red of Lyman-α is somewhat less. Hence a red wing asymmetry may result which will affect the lineshape at wavelengths further than $\sim 10\text{Å}$ into the line wing. However, because of the lack of data points for the photomultiplier response (only three in the region of interest), and because of possible variation in the grating efficiency over the wavelength range 1170-1260Å, the effect of instrumental asymmetry was difficult to calculate.

Nevertheless the lineshapes were analysed using the following asymmetry parameters (expressed in terms of the red and blue wing wavelengths for which the line intensity was equal):

$$\Delta\lambda_1 = \tfrac{1}{2}\,|\lambda_R - \lambda_B| \tag{5.1}$$

$$\Delta\lambda_2 = \tfrac{1}{2}\,(\lambda_R + \lambda_B) - \lambda_0 \tag{5.2}$$

where λ_0 represents the unshifted line centre wavelength. The asymmetry results thus measured are shown in Figures 5.15a-c for the three density conditions.

At the highest density (Figure 5.15a) the asymmetry is plotted both for the raw data of the detailed scan and for the same data with the continuum background subtracted. The line wing structure was roughly the same in each case and was revealed more as a dip in the red wing than as a satellite at $\sim$+8Å. This asymmetry contrasts with the peaks on either side of the self-absorption dip which imply a red asymmetry (since the longer wavelength peak was higher). Alternatively, the different peak intensities could be interpreted as a red shift of the Lyman-α profile of about 0.5Å.

The asymmetry of the intermediate density profile is shown in Figure 5.15b, and was obtained by interpolation between the data points to give the equal intensity wavelengths (as was done in Figure 5.15a). However, a polynomial fit to the lineshape was also used to smooth the large fluctuations present in the emission signal at the lower intensities. The greater line-to-continuum intensity for the intermediate density profile enabled the asymmetry to be measured further into the line wing, but the measurements were limited by the presence of the impurity absorption dip in the red wing. The dip is reflected in the asymmetry turnover at $\Delta\lambda_1 \gtrsim 18$Å, while a cross-over

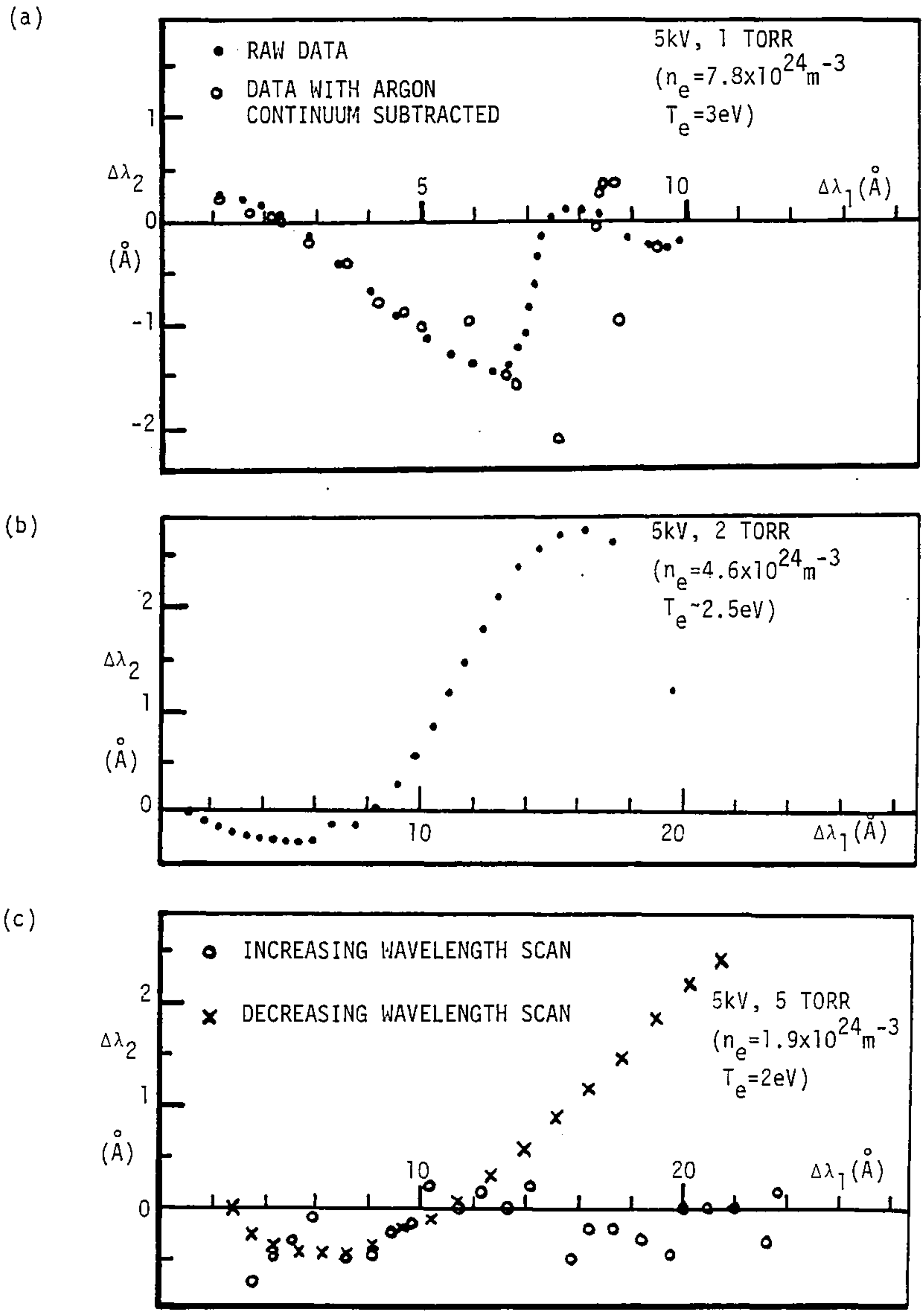

Figure 5.15: Asymmetry parameters for the Lyman-α profiles taken at the three plasma conditions.

from blue to red asymmetry also occurs at $\Delta\lambda_1$ $\sim 9\mathring{A}$. In neither the detailed nor the extended profiles was there any evidence of an asymmetry or shift from the (apparently equal) peaks either side of the self absorption dip.

At conditions more closely resembling those obtained by Baker (Figure 5.15c) it was possible to measure the asymmetry even further into the line wing due to the low continuum contribution and the absence of impurity lines in the Lyman-α profile. Scans were done in both directions, but unfortunately yielded conflicting results. When scanned in decreasing wavelengths (crosses) the profile showed first a blue then a red asymmetry, similarly to the profile obtained at intermediate density (which was scanned in the opposite direction). However the increasing wavelength scan at the lowest density showed a different behaviour for $\Delta\lambda_1 > 14\mathring{A}$, where no asymmetry was evident at all. An explanation for the differing results is not readily apparent, except perhaps that there was a long-term drift in the emission intensity during the second low density scan. The direction of the scan was probably not the cause, since a qualitatively similar asymmetry was observed for the intermediate density and the first low density profiles, which were scanned in opposite directions.

However, the peaks either side of the self absorption dip show the same ratio for both scans at the lowest density, which supports the agreement of the two low density asymmetry measurements for $\Delta\lambda_1 < 14\mathring{A}$. Alternatively, the line centre asymmetry could be interpreted as a shift of $-0.5\mathring{A}$ in the low density Lyman-α profiles.

5.8 Interpretation of Asymmetry Results

The lack of data for the spectral sensitivity of the detection system combined with complications due to the presence of impurity lines meant that it was difficult to draw quantitative conclusions from the asymmetry of the Lyman-α profiles. Nevertheless some qualitative comparisons with theory can be made, and a summary of the data for the feature-free profiles is shown in Figure 5.16, together with various theoretical predictions which will be examined in this section.

5.8.1 Trivial Causes of Asymmetry

A trivial asymmetry arises from a number of frequency dependent factors that are commonly omitted in lineshape calculations. These factors include:

(a) the ω^4 term in the power radiated,

(b) the Boltzmann factor in the populations of the upper state and

(c) the wavelength conversion approximation $\Delta\lambda/[2\pi c\,(\lambda_0+\Delta\lambda)^2] = \Delta\lambda/2\pi c\lambda_0^2$ which yields errors of order $2\Delta\lambda/\lambda_0$ (Griem, 1964, p.94).

These contributions can be written in terms of an equal wavelength separation parameter (Griem, 1964, p.94)

$$\frac{I(\Delta\lambda)-I(-\Delta\lambda)}{\frac{1}{2}(I(\Delta\lambda)+I(-\Delta\lambda))} = \left(-6+\frac{hc}{\lambda_0 kT}\right)\frac{2\Delta\lambda}{\lambda_0} \qquad (5.3)$$

which cannot easily be converted to the equal intensity asymmetry parameters without some assumption as to the lineshape.

However a calculation of the trivial asymmetry for Lyman-α at T_e = 13,800K was given in Figure 4 of Preston (1977) and included by Baker (1977, Figure 7.8). Equation (5.3) indicates that Preston's calculation will not be applicable at the present higher temperatures (2-3 eV) since a change-over to blue asymmetry occurs at $\sim$20,000K.

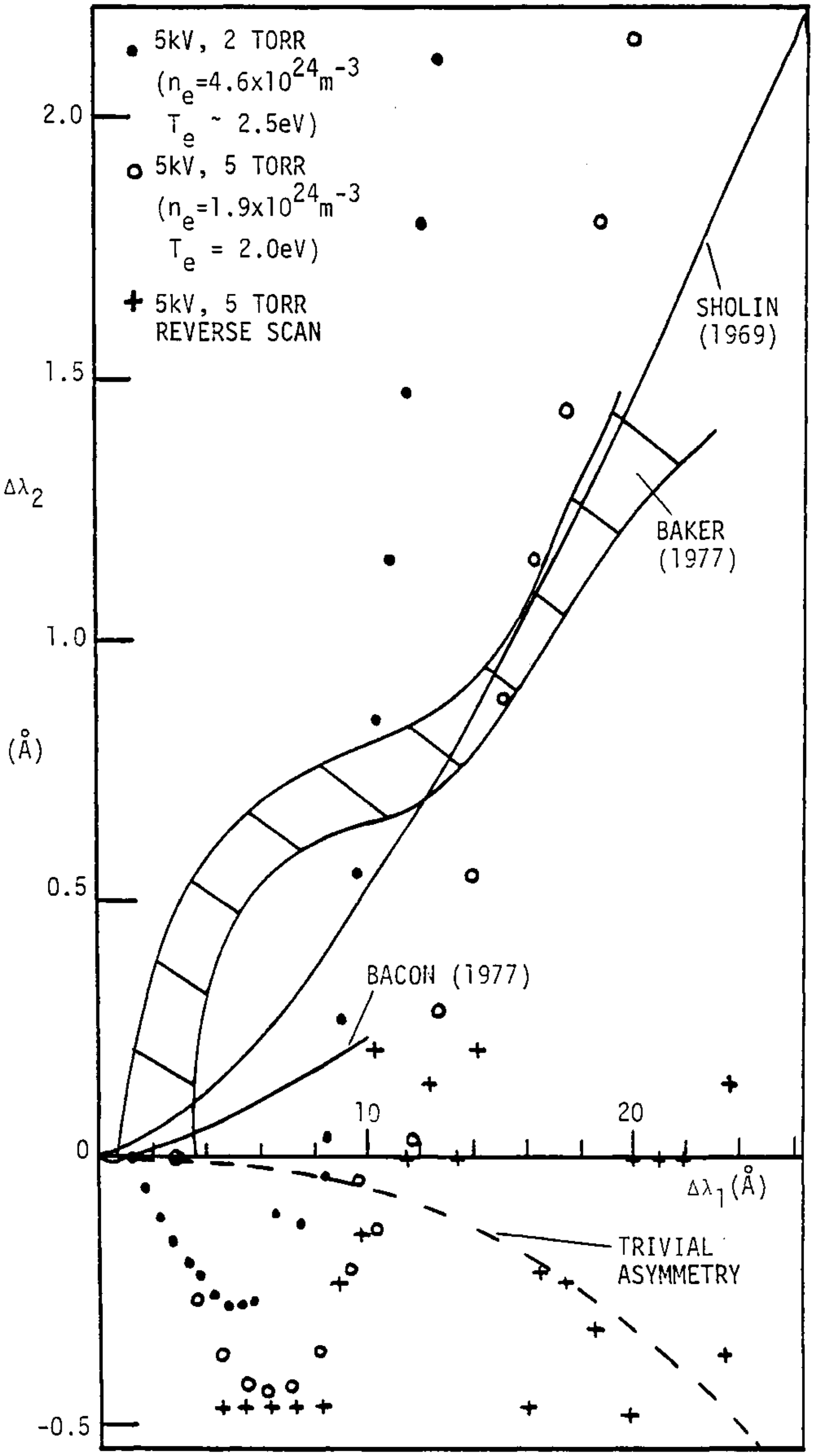

Figure 5.16: Comparison of the asymmetry observed in the present experiment, with the asymmetry predicted by Bacon (for n_e=7.2x10^{22}m^{-3}) and Sholin, and observed by Baker (n_e=1-3x10^{24}m^{-3}). Also shown is the maximum trivial asymmetry, obtained by extrapolation from the calculation of Preston (1979) to the maximum temperature in the present experiment (3.5eV).

However, Equation (5.3) also shows that the absolute value of the blue asymmetry will be less than that calculated by Preston for temperatures $T_e < 35{,}000K (3eV)$. Hence the blue trivial asymmetry plotted in Figure 5.16 (using the same magnitude as the red asymmetry calculated by Preston) represents an upper bound on the (already small) trivial asymmetry in the present experiment.

5.8.2 Quasistatic Ion Quadrupole Asymmetries

As shown in Section 1.3.2.1, the main higher order correction to the linear Stark effect comes from the quadrupole term in the static ion broadening of Lyman-α. Sholin (1969) has derived the following relationship between the equal intensity parameters for ion quadrupole asymmetries:

$$\Delta\lambda_2 = \frac{-0.4\ R_o}{e^{\frac{1}{2}}} \sum_{k>o} \frac{b_k I_k{}^{(o)} + |a_k| I_{+k}^{(1)}}{\sum_k I_k^{(o)} |a_k|^{3/2}} (\Delta\lambda_1)^{3/2} \qquad (5.4)$$

where the parameters for the kth Stark component are tabulated by Sholin (in c.g.s. units). On evaluation for Lyman-α Equation 5.4 yields

$$\Delta\lambda_2 = \frac{-0.4(\frac{3}{4\pi n_e})^{1/3}}{e^{\frac{1}{2}}} \frac{(-9.682x10^{-12} n_e^{1/3} + 9.675x10^{-12} n_e^{1/3})}{2.701x10^{-5}} \times (\Delta\lambda_1)^{3/2}$$

$$\sim 3 \times 10^{-2} [\Delta\ \lambda_1\ (\text{Å})]^{3/2} \quad \text{Å} \qquad (5.5)$$

which is independent of electron density. This expression compares with the value of $1.58x10^{-2} (\Delta\lambda_1)^{3/2}$Å given by Sholin and shown in Figure 5.16. The discrepancy is probably accounted for by the fact that the bracketed term involves a difference of two nearly equal terms, and the four significant figure accuracy of Sholin's tabulated values was insufficient to calculate this difference exactly.

5.8.3 Calculation of the Total Lyman-α Asymmetry at $n_e = 7.2 \times 10^{22} m^{-3}$

Bacon, (1973, 1977) extended the Lyman-α asymmetry calculations by including the second order quadrupole and quadratic Stark effects, which were found to produce small corrections at the densities considered ($n_e = 7.2 \times 10^{22} m^{-3}$). There was no octupole contribution from the ions for Lyman-α.

Most importantly, however, Bacon also calculated the symmetric impact broadened profile due to electrons (but did not include any quasistatic contributions due to the electrons, which would cancel the contributions due to the ions only in the far line wings i.e. for $\Delta\lambda > \frac{\lambda^2 kT}{4hc}$). The addition of the symmetric electron impact profile to the asymmetric ion contribution had the effect of decreasing the overall asymmetry.

For this reason Bacon's calculation yielded a smaller value for the asymmetry compared to Sholin (although both agreed on the magnitude of the ion quadrupole contribution). Bacon further included the ω^4 and frequency-to-wavelength corrections in the trivial asymmetry, and the final calculation for the total Lyman-α asymmetry at $n_e = 7.2 \times 10^{22} m^{-3}$ is shown in Figure 5.16.

However, no calculations of the predicted Lyman-α asymmetry were available for the higher densities of the present experiment.

5.8.4 Comparison of Experimental and Theoretical Asymmetries

Comparison of the theoretical predictions with the results of the present experiment must be made in the light of the uncertainty in the spectral response of the detection system and the uncertainty in the experimental measurement of the asymmetry.

The uncertainty in $\Delta\lambda_1$ arises mainly from the interpolation used to determine the equal intensity wavelength points, and can be estimated to be equal to at most a half the wavelength increment employed (which was 1Å except near line centre where ½Å increments were used). A systematic error in $\Delta\lambda_2$ may arise from estimation of λ_0 from the position of the self absorption dip. However by using the symmetry of the intensity points on each side of the dip, the error in $\Delta\lambda_2$ was probably less than the ∿ 0.2Å instrument width. Since the difference between λ_0 and $(\lambda_R + \lambda_B)/2$ defines $\Delta\lambda_2$, small errors in the equal intensity wavelengths would also be expected to be important, especially if half a wavelength increment is used as a measure of this uncertainty. However, smoothing by use of the polynomial fitting routine and interpolation between the fitted points considerably reduced the uncertainty caused by intensity fluctuations in the line wing intensity. Hence $\Delta\lambda_2$ was also probably accurate to within the 0.2Å instrumental width.

Comparison of the present experiment with the theoretical predictions and with Baker's results shows an unexpectedly large blue asymmetry in the present experiment for $\Delta\lambda_1 < 10$Å (Figure 5.16). This may be due to the blue quadrupole shift of the central component which mainly affects the line centre asymmetry (Bacon, 1977). Bacon predicts this effect to occur for much smaller values of $\Delta\lambda_1$ (< 1Å) at lower densities ($n_e = 7.2\mathrm{x}10^{22}\mathrm{m}^{-3}$).

For $\Delta\lambda_1 \gtrsim 10$Å a red asymmetry is evident in the present results. At $n_e = 4.6\mathrm{x}10^{24}\mathrm{m}^{-3}$ the asymmetry is greater than that measured by Baker, and larger than the asymmetry predicted by Bacon for lower densities ($7.2\text{x}10^{22}\text{m}^{-3}$). The increased asymmetry may reflect the greater contributions from higher terms in the interaction potential expansions mentioned previously in Section 1.3.2.1. This hypothesis is supported by the greater asymmetry at large $\Delta\lambda_1$ in the profile taken at the higher density condition in the present experiment.

5.8.5 Line Shifts as a Cause of Apparent Asymmetry

Finally it remains to consider the effect of line shifts as a cause of the apparent asymmetry, particularly for line centre profiles in which the Lyman-α dip was observed to fall between two peaks of unequal height. This occurred at 5kV, 5 torr (a blue shift of ~0.5Å) and (surprisingly) an opposite ~0.5Å red shift at 5kV, 1 torr. These conditions corresponded to the lowest and highest densities respectively, with no apparent shift for the intermediate density.

5.8.5.1 The Quadratic Stark Effect

The greater contribution of the (red) quadratic Stark shift at higher densities was a possible cause of the change-over from blue to red shifts. From equation (1.32) the quadratic Stark shift is

$$\Delta E_{QS} = \frac{-n^* z^2 e^2 r_o^3}{4\pi\varepsilon_o R_o^4} \tag{5.6}$$

where n* is a function of the quantum numbers for the particular Stark component (n=78 for the central component of Lyman-α from Equation 1.32). For $n_e = 7.8\text{x}10^{24}\text{m}^{-3}$ and a mean perturber charge z=2, Equation (5.6) yields at most a red shift of 0.1Å, which is below the monochromator resolution and a factor of five less than the observed red shift at the highest density. The quadratic Stark effect can therefore be eliminated as a cause of the different red and blue line centre asymmetries at the high and low density conditions.

5.8.5.2. The Plasma Polarisation Shift

Another possible cause of the apparent shift is the shielding of the optical electron from the nuclear potential by plasma particles (the plasma polarization shift e.g. Griem, 1974, p.140). Polarization shifts may be either to the red or the blue depending on whether the shielding effect of the plasma particles decreases or increases the relative energy separation of the transition levels.

Davis and Blaha (1981) have calculated the plasma polarization shift for the hydrogen resonance lines, although the authors indicated caution in the application of their predictions due to the use of simplifying assumptions for the ion distributions. The assumption of a uniform ion distribution gave the largest shift for Lyman-α, which was of the order of 0.1-0.2Å to the red at $n_e = 7.8\text{x}10^{24}\text{m}^{-3}$ (upon extrapolating the predicted results from 2eV to the temperature of $\sim$3eV at 5 kV, 1 torr). This predicted shift was less than the apparent observed shift of $\sim$+0.5Å at 5kV and 1 torr. Similarly for 5kV, 5 torr ($n_e = 1.9 \times 10^{24}\text{m}^{-3}$, $T_e \sim 2$ eV) the shift predicted by Davis and Blaha was $\sim$0.08Å to the red, whereas the apparent shift was ~0.5Å to the blue.

Thus plasma polarization shifts were also insufficient to explain the apparent Lyman-α line centre asymmetries observed.

5.9 Summary of Lyman-α Emission Profile Results

In the present experiment Lyman-α emission profiles were taken at three conditions, corresponding to the conditions obtained by Baker, the highest densities diagnosed on the present pinch, and an intermediate density condition. These are probably the highest density Stark broadened Lyman-α profiles yet measured.

Apart from a weak feature ∿+8Å in the wing of the highest density profile, no satellite features were observed that could be attributed to extrema in the hydrogen/perturber interaction potential. By comparison, Baker observed a number of satellite features which could, however, have corresponded to possible impurity lines given the 0.5Å resolution of the monochromator employed. However, the scaling of the features observed by Baker with the hydrogen concentration was not consistent with the observation of impurity lines, and suggested that close interaction satellite formation may indeed have occurred.

Some asymmetry in the Lyman-α profiles was also observed in the present experiment (although the effect of the detector system response could not be included due to the lack of available data over the 1168-1264Å range of observation). The apparent observed asymmetry was in the blue wing below $\Delta\lambda_1 \sim 10$Å, with a greater red asymmetry for $\Delta\lambda_1 > 10$Å at $n_e = 4.6\times10^{24}\text{m}^{-3}$ than either predicted by Bacon or observed by Baker. The increased asymmetry may have been the result of higher order contributions to the interaction potential at the present higher densities. The apparent shifts in the self reversed, line centre profiles could not be explained by the quadratic Stark effect or by the plasma polarisation shift.

CHAPTER 6

CONCLUSION

6.1 Aims of the Present Project

Following the initial work of Baker on the study of dense, strongly coupled plasmas produced in linear z-pinch devices, it was the intention of the present project to extend these studies by examining more completely the range of conditions achievable in a physically similar device. The aim was to increase the electron density at peak compression beyond the range $n_e = 1\text{-}3\text{x}10^{24}\text{m}^{-3}$ obtained by Baker, while at the same time maintain or decrease the number of particles per Debye sphere ($N_D \sim 3\text{-}5$). The non-Debye plasma source would then allow the study of possible spectroscopic effects arising in strongly coupled plasmas (Chapter 1) over a range of plasma conditions.

A specific aim of the present project was the study of the density dependance of the Lyman-α line wing satellites observed by Baker. It was also proposed that a coherent, tunable Lyman-α source be developed using frequency upconversion techniques so that more detailed profiles of the satellite features could be obtained, and at the same time enable an exact determination of the Lyman-α line wing opacity.

The achievements of the present project in respect of these aims are examined in this concluding chapter, together with an outline of future experiments arising from the present work.

6.2 Creation of the Dense, Non-Debye Z-Pinch Plasma

Using the same z-pinch geometry,spark gap and capacitor bank as Baker, the peak discharge current was increased in the present device by lowering the circuit inductance. Deleterious heating of the plasma was prevented by increasing the filling pressure of the Ar/H mixture, and the pressure at which the electron density maximised was identified by continuum opacity measurements. The spatially resolved electron density was obtained from Abel-inverted interferometric studies, which were limited at the highest densities by continuum absorption of the probe laser beam. The electron density range diagnosed was 1.2-8.5 x $10^{24}m^{-3}$, although higher densities ($\gtrsim 10^{25}m^{-3}$) were obtained that could not be measured by the present laser interferometry.

The high continuum opacity and the presence of many broad and optically deep argon lines also limited the range of temperature diagnostic techniques available, so an approximate temperature estimate was made using the distribution of argon ion species lines from the UV spectrographic survey. Comparison of the Ar ion species with the ionization balance calculated from Saha's equation (L.T.E. could be assumed at the present high densities) yielded temperature estimates of 2-3.5 (±0.5) eV.

Hence the electron densities achieved in the present experiment extended beyond the range obtained by Baker, and were limited only by the absence of a suitable diagnostic at the highest densities. A non-Debye plasma was thus created with few (2-3) particles per Debye sphere.

6.3 Development of the Coherent Lyman-α Source

Frequency upconversion of a tunable, 100 kW, UV dye laser to Lyman-α wavelengths using a krypton tripling cell was successfully demonstrated and produced outputs of $\sim 10^5$-10^6 photons per pulse.

However the system was severely limited by the dye laser pump sources available, with a nitrogen laser used to pump the PBD dye oscillator and a frequency doubled ruby laser used to pump the PPF dye amplifier. Difficulties arose with mismatch of the pump pulse lengths and with synchronisation of the two pump pulses. These factors limited both the reproducibility and intensity of the amplified dye laser pulse as well as the spectral purity, to the extent that use of the Lyman-α system as a source for an absorption experiment was not possible.

However, given the use of a more powerful, higher repetition rate and better beam quality pump laser, the feasibility of the techniques demonstrated in the present project should allow production of a sufficiently powerful coherent Lyman-α source for use in an absorption experiment (see Section 6.6).

6.4 Emission Measurement of the High Density Lyman-α Profiles

Since the coherent Lyman-α source was not bright enough to be visible above the background plasma emission, line profiles were therefore carried out in emission at what are probably the highest plasma density studies of Lyman-α to date. Profiles were taken at the highest densities diagnosable in the present pinch ($7.8\times10^{24}\,m^{-3}$, 3eV), at conditions corresponding to Baker's studies ($1.9\times10^{24}\,m^{-3}$, 2eV) and at an intermediate density ($4.6\times10^{24}\,m^{-3}$, $\sim$2.5eV).

No satellites were seen corresponding to the features observed by Baker, although a possible weak feature was seen $\sim$+8Å in the red wing at the highest density condition in the present experiment. The features observed by Baker were not plasma frequency satellites due to the absence of any change in wavelength with electron density, nor were they likely to be due to molecular hydrogen emission since only some of the many possible Werner band emission lines were observed. One possible explanation for the features observed by Baker was the presence of impurity lines (e.g. from NI) which were absent in the present pinch. Although a number of possible impurity lines possess wavelengths near each of the satellites, the scaling of the satellite intensities with hydrogen concentration was not consistent with impurity line emission. Further, comparable density conditions in the two experiments were diagnosed using the same interferometric methods, and the uncertainty in the temperature estimates (measured using different diagnostics) were shown to yield little difference in the Ar^+ concentrations for the two experiments. Therefore no completely satisfatory explanation was found for the absence in the present experiment of the H-Ar^+ satellites observed by Baker.

Some asymmetry of the Lyman-α profile was also measured in the present experiment. The asymmetries measured at $n_e = 4.6\times10^{24}m^{-3}$ were greater than observed by Baker, possibly as a result of higher order multipole contributions to the lineshape at the higher densities obtained in the present experiment (although effects due to the instrumental frequency response cannot be ruled out at present). Comparison with theoretical asymmetry calculations was also difficult due to the absence of any predicted asymmetries at the present high density conditions. In any event the validity of such calculations (involving multipole and perturbation expansions of the interaction potential) is open to question in dense, strongly coupled plasma.

6.5 Further Calibrated Emission Profile Studies

The relatively line-free Lyman-α emission profiles obtained in the present experiment indicate the feasibility of further emission work on line asymmetries, especially if accurate Lyman-α absorption measurements prove impossible (or are limited by the wavelength range of measurable opacities).

Quantitative emission studies would however require a detailed calibration of the frequency response of the monochromator/photomultiplier detection system over the wavelength range of interest (1190-1240Å). Calibration could be achieved using a deuterium lamp source (Nettleton and Preston, 1980), but calibration is possible only at three wavelengths (1199, 1215 and 1236Å) in this range. More calibration points could be obtained using quasi-continuum, low temperature argon arc sources (Nettleton, private communication), but the reproducibility of such sources is limited by the presence of many lines (some due to impurities) whose intensity is a sensitive function of the running conditions.

However, calibration of the arc sources could be undertaken against absolute irradiance standards at the National Physical Laboratory. Determination of the spectral response of the detector sytem would enable detailed measurement of the Lyman-α profile asymmetry, as well as an absolute measurement of the continuum emissivity outside the Lyman-α line profile. The absolute brightness of the coherent Lyman-α source could also then be determined.

6.6 Subsequent Enhancement of Lyman-α Generation at the Rutherford UV Radiation Facility

Following completion of the present emission profile studies, scheduled experimental time was obtained at the Rutherford Laboratory UV Radiation Facility for use of their recently acquired, high power (1 MW) excimer-laser pumped dye laser system. This dye laser produced much higher output energies (∿ 4mJ) at 3 x Lyman-α wavelengths than were obtained by the system developed in the present project. The higher repetition rate of the Rutherford laser (∿40 Hz) also greatly enhanced the laser alignment and experimental setting up procedures.

The greater dye laser output power consequently increased the efficiency of frequency conversion to Lyman-α. Experiments at the Rutherford UV Radiation Facility using the tripling cell described in Section 4.8.1 have produced Lyman-α outputs some one to two orders of magnitude higher than reported in the present work. The radiation was also tunable over the full range ofpossible phase-matching wavelengths (1203-1236Å).

The most recent experiments have demonstrated measurable transmission of coherent VUV radiation (1209Å) through the z-pinch plasma at peak compression, using the lowest density condition for which Lyman-α emission profiles were taken ($n_e \sim 2\times10^{24}m^{-3}$ at 5kV, 5 torr). With further improvements in the dye laser output and the VUV detection system sensitivity, detailed Lyman-α absorption measurements in dense plasmas may be possible for the first time in the near future.

6.7 Extension of the Plasma Diagnostics

A second diagnostic of the plasma temperature is desirable in order to check the present estimate based on the relative abundance of the Ar ion species lines. With tunable narrowband dye lasers now available, measurement of the complete Ar II 4880Å line profile in absorption would enable correction for the continuum opacity in the resonance radiation absorption technique described in Section 3.13. Although this temperature diagnostic would be limited by the high continuum opacities at the highest densities in the present experiment, the temperature at the lowest densities could nevertheless be measured as a further check of the comparability of the present plasma conditions with those observed by Baker.

The continuum opacity calculations of Section 3.2.1 indicate that laser-based diagnostics in the UV would be considerably less affected by continuum absorption than would diagnostics employing visible lasers. In particular, Thomson scattering using krypton fluoride excimer laser radiation at 2482Å may be feasible, due to reduced heating of the plasma (Equation 3.1) and to reduced absorption of the incident and scattered radiation.

Experiments at the Rutherford UV Radiation Facility have commenced on the application of Thomson scattering to the present z-pinch plasma using a line-narrowed KrF laser. Since the Debye length in the present plasma was of the order of the interparticle separation (30-50Å), the scattering parameter α (Equation 1.49) will be large ($3 < \alpha < 6$) even for large scattering angles. Hence the scattered profile (assuming a Debye scattering form factor) will be collective and will consist of a strong central ion feature with two electron features at separations of 20-60Å from the ion feature. The electron feature separation ($\propto n_e^{\frac{1}{2}}$) will enable verification of the densities obtained by interferometry (as will a measurement of the total Thomson scattered intensity relative to Rayleigh scattering calibrations). If a correlation of the interferometric and Thomson scattering density measurements were obtained, Thomson scattering would then be applied to the conditions $n_e > 8.5\times10^{24}$ m^{-3} which could not be diagnosed interferometrically.

In this way, the present programme of spectroscopic studies in strongly coupled plasmas might be extended to even higher plasma densities.

REFERENCES

Allen, C.W. (1955) - Astrophysical Quantities, Athlone Press, University of London (3rd Edition).

Allen, J.E. (1957) - Proc. Phys. Soc. B70, 24.

Bacon, M.E. (1973) - J.Q.S.R.T. 13, 1161.

Bacon, M.E. (1977) - J.Q.S.R.T. 17, 501.

Baker, E.A.M. (1977) - Ph.D. Thesis, University of London.

Baker, E.A.M. and Burgess, D.D. (1979) - J. Phys. B. 12, 2097.

Baranger, M. and Mozer, B. (1961) - Phys. Rev. 123 (1), 25.

Baranger, M. (1958) - Phys. Rev. 111 (2), 481.

Bates, D.R. (1952) - M.N.R.A.S. 112 (1), 40.

Bekefi, G. (1966) - Radiation Processes in Plasmas, Wiley, New York.

Berlman, I. (1971) - Handbook of Fluorescence Spectra of Aromatic Molecules, Academic Press, New York.

Bjorklund, G.C. (1975) - I.E.E.E. J. Quant. Elect. 11, 287.

Bowen, J. (1982) - Ph.D. Thesis, University of London.

Burgess, D.D. (1965) - Ph.D. Thesis, University of London.

Burgess, D.D. (1970a) - J.Q.S.R.T. 10, 365.

Burgess, D.D. (1970b) - J. Phys. B 3, L70.

Burgess, D.D. (1978) - in Physics of Ionized Gases, (Proc. Symposium) ed. Janev, Institute of Physics (Belgrade), p.501.

Burgess, D.D. (1982) - in Laser Plasma Interactions, Scottish Universities Summer Schoolsin Physics, St. Andrews (to be published).

Burgess, D.D. and Cooper, J. (1965) - Proc. Phys. Soc. 85, 1261.

Burgess, D.D., Dangor, A.E. and Jenkins, J.E. (1967) - British J. Appl. Phys. 18, 1281.

Chambaud, G., Millie, Ph., Ridard, J. and Levy, B. (1979)- J. Phys. B, 12, 221.

Cohn, A., Bashki, P. and Kalman, G. (1972) - Phys. Rev. Lett. 29(6), 324.

Cotter, D. (1979) - Opt. Comm. 31(3), 397.

Davis, J. and Blaha, M. (1981) - NRL Memorandum Report 4689.

De Michelis, C. and Mattioli, M. (1981) - Nuclear Fusion 21(6), 677.

Dieke, G. and Hopfield, J. (1927) - Phys. Rev. 30(4), 400.

Drawin, H-W. and Felenbok, P. (1965) - Data for Plasmas in L.T.E., Gauthier-Villars, Paris.

Dreyfus, R., Bogen, P. and Langer, H.(1982) - A.I.P. Conf. Proc., Laser Techniques for Extreme UV Spectroscopy; eds. T.J. McIlrath and R.R. Freeman; Boulder, Colorado; p.57.

Drummond, J.E. (1961) - in Plasma Physics, Ch. I, McGraw-Hill, New York.

Dufty, J.W.,(1981) - in Spectral Line Shapes, (Proc. Fifth. Int. Conf., Berlin, 1980), ed. B. Wende, pub. Walter de Gruyter, Berlin, p.41.

Ecker, G. and Kroll, W. (1963) - Phys. Fl., 6 (1), 62.

Evans, D.E. and Katzenstein, J. (1969) - Rep. Prog. Phys. 32, 207.

Finken, K.H., Bertschinger, G., Maurmann, S. and Kunze, H-J. (1978) - J.Q.S.R.T. 20, 467.

Fleurier, C. and Chapelle, J. (1974) - Computer Phys. Comm. 7, 200.

Folkierski, A., Frayne, P.G. and Latham, R. (1962) - Nuc. Fusion Supp. Pt. 2, p.627.

Fussmann,G. (1972) - Phys. Lett. 41A (2), 155.

Fussmann,G. (1975) - J.Q.S.R.T. 15, 791.

Gallagher, C.C. and Levine, M.A. (1973) - Phys. Rev. Lett. 30 (19),897.

Griem, H.R. (1962) - Phys. Rev. 128, 997.

Griem, H.R. (1963) - Phys. Rev. 131 (3), 1170.

Griem, H.R. (1964) - Plasma Spectroscopy, McGraw-Hill, New York.

Griem, H.R. (1974) - Spectral Line Broadening by Plasmas, Academic Press, New York.

Grutzmacher, K. and Wende, B. (1977) - Phys. Rev. A. 16 (1), 243.

Hansch, T.W. (1972) - Appl. Optics 11(4), 895.

Hilbig, R. and Wallenstein, R. (1981) - I.E.E.E. J. Quant. Elect. 17(8), 1566.

Hindmarsh, W.R. and Farr, J.M. (1969) - J. Phys. B. 2(2), 1388.

Hofsaess, D. (1978) - J.Q.S.R.T. 19, 339.

Hooper, C.F. (1968) - Phys. Rev. 165, 215.

Huddlestone, R.H. and Leonard, S.L. (1965) - eds., Plasma Diagnostic Techniques, Academic Press, New York.

Kato, M. (1972) - Phys. Fl. 15, 460.

Kelly, R.L. (1959) - Table of Emission Lines in the VUV (6-2000Å), University of California Report UCRL 5612.

Kelly, R.L. (1968) - Atomic Emission Lines Below 2000Å, N.R.L. Report 6648.

Kielkopf, J.F. and Allard, N.F. (1979) - Phys. Rev. Lett. 43(3), 196.

Kim, Y.S. (1975) - Phys. Rev. A. 11(3), 796 and 804.

Kittel, C. (1971) - Introduction to Solid State Physics 4th edition, Wiley, New York.

Kunze, H-J., Griem, H.R., De Silva, A.W., Goldenbaum, G.C. and Spalding, I.J. (1969) - Phys. Fl. 12, 2669.

Langer, H., Puell, H. and Rohr, H. (1980) - Opt. Comm. 34(1), 137.

Le Quang Rang and Voslamber, D. (1975) - J. Phys. B. 8(2), 331.

Le Quang Rang and Voslamber, D. (1981) - J.Q.S.R.T. 25, 35.

Littman, G.M. and Metcalf, H.J. (1978) - Appl. Optics 17(14), 2224.

Lucatorto, T.B., McIlrath, T.J. and Roberts, J.R. (1979) - Appl. Optics 18(14), 2505.

Mahon, R., McIlrath, T.J. and Koopman, D.W. (1978) - Appl. Phys. Lett. 33, 305.

Mahon, R., McIlrath, T.J. and Koopman, D.W. (1979a) - Appl. Optics 18 (6), 891.

Mahon, R., McIlrath, T.J., Myerscough, V.P. and Koopman, D.W. (1979b) I.E.E.E. J. Quant. Electr. 15(6), 444.

Mattuck, R.D. (1967) - A Guide to Feynman Diagrams in the Many-Body Problem, McGraw-Hill, London.

McCartan, D.G., Farr, J.M. and Hindmarsh, W.R. (1974) - J. Phys. B. 7(2), 208.

McKee, T.J., Lobin, J. and Young, W. (1982) - Appl. Optics 21(4), 725.

More, R.M. (1982) - in Applied Atomic Collision Physics, Vol. II, Academic Press, New York.

Nettleton, D.H. and Preston, R.C. (1980) - NPL report Qu 60.

Niemax, K. (1980) - J. Phys. B. 13, 1791.

Peacock, N.J. (1978) - Culham Report CLM-P519.

Pines, D. and Bohm, D. (1952) - Phys. Rev. 85(2), 338.

Preston, R.C. (1977) - J. Phys. B. 10, 523.

Quefflec, J.L. and Girault, M. (1974) - Comptes Rendues 297B, 649.

Roberts, D.E. (1972) - Phys. Fl. 15(1), 192.

Rohr, H. (1967) - Phys. Lett. 25A, 167.

Salpeter, E.E. (1960) - Phys. Rev. 120(5), 1528.

Sanderson, J.J. (1981) - in Plasma Physics and Nuclear Fusion Research, ed. R.D. Gill, Academic Press, London.

Sando, K.M. and Wormhoudt, J.C. (1973) - Phys. Rev. A. 7(6), 1889.

Schnehage, S.E., Kock, M. and Schulz-Gulde, E. (1982) - J. Phys. B. 15, 1131.

Schulz-Gulde, E. (1970) - Z. Phys. 230, 449.

Seidel, J. (1981)- in Spectral Line Shapes, (Proc. Fifth Int. Conf., Berlin, 1980), ed. B. Wende, pub. Walter de Gruyter, Berlin; p.3.

Sholin, G.V. (1969) - Opt. and Spectr. 26(4), 275.

Smith, C.C. and Burgess, D.D. (1978) - J. Phys. B. 11, 2087.

Sommer, K. (1982) - D.I.C. Thesis, University of London.

Stewart, J.C., Peek, J.M. and Cooper J. (1973) - Astr. J. 179, 983.

Stewart, J.C. and Pyatt, K.D. (1966) - Astr. J. 144(3), 1203.

Stoicheff, B., Banic, J., Herman, P., Jamroz, W., La Rocque, P. and Lipson, R. (1982) - A.I.P. Conf. Proc., Laser Techniques for

Extreme UV Spectroscopy; eds. T.J. McIlrath and R.R. Freeman; Boulder, Colorado; p.19.

Striganov, A.R. and Sventitskii, N.S. (1968) - Tables of Spectral Lines of Neutral and Ionized Atoms, Plenum, New York.

Szudy, J. and Baylis, W.E. (1975) - J.Q.S.R.T. 15, 641.

Tatum, J.B. (1967) - Pub. of the Dominion Astrophys. Observatory, Vol. XIII, no. 1, Victoria, British Columbia.

Theimer, O. (1966) - Phys. Lett. 20(6), 639.

Thorne, A.P. (1974) - Spectrophysics, Chapman and Hall, London.

Vallee, O., Tranh Minh and Chapelle, J. (1979) - J. Phys. B. 12(1), L9.

Vidal, C.R. (1980) - Appl. Optics 19(23), 389.

Vinogradov, A.V., Sobel'man, I.I. and Yukov, E.A. (1974) - Sov. Phys. (Sov. J.Q.E.) 4, 149.

Wallenstein, R. and Zacharias, H. (1980) - Opt. Comm. 32(3), 429.

Weast, R.C. (1974) - ed., Handbook of Chemistry and Physics, 55th Edition, C.R.C. Press, Cleveland.

Weisheit, J.C. and Pollock, E.L. (1981) - in Spectral Line Shapes, (Proc. Fifth Int. Conf., Berlin, 1980), Ed. B. Wende, pub. W. de Gruyter, Berlin, p.433.

Wheeler, C.B. and Troughton, J. (1969) - Plasma Physics 11, 391.

Ya'akobi, B. and Bekefi, G. (1969) - Phys. Lett. 30A(9), 539.

Yiu, Y.M., McIlrath, T.J. and Mahon, R. (1977) - Phys. Rev. A 20, 2470.

Zimmerman, G.B. and More, R.M. (1980) - J.Q.S.R.T. 23, 517.